

ISSN 1220-8434

VOLUME 18, 2010

ACTA
TRIBOLOGICA

University of Suceava, Romania

ACTA TRIBOLOGICA

Volume 18, 2010

ACTA TRIBOLOGICA

A Journal on the Science of Contact Mechanics, Friction, Lubrication,
Wear, Micro/Nano Tribology, and Biotribology

Volume 18, 2010

EDITOR

E. Diaconescu, *University of Suceava, ROMANIA*

EDITORIAL BOARD

N.N. Antonescu, *Petroleum-Gas University of Ploiesti, ROMANIA*

J.R. Barber, *University of Michigan, U.S.A*

Y. Berthier, *INSA de Lyon, FRANCE*

M. Ciavarella, *Politecnico di Bari, ITALY*

T. Cicone, *University Politehnica of Bucharest, ROMANIA*

S. Cretu, *Technical University of Iasi, ROMANIA*

L. Deleanu, *University of Galati, ROMANIA*

D. Dini, *Imperial College London, UNITED KINGDOM*

V. Dulgheru, *Technical University of Moldova, MOLDOVA*

I. Etsion, *Technion, Haifa, ISRAEL*

M. Glovnea, *University of Suceava, ROMANIA*

R. Glovnea, *University of Sussex, UNITED KINGDOM*

I. Green, *Georgia Institute of Technology, U.S.A*

M. Khonsari, *Louisiana State University, U.S.A*

Y. Kligerman, *Technion, Haifa, ISRAEL*

D. Nelias, *INSA de Lyon, FRANCE*

D. Olaru, *Technical University of Iasi, ROMANIA*

M. Pascovici, *University Politehnica of Bucharest, ROMANIA*

M. Ripa, *University of Galati, ROMANIA*

A. Tudor, *University Politehnica of Bucharest, ROMANIA*

ASSISTANT EDITOR

S. Spinu, *University of Suceava, ROMANIA*

University of Suceava, Romania

Published by the Applied Mechanics Section of the University of Suceava

University “Stefan cel Mare” of Suceava Publishing House

13th University Street, Suceava, 720229, Suceava, ROMANIA
Phone: (40) – 0230 – 216 – 147 int. 273, E-mail: editura@usv.ro

CONTENTS

- 1 **A. URZICĂ, S. CRETU**
A Numerical Procedure to Generate Non-Gaussian Rough Surfaces
- 7 **C. CIORNEI, E. DIACONESCU**
Preliminary Theoretical Solution for Electric Contact Resistance between Rough Surfaces
- 12 **C.-I. BARBINTA, S. CRETU**
The Influence of the Rail Inclination and Lateral Shift on Pressure Distribution in Wheel - Rail Contact
- 19 **C. SUCIU, E. DIACONESCU**
Preliminary Theoretical Results upon Contact Pressure Assessment by Aid of Reflectivity
- 27 **S. SPINU**
Numerical Simulation of Elastic-Plastic Contact
- 34 **Y. NAGATA, R. GLOVNEA**
Dielectric Properties of Grease Lubricants
- 42 **J. PADGURSKAS, R. KREIVAITIS, A. KUPČINSKAS, R. RUKUIŽA, V. JANKAUSKAS, I. PROSYČEVAS**
Influence of Nanoparticles on Lubricity of Base Mineral Oil
- 46 **A.V. RADULESCU, I. RADULESCU**
Influence of the Rheometer Geometry on the Rheological Properties of Industrial Lubricants
- 52 **V.-F. ZEGREAN, E. DIACONESCU**
Measurement of Lubricant Oil Microviscosity Based on Resonant Frequency Shift of AFM Cantilever
- 58 **M.C. CORNECI, A.-M. TRUNFIO-SFARGHIU, F. DEKKICHE, Y. BERTHIER, M.-H. MEURISSE, J.-P. RIEU**
Influence of Lubricant Physicochemical Properties on the Tribological Operation of Fluid Phase Phospholipid Biomimetic Surfaces

- 65 S. LE FLOC'H, M.C. CORNECI, A.-M. TRUNFIO-SFARGHIU, M.-H. MEURISSE, J.-P. RIEU, J. DUHAMEL, C. DAYOT, F. DANG, M. BOUVIER, C. GODEAU, A. SAULOT, Y. BERTHIER**
Imagerie Medicale pour Evaluer les Conditions du Fonctionnement Tribologiques des Articulations Synoviales
- 77 M.C. CORNECI, A.-M. TRUNFIO-SFARGHIU, F. DEKKICHE, Y. BERTHIER, M.-H. MEURISSE, J.-P. RIEU, M. LAGARDE, M. GUICHARDANT**
Phospholipides dans le Fluid Synovial - Influence sur le Fonctionnement Tribologique des Articulations Synoviales Pathologiques
- 85 I.C. ROMANU, E. DIACONESCU**
Bioarticular Friction
- 89 A.-M. TRUNFIO-SFARGHIU, M.C. CORNECI, Y. BERTHIER, M.-H. MEURISSE, J.-P. RIEU**
Mechanical and Physicochemical Analysis of the Tribological Operation of Joint Replacements
- 106 D. N. OLARU, C. STAMATE, A. DUMITRASCU, G. PRISACARU**
Rolling Friction Torque in Microsystems
- 113 L. DELEANU, S. CIORTAN**
Evaluating Tribological Damages by 3D Profilometry
- 120 M. RÎPĂ, S. BOICIUC**
Characterisation of Laser Cladding with Ni–Cr–B–Fe–Al Alloy by Profilometric Study of the Scratch Tracks
- 128 M. VLASE, A. TUDOR**
An Analytical Wear Model of the Pipes for Concrete Transportation

Ana URZICĂ
e-mail: sf_ana8107@yahoo.com

Spiridon CREȚU
e-mail: spcretu@mail.tuiasi.ro

Department of Machine Design,
Technical University of Iași,
ROMANIA

A NUMERICAL PROCEDURE TO GENERATE NON-GAUSSIAN ROUGH SURFACES

The paper presents an algorithm for computer simulation of non-Gaussian surfaces. By using a random number generator, a input matrix is formed as a first representation of a Gaussian roughness with zero mean, and unit standard deviation. The autocorrelation function was assumed to have an exponential form. To fulfill this requirement, in the first step, the matrix containing the roughness heights was obtained by a linear transformation of the input matrix. In the second step the *skewness* and *kurtosis* of the input sequence have been established for the desired *skewness* and *kurtosis* of an output sequence. Finally the non-Gaussian random series have been generated by using the Johnson translator system.

The numerical results pointed out that the developed algorithm can be further used to simulate manufacturing processes that produce real surfaces which may present a non-Gaussian distribution, as well as the abrasive wear and running in phenomena.

Keywords: roughness, autocorrelation, skewness, kurtosis

1. INTRODUCTION

Both experimental and numerical studies have pointed out that roughness acts as stress concentration sites and induce stresses greater than in an equivalent smooth contact. The real areas of contact and the asperity contact pressures are essential parameters for any wear modeling. These parameters can vary significantly depending on surface topography. A small change in the distribution of heights, wave length and curvature of the surface roughness can have a noticeable effect on the deformation behaviors of the rough surfaces.

Manufacturing processes produce real surfaces which are sometimes quite different from Gaussian distribution. For example, a lathe turned surface is far from random; its peaks are nearly all the same height and its valley nearly all the same depth. A ground surface which is subsequently polished so that the tips of the higher asperities are removed departs markedly from being Gaussian.

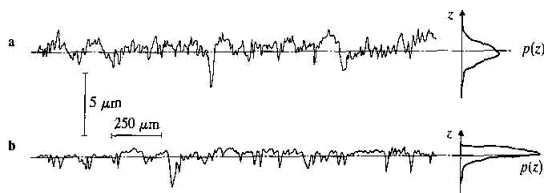


Figure 1. The changes in profile caused by running in and abrasive wear

Similar profiles are presented by surfaces that had carried out abrasive wear or running in processes, Figure 1.

Any parametric study involving roughness requires surfaces with known statistical proprieties and it is much more convenient to generate them numerically rather to measure manufactured rough surfaces. An essential requirement for any numerical algorithms for roughness simulation is their abilities to generate rough surface which have statistical proprieties similar to real surfaces.

Most of the statistical proprieties of a rough surface can be derived from knowledge of two statistical functions: the frequency density function and the autocorrelation function, Bakolas V. [1], Bushan B. [2], Greenwood J.A. [6], Robbe - Valloire F. [11]. J.Mc.Cool [9] shows that it is possible to describe any statistical distribution through knowledge of only four central moments of cumulative distribution function of probabilities.

Consequently, a good algorithm should be able to generate surfaces having prescribed frequency density functions and autocorrelation functions.

The developed procedure starts from the imposed values for the normalized central moments: the mean height, R_a , standard deviation R_q , *skewness* parameter S_k , *kurtosis* parameter K , as well as for the correlation lengths λ_x , λ_y , of the autocorrelation function.

2. SPATIAL AND SPECTRAL PARAMETERS OF ROUGHNESS

2.1 Probability Density Function (PDF)

If for convenience z was measured from the mean plane of the surface, then the height $z(x, y)$ of a rough surface may be considered as a two-dimensional random variable. The spatial characteristics can be adequately described with the use of probability function $p(z)$ which denotes the probability that a point on the surface has a height equal to z . It has been found, Bakolas V. [1], Bhushan B. [2], Patir N. [10], that many real surfaces, notably freshly grounded surfaces, reveal a height distribution which is close to the normal Gaussian probability function:

$$p(z) = \frac{\sigma}{\sqrt{2\pi}} \exp\left(-\frac{z^2}{2\sigma^2}\right), \quad (1)$$

where σ is the standard (r.m.s.) deviation from the mean height.

The shape of the probability function can provide useful information about the nature of the roughness profile. A mathematical presentation of this shape is provided by the moments of the probability density function about the mean.

2.2 The normalized moments of PDF

The first normalized central moment is the mean height, R_a which is generally removed before data processing and is therefore zero:

$$R_a = \int_{-\infty}^{\infty} z \cdot p(z) \cdot dz. \quad (2)$$

The second moment is the variance R_q^2 of the roughness heights, meaning the standard deviation R_q , or the root mean square (r.m.s.) σ , of the surface heights:

$$\sigma^2 = \int_{-\infty}^{\infty} z^2 \cdot p(z) \cdot dz. \quad (3)$$

The third normalized central moment is called „skewness”:

$$Sk = \frac{1}{\sigma^3} \int_{-\infty}^{\infty} z^3 \cdot p(z) \cdot dz. \quad (4)$$

The *skewness* parameter represents a measure of the symmetry of the statistical distribution. Symmetrical distributions have *skewness* equal to 0, which means that they have evenly distributed peaks and valleys of specific height. Profiles with high peaks and shallow valleys present a positive *skewness*, while profiles with larger valleys than peaks present a negative *skewness*, Figure 2.

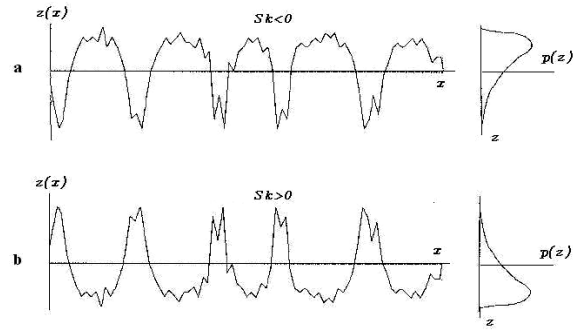


Figure 2. Profiles with different degrees of asymmetry and the shapes of PDF

The fourth normalized central moment is called „kurtosis”:

$$K = \frac{1}{\sigma^4} \int_{-\infty}^{\infty} z^4 \cdot p(z) \cdot dz. \quad (5)$$

Kurtosis represents the spikiness of the statistical distribution and is a measure of the degree of pointedness or bluntness, Figure 3. Symmetric Gauss distribution has a *kurtosis* of 3, Figure 4.

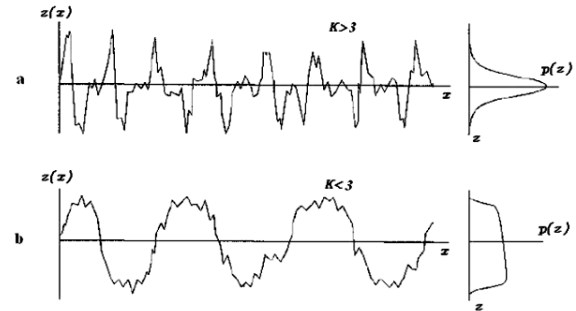


Figure 3. Profiles with different *kurtosis* values and the shapes of PDF

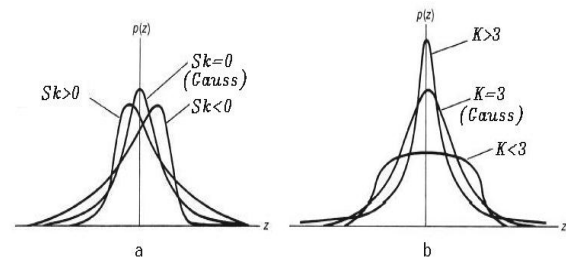


Figure 4. PDF for random distributions with different skewness values (a), and for symmetrical distributions ($Sk=0$) with different *kurtosis* values (b)

Typical *skewness* and *kurtosis* envelopes for various manufacturing technologies are presented in the Figure 5.

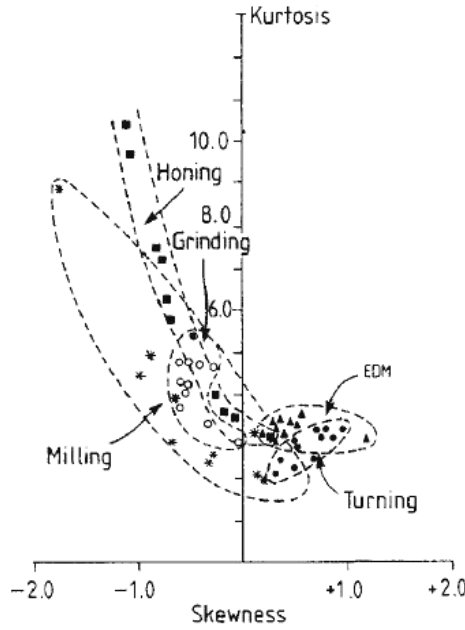


Figure 5. *Skewness and kurtosis values for some manufacturing technologies*

3. NUMERICAL GENERATION OF NON-GAUSSIAN RANDOM SURFACES

A 2D digital filter, as suggested by Hu and Tonder [8], has been involved to change the input sequence $\eta(k, \ell)$ into an output sequence $z(I, J)$:

$$z(I, J) = \sum_{k=0}^{n-1} \sum_{\ell=0}^{m-1} h(k, \ell) \eta(I-k, J-\ell), \quad (6)$$

$$I = 0, 1, \dots, N-1; \quad J = 0, 1, \dots, M-1; \quad n = N/2 \\ m = M/2,$$

where the $h(k, \ell)$ is the digital filter function.

To establish the filter function $h(k, \ell)$ the following steps has to be fulfilled:

1. Obtain the autocorrelation function (ACF) and the power spectral density (PSD) for the input sequence η .
2. Simulate a random matrix (surface) with a negative exponential function for the ACF.
3. Obtain the PSD for the new random matrix with negative exponential function for the ACF.
4. Determine the digital filter function.
5. Determine the needed *skewness* Sk_η and *kurtosis* K_η of the input sequence for desired *skewness* and *kurtosis* of an output sequence.
6. Generate a non-Gaussian random series η' by using Johnson translator system.

The steps 1 – 4 have been previously presented by Cretu [3,4] and will not be further discussed in the present paper.

3.1 Determine the skewness Sk_η and kurtosis K_η of the input sequence

To generate a rough surface which has a non-Gaussian distribution, the procedure will be to transform the input sequence into a output sequence which has similar values with the values we wish to impose for *skewness* and *kurtosis*. To obtain the *skewness*, Sk_z and *kurtosis*, K_z close to the required values, the following equation was used:

$$Sk_z = \frac{\sum_{i=1}^q \theta_i^3}{\left(\sum_{i=1}^q \theta_i^2\right)^{\frac{3}{2}}} Sk_\eta; \quad (7)$$

$$K_z = \frac{K_\eta \sum_{i=0}^q \theta_i^4 + 6 \sum_{i=0}^{q-1} \sum_{j=i+1}^q \theta_i^2 \theta_j^2}{\left(\sum_{i=1}^q \theta_i^2\right)^2}. \quad (8)$$

These relationships have been proposed by Watson and Spending [12] and are valid for linear transformation of the form:

$$x_z = \theta_0 \eta_x + \theta_1 \eta_{x-1} + \theta_2 \eta_{x-2} + \dots + \theta_{q-1} \eta_{x-q+1} + \theta_q \eta_{x-q}; \quad (9)$$

where Sk_z , K_z and are the required *skewness* and *kurtosis*, and Sk_η , K_η are the input *skewness* and *kurtosis* for Johnson's translator system, and

$$\theta_i = h(k, \ell); \quad (10)$$

$$i = (k-1)m + \ell; \quad k = 1, 2, \dots, n; \quad \ell = 1, 2, \dots, m$$

The validity of the following algebraic equation:

$$\sum_{i=1}^{q-1} \sum_{j=i+1}^q (\theta_i^2 \theta_j^2) = \frac{1}{2} \left[\left(\sum_{i=1}^q \theta_i^2 \right)^2 - \sum_{i=0}^q \theta_i^4 \right] \quad (11)$$

allows to obtain a simpler form for the *kurtosis* parameter:

$$K_z = \frac{\sum_{i=0}^q \theta_i^4}{\left(\sum_{i=1}^q \theta_i^2\right)^2} (K_\eta - 3) + 3. \quad (12)$$

When arbitrary *skewness* and *kurtosis* are set, they must fulfill the following relationship:

$$K_z - Sk_z - 1 \geq 0. \quad (13)$$

3.2 Generation of the non-Gaussian random series η' by using the Johnson translator system

The non-Gaussian random series with different *skewness* can be generated by using the Johnson translator system. The Johnson system was presented in their works by W.P.Elderton and N.L.Johnson [5] and V.Bakolas [1]. The Johnson system of frequency curves is based on the method of moments and provides some curves that can be used to generate a random distribution for which the four moments are known. The Johnson system uses three main conversion curves: S_U , S_B and S_L :

$$S_U: \eta = \gamma + \frac{\delta}{\sinh\left(\frac{\eta' - \xi}{\lambda}\right)}; \quad (14)$$

$$S_L: \eta = \gamma + \delta \cdot \ln\left(\frac{\eta' - \xi}{\lambda}\right) \quad (\eta' > \xi); \quad (15)$$

$$S_B: \eta = \gamma + \delta \cdot \ln\left(\frac{\eta' - \xi}{\xi + \lambda - \eta'}\right) \quad (\xi < \eta' < \xi + \lambda) \quad (16)$$

where:

- η is a sequence of random numbers with normal distribution, $m = 0$, $\sigma = 1$, $Sk = 0$ and $K = 3$;
- η' is the sequence of random number derived with desired values for the parameters *skewness* and *kurtosis*, $Sk_{\eta'}$ and $K_{\eta'}$;
- γ, δ, ξ and λ are constants to be determined for the first four given moments by using method of moments.

The initial distribution of random number had to be chosen to follow a statistical distribution that ensures the following constraints:

- the average value is zero, ($m = 0$);
- standard deviation equal to unity, ($\sigma = 1$);
- the required value for *skewness* parameter, Sk ;
- the required value for *kurtosis* parameter, K .

4. RESULTS

Three-dimensional surfaces maps of the non-Gaussian random numbers with zero mean and unit variance and the autocorrelation length $\lambda_x = \lambda_y = 1 \mu\text{m}$, but different *skewness* (Sk) and *kurtosis* (K) values, are presented successively in the Figure 6.

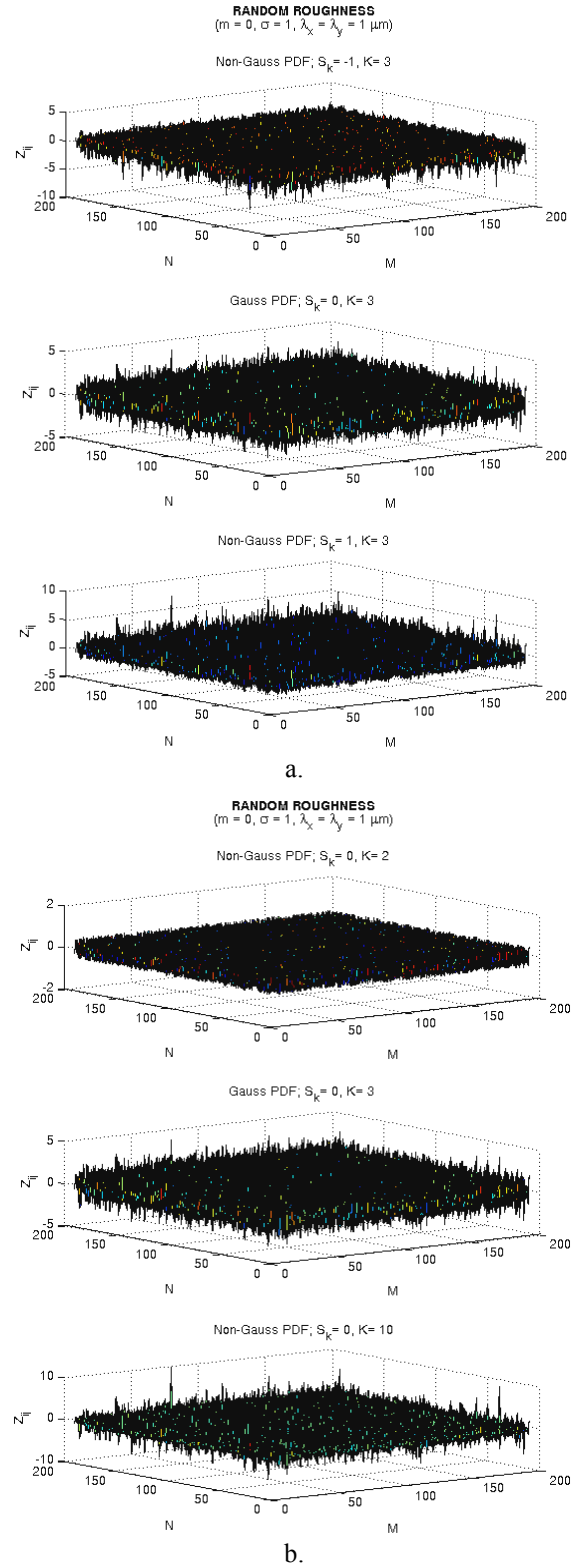


Figure 6. 3D random matrices with different a. *skewness* (Sk); b. *kurtosis* (K)

In Figure 6a the *skewness* parameter was changed between limits while the *kurtosis* function maintained the value $K = 3$. In the same manner, in Figure 6b the *kurtosis* parameter was changed between limits while the *skewness* function maintained the value $Sk = 0$.

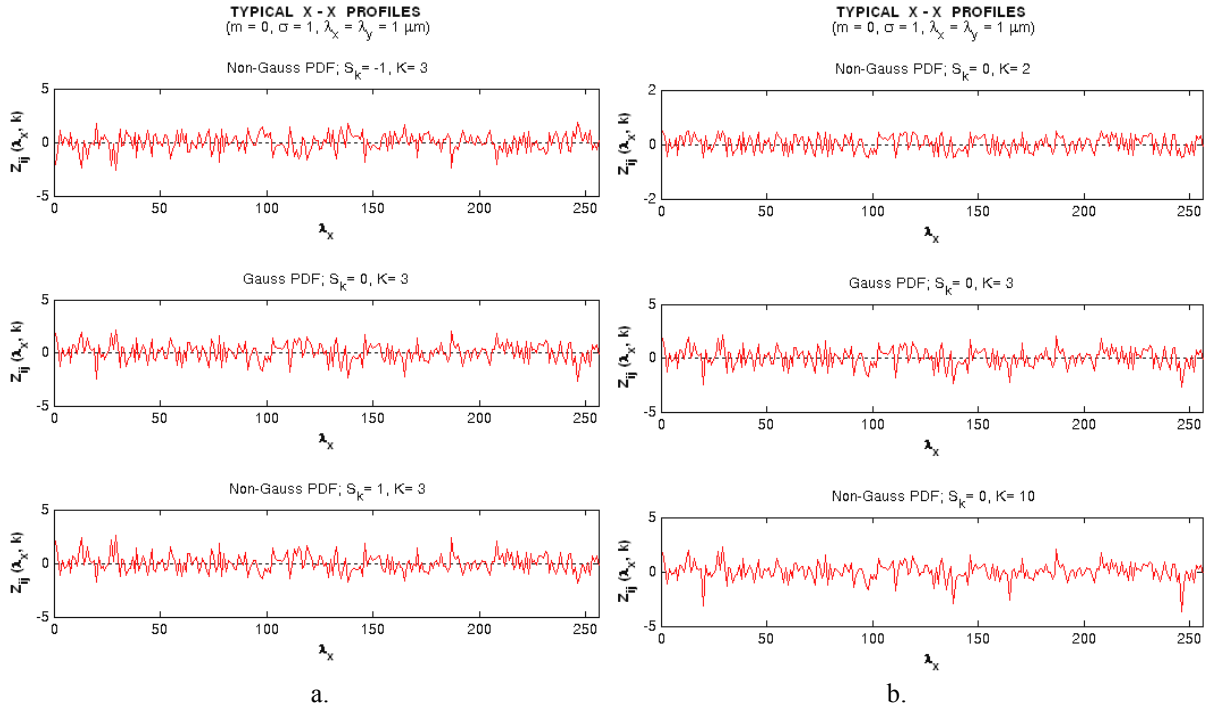


Figure 7. 2D profiles of the random matrices with different (a) *skewness* (Sk) and (b) *kurtosis* (K)

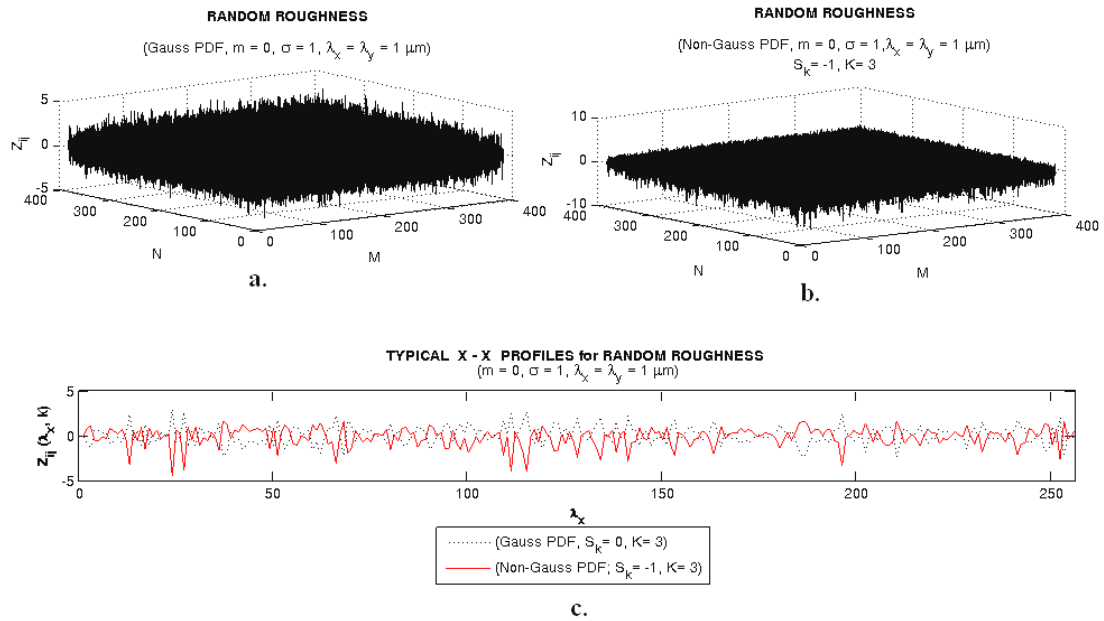


Figure 8. 3D random simulation for a worn surface and the corresponding 2D profiles

To highlight the effect of varying the *skewness* and *kurtosis* parameters on the general shape of the profile, the Figure 7 presents extracted profiles along the x - x direction of surfaces represented in Figure 6.

A worn surface is characterized by negative values for the *skewness* function while the *kurtosis* function has values equal or greater than 3, so that the values $Sk = -1$ and $K = 3$ have been chosen for the numerical simulation.

The Gaussian random matrix is presented in the Figure 8a, while the non-Gaussian random

matrix with imposed values for the *skewness* and *kurtosis* functions is presented in the Figure 8b. The correspondent profiles of the two matrices are given in the Figure 8c.

5. CONCLUSIONS

1. Manufacturing processes provide real surfaces that may be quite different from Gaussian. A ground surface which is subsequently polished departs markedly from being Gaussian; similar

surfaces are caused by abrasive wear or running in processes.

2. By using a random number generator an input matrix is formed as a first representation of a Gaussian roughness with zero mean, ($m = 0$), and unit standard deviation, ($\sigma = 1$). The autocorrelation function was assumed to have an exponential form. To fulfill this requirement, the matrix containing the roughness heights was obtained by a linear transformation of the input matrix.

3. To simulate the non-Gaussian surface, the *skewness* and *kurtosis* of the input sequence has been established for the desired *skewness* and *kurtosis* of an output sequence. Finally the non-Gaussian random series has been generated by using the Johnson translator system.

4. The developed algorithm can be used to simulate manufacturing processes, abrasive wear or running in phenomena. This kind of simulation can be further incorporated into a particular stress analysis for tribological designs or contact failure predictions.

ACKNOWLEDGEMENT

This paper was realized with the support of BRAIN "Doctoral scholarships as an investment in intelligence" project, financed by the European Social Found and Romanian Government.

REFERENCES

1. **Bakolas V.**, 2003, "Numerical Generation of Arbitrarily Oriented Non-Gaussian Three-

Dimensional Rough Surfaces". *Wear*, 254, pp. 546-554.

2. **Bushan B., Kim T.W. and Cho Y.J.**, 2006, "The Contact Behavior of Elastic/Plastic non-Gaussian rough surfaces". *Tribology Letters*, 22, pp. 1-12.

3. **Crețu S. Sp.**, 2006, "Random Simulation of Gaussian Rough Surfaces. Part 1- Theoretical Formulations.", *Bul. IPI, LII (LVI)*, 1-2, pp. 1-17.

4. **Crețu S. Sp.**, 2006, "The Influence of the Correlation Length on Pressure Distribution and Stresses State in Elastic-Plastic Rough Contacts", *IJTC-2006*, paper 12339, San Antonio, TX, USA.

5. **Elderton W.P. and Johnson N.L.**, 1969, "System of Frequency Curves." *Cambridge University Press*, London.

6. **Greenwood J.A., Wu J.J.**, 2001, "Surface Roughness and Contact: An Apology." *Meccanica*, 36, pp. 617-630.

7. **Hill I.D., Hill R., Holder R. L.**, 1976, "Fitting Johnson's Curves by Moments." *Applied Statistics*, 25, pp. 180-189.

8. **Hu Y.Z. and Tonder K.**, 1992, "Simulation of 3-D Random Rough Surface by 2-D Digital Filter and Fourier Analysis.", *Int. J. Mach. Tools Manufact.*, Vol. 32, pp. 83-90.

9. **McCool J.**, 1986, "Comparison Models for the Contact of Rough Surfaces.", *WEAR*, 107, pp. 37-60.

10. **Patir N.**, 1978, "A Numerical Procedure for Random Generation of Rough Surfaces.", *Wear*, 263-277.

11. **Robbe-Valloire F.**, 2001, "Statistical Analysis of Asperities on a Rough Surface.", *Wear*, 249, pp. 401-408.

12. **Watson W. and Spedding T.A.**, 1982, "The Time Series Modelling of Non-Gaussian Engineering Processes.", *Wear*, 83, pp. 215-231.

Cristina CIORNEI
email: *tina_criss2005@yahoo.com*

Emanuel DIACONESCU
email: *emdi@fim.usv.ro*

Department of Mechanical Engineering,
Stefan cel Mare University of Suceava,

ROMANIA

PRELIMINARY THEORETICAL SOLUTION FOR ELECTRIC CONTACT RESISTANCE BETWEEN ROUGH SURFACES

In contacts design, it is important to know the contact pressure, the real contact area and the electrical contact resistance. This depends on the material conductivity, on the geometry of the contacting surfaces, on the applied load and on the current through the contact. This paper aims to determine numerically, by CG-DCFFT technique, contact area configuration and dimensions, in the case of rough surfaces. Knowing the microcontact areas configuration and dimensions, the electrical resistance is computed with analytical formulas.

Keywords: numerical simulation, electrical contact resistance, CG-DCFFT

1. INTRODUCTION

When electric current passes through a contact, the size of the contact area has an important influence on the contact resistance characteristics due the constriction of the current lines at very small contact areas. In theory, it was proved that up to the nano-scale, the contact conductance, which is the reverse of the electrical resistance, is proportional to the contact domain perimeter. At nano-scale, the contact conductance is proportional to the contact area [1].

Analytical approaches of contact problems are limited to a small number of contact geometries and therefore numerical solution was imposed. Since this requires meshes with large numbers of nodes in the estimated contact domain, unconventional fast numerical methods, such as the multi-level multi-summation (MLMS) and the fast Fourier transform (FFT) techniques, have been developed. The best known algorithm was proposed by Polonsky and Keer [2]. The most efficient method in terms of computational effort combines the Discrete Convolution Fast Fourier Transform (DCFFT) algorithm with the conjugate gradient (CG) method [3]. Creu [4] developed a fast and original algorithm based on CG-FFT to study the finite length line contact. Spinu [5] implemented a CG algorithm similar to that proposed in [2], where the MLMS routine was replaced with one based on the DCFFT technique.

This study aims to find the shape and dimensions of total contact area, as well as individual micro-areas, using the CG-DCFFT method combined with contact resistance calculus for rough surfaces under normal loading.

2. FORMULATION

A contact between a curved rough surface and a flat is considered. Coordinate system origin is established in the common plane of contact, namely the plane tangential to both bodies if they were smooth enough and would initially form a point contact. In this plane, analysis domain is divided into elements of the same size, centered on grid nodes.

To describe the initial contact, the geometry was acquired using a 3D scanner. The obtained data, namely heights associated to nodes of a uniformly spaced rectangular grid with M lines and N columns, represent the surface topography of the equivalent punch. Consequently, punch geometry is inserted as a matrix describing the digitized topography of the rough surface.

The digitization of the equations and inequalities which describe the elastic contact problem lead to the following formulation [5]:

$$r_{ij} = w_{ij} + z_{ij} - \delta, \quad (i, j) \in D; \quad (1)$$

$$w_{ij} = \sum_{k=1}^M \sum_{\ell=1}^N K_{|i-k||j-\ell|} \cdot p_{k\ell}, \quad (i, j) \in D; \quad (2)$$

$$Q = ab \cdot \sum_{i=1}^M \sum_{j=1}^N p_{ij}; \quad (3)$$

$$r_{ij} = 0, \quad p_{ij} > 0, \quad (i, j) \in A; \quad (4)$$

$$r_{ij} > 0, \quad p_{ij} = 0, \quad (i, j) \in D \setminus A; \quad (5)$$

where \mathbf{r} is the gap between the deformed surfaces, \mathbf{w} is the total displacement in z -axis direction, \mathbf{z} is the initial contact geometry, \mathbf{K} is the influence

coefficients matrix, \mathbf{p} is the contact pressure, $M \cdot N$ is the number of grid nodes, $a \cdot b$ is the area of the elementary cell, A is the real contact area, D is the analysis domain and Q is the static force. The system is to be solved in pressures in the contact area, namely the set of nodes in contact.

In the DC-FFT algorithm, which is efficient in both computational time and storage, the linear convolution is computed as a cyclic convolution. The influence coefficients $K(i-k, j-l)$, which represents the deflection of a node (i, j) due to a uniform pressure acting on the rectangular element (k, l) , is obtained using closed-form expressions [6]. The influence coefficients matrix \mathbf{K} , of size $M \cdot N$, is symmetric and positive definite, which leads to application of methods like Steepest Descent or Conjugate Gradient. If the mesh is uniform, \mathbf{K} has at most $M \cdot N$ distinct elements. The extension of the two members of convolution is made differently. The pressure domain is extended with a ratio of two in every direction, by maintaining the original pressures in place and by completing the rest of positions with zeros. This technique, called zero-padding, differs from the one used for the influence coefficients matrix, namely zero-padding and wrap-around order, which is described in [5]. Then, \mathbf{p} and \mathbf{K} are transferred from the space domain into frequency domain, by applying a two-dimensional fast Fourier transform to the extended matrix. The domain extensions are removed and only the real part of convolution is retained.

By combining the DCFEFT technique with conjugate gradient method, an efficient algorithm for the resolution of pressure distribution and contact area is obtained. Since the computational process is iterative, a initial guess value for pressures is required. The starting nodal pressures must be all positive and must obey the static equilibrium condition (3). In the case of electrical contacts, where the load is applied centrally, the initial guess value is the mean pressure acting on the potential contact domain:

$$p_{ij} = p_m = \frac{Q}{MaNb} = \frac{Q}{L_1 L_2}, \quad (i, j) \in D \quad (6)$$

A distinctive feature of this scheme is that the normal displacement is not computed during the iterative process. In most contact solvers, the displacement is subject to the outermost level of iteration, in order to satisfy the force balance equation. Here, this is imposed by updating the pressure distribution at each iteration, according to the relation between numerical and imposed load.

3. ELECTRICAL CONTACT RESISTANCE

The contact resistance is the electrical resistance the current has to overcome when passing

through a closed contact. In the case of clean metallic surfaces, electrical contact resistance is defined of the constriction of the lines current, when is forced to pass through a small contact area. For a circular monocontact, the contact resistance is given by Holm's formula [7]:

$$R_c = \frac{\rho}{2a}, \quad (7)$$

where ρ is the contact material resistivity and a is the contact radius.

For an elliptic monocontact, the expression for resistance is:

$$R_c = \frac{\rho}{\pi(a+b)} U(m), \quad m = \frac{b-a}{b+a}, \quad (8)$$

where $U(m)$ is a elliptic integral of the first kind.

For a contact having a square area of side L , the resistance is [8]:

$$R_c = 0,868 \frac{\rho}{L}, \quad (9)$$

while for a rectangular contact, of width w and length ℓ :

$$R_c = 0,868 \frac{\rho}{\sqrt{w \cdot \ell}}. \quad (10)$$

One can observe that contact resistance is inversely proportional to the contact perimeter, not to the contact area. These formulas are valid in case of smooth surfaces. In real cases, the surfaces of the contact elements are not smooth, but have an inherent roughness. Therefore, a single contact is no longer established between the two bodies, but a multiple contact, formed by many spots created between asperities.

Usually, the micro-contacts are made in the form of revolution bodies, so that when two elements are brought into contact, they do not form a single point contact, but an assembly of individual contacts. Under load, instead of contact nominal surface, many individual contact areas will form. In this case, current flows through contact micro-areas, namely at their peripheries. The electrical contact resistance is proportional to the radius of the contact between the asperities. To determine the contact resistance of such a contact, roughness distribution is assumed to be homogeneous. The asperity tips are assumed spherical and form an elementary Hertz contact, of radius a , while R is the contact radius assumed smooth and computed with Hertz formula. Since these contacts are electrically independent, the resistance of the micro-contacts is given by their parallel resistance. Experimental tests show that the contact resistance is bigger than parallel resistance due to interactions between micro-contacts and lines

current flow distribution. The micro-contacts are not independent, due to field pattern division. In such a situation, the electrical contact resistance is given by:

$$R_c = \frac{\rho}{2na} + \frac{\rho}{2R\sqrt{n}}, \quad (11)$$

where n is the number of micro-contacts.

To obtain a smaller contact resistance, one must act on the contact macro and micro-geometries. Therefore, to achieve a uniform current distribution on the contact area, it is required that the tip radius and maximum pressure are the same on all asperities. Maximum Hertz pressure depends on the local load which is proportional to the mean contact pressure, namely to the contact pressure between the equivalent smooth surfaces. In order to obtain a more uniform distribution of current density over contact area, the pressure between equivalent smooth surfaces must be as uniform as possible. Contact pressure optimization is realised by rounding the edge concentrators in a contact between a flat ended rigid punch and an elastic half-space. The pressure distribution is computed by a simple numerical method [9]. Uniform contact pressure can not be obtained for a flat equivalent punch, but by using a curved surface, crowned towards the middle.

These formulas are valid up to the micro and submicroscopic scale, namely up to approximately 10 nm.

At nano-scale, the contacts behave differently. A nano-contact is a contact between two macroscopic bodies of a size comparable to electron average mean free path; ballistic phenomena occur. Usually, the size area of nano-contacts is less than 40 nm. Thus, at nano-scale the contact resistance is given by Sharvin's formula [10]:

$$R_c = \frac{4\rho\lambda}{3\pi a^2}, \quad (12)$$

where λ is the electron average mean free path and a is the transversal section radius. This formula is valid only in the case where the contact size is smaller than electron average mean free path.

4. RESULTS

The real surfaces were measured with an optical profilometer. Using conversion of the measured data in ASCII form, rough contact geometry was inputted to the described numerical program. Pressure distribution and real contact area between a curved rough surface and a smooth plane were obtained. The values of applied force ranged from 0.01 N to 0.7 N. Electroplated gold micro-contacts were used, whose curvature radii are less

than 1 mm. Figure 1 illustrates typical contact pressures for a 255x255 [$\mu\text{m} \times \mu\text{m}$] domain, meshed in a 256x512 grid.

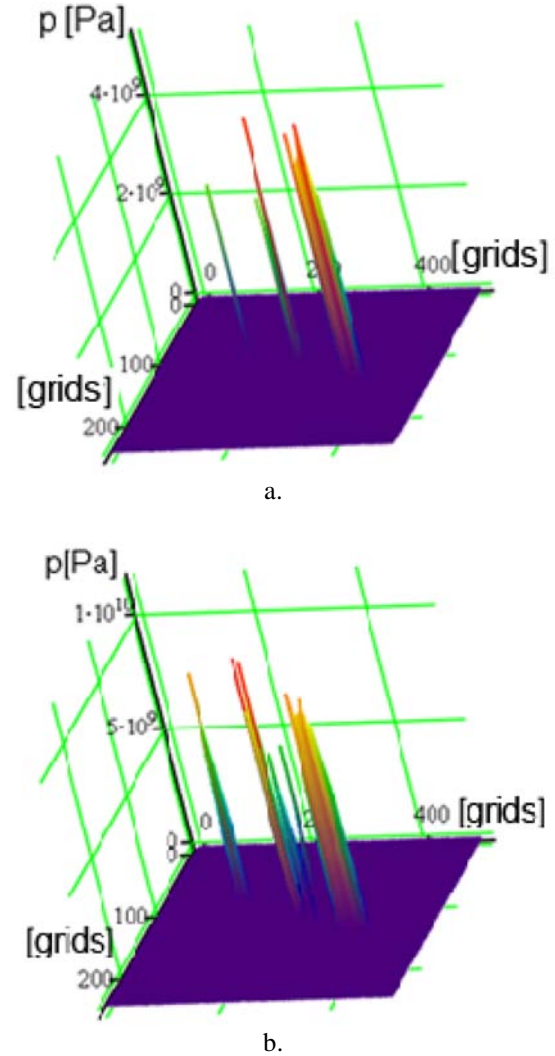


Figure 1. Pressure distribution at 0.1 N (a) and 0.4 N (b)

Figure 2 illustrates the variation of real contact area at different loads. One can observe that as force increases, the number of asperities brought into contact also increases.

The numerical program yields the pressure distribution, the number of micro-contacts, and their shape and dimensions also. At the considered loads, because the punch surface asperities have an ellipsoidal shape and the meshed domain is divided into rectangular elements, the micro-contacts are also rectangular and distributed within the apparent contact area, which is also rectangular in shape. Therefore, equation (10) is employed to assess the contact resistance. The global micro-contacts resistance is found by summing parallel and interaction resistances. Figure 3 illustrates the obtained dependence of conductance on the real area and perimeter.

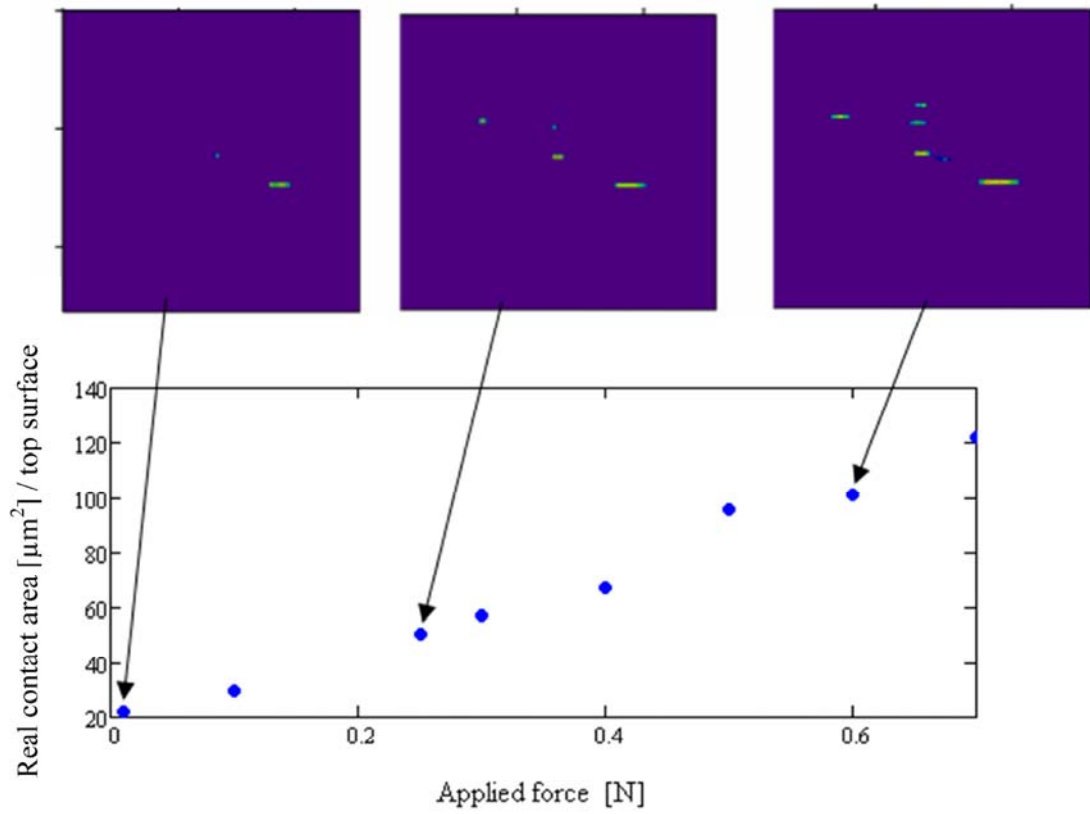


Figure 2. Dependence between real contact area and applied force

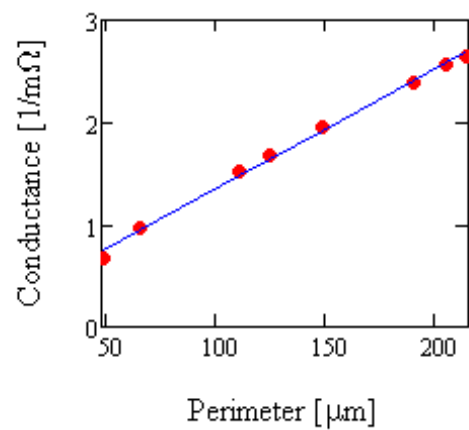
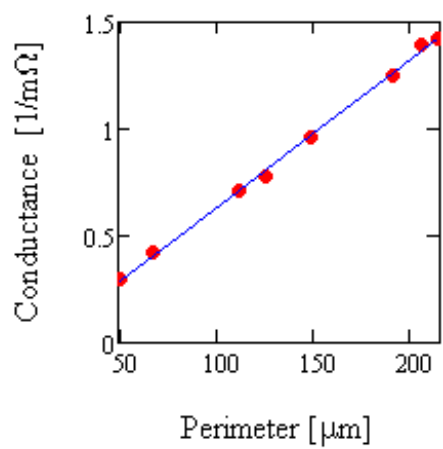
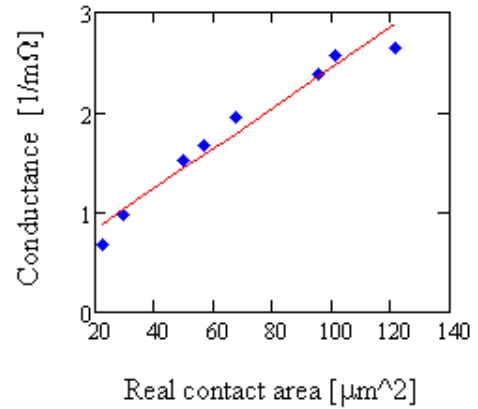
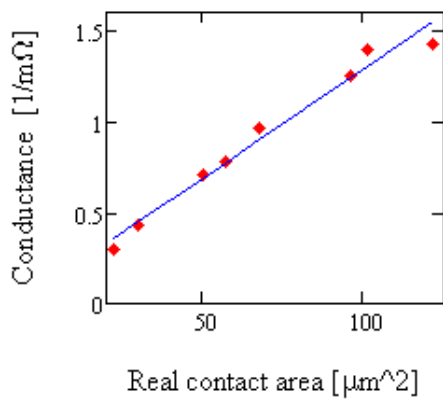


Figure 3. Contact resistance dependence on contact area and perimeter

Figure 4. Contact resistance dependence on contact area and perimeter for elliptical micro-contacts

If micro-contacts are considered elliptical, the resistance is computed using equation (8). Conductance dependence on contact area and on perimeter are depicted in Figure 4. In this case, conductance has higher values.

5. CONCLUSIONS

The work reported herein can be summarized by the conclusions reviewed below.

Theoretical investigations of the electrical contact resistance show that its inverse counterpart, the conductance, is proportional to the contact circumference in macro and micro-contacts. In nano-contacts, the conductance is proportional to the contact area.

From a mechanical point of view, improving or optimizing electrical contacts means altering micro-asperity surfaces according to a polynomial law, so that the micro-contact areas increase rapidly with the load, leading to a low contact resistance even at low loading levels.

The present numerical model can be used to compute the shape and dimensions of total contact area, as well as individual micro-areas for rough surfaces under normal loading.

Reported results show that contact resistance decreases when the load increases, and that contact conductance depends linearly on the contact area circumference, in agreement with general theory.

REFERENCES

1. **Gloneva, M.**, 2006, *Investigations upon micro and nanocontacts with MEMS applications* (in Romanian), Research Report, Grant CNCISIS.
2. **Polonsky, I.A., Keer, L.M.**, 1999, "A Numerical Method for Solving Rough Contact Problems Based on the Multi-Level Multi-Summation and Conjugate Gradient Techniques," *Wear*, 231, pp. 206-219.
3. **Gr dinaru, D.**, 2006, *Model ri numerice în teoria contactului elastic* (in Romanian), PhD Thesis, Suceava, Romania.
4. **Cre u, S., Antaluca, E., Cre u, O.**, 2003, "The Study of Non-Hertzian Concentrated Contacts by a CG-DCFFT Technique," *Rotrib'03 National Tribology Conference*, Gala i.
5. **Spinu, S., Gradinaru, D., Marchitan, M.**, 2006, "FFT Analysis of Elastic Non-Hertzian Contacts – Effect of Rounding Radius upon Pressure Distribution and Stress State," *VAREHD 13*, Suceava.
6. **Johnson, K.L.**, 1985, *Contact Mechanics*, Cambridge University Press.
7. **Holm, R.**, 2000, *Electrical Contacts Theory and Application*, 4th edn, Springer Verlag, Berlin, Heidelberg, New York.
8. **Braunovic, M., Konchits, V.V, Myskin, N.K.**, 2006, *Electrical Contacts. Fundamental, Applications and Tehnology*, CRC Press, Boca Raton, London, New York.
9. **Gloneva, M., Diaconescu, E.**, 2006, "Improvement of Punch Profiles for Elastic Circular Contacts," *Transactions of the ASME, Journal of Tribology*, Vol. 128, July 2006, 486 – 492.
10. **Sharvin, Y.V.**, 1965, "A Possible Method For Studying Fermi Surfaces," *Soviet Physics Jetr*, Vol. 21, pp. 65.

Constantin-Ioan BARBINȚĂ
e-mail: costelbarbinta@yahoo.com

Spiridon CREȚU
e-mail: spcretu@mail.tuiasi.ro

Machine Design Department
"Gheorghe Asachi" Technical University – Iasi
ROMANIA

THE INFLUENCE OF THE RAIL INCLINATION AND LATERAL SHIFT ON PRESSURE DISTRIBUTION IN WHEEL - RAIL CONTACT

Even though the UIC60 wheel profile and the S1002 rail are the most used combination in the European rail transportation, the interoperability is affected by the different rail inclination that varies between the values of 1/40 and 1/20. The hunting motion and the specific train motion in curve determine a permanently lateral shift of the axle and, consequently, a permanent change of the initial wheel-rail contact point. To find out the influence of these modifications on pressure distributions, a fast and robust algorithm has been used to solve the stress state in the general case of non-Hertzian contacts. Brent's method has been involved to find the contact point for the unload conditions. To limit the pressure, an elastic-perfectly plastic material has been incorporated into the computer code.

Keywords: rail, wheel, lateral shift, rail inclination, pressure distributions

1. INTRODUCTION

The running, as well as the reliability of the wheel-rail unit, are based on the phenomena developed within the concentrated contact loading.

Even though the UIC60 wheel profile and the S1002 rail are the most used combination in the European rail transportation, the interoperability is affected by the different rail inclination that varies between the values of 1/40 (Germany and Austria), 1/30 (Sweden) and 1/20 (France and Romania).

On the other hand, the hunting motion and the specific train motion in curve determine a permanently lateral shift of the axle and, consequently, a permanent change of the initial wheel-rail contact point.

The problem was first solved by Carter by regarding the wheel-rail contact as a cylinder rolling over a plane (a two-dimensional problem), (see Ayasse, [1], Enblom, [2]).

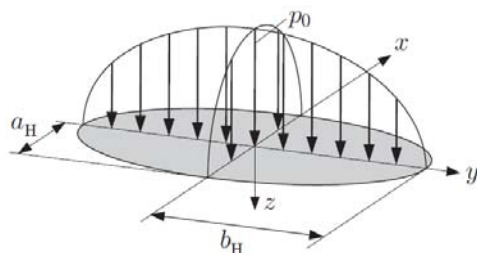


Figure 1. The contact ellipse and ellipsoidal pressure distribution (Hertzian) [2]

Three decades later, de Pater and Johnson, (see Enblom, [2]), predicted the shape and size of the contact area and pressure distribution considering the Hertzian three-dimensional solution, Figure 1.

In fact, the wheel-rail concentrated contact appears as a non-Hertzian contact because of the following violations of the Hertzian assumptions:

- the surfaces separation around the initial contact point can not be expressed as a quadratic form;
- the common generatrix has a finite length;
- the contacting surfaces are no longer smooth;
- friction is present on the contacted area.

Figure 2 points out the longitudinal and lateral creepages accompanying the main rolling loading.

Apart from the approximated solutions, the general case for modeling the wheel-rail contact must be solved numerically. Kalker was the first to solve the general wheel - rail contact, for which he developed the numerical program CONTACT, Wiest [3].

For vehicle dynamics problems, where the external contact parameters change continuously, i.e. lateral position between wheel and rail profiles, the program CONTACT cannot be used due to the high computational time.

To overcome this, Kalker proposed a new contact model called FASTSIM. A survey of these methods is made in [2,3].

Finite element methods are also applied to the wheel-rail contact problem and significant simulations and developments have been recently reported in literature, Damme [4].

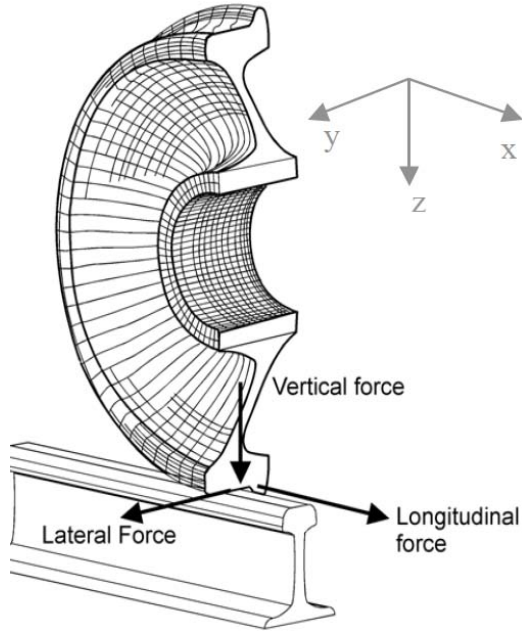


Figure 2. Wheel-rail loads, [2]

The state-of-the-art papers of Knothe et al. [5] discuss in more detail the above methods of contact mechanics applicable for wheel - rail contact.

More recent work on the elastic non-Hertzian contact was made by Cretu [6,7], who solved the contact between two randomly shaped bodies described as half-spaces by using the Papkovici - Boussinesq solution.

The developed numerical program is called NON-HERTZ and its solving algorithm uses the Conjugate Gradient Method involving the Discrete Convolution with the process of zero padding and wrap-around order associated with FFT. Displacement is regarded as a convolution of pressure and elastic response.

In the wheel-rail contact, the separation between the contacting surfaces depends on a lot of variables, as wheel and rail profiles, rail inclination, track gauge, inside gauge and lateral shift of the axle.

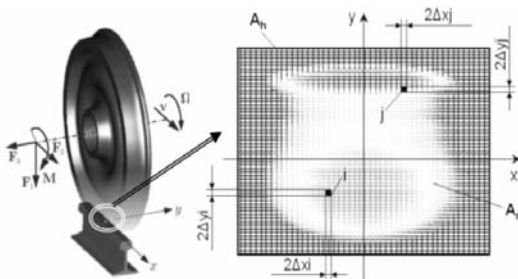


Figure 3. The real and hypothetical contact areas

2. NUMERICAL FORMULATIONS

A hypothetical rectangular contact area denoted by A_h is considered in the common tangent plane, around the initial contact point. The hypothetical area is large enough to overestimate the unknown real contact area, $A_h \geq A_r$, Figure 3.

A Cartesian coordinate system (x, y, z) is introduced, its xOy plane being the common tangent plane, and with its origin located at the left corner of the hypothetical rectangular area. The elastic deflection of each surface is measured in the direction of the corresponding outer normal and is denoted by $w_I(x, y)$ and $w_{II}(x, y)$, respectively. The sum of the individual deflections at any generic point (x, y) is defined as a composite deflection, denoted by $w(x, y)$.

A uniformly spaced rectangular array is built on the hypothetical rectangular contact area with the grid sides parallel to the x and y -axes, Figure 3. The nodes of the grid are denoted by (i, j) , where indices i and j refer to the grid columns and rows, respectively. In the considered Cartesian system, the coordinates of the grid node (i, j) are denoted by (x_i, y_j) and are given by:

$$x_i = i \cdot \Delta x, (0 \leq i < N_x), \quad (1)$$

and

$$y_j = j \cdot \Delta y, (0 \leq j < N_y), \quad (2)$$

where Δx and Δy are the grid spaces in the x and y -directions, respectively. The real pressure distribution is approximated by a virtual pressure distribution, a piecewise-constant approximation between grid nodes being typically used, Figure. 4.

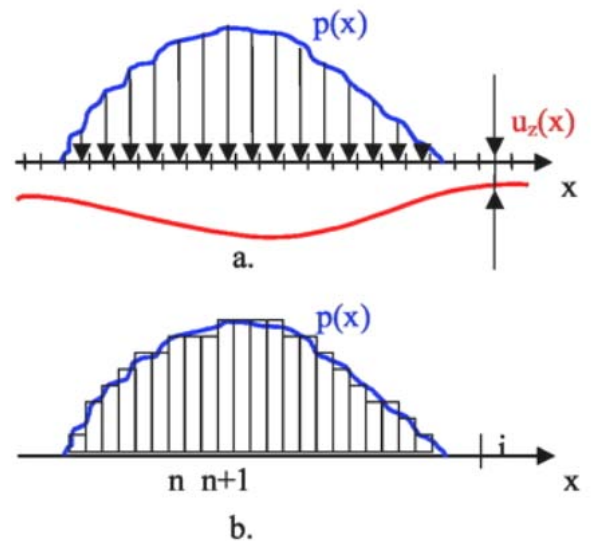


Figure 4. The real pressure distribution and piecewise-constant approximation

The numerical formulation is given by the following set of discrete equations:

- a) the geometric equation of the elastic contact:

$$g_{ij} = h_{ij} - R_{ij} + w_{ij} - \delta_0 ; \quad (3)$$

- b) the integral equation of the normal surface displacement, (Boussinesq formula):

$$w_{ij} = \sum_{k=0}^{N_x-1} \sum_{\ell=0}^{N_y-1} K_{i-k,j-\ell} P_{k\ell} , \quad (4)$$

where the influence function K_{ij} describes the deformation of the meshed surface due to a unit pressure acting in element (k, ℓ) , Cretu [7];

- c) the load balance equation:

$$\Delta x \Delta y \sum_{i=0}^{N_x-1} \sum_{j=0}^{N_y-1} p_{ij} = F , \quad (5)$$

where F is the applied normal force.

- d) the constraint equations of non-adhesion and non-penetration:

$$g_{ij} = 0, p_{ij} > 0, (i, j) \in A_r ; \quad (6)$$

$$g_{ij} > 0, p_{ij} = 0, (i, j) \notin A_r ; \quad (7)$$

- e) the *elastic-perfectly plastic* behavior of the material:

$$p_{ij} \geq p_Y \Rightarrow p_{ij} = p_Y , \quad (8)$$

where p_Y is the value of the pressure able to initiate the plastic yielding.

The components of the stress tensor induced in the point $M(x, y, z)$ are obtained by superposition:

$$\sigma_{ij}(x, y, z) = \sum_{k=0}^{N_x-1} \sum_{\ell=0}^{N_y-1} C_{ijk\ell} P_{k\ell} , \quad (9)$$

where the influence function $C_{ijk\ell}(x, y, z)$ describes the stress component $\sigma_{ij}(x, y, z)$ due to a unit pressure acting in patch (k, ℓ) .

That is a Neumann type problem of the elastic half-space theory. Closed form expressions can be found in Hill [8].

3. ELASTIC-PERFECTLY PLASTIC SOLVER

A numerical algorithm has been developed to solve the problems connected with the non-Hertzian concentrated contact, Cretu [6]. The Conjugate Gradient Method (CGM), with the iterative scheme proposed by Polonsky and Keer, [9,10], has been

chosen to solve the mentioned algebraic system of equations.

In order to increase the efficiency of the numerical algorithm, a dedicated real discrete fast Fourier transform routine for 3D contact problems has been developed and incorporated into the code, Crețu [6], Nélias [11]. In the following the name *non-Hertz* is used for the computer code.

This algorithm has been further applied to the wheel-rail concentrated contacts and a solver code in C++ language has been finally obtained. This solver appears as a robust and fast alternative solution to the finite element models that require large memory and important computational resources, as well as to the experimental tests which require expensive equipments and very long duration.

By entering the input data (wheel profiles, external normal load, wheel radius, yaw angle, inside gauge, lateral shift of the axle, rail profiles, rail inclination, track gauge, traction coefficient, elasticity modulus, Poisson ratio etc) the pressure distribution and the appropriate stress state for various running conditions are obtained.

4. THE CONTACT GEOMETRY AND RIGID SEPARATION

4.1 Rail and wheel

The wheelset and track gauges are shown schematically in Figure 5. The track gauge is measured between the points on the rail profile located inside the track at a distance of 14.1 mm from the common tangent in the profiles of both rails. Assuming the track is in a straight line, the mentioned tangent will be horizontal. The wheel radius is measured at the mean wheel circle, usually at 70 mm from the back of the wheel.

The two considered counterparts are a S1002 wheel profile and a UIC60 rail. The wheel has a radius in rolling direction of 460 mm and the rail is inclined at 1/40. The inner gauge of the wheelset is 1360 mm and the track gauge is standard, i.e. 1435 mm.

When the wheelset is in perfect alignment with the track, the above dimensions would result in a lateral shift between the left wheel and rail of 3 mm. Of course, during train movement, the wheelset changes its relative position to the rail.

The standard UIC60 rail profile is defined by arcs of circles and it is geometrically given as a technical drawing. For keeping the same format as for the wheel, the circles are approximated by equations. Since the (not inclined) rail profile is symmetrical, only half of it will be described in four sections.

The standard S1002 divides the wheel profile in eight sections; in each of these sections the profile is defined by a specific algebraic polynomial.

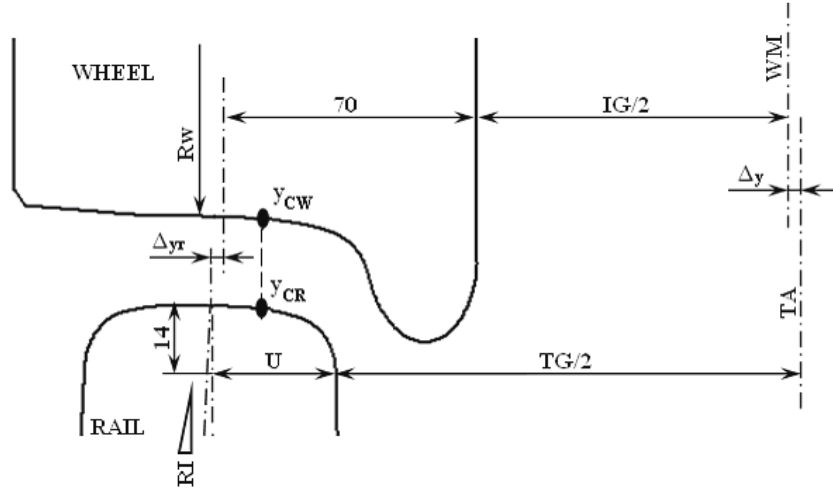


Figure 5. Wheel-rail contact geometry

Table 1. Rail inclination

		Δy	3	2	1	0	-1	-2	-3	-4	-5
Rail inclination	0	Δy_r	6.491	5.491	4.491	3.491	2.491	1.491	0.491	-0.509	-0.509
		y_{CR}	11.96	12.485	13.07	13.745	14.54	15.545	16.925	26.27	26.72
		y_{CW}	8.96	10.485	12.07	13.745	15.54	17.545	19.925	30.27	31.72
	1/40	Δy_r	6.063	5.063	4.063	3.063	2.063	1.063	0.063	-0.937	-1.937
		y_{CR}	-4.21	-3.55	-2.44	-0.28	11.33	12.05	12.92	14.045	15.755
		y_{CW}	-7.21	-5.55	-3.44	-0.28	12.33	14.05	15.92	18.05	20.76
	1/30	Δy_r	5.911	4.911	3.911	2.911	1.911	0.911	-0.089	-1.089	-2.089
		y_{CR}	-7.345	-7.195	-6.877	-6.31	-5.395	-3.73	11.78	12.755	14.09
		y_{CW}	-10.345	-9.195	-7.877	-6.31	-4.395	-1.73	14.78	16.755	19.09
	1/20	Δy_r	5.597	4.597	3.597	2.597	1.597	0.597	-0.403	-1.403	-2.403
		y_{CR}	-10.915	-10.96	-10.99	-10.99	-10.96	-10.915	-10.825	-10.72	-10.585
		y_{CW}	-13.915	-12.96	-11.99	-10.99	-9.96	-8.915	-7.825	-6.72	-5.585

An estimated target domain was meshed and the separation matrix was used as input into the *NON-HERTZ* code.

In the Table 1, Δy is the lateral shift of wheelset relative to the track and Δy_r is the lateral position of the wheel relative to the rail. y_{CR} is the lateral coordinate of the contact point in rail coordinates and y_{CW} the lateral coordinate of the contact point in wheel coordinates.

The standard notation and main dimensions, involved in the contact geometry are as follows, (Fig. 5):

- WM – the middle of the mounted axle;
- TA – the railway axis..
- track gauge: $TG = 1435$ [mm];
- inside gauge: $IG = 1360$ [mm];
- wheel radius: $R_w = 460$ [mm];
- rail inclination: $RI = 1/40$;
- lateral shift of the axle: $\Delta y = 0$ [mm];
- yaw angle: 0° ;
- roughness amplitude: 0.0 [μm];
- wheel profiles: S1002, are described by polynomials;

- rail profiles: UIC60, are described by polynomials.

4.2. The rigid contact separation

The separation $h(x, y)$ between the contacting surfaces depends on a lot of variables as wheel profiles, rail profiles, rail inclination, track gauge, inside gauge and lateral shift of the axle, Figure 5.

The transversal positioning of the wheel against the rail is achieved according to the following equation:

$$\Delta y_r = U + TG / 2 - 70 - IG / 2 - \Delta y . \quad (10)$$

The Brent's method has been incorporated into the computing scheme to find, for the unloaded conditions, the first contact point of the two surfaces. The Brent's method combines root bracketing, bisection, and inverse quadratic interpolation to converge from the neighbourhood of a zero crossing. The final form for the separation $h(x, y)$ was found as follows:

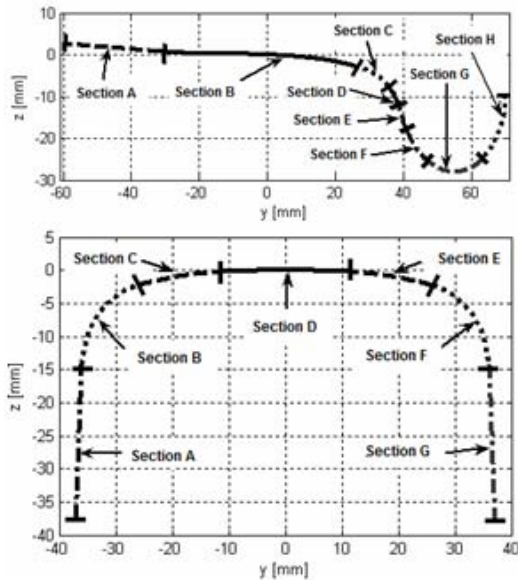
$$h(x, y) = zw(y) + rw(y) - \sqrt{rw(y)^2 - zw(x)^2} - zr(y) \quad (11)$$

where $zw(y)$ is wheel profile at the coordinate y , $rw(y)$ is the wheel radius at coordinate y , $zw(x)$ is the wheel profile at coordinate x , and $zr(y)$ is the rail profile at coordinate y .

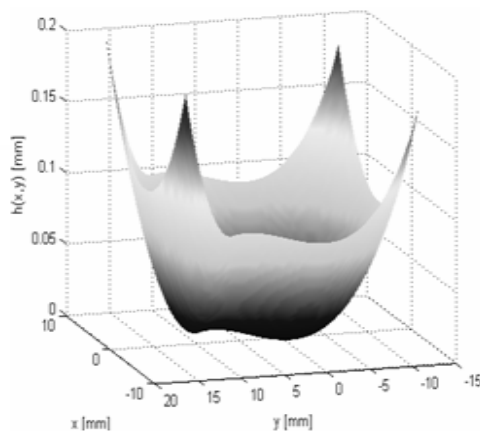
The 2D profiles and 3D rigid separation $h(x, y)$ are exemplified in Figure 6.

4.3 Material properties and load:

- Young modulus: $2.1 \cdot 10^5$ [MPa];
- Poisson ratio: $\nu = 0.28$;
- yield limit: $p_Y = 580$ [MPa], corresponding to R7T steel;
- external normal load 90 [kN].



a. 2D profiles



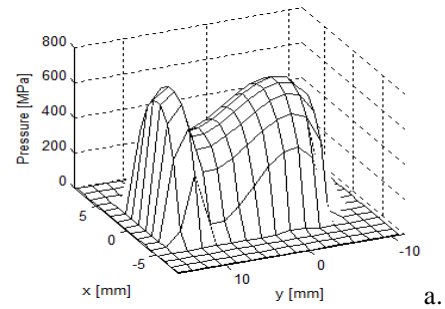
b. 3D rigid separation

Figure 6. Wheel-rail contact geometry (a) and 3D rigid separation (b)

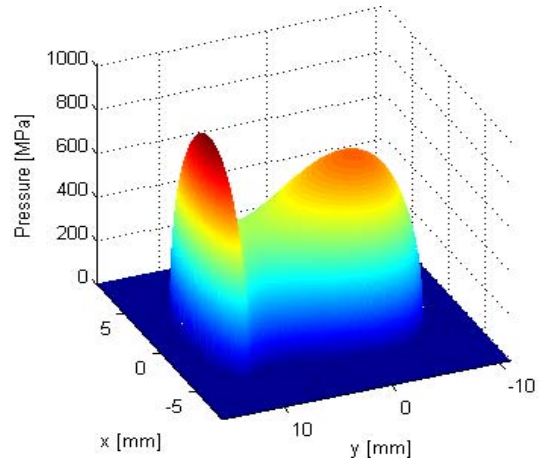
5. ELASTIC ANALYSIS

5.1 Elastic pressure distributions

The constraint (8) has not been involved in the elastic analysis. The accuracy of the results depends on the size of the uniformly spaced rectangular array built on the hypothetical rectangular contact area, Figure 7. The 3D pressure distributions are exemplified in Figure 7a for an array with $16 \times 16 = 256$ mesh points, and in Figure 7b for an array with $512 \times 512 = 262,144$ mesh points. The elastic conditions, normal loads and a lateral shift $s = 0$ has been considered. The corresponding 2D distributions are plotted in Figure 8.



a.



b.

Figure 7. 3D pressure distributions (elastic model, lateral shift $s=0$)

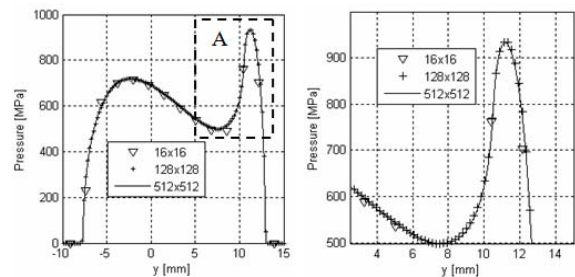


Figure 8. 2D pressure distribution (elastic model, lateral shift $s=0$)

5.2. Influence of the lateral shift

The lateral shift of the wheel has a strong influence on both shape of the real contact area and maximum value of pressure distribution, as depicted in Table 1 and in Figures 9 to 12.

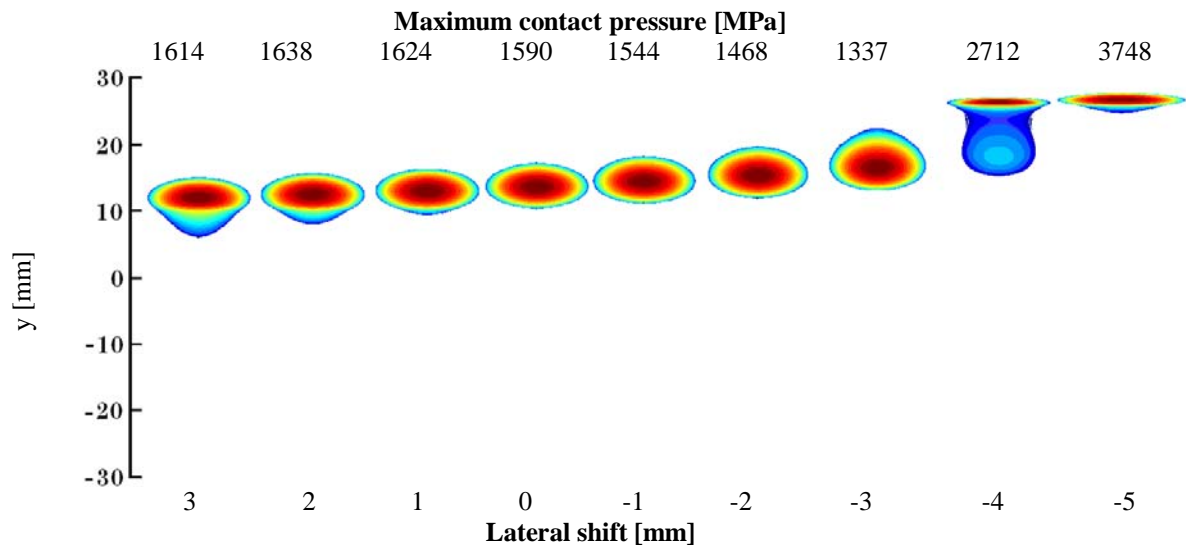


Figure 9. Wheel S1002-Rail UIC60 with 0 inclination

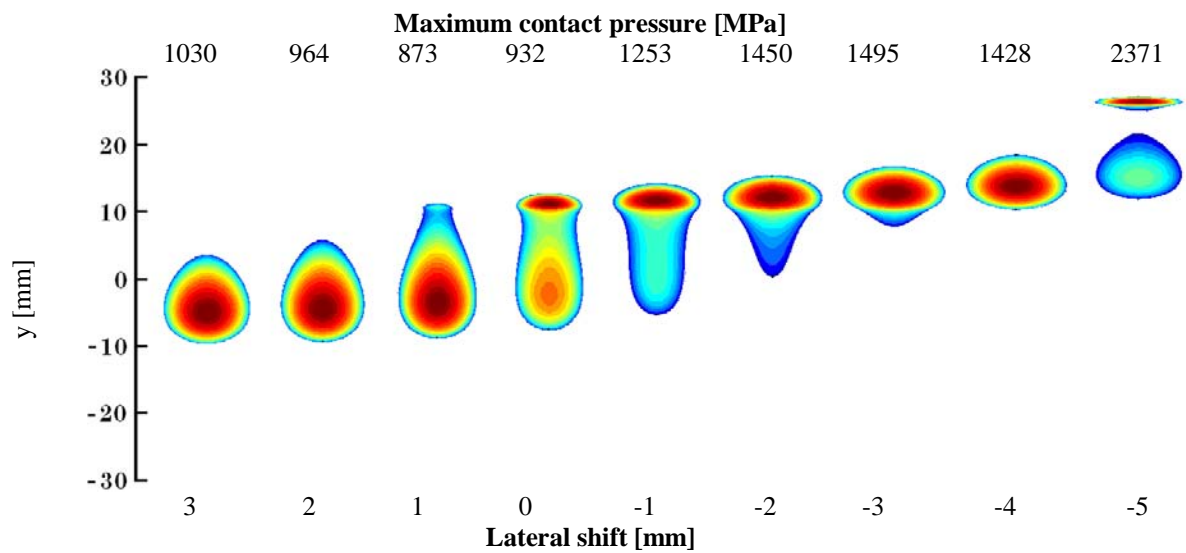


Figure 10. Wheel S1002-Rail UIC60 with 1/40 inclination (Germany, Austria)

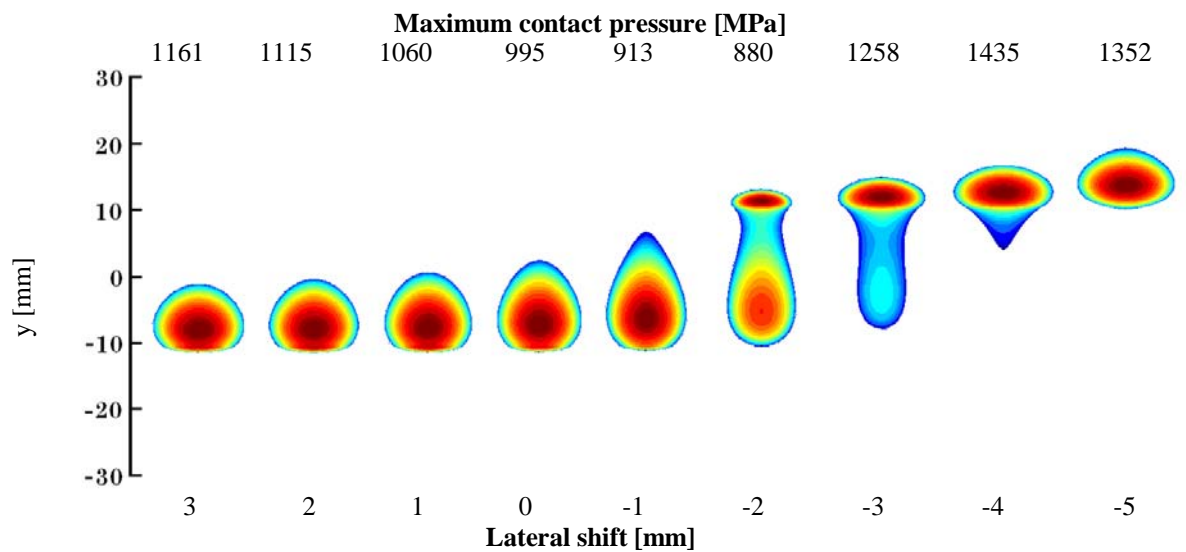


Figure 11. Wheel S1002-Rail UIC60 with 1/30 inclination (Sweden)

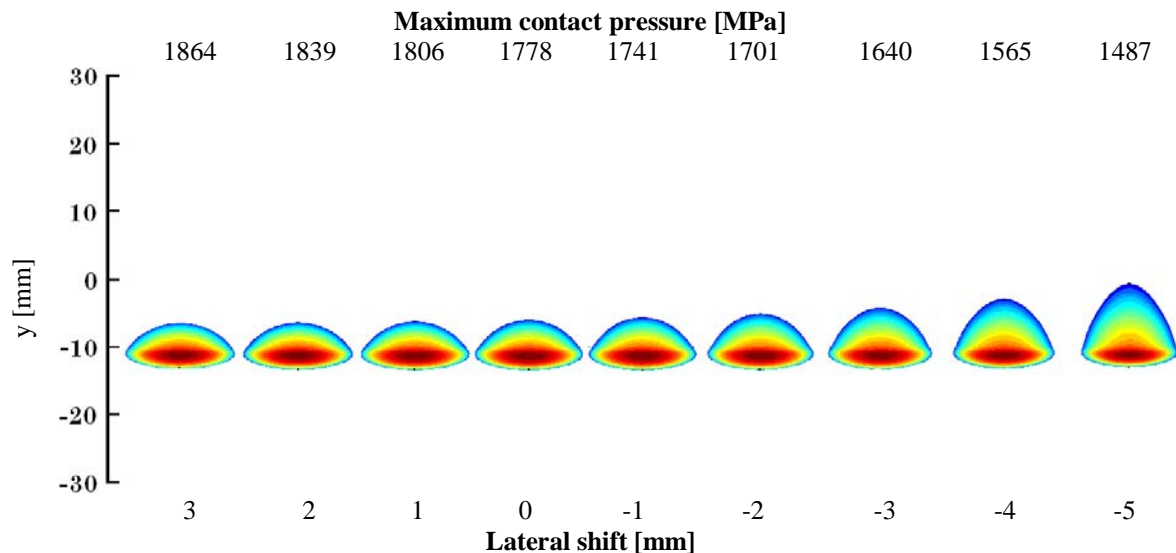


Figure 12. Wheel S1002-Rail UIC60 with 1/20 inclination (Romania, France)

5.3. Influence of the rail inclination

As shown in Figures 9 to 12, the rail inclination appears to be a major factor influencing the shape of the real contact area and, consequently, the entire 3D elastic pressure distributions.

It can be noticed that a greater rail inclination provides a greater maximum pressure.

6. CONCLUSIONS

1. The interoperability of the European rail transportation is affected by the different rail inclination that varies between 1/40 and 1/20.
2. A numerical solver has been involved to obtain the 3D pressure distribution in non-Hertzian wheel-rail contacts. This solver appears as a robust and fast alternative solution to the finite element models that require large memory and important computational resources, as well as to the experimental tests which require expensive equipments and very long duration.
3. The lateral shift of the wheel alters considerably both shape of the real contact area and maximum value of the pressure distribution.
4. The rail inclination appears to be a major factor influencing the shape of the real contact area and, consequently, the entire 3D elastic pressure distributions. Numerical simulations pointed out that greater rail inclinations provide greater maximum pressures.

REFERENCES

1. Ayasse, J. B., and Chollet, H., 2006, *Wheel-rail contact*, in *Handbook of Railway Vehicle*

Dynamics, S. Iwnicki (Ed.), Taylor & Francis, pp. 85–120.

2. Enblom, R., and Berg, M., 2008, “Impact of non-elliptic contact modelling in wheel wear simulation”, *Wear*, **265**, pp 1532–1541.

3. Wiest M., Kassa E., Nielsen J.C.O., and Ossberger H., 2008, “Assessment of methods for calculating contact pressure in wheel-rail/switch contact”, *Wear*, **265**, pp. 1439-1445.

4. Damme, S., 2006, *Zur Finite-Element-Modellierung des stationären Rollkontakts von Rad und Schiene*, PhD thesis, Berichte des Instituts für Mechanik und Flächentragwerke Heft.

5. Knothe K., Wille R., and Zastra, B., 2001, “Advanced contact mechanics-road and rail”, *Vehicle System Dynamics*, **35**, (4-5), pp. 361-407.

6. Crețu, S., 2005, “Pressure distribution in concentrated rough contacts”, *Bull.I.P. Iași*, LI (LV), 1-2, pp. 1-31.

7. Crețu S., 2009, *Elastic-Plastic Concentrated Contact*, Iași: Polytechnium.

8. Hill, D. A., Nowell D., and Sackfield, A., 1993, *Mechanics of Elastic Contacts*, Oxford: Butterworth.

9. Polonsky, I. A., and Keer, L. M., 1999, “A numerical method for solving contact problems based on the multilevel multisumation and conjugate gradient techniques”. *Wear*, **231**, pp. 206-219.

10. Polonsky, I. A., and Keer, L. M., 2000, “Fast methods for solving rough contact problems: A comparative study”. *Trans. ASME, Journal of Tribology.*, **122**, pp 36-41.

11. Nelias D., Antalucă E., Boucly V., and Crețu S., 2007, “A 3D semi-analytical model for elastic-plastic sliding contacts”, *Trans. ASME, Journal of Tribology*, **129**, pp. 671-771.

Cornel SUCIU
e-mail: *suciu@fim.usv.ro*

Emanuel DIACONESCU
e-mail: *emdi@fim.usv.ro*

Department of Mechanical Engineering,
University of Suceava,

ROMANIA

PRELIMINARY THEORETICAL RESULTS UPON CONTACT PRESSURE ASSESSMENT BY AID OF REFLECTIVITY

Several different experimental methods for investigating contact features can be found in literature. The idea to optically investigate the surfaces of contacting bodies [1-8], led to the development of a new technique to measure the pressure distributions in a real contact [9-11].

One of the contacting surfaces is covered, prior to contact establishment, by a special gel. The contact closing removes the excess gel and, during a certain time interval, the contact pressure transforms the entrapped substance in an amorphous solid. In each point, the refractive index of this solid depends on the pressure acting during transformation. After contact opening, the reflectivity of this coating depends on the former contact pressure and it is mapped by aid of a laser profilometer, thus becoming an indicator of contact pressure.

This paper studies the effect of pressure on the refractive index of the solidified gel layer, as well as the different parameters that influence its reflectivity. Using molecular physics and optics, a theoretical model of reflectivity is studied and it is found to be strongly influenced by both pressure and gel layer thickness. From this model, pressure distribution laws are found for different ranges of reflectivity and gel layer thickness.

Keywords: contact pressure, refractive index, reflectivity, solidified gel layer

1. INTRODUCTION

Many different experimental methods can be found in literature for the study of contact features. The most advanced methods supply point to point information on contact features, such as the deformed surface of one or both contacting bodies, or measurement of contact pressure and contact stresses. An accurate method to find the deformed surface of a metallic equivalent punch pressed against a thick sapphire window as well as the actual contact area was recently advanced by Diaconescu and Glovnea [2-7] by aid of laser profilometry. By using these experimental results as input data for normal displacement, numerical calculations yield the contact pressure responsible for these deformations.

Yamaguchi, Uchida and Abraha [7] advanced an interesting method of contact pressure evaluation, based on measurement of intensity of a laser beam reflected by the same surface, prior and after the contact. They found that after contact the intensity of reflected light increases in the former points of contact area and become proportional to contact

pressure. Etching of the surface was found to improve the method's sensibility.

Yamaguchi, Uchida and Abraha [8], proposed a method for the assessment of contact pressure distribution by means of a transferred oil film. In this method, a thin film of oil is spread onto the specimen and pressure is applied between this surface and a clean, flat reference surface. Upon releasing the load, part of the oil film is transferred onto the measuring surface. The surface covered by the transferred oil film is considered to be the real contact area. The ratio of the area of the transferred oil film to the apparent surface area is then detected by the reflection of light.

The idea of Yamaguchi, Uchida and Abraha to investigate optically the surface after contact was opened led to the development of a new technique for the evaluation of contact pressure in real contacts [9-11]. This consists in measuring the reflectivity of a thin coating formed on one of the contacting surfaces as a result of transformation of a gel into an amorphous solid at contact pressure.

As the refractive index of the coating depends on the pressure inducing the change of phase, the

measured reflectivity is a useful indication of contact pressure.

2. REFRACTIVE INDEX OF A SOLIDIFIED GEL LAYER

As shown in the introduction, the experimental method presented herein consists in covering one of contacting surfaces with a special molecular gel, prior to contact establishment. After a well defined time, the contact is closed, the normal load is applied and the system is maintained in this state another adequate time interval. Although most of the gel is expelled at contact establishment, a minute quantity remains at the interface of the two contacting bodies. Under the action of the contact pressure, the entrapped gel suffers a phase transformation. Because the rate of pressure increase to the nominal value is quite high, the available time for molecular rearrangement in a low viscosity state is short, of a few seconds only. The gel viscosity, already high at contact establishment, increases rapidly at contact pressure and impedes molecular rearrangements. Consequently, the solid state resulting from this transformation is an amorphous one, and, therefore, isotropic. Finally, the contact is opened and a very thin coating of solidified gel is found on the previously covered surface. This is an optical medium, characterized by a refractive index.

The absolute refractive index is defined as the ratio of the speed of the electromagnetic wave in vacuum to the speed of the same wave when passing the studied medium:

$$n = \frac{c}{v} = \sqrt{\varepsilon\mu}, \quad (1)$$

where: n – real part of the refractive index; c – speed of light in vacuum; v – speed of light in the studied optical media; ε – dielectric constant or permittivity; μ – magnetic permeability.

Optical media can be transparent or absorbing. A transparent medium has zero conductivity and its magnetic relative permeability differs from a unit value by a negligible amount. Consequently, for such media, the refractive index is:

$$n = \sqrt{\varepsilon}. \quad (2)$$

No medium, except for vacuum, is perfectly transparent. All material media show strong absorption, at least in some regions of the electromagnetic spectrum. An absorbing medium has a finite conductivity and, consequently, a finite current density. Nevertheless, in such media, the volume charge density vanishes. The permittivity is constant, but complex, because a phase-shift occurs

between the component field vectors. Similarly, the conductivity is also complex. As a result, the refractive index is complex, therefore symbolized by \tilde{n} , the dielectric constant by $\tilde{\varepsilon}$ and the conductivity by $\tilde{\sigma}$. According to Ditchburn [12], the *complex refractive index* is given by:

$$\tilde{n} = n(1 - i\chi) = n - n\chi i. \quad (3)$$

Optically, the gel coating belongs to the class of absorbing media and therefore its refractive index is complex. The real part of this index depends on pressure. If the value of the refractive index for a reference pressure is known, its value at different pressures is found by using the following equation [9]:

$$n = \sqrt{\frac{2\rho_r - 2\rho + 2\rho \cdot n_r^2 + n_r^2 \cdot \rho_r}{\rho + 2\rho_r - \rho \cdot n_r^2 + n_r^2 \cdot \rho_r}}. \quad (4)$$

If a dimensionless density, $\bar{\rho}$, defined as the ratio of density at pressure p to that at reference pressure is introduced in equation (4), the following expression for the real part of the refractive index at a given pressure p is obtained:

$$n = \sqrt{\frac{2 + n_r^2 + 2(n_r^2 - 1)\bar{\rho}}{2 + n_r^2 - (n_r^2 - 1)\bar{\rho}}}. \quad (5)$$

As shown in [13], the dimensionless density can be expressed as a function of pressure if the molecular interaction of specified substance is known. To that end, it is first necessary to evaluate energy for the crystalline lattice in the case of a simple molecular crystal. To simplify the calculus, this energy was determined for a perfect crystalline lattice. It was assumed that molecular interactions in such a lattice are governed by a Lennard-Jones-London intermolecular potential, having the following expression:

$$\varphi(r) = 4 \cdot \psi \left[\left(\frac{\sigma}{r} \right)^{12} - \left(\frac{\sigma}{r} \right)^6 \right], \quad (6)$$

where r denotes the distance between the interaction centers of observed molecules, σ is the value of r at which $\varphi(r)$ vanishes and ψ is the minimum value of the intermolecular potential.

Molecular lattice energy represents the necessary work to extract a given molecule from the lattice and to send it towards infinity. In fact, this energy is equal to the half-sum of all potentials between the observed molecule and all other molecules in the crystal.

As shown by equation (6) of the Lennard-Jones-London molecular interaction potential, this

potential decreases exponentially as the distance between molecules increases. Thus, when determining lattice energy for a certain molecule, only molecules from neighboring layers have important contributions, the effect of farther molecules being negligible.

If the refractive index at atmospheric pressure n_r , is known, and dimensionless density is calculated as shown in [11], the refractive index at a given pressure p can be determined using equation (5). The refractive index of the solidified gel layer is determined during solidification and depends on

contact pressure in each point. After contact opening, the solidified gel layer retains contact pressure distribution through its refractive index. As this index varies along contact surface, gel layer reflectivity becomes a function of applied contact pressure.

Figure 1 illustrates how the real part of the refractive index varies with increasing pressure applied during solidification.

When a Hertz like pressure distribution is applied the real part of the refractive index will vary as shown in Figure 2.

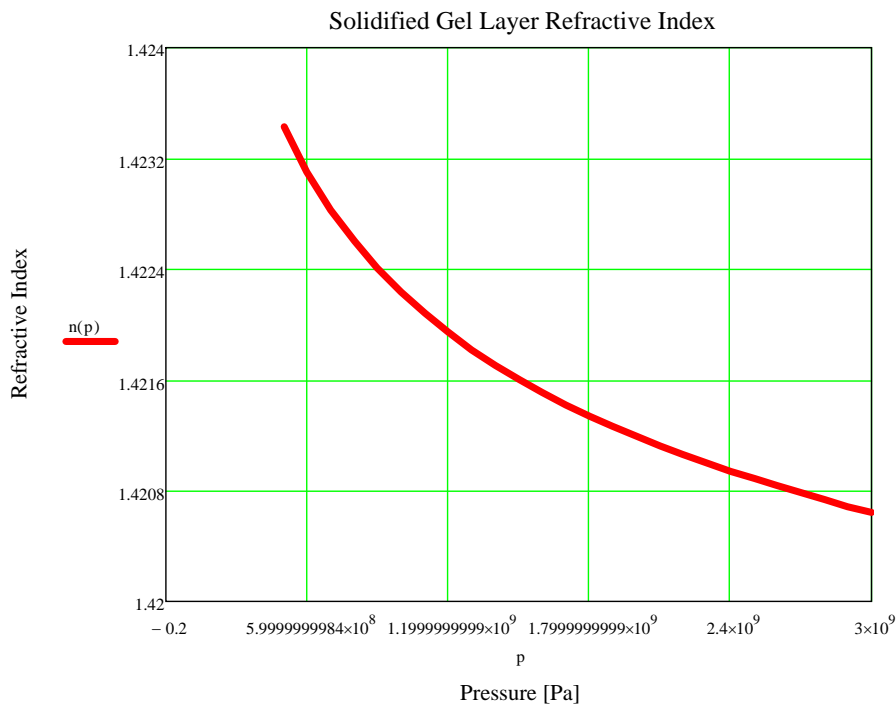


Figure 1. Variation of the real part of solidified gel layer refractive index with increasing pressure

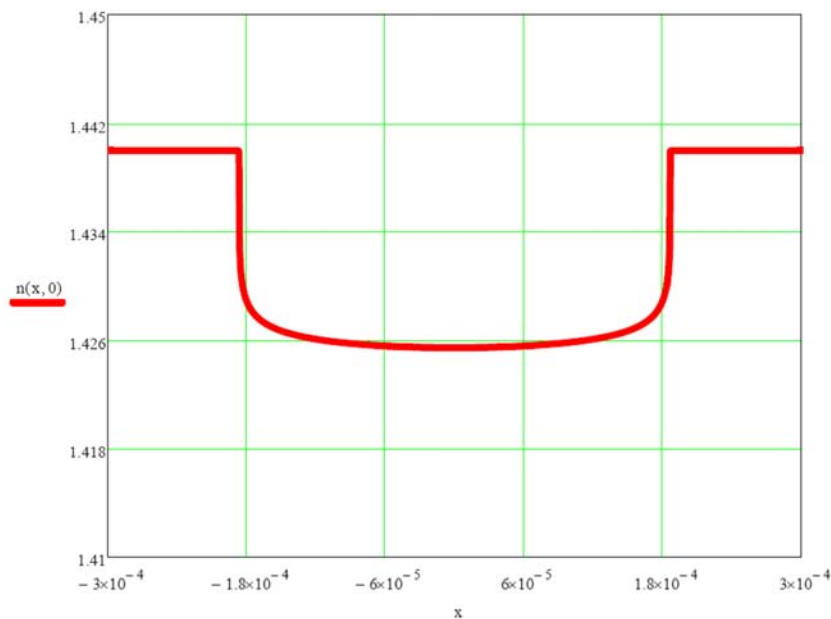


Figure 2. Refractive index variation along contact area, for Hertz pressure distribution

Since the reflectivity of the solidified gel layer depends on the refractive index and the extinction coefficient [9], it can be used as an indicator of the pressure that occurred during contact establishment.

Experimentally, reflectivity and gel layer thickness are recorded using a laser profilometer and used to determine the pressure distribution during solidification.

3. REFLECTIVITY OF SOLIDIFIED GEL LAYER

As shown in the introduction, solidified gel layer reflectivity and thickness are mapped by laser profilometry. When the laser beam meets the air – solidified gel layer interface, part of its energy returns via reflection, while the rest traverses the absorbent optical layer. Part of the incident energy is lost by absorption, while the rest suffers a reflection-refraction phenomenon at the gel layer – metal interface. Again, part of the light energy is absorbed and part reflected. The reflected beam traverses the gel layer, again being part reflected – part refracted at gel-air interface. When returning into the air, the remainder of the beam energy combines with the one first reflected by the gel layer. The combined light wave is measured by the laser profilometer, the ratio of incident light energy to the reflected one yields the system's reflectivity.

This is a typical reflection – refraction problem, involving a three layer optical medium having two optical interfaces, namely the air – gel layer interface and gel layer – metal interface respectively. As shown by Born and Wolf [14], at each passing through one of these interfaces, the incident laser beam is partly reflected and partly transmitted, as shown in Figure 3. The process of reflection – refraction depends on the optical properties of the two adjacent media.

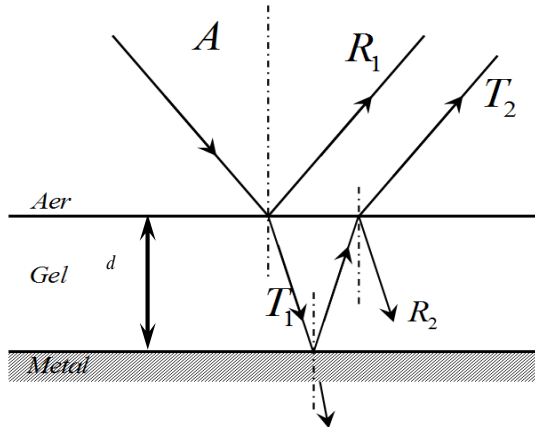


Figure 3. Laser beam reflection-refraction when passing through the solidified gel layer

Global reflectivity, measured by the laser profilometer, is determined by several waves

reflected by the air-gel-metal optical system. The gel surface reflectivity is given by a wave returning from the surface \mathfrak{R}_1 , given by the following equation [9]:

$$\mathfrak{R}_1 = \frac{(n_2 - 1)^2 + n_2^2 \chi_2^2}{(n_2 + 1)^2 + n_2^2 \chi_2^2}. \quad (7)$$

This wave is then combined with a second one, \mathfrak{R}_2 , reflected by the gel – metal interface after passing through the gel layer. According to [9], this second reflectivity can be calculated with:

$$\mathfrak{R}_2 = \frac{16 \cdot n_2 \cdot \left[(n_3 - n_2)^2 + (n_3 \chi_3 - n_2 \chi_2)^2 \right]}{\left[(1 + n_2)^2 + n_2^2 \chi_2^2 \right]^2} \times \frac{\exp(-4 \cdot \alpha \cdot d)}{(n_3 + n_2)^2 + (n_3 \chi_3 + n_2 \chi_2)^2}. \quad (8)$$

The global, measured reflectivity is given by the combination of the two waves, as follows:

$$\mathfrak{R}^2 = \mathfrak{R}_1^2 + \mathfrak{R}_2^2 + \sqrt{\mathfrak{R}_1 \mathfrak{R}_2}. \quad (9)$$

Of great importance among the solidified gel layer optical properties is its extinction coefficient. If this coefficient is assumed constant in relation to pressure, the phase shifting between the two waves would remain constant, which is not the case. Unfortunately, little information on the subject is available in literature. Therefore, in order to find theoretical profiles of reflectivity similar to those measured experimentally, a relation between extinction coefficient and pressure was adopted in [9], based on experimental investigations:

$$\chi_2(p) = \chi_{20} \left[1 - e \cdot \left(\frac{p}{p_{00}} \right)^2 \right], \quad (10)$$

where $\chi_{20} = 0.12$ is the extinction coefficient for the gel layer solidified at atmospheric pressure, p_{00} is an important pressure, chosen equal to 5 GPa, and e is a proportionality constant of 0.8.

In the reflectivity equations presented above, several notations were used, as follows: n_2 – real part of solidified gel layer refractive index, given by either (4) or (5); χ_2 – solidified gel layer extinction coefficient, given by (10); n_3 – metal refractive index (considered to be $n_3 = 2.41$ in shown results); χ_3 – metal extinction coefficient (considered to be $\chi_3 = 1.38$ in shown results); d – gel layer thickness, measured by laser profilometry; α –

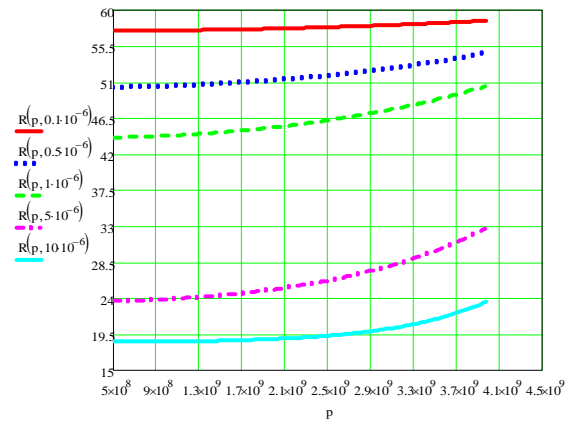
absorption coefficient of solidified gel layer, given by:

$$\alpha = \chi_2 \cdot \frac{2\pi \cdot n_2}{\lambda}, \quad (11)$$

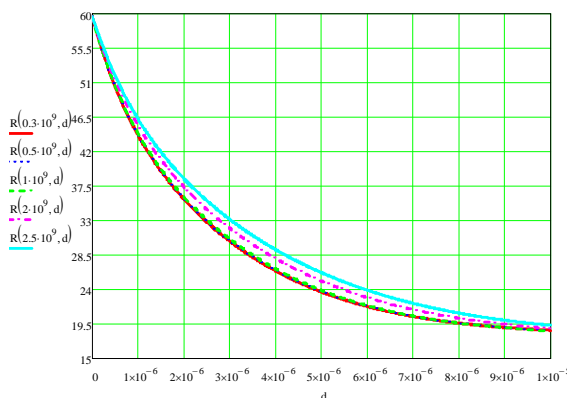
where $\lambda = 780 \text{ nm}$ is the wavelength of the laser beam used to scan the surface.

Both theoretical model and experimental measurements obtained in [10-11], show that the solidified gel layer global reflectivity is influenced in each point by both solidification pressure and gel layer thickness. As layer thickness was experimentally found not to be constant along contact area, its variation must be considered when assessing contact pressure using reflectivity.

Figure 4.a depicts the theoretical variation of global reflectivity with increasing pressure, for various gel layer thicknesses between $0.1\mu\text{m}$ and $10\mu\text{m}$. In Figure 4.b, the curves showing the dependence of reflectivity on gel layer thickness were traced at several constant pressures of solidification.



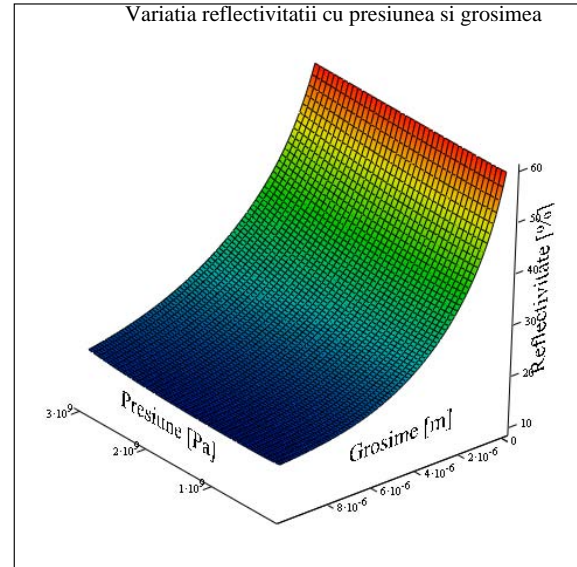
a)



b)

Figure 4. a) Reflectivity versus pressure, for several gel layer thicknesses; b) Reflectivity versus gel layer thickness, for several pressures

The surface illustrated in Figure 5 represents global reflectivity variation when both pressure and gel layer thickness are considered.



(R)

Figure 5. Global reflectivity variation with both pressure and gel layer thickness

4. PRESSURE DISTRIBUTION ASSESSMENT

In order to assess pressure variation using reflectivity, equation (9) must be solved with pressure as an unknown. It was found that equation (9) accepts solutions only for certain pairs of ranges for gel layer thickness and global reflectivity. By numerically solving this equation, for ranges of gel layer thicknesses reflectivity values and the corresponding values in pressure, pressure variation curves were traced as shown in Figure 6.

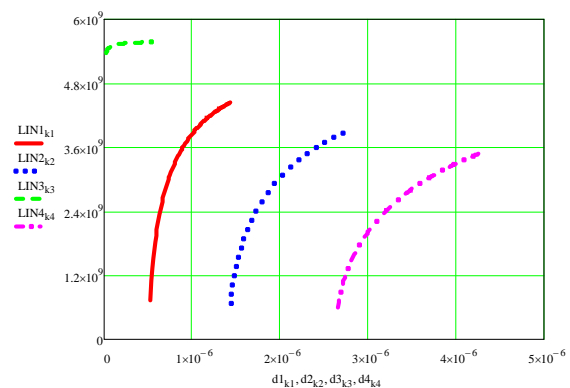


Figure 6. Pressure variation with gel layer thickness for different reflectivity values

By varying both reflectivity and gel layer thickness when solving equation (9), several corresponding pressure variation laws were obtained, as illustrated by the surfaces traced in Figures 7.a, 7.b, 7.c and 7.d respectively:

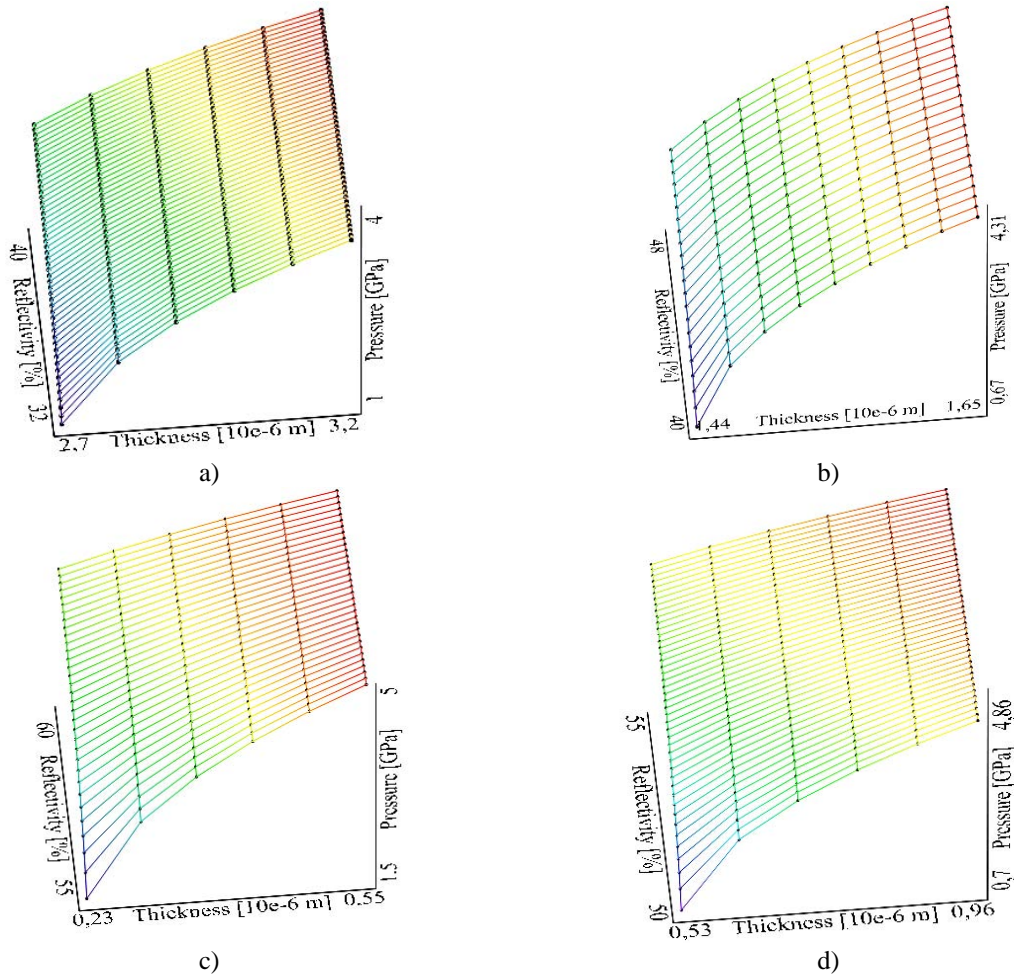


Figure 7. Pressure variation for several reflectivity and gel layer thickness ranges:

- a) a gel layer thickness range of $2.7 \div 3.2 \mu\text{m}$ and a reflectivity variation between 32% and 40% ;
- b) a gel layer thickness range of $1.44 \div 1.65 \mu\text{m}$ and a reflectivity variation between 40% and 48% ;
- c) a gel layer thickness range of $0.53 \div 0.96 \mu\text{m}$ and a reflectivity variation between 50% and 55% ;
- d) a gel layer thickness range of $0.23 \div 0.55 \mu\text{m}$ and a reflectivity variation between 55% and 60% .

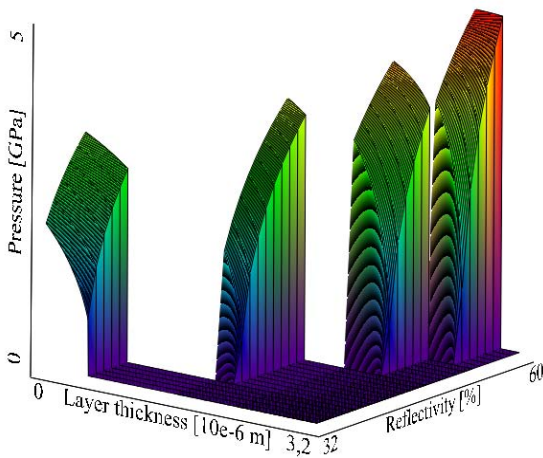


Figure 8. Pressure variation with reflectivity and gel layer thickness

Figure 8 reunites in the same graph the surfaces shown in Figure 7 in order to better distinguish the different pressure variation laws obtained by numerically solving equation (9).

Although it was found that solving equation (9) with pressure as an unknown is only possible for certain pairs of ranges in reflectivity and gel layer thickness values, these ranges were found to be consistent with practical application of the method, as experimental measurements were contained within these ranges.

Figure 9.c illustrates a typical pressure distribution obtained when experimental data for reflectivity (Figure 9.a) and corresponding gel layer thickness (Figure 9.b) are taken into account when solving equation (9). The shown experimental data corresponds to a contact between a spherical metallic punch and a metallic plate, with molecular gel at the interface, as presented in [10-11].

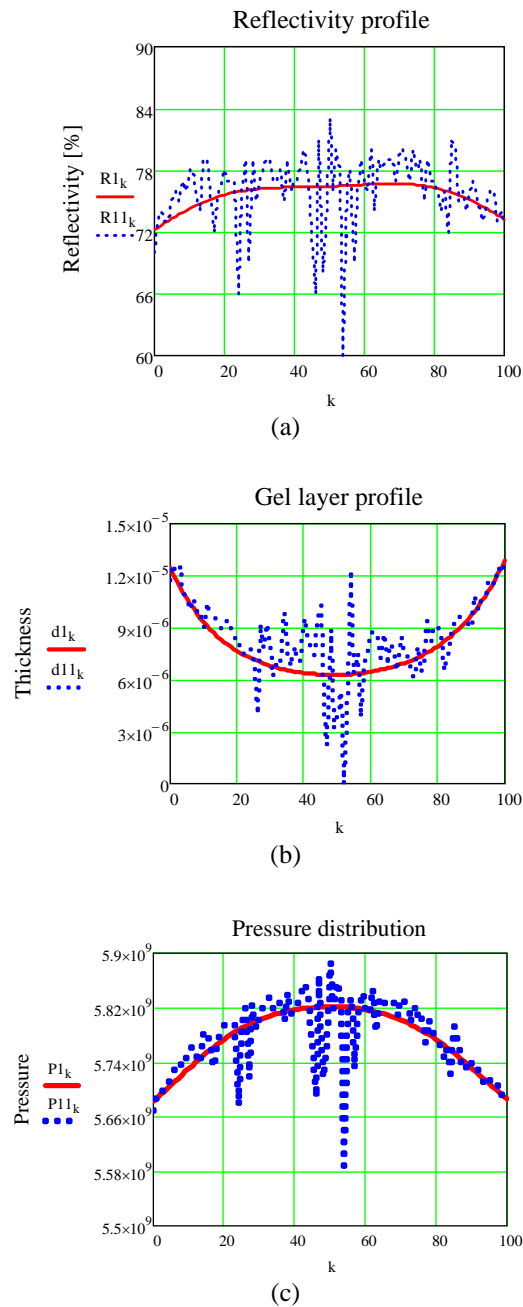


Figure 9. Reflectivity profile (a), corresponding gel layer thickness (b) and pressure distribution (c), for the contact between a metallic spherical punch and a metallic plate

In Figure 9, the experimental data and resulting real pressure distributions are traced with dotted lines, and the continuous line represents the approximation of the respective profiles when disregarding the roughness effect.

Neither reflectivity profile, nor gel layer thickness profile aren't smooth because asperity interactions generate steep peaks and deep valleys with respect to ideal surfaces. At high resolutions, the method can supply the shapes of reflectivity and gel layer peaks and therefore yield asperity pressure.

5. CONCLUSIONS

The work reported herein can be summarized by the conclusions reviewed below.

- Contact pressure assessment using reflectivity is an experimental method based on the solidification, inside the contact region, of a molecular gel film applied on one of contacting surfaces. The refractive index of the solidified gel, as well as its extinction coefficient, depends on the pressure acting during transformation, i.e. on contact pressure.

- After contact opening, the reflectivity of the surface initially covered with gel is scanned by aid of a laser profilometer. Measured reflectivity depends on refractive index, extinction coefficient and local thickness of gel coating.

- The effect of solidification pressure upon different optical properties of a gel layer (refractive index, extinction coefficient etc.) was studied and variation curves were traced.

- For a given set of molecular and optical parameters, theoretical variation curves of reflectivity were traced and its dependence on pressure and on local gel layer thickness was assessed.

- It was found that pressure has different variation laws for different ranges of reflectivity and of gel layer thickness.

- Experimental measurements of reflectivity and corresponding solidified gel layer local thickness were introduced in the numerical program, thus obtaining real contact pressure distributions.

- Further research is needed to improve accuracy of the method in order to find asperity pressure distributions.

REFERENCES

1. Diaconescu, E.N., and Glovnea, M.L., "Evaluation of Contact Area by Reflectivity," *Proc., 3rd AIMETA International Tribology Conference*, Italy, on CD, 2002
2. Glovnea, M.L., and Diaconescu, E.N., "A New Method for Experimental Investigation of Elastic Contacts," (in Romanian), *Symp. on Tradition and Continuity in Railway Research*, Vol.II, Bucharest, 1994, pp. 77-82.
3. Diaconescu, E.N., "A New Tool for Experimental Investigation of Mechanical Contacts, Part I: Principles of Investigation Method," *VAREHD 9*, Suceava, 1998, pp. 255-260.
4. Diaconescu, E.N. and Glovnea, M.L., "A New Tool for Experimental Investigation of Mechanical Contacts, Part II: Experimental Set-Up and Preliminary Results," *VAREHD 9*, Suceava, 1998, pp. 261-266.
5. Diaconescu, E.N., and Glovnea, M.L., "Validation of Reflectivity as an Experimental Tool

in Contact Mechanics,” *VAREHD 10*, Suceava, 2000, pp. 471 – 476

6. Diaconescu, E.N., and Glovnea, M.L., “Visualization and Measurement of Contact Area by Reflectivity,” *Trans. of the ASME, J. of Trib.*, Vol. 128, October 2006, 915 – 917

7. Yamaguchi, K., Uchida, M., and Abraha, P., “Measurement of Pressure on Contact Surface by Reflection of Light (Effect of Surface Etching),” *Proceedings of the Japan International Tribology Conference*, Nagoya, 1990, pp. 1271-1276.

8. Yamaguchi, K., Uchida, M., and Abraha, P., “Measurement of the Pressure Distribution on Contact Surfaces by the Detection of a Transferred Oil Film,” *Surface Science* 377–379 (1997), 1015–1018

9. Diaconescu, E. N., Glovnea, M. L., Petro el, O., “A New Experimental Technique to Measure Contact Pressure,” *Proc. of 2003 STLE/ASME Joint International Tribology Conference*, Ponte Vedra Beach, Florida USA, 2003.

10. Suciu, C., Diaconescu, E., Spinu, S., “Experimental Set-Up And Preliminary Results Upon A New Technique To Measure Contact Pressure,” *Proceedings of VarEHD14*, Suceava, 9-11 October, 2008, ISSN 1844-8917, Acta Tribologica, vol. 16, 2008 ISSN 1220 - 8434.

11. Suciu, C., Diaconescu E., “Contact Pressure Assessment by Reflectivity of a Solidified Gel Layer,” *Proceedings of the 2nd European Conference on Tribology, ECOTRIB 2009*, Faculty of Engineering, Pisa, Italy, June 7 - 10, 2009

12. Ditchburn, R. W., *Light*, Vol. II, Blackie & Son, Second Edition, 1963.

13. Diaconescu, E. N., 2004, „Solid-Like Properties of Molecular Liquids Subjected to EHD Conditions - Theoretical Investigations”, *Proceedings of 2004 ASME/STLE International Joint Tribology Conference*, Long Beach, California USA, October 24-27,

14. Born, M., and Wolf, E., 1980, *Principles of Optics*, Sixth Edition, Pergamon Press.

Sergiu SPINUe-mail: *sergiu.spinu@fim.usv.ro*Department of Mechanical Engineering,
University of Suceava,
ROMANIA**NUMERICAL SIMULATION OF
ELASTIC-PLASTIC CONTACT**

A fast algorithm for elastic-plastic non-conforming contact simulation is presented in this paper. The plastic strain increment is determined using a universal integration algorithm for isotropic elastoplasticity proposed by Fotiu and Nemat-Nasser. Elastic-plastic normal contact problem is solved iteratively based on the relation between pressure distribution and plastic strain, until the latter converges. The contact between a rigid sphere and an elastic-plastic half-space is modeled using the newly proposed computer program. Numerical simulations predict that residual stresses decrease the peak intensity of the stresses induced by contact pressure, thus impeding further plastic flow. Computed pressure distributions appear flattened compared to elastic case, due to changes in both hardening state of the elastic-plastic softer material and contact conformity.

Keywords: elastoplasticity, plastic strain increment, effective accumulated plastic strain, elastic-plastic contact

1. INTRODUCTION

While the elastic response of a material subjected to load application is reversible, plasticity theory describes the irreversible behavior of the material in reaction to loading beyond the limit of elastic domain. The transition between elastic and plastic deformation is marked by the yield strength of the softer material.

The modern approach in modeling elastic-plastic contact is based on the algorithm originally proposed by Mayeur, [1], for the elastic-plastic rough contact. However, his implementation was limited to two-dimensional contact, as influence coefficients were derived for this case only. Problem generalization is due to Jacq, [2], and to Jacq et al. [3], who advanced a complete semi-analytical formulation for the three-dimensional elastic-plastic contact.

The algorithm was later refined by Wang and Keer, [4], who improved the convergence of residual and elastic loops. The main idea of the newly proposed Fast Convergence Method (FCM) is to use the convergence values for the current loop as initial guess values for the next loop. This approach reduces the number of iterations if the loading increments are small. Wang and Keer used two-dimensional Discrete Convolution Fast Fourier Transform (DCFFT), [5], to speed up the computation of convolution products.

Jacq's influence coefficients for residual stresses were based on the problem decomposition

advanced by Chiu [6,7]. An alternative approach was proposed by Liu and Wang, [8], who also suggested that three-dimensional DCFFT can be used in a hybrid algorithm incorporating convolution and correlation with respect to different directions. Their Discrete Correlation Fast Fourier Transform (DCRFFT) algorithm uses convolution theorem to assess correlation, by substituting one term of the convolution product by its complex conjugate.

Nélias, Boucly, and Brunet, [9], improved the convergence of the residual loop, by assessing plastic strain increment with the aid of an algorithm for integration of elastoplasticity constitutive equations proposed by Fotiu and Nemat-Nasser, [10], as opposed to existing formulation, based on Prandtl-Reuss equations, [2]. As stated in [9], this results in a decrease of one order of magnitude in the CPU time.

Influence of a tangential loading in elastic-plastic contact with isotropic hardening was investigated by Antaluca, [11]. Kinematic hardening was added to the model by Chen, Wang, Wang, Keer, and Cao, [12], who advanced an algorithm for simulating the three-dimensional repeated rolling or sliding contact of a rigid sphere over an elastic-plastic half-space.

Cretu and Benchea, [13], and Benchea and Cretu, [14], employed an improved incremental algorithm for elastic-plastic non-conforming contact modeling, based on the method originally proposed by Cretu and Hatmanu, [15]. This alternative formulation uses an assumption of compatibility

between elastic and plastic strains, and can be used to achieve accurate results with a moderate computational effort, as implies fewer iterative levels.

A numerical program for elastic-plastic contact modeling is overviewed in this paper, and the sequence used to assess the plastic strain increment is presented in detail. The solver is used to simulate the elastic-plastic contact between a rigid sphere and an elastic-plastic half-space having a hardening behavior described by Swift's law. Numerical predictions agree well with results obtained with alternative numerical codes or using finite element analysis.

2. ELASTIC-PLASTIC CONTACT ALGORITHM OVERVIEW

Since the works of Mayeur, [1] and of Jacq, [2], Betti's reciprocal theorem is used in elastic-plastic contact modeling to assess surface normal displacement and stress state in an elastic half-space in the presence of plastic strains. Resulting equations suggest elastic-plastic contact problem split in an elastic and a residual part. The elastic part comprises the static force equilibrium, interference equation, and complementarity conditions, while the residual part expresses the plastic strain increment and plastic zone contribution to surface normal displacement and to stress field in the elastic-plastic body. However, the two subproblems cannot be solved independently, as residual displacement, computed in the residual subproblem, enters interference equation in the elastic part, while contact stress, assessed in the elastic subproblem, is needed to find the plastic strain increment in the residual part.

Analytical resolution of resulting equations is available for neither the elastic, nor the residual part, as integration domains, namely boundary region with tractions and plastic strain volume respectively, not known a priori, are arbitrarily shaped. Therefore, numerical approach is preferred.

The principle of numerical approach consists in considering continuous distributions as piece-wise constant on the cells of a three-dimensional grid imposed in a volume enveloping integration domains. With this formulation, integration in the continuous model of the elastic-plastic contact model is replaced by multi-summation of elementary cells individual contributions, known from the influence coefficients or the Green functions. As these multi-summation operations are in fact convolution and/or correlation products, spectral methods are applied to speed up the computation.

The numerical model of the elastic part is obtained from that corresponding to a normal elastic contact problem completed with the residual term, namely the residual displacement, which is superimposed into the interference equation.

Consequently, the elastic subproblem can be treated as an elastic contact problem with a modified initial contact geometry. The most efficient solver is based on the conjugate gradient algorithm advanced by Polonsky and Keer, [16], tweaked with the DCFFT technique for convolution evaluation.

In the same manner, the residual part is reformulated numerically, by imposing digitized plastic strain distribution and finite load increments. Plastic strain contribution to normal surface displacement is expressed as a two-dimensional convolution, computed by two-dimensional DCFFT, [2]. The problem of residual stresses induced in the half-space by an arbitrary distribution of inelastic deformations is solved following a method originally suggested by Chiu [6,7]. The hybrid three dimensional spectral algorithms newly proposed by Spinu, [17], result in a dramatic decrease in computational effort.

The algorithm proposed for simulation of elastic-plastic non-conforming contact with isotropic behavior is based on three levels of iteration.

The innermost level, which assesses plastic strain increment, corresponds to the residual part, and has a fast convergence, as described in the following section. The second level adjusts contact pressure and residual displacement in an iterative approach specific to elastic contact problems with arbitrarily shaped contact geometry.

The outermost level is related to the fact that, unlike elastic solids, in which the state of strain depends on the achieved state of stress only, deformation in a plastic body depends on the complete history of loading. This level applies the load incrementally, until the imposed value is reached.

The algorithm for solving one loading step in the elastic-plastic normal contact problem is summarized in Figure 1.

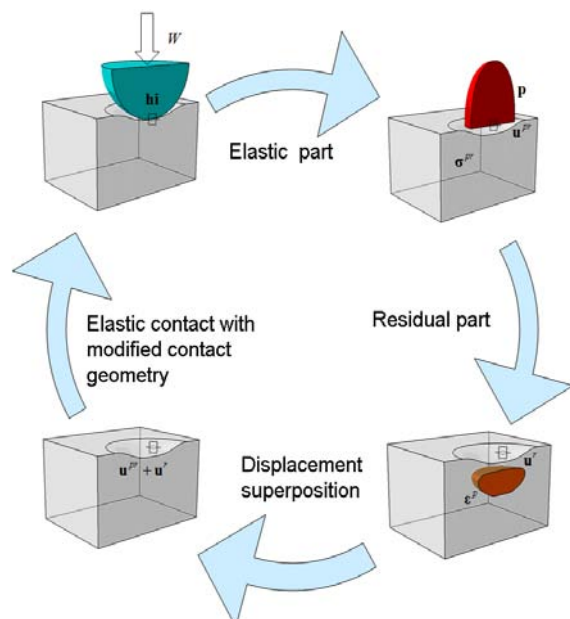


Figure 1. Elastic -plastic algorithm

Firstly, the elastic problem with modified contact geometry h_i is solved, yielding contact area and pressure distribution p . The latter can be used to assess elastic displacement field u^{pr} and stress field σ^{pr} . These terms represent the elastic part of displacement and stress, namely that part that is recovered once loading is removed. The stresses induced by pressure are used in the residual subproblem, to assess plastic strain increment. The algorithm, based on a method originally proposed by Fotiu and Nemat-Nasser, [10], is discussed in detail in the following section. The computed plastic strain increment is used to adjust the achieved plastic zone e^p . Once the volume with plastic strains is known, residual parts of displacement, u^r , and of stresses, σ^r , can be computed. As opposed to their elastic counterparts, terms u^r and σ^r express a potential state, that remains after contact unloading, if no plastic flow occurs during contact relief. The total displacement can then be computed, $u^{pr} + u^r$, thus imposing a new interference equation in the elastic subproblem. These sequences are looped until convergence is reached.

3. PLASTIC STRAIN INCREMENT

According to general theory of plasticity, plastic flow occurrence can be described mathematically with the aid of a yield function, assessing the yield locus in the multidimensional space of stress tensor components. If von Mises criterion is used to express stress intensity, this function can be expressed as:

$$f(e^p) = \sigma_{VM} - \sigma_Y(e^p), \quad (1)$$

where e^p denotes the effective accumulated plastic strain, $e^p = \sqrt{2\varepsilon_{ij}^p \varepsilon_{ij}^p / 3}$, and $\sigma_Y(e^p)$ is the yield strength function. The latter satisfy the relation for the initial yield strength σ_{Y0} :

$$\sigma_Y(0) = \sigma_{Y0}. \quad (2)$$

The following conditions must be met:

$$f \leq 0; de^p \geq 0; f \cdot de^p = 0, \quad (3)$$

with conditions $f = 0$ and $de^p > 0$ corresponding to plastic flow.

For elastic-perfectly plastic materials, relation (2) is verified for any value of e^p . However, for metallic materials, more complex models of elastic-plastic behavior are used, as the isotropic, or the kinematic hardening laws. The isotropic hardening law of Swift,

$$\sigma_Y(e^p) = B(C + e^p)^n, \quad (4)$$

with B, C and n material constants, is used in the current formulation.

According to flow rule, plastic strain increment can be expressed as:

$$d\varepsilon_{ij}^p = de^p \frac{\delta f}{\delta \sigma_{ij}} = de^p \frac{3S_{ij}}{2\sigma_{VM}}, \quad (5)$$

where S_{ij} denotes the deviatoric stress tensor.

The algorithm used to derive the plastic strain increment was advanced by Fotiu and Nemat-Nasser, [10], who developed a universal algorithm for integration of elastoplasticity constitutive equations. As stated in [10], the algorithm is unconditionally stable and accurate for large load increments, as it takes into account the entire non-linear structure of elastoplasticity constitutive equations, which are solved iteratively, via Newton-Raphson numerical method, at the end of each loading step. The yield function f is linearized at the beginning of the load increment, by employing an elastic predictor. This places the state point far outside the yield surface $f = 0$, since elastic-plastic modulus is small compared to the elastic one. The return path to the yield surface is generated by the plastic corrector, via Newton-Raphson iteration. This approach, also referred to as elastic predictor - plastic corrector, is efficient when most of the total strain is elastic. In the fully plastic regime, which occurs usually after the elastic-plastic one, the plastic strain is predominant, thus the return path may require numerous iterations. Thus, linearization at the beginning of the loading step is performed by a plastic predictor, and return path is generated with an elastic corrector.

A yield occurs when von Mises stress exceeds current yield stress, namely when $f > 0$. The elastic domain expands or translates to include the new state point, namely to verify condition $f = 0$. The actual increment of effective accumulative plastic strain should satisfy equation of the new yield surface in the plastic zone:

$$f(e^p + \delta e^p) = 0. \quad (6)$$

Here, δe^p denotes the finite increment of effective plastic strain, as defined in [2]. Relation (6) can be considered as an equation in δe^p , which is solved numerically by Newton-Raphson iteration. To this end, yield surface relation is linearized along plastic corrector direction:

$$f(e^p + \delta e^p) = f(e^p) + \delta e^p \frac{\partial f(e^p)}{\partial e^p} = 0, \quad (7)$$

yielding the plastic corrector:

$$\delta e^p = -\frac{f(e^p)}{\frac{\partial f(e^p)}{\partial e^p}} = \frac{f(e^p)}{\frac{\partial \sigma_Y(e^p)}{\partial e^p} - \frac{\partial \sigma_{VM}}{\partial e^p}}. \quad (8)$$

For isotropic hardening, the derivate of equivalent von Mises stress with respect to effective accumulative plastic strain was derived by Nélias, Boucly and Brunet, [9], from the general equations presented in [10] for rate-dependent elastoplasticity:

$$\frac{\partial \sigma_{VM}}{\partial e^p} = -3G. \quad (9)$$

where G is the shear modulus, or the μ Lamé's constant.

With these results, the following return-mapping algorithm with elastic predictor - plastic corrector can be formulated:

1. Acquire the state at the beginning of the loading step and impose the elastic predictor. For elastic-plastic contact problems, this is equivalent to solving an elastic loop without imposing any residual displacement increment. Corresponding parameters are identified by an "a" superscript, as opposed to a "b" superscript, used to denote the state at the end of the load increment: $e^{p(a)}$, $\sigma_Y^{(a)} = \sigma_Y(e^{p(a)})$, $\sigma_{ij}^{(a)}$ ($\sigma_{ij}^{(a)} = \sigma_{ij}^{pr(a)} + \sigma_{ij}^{r(a)}$), $\sigma_{VM}^{(a)}$, $f^{(a)} = \sigma_{VM}^{(a)} - \sigma_Y^{(a)}$. These variables also represent the input for the Newton-Raphson iteration. Thus, by using superscripts to denote the Newton-Raphson iteration number, $e^{p(1)} = e^{p(a)}$, $\sigma_Y^{(1)} = \sigma_Y^{(a)}$, $\sigma_{ij}^{(1)} = \sigma_{ij}^{(a)}$, $\sigma_{VM}^{(1)} = \sigma_{VM}^{(a)}$, $f^{(1)} = f^{(a)}$.

2. Start the Newton-Raphson iteration. Compute the plastic corrector according to relations (8) and (9):

$$\delta e^{p(i)} = f^{(i)} / \left(\frac{\partial k(e^{p(i)})}{\partial e^{p(i)}} + 3G \right). \quad (10)$$

3. Use the plastic corrector to adjust model parameters:

$$\sigma_{VM}^{(i+1)} = \sigma_{VM}^{(i)} - 3G\delta e^{p(i)}; \quad (11)$$

$$e^{p(i+1)} = e^{p(i)} + \delta e^{p(i)}; \quad (12)$$

$$\sigma_Y^{(i+1)} = \sigma_Y(e^{p(i+1)}); \quad (13)$$

$$S_{ij}^{(i+1)} = \frac{\sigma_{VM}^{(i+1)}}{\sigma_{VM}^{(i)}} S_{ij}^{(i)}. \quad (14)$$

4. Verify if Eq. (6) is verified to the imposed tolerance ϵ . If condition

$$|f^{(i+1)}| = |\sigma_{VM}^{(i+1)} - \sigma_Y^{(i+1)}| > \epsilon \quad (15)$$

is satisfied, go to step 2. If else, convergence is reached, and the state point at the end of the loading step is described by the newly computed parameters: $e^{p(b)} = e^{p(i+1)}$, $\sigma_{VM}^{(b)} = \sigma_{VM}^{(i+1)}$, $S_{ij}^{(b)} = S_{ij}^{(i+1)}$.

5. Compute the plastic strain increment, according to Eq. (5):

$$\delta \epsilon_{ij}^p = \left(e^{p(b)} - e^{p(a)} \right) \frac{3S_{ij}^{(b)}}{2\sigma_{VM}^{(b)}}. \quad (16)$$

This increment is used to update the plastic zone. The residual parts of displacement and of stress can then be computed, and superimposed to their elastic counterparts.

4. NUMERICAL SIMULATIONS

The contact between a rigid sphere of radius $R = 105 \cdot 10^{-6}$ m and an elastic-plastic half-space is modeled, allowing for comparison with results published by Boucly, Nélias and Green, [18]. Elastic half-space parameters are: Young modulus, $E_2 = 210$ GPa, Poisson's ratio, $\nu_2 = 0,3$. The hardening law of the elastic-plastic material is chosen as a power law (Swift), according to El Ghazal, [19]:

$$\sigma_Y(e^p) = B(C + e^p)^n, \quad (17)$$

with $\sigma_Y(e^p)$ the yield strength function, e^p the effective accumulated plastic strain, expressed in microdeformations, and the following parameters: $B = 1280$ MPa, $C = 30$, $n = 0.085$. The imposed hardening curve is depicted in Figure 1.

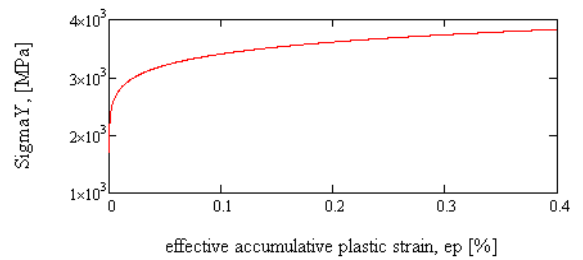


Figure 2. Swift's hardening law

The contact is loaded incrementally to a maximum value of $W = 0.650$ N, for which the purely elastic model predicts a contact radius $a_H = 6.053 \mu\text{m}$ and a hertzian pressure $p_H = 8470$ MPa.

Dimensionless coordinates are defined as ratios to a_H , $\bar{x}_i = x_i/a_H$, and dimensionless

pressure or stresses as ratios to p_H . The computational domain is a rectangular cuboid of sides $L_1 = L_2 = 3a_H$, $L_3 = 1.6a_H$, which is discretized into $N_1 = N_2 = 120$, $N_3 = 80$ elementary cells. Due to the fact that problem is axisymmetric, three dimensional distributions are depicted in the plane $x_2 = 0$ only.

Pressure profiles predicted by the numerical program for six loading levels corresponding to elastic-plastic domain are presented in Figure 3. Hertz pressure corresponding to maximum load is also plotted for reference.

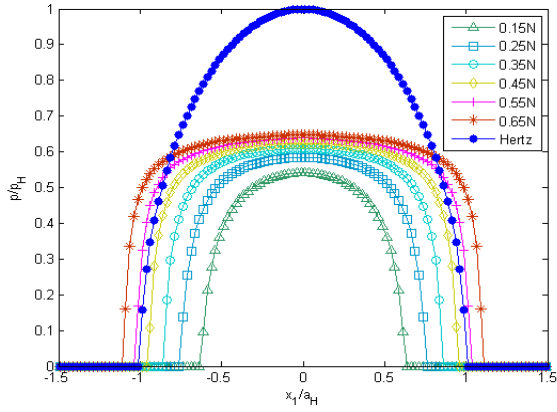


Figure 3. Pressure profiles in the plane $x_2 = 0$, various loading levels

Plastic strain region generates residual displacements, namely displacements that would persist if a purely elastic unloading would occur. These displacements increase contact conformity, as depicted in Figure 4, resulting in a more uniform pressure distribution on an enlarged contact area. The curve describing the residual print maximum depth versus loading level, Figure 5, is the same with the one obtained by Jacq. et al, [3], and by Benchea and Cretu, [20].

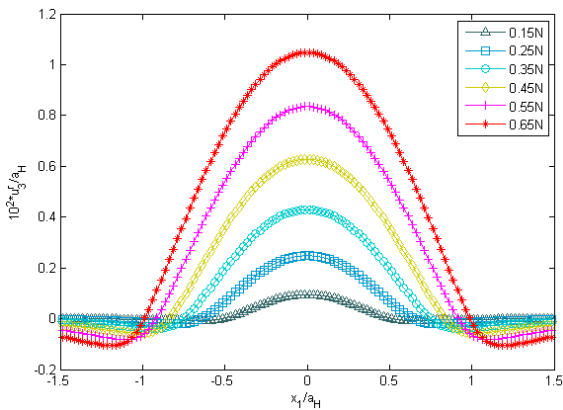


Figure 4. Residual print profiles in elastic-plastic spherical contact

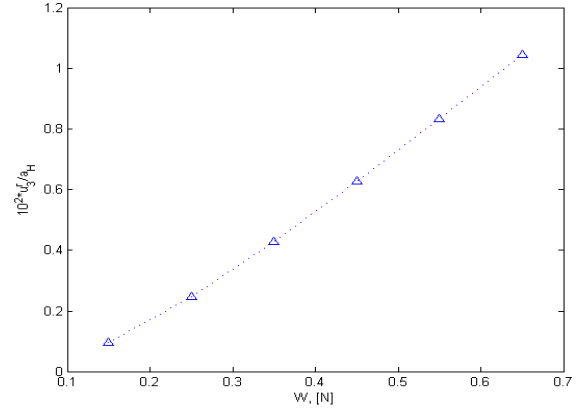


Figure 5. Residual print depth

Effective accumulated plastic strain distribution is presented in Figure 6. Plastic zone, initially occupying a hemispherical region located at hertzian depths, advances toward the free surface with increased loading, enveloping a purely elastic core. This development is consistent with the one suggested by Johnson, [21].

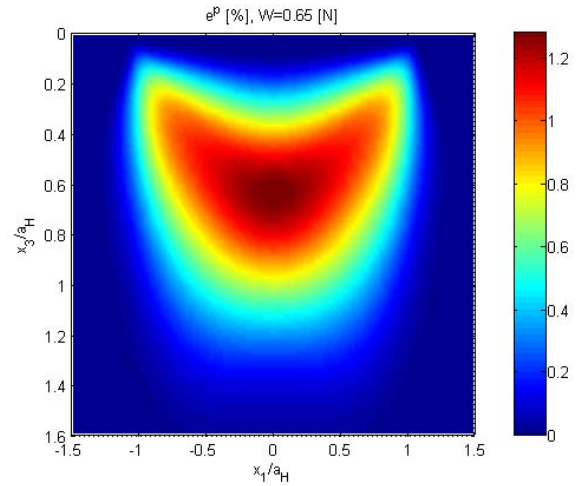


Figure 6. Effective accumulated plastic strain

Plastic strains induce residual stresses, namely elastic stresses which persist in the elastic-plastic body after contact unloading. These residual stresses superimpose stresses induced by contact pressure, the resulting state being responsible for further plastic strain. Consequently, an accurate estimation of stress field in the elastic-plastic body is essential to plastic strain increment prediction.

Figures 7 and 8 depict distributions of equivalent von Mises residual and contact stress. Summation of these two states yields elastic-plastic stress state, presented in Figure 9. To allow for a better comparison, the same scale is used in Figures 7-9. Residual stress intensity is one order of magnitude smaller than equivalent contact stress. Comparison of distributions depicted in Figures 8 and 9 suggests that residual stress reduces peaks in contact stress intensity, thus making the resulting field more uniform. This behavior is also suggested

by the curves traced in Figure 10. Maximum intensity of contact stress increase more rapidly than the maximum of the total field, due to contribution of residual stress. Consequently, residual stresses act to impede further plastic flow, until the new stress point reaches the new yield locus.

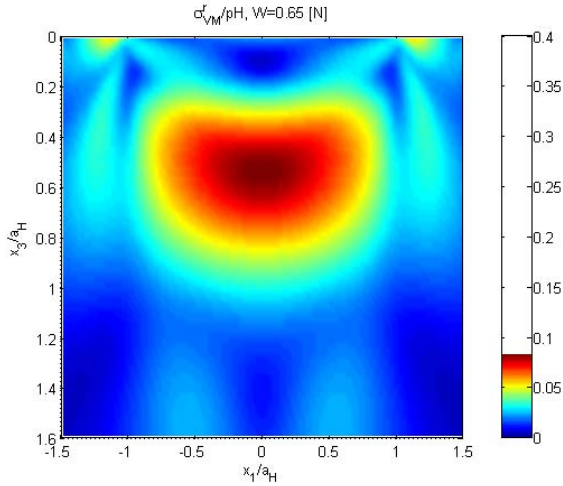


Figure 7. Von Mises residual stress

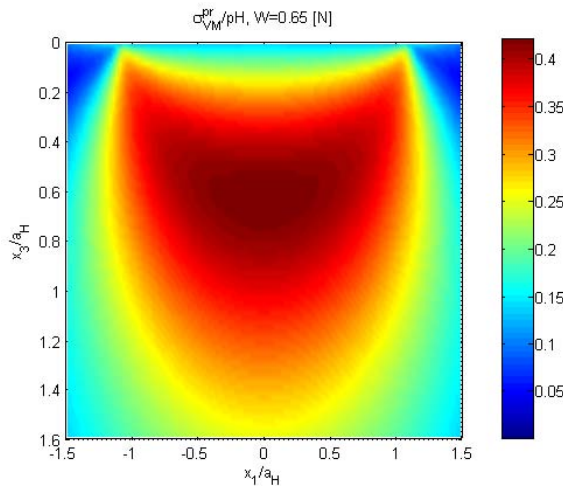


Figure 8. Von Mises contact stress

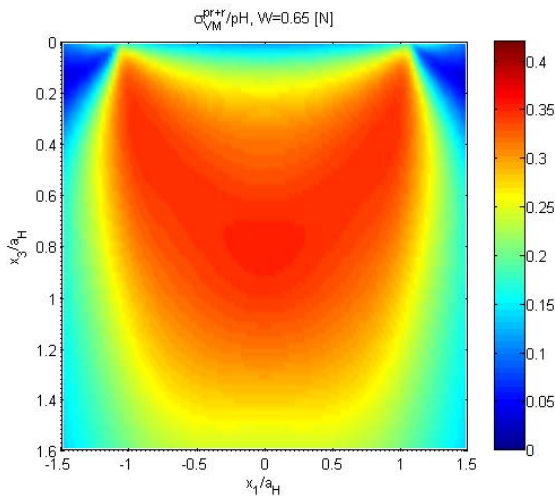


Figure 9. Resulting Von Mises stress in elastic-plastic body

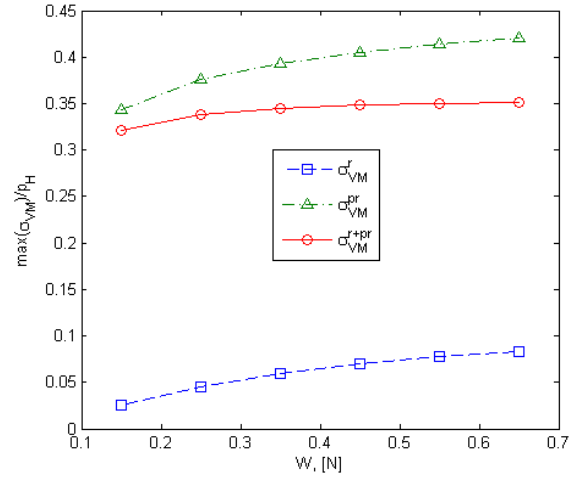


Figure 10. Maximum intensities of stress fields versus loading level

5. CONCLUSIONS

This paper summarizes an efficient algorithm for simulation of elastic-plastic contacts. Computation of plastic strain increment is presented in detail. The plastic strain increment is determined in a fast convergent Newton-Raphson procedure which iterates a scalar, namely the effective accumulative plastic strain. The method, originally suggested by Fotiu and Nemat-Nasser, employs an elastic predictor, which places the state outside yield surface, and a plastic corrector, assessing the return path to the yield locus. The method is fast, stable and accurate even for large loading steps.

Plastic strain modifies contact pressure by superimposing induced residual surface displacement into the initial contact geometry. Contact pressure, in its turn, contributes to the subsurface stress state, responsible for plastic zone development. Consequently, the model is solved iteratively based on the relation between pressure distribution and plastic strain, until the latter converges.

The newly proposed elastic-plastic contact program is used to simulate the contact between a rigid sphere and an elastic-plastic half-space following a Swift isotropic hardening law. Pressure profiles predicted numerically agree well with already published results. Pressure appears flattened compared to the elastic case, due to changes in both hardening state of the softer material and contact conformity.

Plastic zone, initially occupying a hemispherical region located at hertzian depths, advances toward the free surface with increased loading, enveloping a purely elastic core. Residual stress intensity is one order of magnitude smaller than stresses induced by contact pressure. They contribute to the total elastic field by decreasing the peaks in contact stress intensity, thus impeding

further plastic flow. The resulting field is more uniform, suggesting that material responds by change in hardening state as to delay further plastic flow until the state reaches the new yield locus.

ACKNOWLEDGEMENT

This paper was supported by the project “Progress and development through post-doctoral research and innovation in engineering and applied sciences – PRiDE - Contract no. POSDRU/89/1.5/S/57083”, project co-funded from European Social Fund through Sectorial Operational Program Human Resources 2007-2013.

REFERENCES

1. **Mayeur, C.**, 1995, *Modélisation du contact rugueux élastoplastique*, Ph.D. Thesis, INSA Lyon, France.
2. **Jacq, C.**, 2001, *Limite d'endurance et durée de vie en fatigue de roulement du 32CrMoV13 nitruré en présence d'indentations*, Ph.D. Thesis, INSA Lyon, France.
3. **Jacq, C., Nélias, D., Lormand, G., and Girodin, D.**, 2002, “Development of a Three-Dimensional Semi-Analytical Elastic-Plastic Contact Code,” *ASME J. Tribol.*, 124, pp. 653–667.
4. **Wang, F., and Keer, L. M.**, 2005, “Numerical Simulation for Three Dimensional Elastic-Plastic Contact With Hardening Behavior,” *ASME J. Tribol.*, 127, pp. 494–502.
5. **Liu, S. B., Wang, Q., and Liu, G.**, 2000, “A Versatile Method of Discrete Convolution and FFT (DC-FFT) for Contact Analyses,” *Wear*, 243 (1–2), pp. 101–111.
6. **Chiu, Y. P.**, 1977, “On the Stress Field Due to Initial Strains in a Cuboid Surrounded by an Infinite Elastic Space,” *ASME J. Appl. Mech.*, 44, pp. 587–590.
7. **Chiu, Y. P.**, 1978, “On the Stress Field and Surface Deformation in a Half Space with Cuboidal Zone in Which Initial Strains Are Uniform,” *ASME J. Appl. Mech.*, 45, pp. 302–306.
8. **Liu, S. Wang, Q.**, 2005, “Elastic Fields due to Eigenstrains in a Half-Space,” *ASME J. Appl. Mech.*, 72, pp. 871–878.
9. **Nélias, D., Boucly, V., and Brunet, M.**, 2006, “Elastic-Plastic Contact Between Rough Surfaces: Proposal for a Wear or Running-in Model,” *ASME J. Tribol.*, 128, pp. 236 - 244.
10. **Fotiu, P. A., and Nemat-Nasser, S.**, 1996, “A Universal Integration Algorithm for Rate-Dependant Elastoplasticity,” *Comput. Struct.*, 59, pp. 1173–1184.
11. **Antaluca, E.**, 2005, *Contribution a l'étude des contacts élasto-plastiques - effet d'un chargement normal et tangentiel*, Ph.D. Thesis, INSA Lyon, France.
12. **Chen, W. W., Wang, Q. J., Wang, F., Keer, L. M., and Cao, J.**, 2008, “Three-Dimensional Repeated Elasto-Plastic Point Contacts, Rolling, and Sliding,” *ASME J. Tribol.*, 75, pp. 021021-1 - 021021-12.
13. **Cretu, S. Sp., Benchea, M.**, 2008, “An Improved Incremental Model to Analyse Elastic-Plastic Concentrated Contacts,” *Proc. of 16th International Colloquium Tribology*, Esslingen, Germany, pp.33 (on CD also).
14. **Benchea, M., Cretu, S. Sp.**, 2007, “A Three Dimensional Elastic Plastic Analysis of Rolling Contacts,” *ROTRIB-07*, Nov. 6-9, Bucharest, Romania.
15. **Cretu, S., Hatmanu, V.**, 1985, “A Numerical Analysis of Permanent Deformation in Elastic-Plastic Line Contact,” *Bul. Inst. Polit. Iasi*, XXXI, (1-4), pp. 19-25.
16. **Polonsky, I. A., and Keer, L. M.**, 1999, A “Numerical Method for Solving Rough Contact Problems Based on the Multi-Level Multi-Summation and Conjugate Gradient Techniques,” *Wear*, 231(2), pp. 206–219.
17. **Spinu, S.**, 2009, *Contributions to the Solution of the Elastic-Plastic Normal Contact Problem*, (in Romanian), PhD Thesis, University of Suceava, Romania.
18. **Boucly, V., Nélias, D., and Green, I.**, 2007, “Modeling of the Rolling and Sliding Contact Between Two Asperities,” *ASME J. Tribol.*, 129, pp. 235 - 245.
19. **El Ghazal, H.**, 1999, *Etude des propriétés microstructurales et mécaniques des aciers 16NiCrMo13 cémenté et 32CrMoV13 nitrure - Application a la prevision de leur limite d'endurance en fatigue de roulement*, Ph.D. Thesis, INSA Lyon, France.
20. **Benchea, M., and Cretu, S.**, 2008, “An Improved Incremental Model to Analyse Elastic - Plastic Concentrated Contacts – The Finite Element Analysis and Validation,” *Acta Tribologica*, Vol. 16, ISSN 1220-8434.
21. **Johnson, K. L.**, 1985, *Contact Mechanics*, Cambridge University Press.

Yuichiro NAGATA
e-mail: y.nagata@sussex.ac.uk

Romeo GLOVNEA
e-mail: r.p.glovnea@sussex.ac.uk

School of Engineering and Design,
University of Sussex,
UNITED KINGDOM

DIELECTRIC PROPERTIES OF GREASE LUBRICANTS

Grease lubricants are often preferred in machine elements working under elastohydrodynamic conditions such as rolling element bearings and constant velocity joints due mainly to the fact that they do not need resupply and filtering systems and provide lower lubricant losses. At the same time greases are complex materials, with liquid and solid phases, which make difficult the prediction of their behaviour in those contacts. In the present paper dielectric properties of lubricating greases are studied, as a step towards the understanding of their behaviour and predicting their in-contact rheological properties.

Keywords: elastohydrodynamic lubrication, grease, dielectric properties, rheology

1. INTRODUCTION

Elastohydrodynamic lubrication regime (EHD) occurs in machine elements such as rolling element bearings, gears, cams, traction drives and others. The non-conformal contacts of these machine elements are characterized by very thin lubricating films (typically under one micrometer) which support extremely large pressures due to a combined effect of hydrodynamic action of the fluid, the elastic deformation of the surfaces and the variation of lubricant viscosity with pressure. In the case of oil-lubricated EHD contacts there are currently techniques for measuring experimentally or predicting theoretically, with sufficient accuracy, the film thickness. Optical interferometry on one hand and various numerical techniques on the other have been used in the past to successfully evaluate the behaviour of elastohydrodynamic films in both steady state and transient conditions [1]. The same cannot be said about grease lubricated contacts, where their dual, liquid-solid phase makes it difficult to correlate their bulk properties to their film forming capabilities.

The current paper is part of a wider study on the rheology of lubricating greases in EHD contacts and is focused on the correlation between their dielectric characteristics and their in-contact rheological properties.

2. BACKGROUND

Greases are very common lubricants in rolling element bearings where they can provide a life-long solution for these machine element

lubrication needs. However it is difficult to predict the behaviour inside the contact or the film thickness based on grease's bulk properties as it is the case with liquid lubricants.

Film thickness measurements by optical interferometry have revealed that in general greases give thicker film than their base oils at low speed, but the dependence of the film thickness on the entrainment speed is similar to that found for oils. On the other hand, at greater speeds, the film thickness decreases sharply due to starvation [2]. Errikson et al [3] have shown that soap particles are able to pass through the EHD conjunction in a certain proportion, not necessarily related to their weight percentage in the grease composition. The effect of the thickener on the film thickness has also been studied by Couronne et al [4]. They have found that thickener microstructure is not a determinant factor for the formation of a thick lubricant film, however, it influences oil bleeding, mechanical stability, and rheological behaviour. Cann et al suggested that the film thickness of grease lubricated contacts increases approximately linearly with soap concentration [5].

The rheological behaviour of lubricants in elastohydrodynamic conditions has been a debated subject for many years and a number of models have been proposed by various researchers in the field. The near exponential increase of the viscosity of the lubricant with pressure has led to the conclusion that this behaves like a visco-elastic solid with a response depending on pressure, temperature and shear rate.

Hirst and Moore [6] showed, based on extensive experimental traction results, that the EHD films behave elastically at low shear rates, but lose

elastic properties at higher rates of shear, when they behave like viscous, non-Newtonian fluids. They propose a traction coefficient (T/W) of the form:

$$\frac{T}{W} = \bar{\alpha}\tau_0 - \frac{\tau_0}{p} \ln\left(\frac{\tau_0}{2\eta_0\dot{\gamma}}\right), \quad (1)$$

where $\bar{\alpha}$ is the pressure viscosity coefficient, τ_0 is a characteristic shear stress, η_0 is the viscosity at ambient pressure and $\dot{\gamma}$ is the shear rate.

Bair and Winer [7] suggest a modified Maxwell model which allows for a limiting shear stress of the lubricant film, based only on primary laboratory results. Evans and Johnson [8] investigated the behaviour of a number of lubricating oils with different chemical structure using a disc machine as a high-pressure rheometer. By extending a previous model proposed by Johnson and Tevaarwerk [9] they suggest that the behaviour of lubricants in EHD conditions can be described by the following relationship:

$$\dot{\gamma} = \frac{\dot{\tau}}{G} + \frac{\tau_0}{\eta} \sinh\left(\frac{\tau}{\tau_0}\right). \quad (2)$$

Diaconescu [10] has showed theoretically that molecular liquids possess solid-like behaviour when subjected to short duration shear, exhibiting a shear modulus and limiting shear stress.

From an experimental point of view the film formation in elastohydrodynamic contacts has been investigated by either optical or electrical methods. The former are mainly based on optical interferometry requiring that one of the contacting bodies is transparent, while in the latter, either the resistance or capacitance of the contact between two metallic bodies is analysed. Electrical methods are relatively simple to implement and inexpensive but are only able to give average values of the measured parameters. When used to evaluate film thickness they are also difficult to calibrate.

The electrical capacitance has traditionally been used to measure film thickness in various EHD lubricated system, such as piston-ring of IC engines [11-13] and cam-tapet and gears mechanisms [14-16]. Electrical capacitance depends of the frequency of the electrical current passed through it because the electric dipoles of the molecules need time to align with the electric field. This property is exploited in an experimental technique called dielectric spectroscopy or dielectric relaxation spectroscopy which is able to correlate molecular processes with the rheological behaviour of a sample.

In this paper dielectric spectroscopy has been used in parallel with traction measurements to analyse rheological parameters of various composition grease lubricants.

3. EXPERIMENT

3.1 Experimental setup and procedure

Two types of tests were carried out, denoted here as static and dynamic. Details and schematics of the experimental setups of the static measurements can be found in [17]. In these, a plane capacitor has been set up between the jaws of a micrometer, which allowed the separation between plates to be set with a micrometer precision. The gap between the plates was set at 0.2 millimetres in these tests. After the capacitance of this capacitor in air was measured, the space between the plates was filled with grease and the capacitance measured again. Capacitance has been measured in a frequency range of 100Hz to 10MHz by an impedance phase shift analyser. In this study an extra resistor, 500k Ω , was connected in series with the capacitor so that the dielectric constant ϵ' and the loss factor ϵ'' were calculated from the measured capacitance C, resistance R and the circular frequency ω by using the following equations:

$$\epsilon' = \frac{C}{C_0 [1 + (\omega RC)^2]}, \epsilon'' = \frac{\omega RC^2}{C_0 [1 + (\omega RC)^2]}. \quad (3)$$

Although non-polar substances do not show relaxation behaviour, the introduction of the external resistor made possible that all samples show relaxation behaviour. To calculate the relaxation time τ_r of the samples, the Havriliak-Negami equation (4) was fitted to the obtained data between 1kHz and 100kHz.

$$\epsilon' - i\epsilon'' = \frac{\epsilon_0 - \epsilon_\infty}{[1 + (i\omega\tau_r)^\alpha]^\beta} \quad (0 \leq \alpha, \beta \leq 1), \quad (4)$$

where ϵ_0 and ϵ_∞ are the relative permittivity at low frequency and at high frequency respectively.

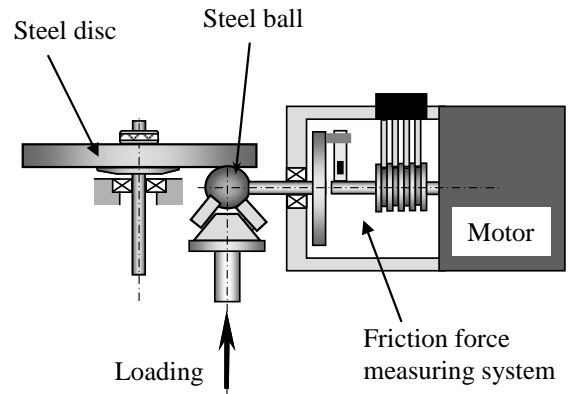


Figure 1. Traction coefficient measurement setup

Table 1. Composition of tested greases

Name of Grease	Base oil	Thickener	Weight percentage (%)	Viscosity (mm ² /s) at 40 , 100	Worked Penetration
Grease 1	PAO	12OH-LiSt	12	31, 5.8	236
Grease 2	PAO	12OH-LiSt	12	66, 10	291
Grease 3	PAO	12OH-LiSt	12	411, 41	386
Grease 4	PAO	Di-Urea	13.4	31,5.8	280
Grease 5	PAO	LiSt	12	19, 4.1	336
Grease 6	PAO	LiSt	12	411, 41	339
RL2	HVI160S	Di-Urea	N/A	107, 12	280
RLS2	PAD1450	Poly-Urea	N/A	100, 13	265 - 295
SB-M	Synthetic HC	Urea	10 - 20	45, 7.7	220
SRL	Synthetic Ester	LiSt	5 - 15	23, 4.7	250

EHD traction measurements, called here dynamic tests, were performed in rig normally used for measuring elastohydrodynamic film thickness. In this study the EHD contact was formed between a flat steel disc and a ball loaded together and driven at appropriate velocities, such that desired slide/roll ratios were obtained. The grease under study was spread onto the surface of the disc and was not re-supplied during the test. A schematic of the rig is shown in Figure 1. The normal force was measured by a load cell within the loading system, while the traction force was measured by strain gauges placed on a thin plate which drove the ball's shaft.

3.2 Materials and testing conditions

Ten different types of grease were employed in this study with their detailed composition listed in Table 1. Greases 1 to 6 are made by NSK for research purposes, containing no additives, solely to see the effect of the base oil or thickener upon the bulk properties and the behaviour of the grease. RL2 and RLS2 are commercially produced by Shell and they contain some additives. SB-M and SRL are also available as commercial greases, and are made by Kyodo Yushi. Both greases contain additives for which details are not available, while SB-M is produced specifically as a low-noise grease.

Traction measurements were carried out at an entrainment speed of 0.02m/s and for several loads from 10N to 50N. The Hertzian pressure varied between 0.6GPa and 1.1GPa and the contact diameter between 170µm and 290µm. The slide/roll ratio was varied between zero and 0.6. All tests were performed at ambient temperature.

4. RESULTS AND DISCUSSION

4.1 Dielectric measurements

The dependence of the real and imaginary parts of the dielectric constant of SRL grease and its base oil with frequency are shown in Figure 2.

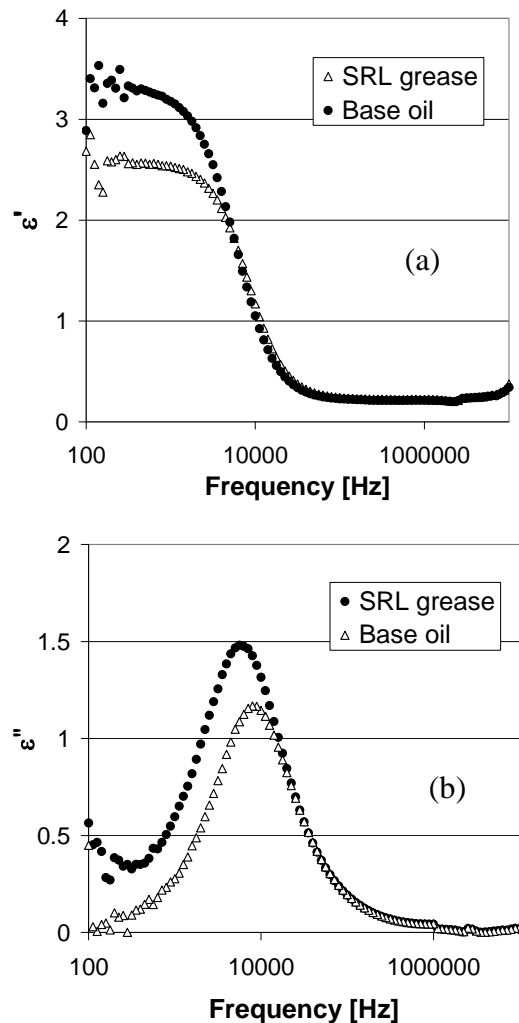


Figure 2. Dielectric permittivity of SRL grease

As explained in the previous section a resistor has been fitted in series with the measured capacitor, in order to evaluate the relaxation behaviour of the PAO oil, which is known to have very low polarity. This means that the relaxation time extracted from curves similar to those seen in Figure 2b depends of

the value of this resistor and thus it is not the real dielectric relaxation time of the oils and grease used in these tests. Even for polar greases, which naturally show relaxation behaviour, the relaxation time could not be measured without the additional resistor because the maximum is reached at frequencies outside the measuring range of the instrument, i.e. 30MHz. Although a quantitative evaluation of the dielectric relaxation time was possible, a quantitative comparison of this parameter between the studied greases and between the grease and their base oil was performed using this artefact.

For all greases it has been found that they have higher dielectric constant and longer relaxation time than the corresponding base oils.

Figure 3 shows the relationship between the dielectric constant and the relaxation time. From these results it can be seen that SRL grease, which consists of a polar base oil and non-polar thickener has the largest dielectric constant and longest relaxation time among all ten studied greases. Greases 1 to 3 which consist of a non-polar base oil and a polar thickener have relatively high dielectric constant, while Lithium Grease 5 has the smallest permittivity and the shortest relaxation time.

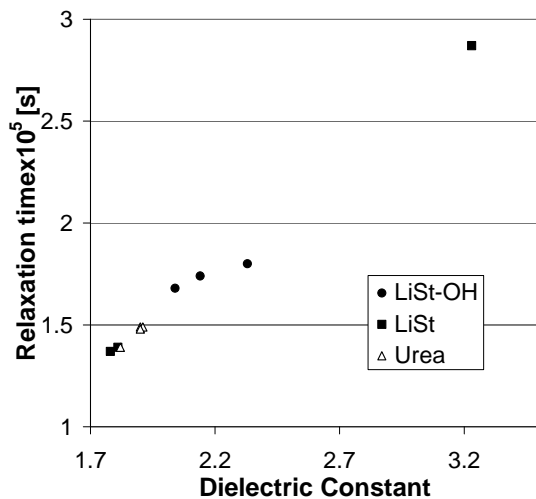


Figure 3. Dielectric properties of studied greases

Figure 4 shows, comparatively the relaxation time for polar and non-polar greases. In this Figure, the name and values inside the boxes indicate the name of corresponding base oil and its viscosity at 40°C and 100°C. Also, for better clarity, the scales in these graphs are different. The distinguishing feature observed in these graphs is that the greases made from higher viscosity oil give larger dielectric constant than that made from lower viscosity oil. However, the same thing cannot be said about polar greases. Grease 6 has the largest dielectric constant between greases of the same type, while grease 1 has the largest dielectric constant among 12OH-LiSt greases. The explanation for this behaviour can be given by the chain lengths of the oil molecules. It is well known that oils which contain a longer chain in

their chemical structure tend to have high viscosity and the higher the viscosity of the oil, the higher the relative permittivity becomes. In the case of non-polar greases, this mechanism can be applied and the dielectric constant of bulk grease increases with its base oil's viscosity. On the other hand, in the case of polar grease, the dipole moment of bulk structure may become weak when the polar substance is attached to the long molecular structure. From this perspective it could be explained why the 12OH-LiSt grease, formed from a high viscosity base oil, shows small dielectric constant.

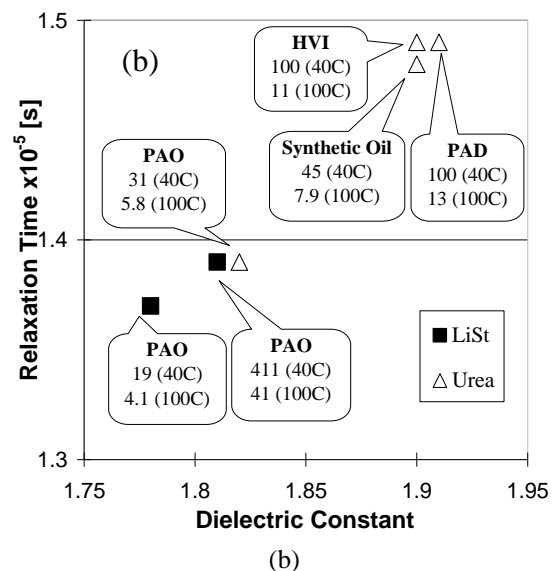
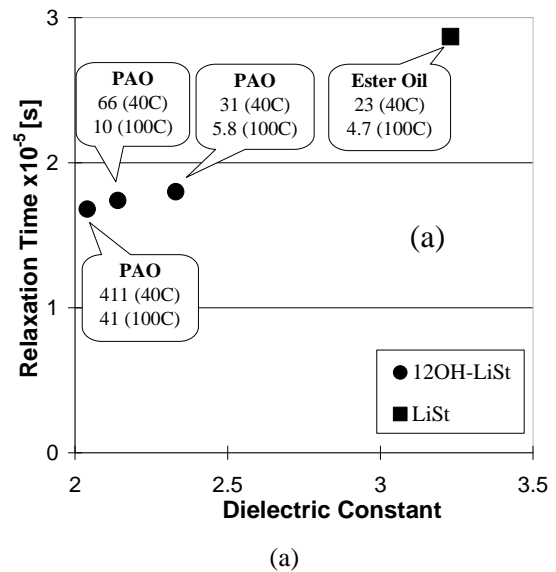


Figure 4. Dielectric properties of polar greases (a) and non-polar greases (b)

In the low frequency region of the dielectric measurements, the loss tangent factor,

$$\tan \delta = \frac{\epsilon''}{\epsilon'} \quad (4)$$

indicates the electrical conductivity of material [18]. Of all tested greases, only SRL shows good conductivity, as seen in Figure 5, where the tangent loss of SRL grease, grease 1, grease 5 and SB-M, are shown as a function of frequency.

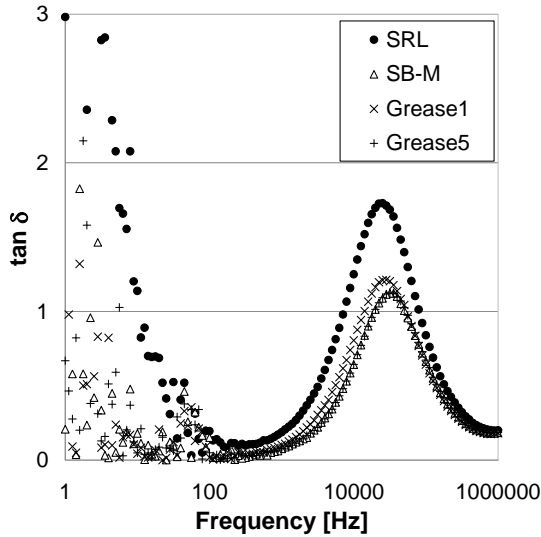


Figure 5. Loss tangent factor of four greases

4.2 EHD Traction Measurements

Traction curves of SRL at 10N load are shown in Figure 6.

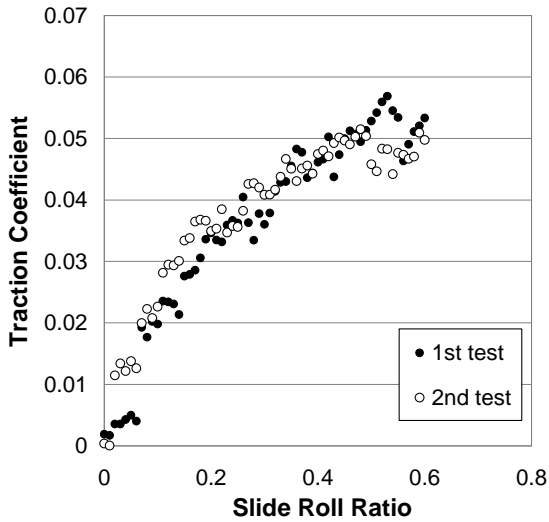


Figure 6. Traction curves for SRL grease

In each test, the measurement of the traction coefficient was carried out twice. After a first test the rig was left to run for five minutes in pure rolling conditions and after that, the test was run again in order to check whether starvation of the contact occurs, due to the ball pushing the grease to the sides of the track.

Graphs like those seen in Figure 6 can be transformed to show the dependence between the shear stress and shear strain rate. Such dependence

for some of the greases studied in this work is shown in Figure 7.

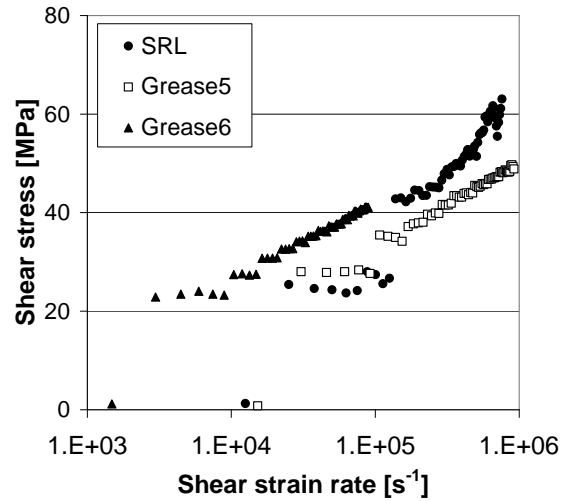


Figure 7. Shear stress function of shear rate

The traction curves obtained were subsequently used in an analysis similar to that done by Evans and Johnson [9], to extract the effective viscosity η and the Eyring stress τ_0 of the tested lubricants. For large shear strain the hyperbolic sine function can be approximated with an exponential, and for a negligible elastic term, equation (2) becomes:

$$\tau \cong \tau_0 \ln \dot{\gamma} + \tau_0 \ln \left(\frac{2\eta}{\tau_0} \right). \quad (5)$$

In this relationship, τ is the shear stress, τ_0 is the Eyring stress and $\dot{\gamma}$ is the shear rate. In a logarithmic representation, the slope of the linear region of the shear stress/shear rate dependence, seen in Figure 7 for large values of the shear rate, represents the Eyring stress of the lubricant, as predicted by Equation (5).

In general, the Eyring stress has been found to have similar values of that of the base oils, except four greases, RL2, RLS2, SB-M and SRL, which showed larger Eyring stress than that of the corresponding base oils. As seen in Table 1, RL2, RLS2 and SB-M, have different composition, although for all of them, the thickener is urea based. Their base oil is also different from one another: mineral oil for RL2 and synthetic oils of for RLS2 and SB-M. As shown in Figure 4, these greases have very similar dielectric relaxation times. The SRL grease, on the other hand, is very different from the composition point of view, with a ester base oil and a lithium soap as thickener. The Eyring stress for this grease and its base oil can be seen in Figure 8. As this parameter is not directly measured, but it is calculated as explained above, it is very sensitive

to the accuracy of the traction coefficient and film thickness measurements. For this reason, the tests have been repeated and the average values, together with error bars have been shown. It is clear that the Eyring stress of the grease is larger than that of the base oil.

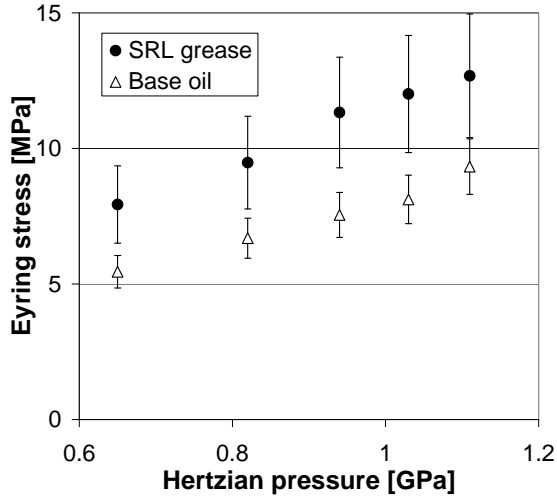


Figure 8. Eyring stress for SRL grease and base oil

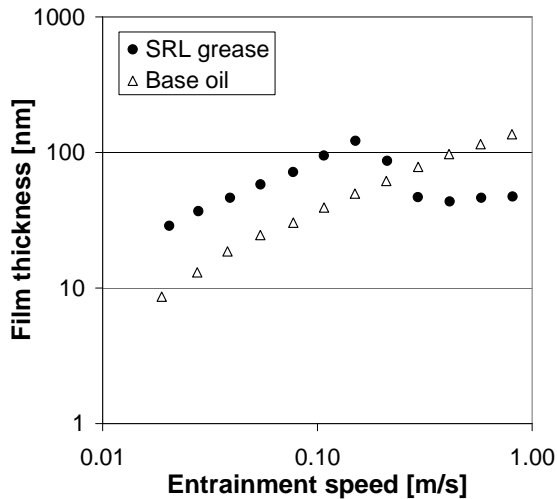


Figure 9. Film thickness measurements of SRL and its base oil

The shear rate involved in the evaluation of the Eyring stress is determined as the rate between the sliding speed in the contact and the film thickness. A comparison of the central film thickness for the grease and the base oil is shown in Figure 9. For the low speeds region, where the traction coefficient tests have been conducted, the grease has a film thickness about four times larger than that of the base oil. It is not clear, at this point, whether the larger value of the Eyring stress for these greases is a genuine effect, or an experimental artifact, however, the fact that this tendency appeared every time the test was repeated, and that the tests for all greases are done in identical conditions, suggest indeed, among all greases tested

in this study, that their Eyring stress has larger values than their base oil.

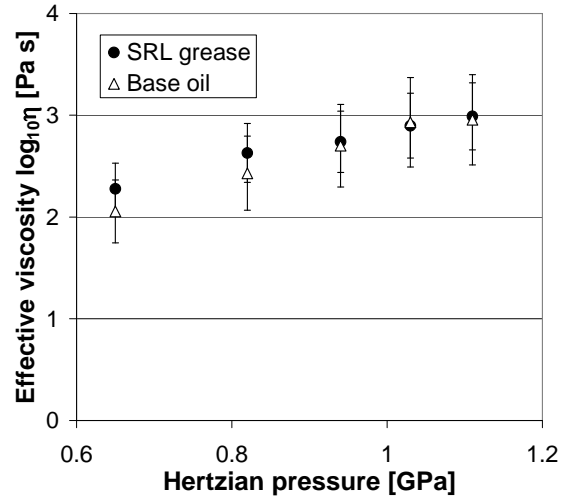


Figure 10. Effective viscosity of SRL grease

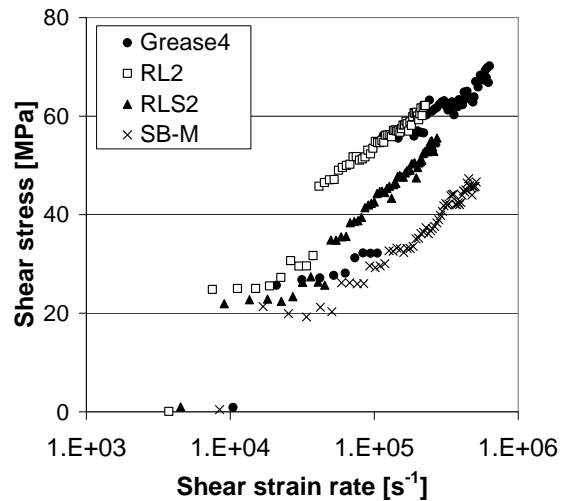


Figure 11. Shear stress for urea-type greases

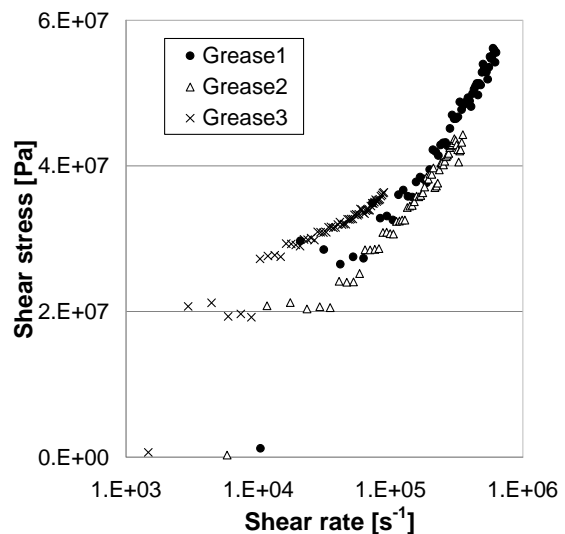


Figure 12. Shear stress for 120H-LiSt greases

After determining the Eyring stress, from equation (5) the effective, average viscosity of the lubricant inside the contact can be extracted. This was done by fitting equation (5) to the experimental data. The results for SRL grease are shown in Figure 10. As seen, unlike the Eyring stress, the values of the effective viscosity of the grease tend to be below the value of its base oil at high pressure.

From the traction results for all greases, it can be concluded that urea greases tend to show relatively high shear stress. An exception to this rule is SB-M, which shows relatively low shear stress. This grease, which is produced especially as low-noise grease, also has the smallest permittivity among urea greases. Four types of urea greases are compared in Figure 11. Figure 12 shows the shear stress function of the shear rate for polar thickener greases (12OH-LiSt). It can be seen that the shear stress of grease 3 increases slightly and has lower value, at high shear rate, compared with the other greases of the same type. It can be noted that the dielectric results for these greases showed that Grease 1 has the largest permittivity, 2.30, while the dielectric constant of Grease 2 and 3 are 2.15 and 2.06, respectively.

A similar trend was observed for the Li-St greases shown in Figure 7. Grease 6, which has slightly larger dielectric permittivity than Grease 5, also shows larger shear stress.

5. CONCLUSIONS

A dielectric spectroscopy study, coupled with EHD traction measurements were carried out for a number of ten greases with various compositions and properties. The following conclusions have been drawn from this study.

- (1) From the dielectric measurements, it has been found that greases always have larger dielectric constant than their base oil and that the base oil has a stronger influence than the thickener on the grease dielectric constant. In greases containing polar components, the dielectric constant of the grease decreases with increasing the viscosity of its base oil. In non-polar greases, on the other hand, the dielectric constant of the grease increases with the viscosity of its base oil.
- (2) The dielectric properties, especially in the low frequency range, seem to be related to the film formation in EHD contacts. SRL grease, which has good conductivity, revealed by the dielectric measurements, shows poor film formation ability compared to other greases.
- (3) The effective viscosity of grease inside the EHD contact has been calculated from the measured value in traction test and characteristic similar to oil is found in case of grease. The logarithm of viscosity of greases varies linearly with pressure, but the degree of

inclination is moderate compared to base oils. On the other hand, the Eyring stress of greases rapidly increases and it has been found that for three of the studied greases the value of this parameter is greater than that corresponding to the base oil.

- (4) From the traction measurements, it can be concluded that, in general, urea thickener greases exhibit large shear stress in their operation. It has also been found that greases with higher dielectric constant show larger shear stress when compared to greases containing the same type of thickener.

ACKNOWLEDGEMENT

Yuichiro Nagata is grateful to Shell and Kyodo Yushi for supplying their greases and base oils and to professor Joichi Sugimura of Kyushu University, Japan and his colleagues for allocating their greases from NSK.

REFERENCES

1. **Glovnea, R.P.** 2010, "Transient Phenomena in Elastohydrodynamic Lubrication," *Recent development in Wear Prevention, Friction and Lubrications*, ed. G. Nikas, Research Signpost Publ., pp. 227-262.
2. **Cann, P.M.E.**, 1999, "Starved Grease Lubrication of Rolling Contacts," *Tribology Transactions*, Vol:42, pp. 867-873
3. **Eriksson P., Wikstroem V. and Larsson R** 2000, "Grease Passing Through an EHD Contact Under Pure Rolling Conditions," *Proc Instn Mech Engrs*, 214, pp. 309-316.
4. **Couronne, I., Mazuyer, D., Vergne, P., Truong-Dinh, N., Girodin, D.** 2003, "Effects of Grease Composition and Structure on Film Thickness in Rolling Contact," *Trib. Trans.*, vol. 46, 1, pp. 31-36
5. **Cann, P.M., Williamson, B.P., Coy, R.C., and Spikes, H.A.**, 1992, "The Behaviour of Greases in Elastohydrodynamic Contacts," *J. Phys. D: Appl. Phys.*, 25.
6. **Hirst, W., Moore, A.J.**, 1979, "Elastohydrodynamic Lubrication at High Pressures-Non-Newtonian Behaviour", *Proc. Roy. Soc. Lond., A*, 365, pp. 537-565
7. **Bair, S., and Winer, W.O.**, 1979, "A Rheological Model for Elastohydrodynamic Contacts Based on Primary Laboratory Data," *J. Lub. Tech.*, Vol 101, pp.258-265
8. **Johnson, K.L., and Tevaarwerk, J.L.**, 1977, "Shear Behaviour of Elastohydrodynamic Oil Films", *Proc. R. Soc., Lond., Ser.A.*, 356, pp.215-236

- 9. Evans, C.R., and Johnson, K.L.,** 1986, "The Rheological Properties of Elastohydrodynamic Lubricants," *Proc Instn Mech Engrs*, 200, No C5, pp. 303-312.
- 10. Diaconescu, E.N.,** 2004, "Solid-Like Properties of Molecular Liquids Subjected to EHD Conditions: Theoretical Investigations," *Proc. ASME/STLE Joint Int. Trib. Conf.*, 24-27 Oct., Long Beach, USA
- 11. Furakama, S., and Sumi, T.,** 1961, "A Dynamic Theory of Piston-Ring Lubrication", *Bull. of JSME*, Vol. 4, 16, pp.744-752
- 12. Hamilton, G.M. and Moore, S.L.,** 1974, "Measurement of the Oil Film Thickness Between the Piston Rings and Liner of a Small Diesel Engine", *Proc. Inst. Mech. Engrs.*, Vol 188, pp. 253-261
- 13. Sherrington, I., and Smith, E.H.,** 1985 "Experimental Methods for Measuring the Oil-Film Thickness Between the Piston-Rings and Cylinder-Wall of Internal Combustion Engines", *Trib. Int.*, vol. 18, 6, pp. 315-320
- 14. Ibrahim, M., and Cameron, A.,** 1963, "Oil Film Thickness and Mechanisms of Scuffing in Gear Teeth", *Proc. Inst. Mech. Engrs Lubrication and Wear Convention*, pp. 228-238
- 15. Vichard, J.P.,** 1971, "Transient Effects in the Lubrication of Hertzian Contacts," *J. Mech. Eng. Sci.*, Vol. 13, pp. 173-189
- 16. Van Leeuwen, H, H. Meijer, H., Schouten, M.,** 1987, "Elastohydrodynamic Film Thickness and Temperature Measurements in Dynamically Loaded Concentrated Contacts: Eccentric Cam-Flat Follower", *Fluid film lubrication-Osborne Reynolds Centenary*, Elsevier, pp. 611-625
- 17. Nagata, Y., Furtuna, M.D., Bell, C.A., and Glovnea, R.P.,** 2008, "Evaluation of Electric Permittivity of Lubricating Oils in EHD Conditions", *Proc. iCAT2008*, Dec. 2008, Singapore, p.155-158
- 18. Aliotta, F., Fontanella, M.E., Galli, G., Lanza, M., Migliardo, P. and Salvato, G.,** 1983, "Low-Frequency Dielectric Investigations in Polymer-like Lecithin Gels," *J. Phys. Chem.*, 97, pp.733-736.

Juozas PADGURSKAS¹
e-mail: Juozas.Padgurskas@lzuu.lt

Raimondas KREIVAITIS¹
e-mail: raimondaskreivaitis@gmail.com

Arturas KUP INSKAS¹
e-mail: Arturas.Kupcinskas@lzuu.lt

Raimundas RUKUIŽA¹
e-mail: raimundas.rukuiza@lzuu.lt

Vytenis JANKAUSKAS¹
e-mail: vytenis.jankauskas@lzuu.lt

Igoris PROSY EVAS²
e-mail: igorpros@mail.ru

¹ Department of Mechanical Engineering,
Lithuanian University of Agriculture - Kaunas,
LITHUANIA

² Institute of Physical Electronics
Kaunas University of Technology – Kaunas
LITHUANIA

INFLUENCE OF NANOPARTICLES ON LUBRICITY OF BASE MINERAL OIL

The tribological properties of mineral oil SAE 10 modified with metallic nanoparticles were investigated. The tribological tests were performed using four-ball test rig. Friction and wear reduction properties were measured. The positive influence of nanoparticles on lubricity of mineral oil was observed. The best result was obtained when using the copper nanoparticles for a single metal nanosuspension (0.25 % Cu). Using double metal nanoparticles the best result show iron – copper nanosuspension (0.125 % Fe + 0.125 % Cu). The use of those suspensions was most efficient for pure base mineral oil. The cobalt nanosuspension does not show a significant increase in lubricity. It was observed that nanosuspensions stabilize and decrease the friction during the tests.

Keywords: nanoparticles, friction wear, lubricity, mineral oil

1. INTRODUCTION

Presently there is an increasing interest in the use of nanoparticles. A lot of scientists worldwide perform many tests simulating the possible applications of nanoparticles. One of the interesting nanoparticles' applications is to make nanosuspensions in lubricants. It is observed that metal or even non-metal nanoparticles have a positive influence on lubrication properties. Nanoparticles suspensions in lubricants can significantly reduce friction and wear of friction surfaces [1-5].

Such factors as the material, size, shape and mechanical properties of nanoparticles, their concentration in the suspension have important influence on tribological properties of friction pairs [1,2].

Usually the lubricants are modified by the nanoparticles of metal or metal oxide (Cu, CuO, TiO₂, ZrO₂, ZnO and so on) and some non-metal materials (SiO₂, diamond, inorganic fullerene, graphite) [1-7]. It is highly evident that only a small amount of nanoparticles is required to obtain the positive tribological effect: 0.01 % graphite [6], <1 % diamond [1], 1 % TiO₂ [1], 5 % IF-WS₂ [4], 0.5...2 % CuO, ZnO, ZrO₂ [3], 0.2 % SiO₂ [7].

Usually, the main research purpose is to estimate optimal concentration [3,7].

In most cases the commonly manufactured nanoparticles are simply added to the lubricants [3, 4,6,7]. However there is increasing interest on synthesis nanosuspensions by the sintering of nanoparticles directly in the lubricants [8]. The aim of our study is to estimate the tribological properties of some nanosuspensions directly sintered in the base mineral oil.

2. EXPERIMENT

The synthesis of Fe, Cu, Co and Fe+Cu, Fe+Co, Co+Cu nano-particles is performed by the CEWLS method when the converse emulsion of water in lubricant synthesis is used. For that reason is prepared 100 ml mineral oil SAE10 emulsion with 0.2 ml H₂O which includes dissolved sulphates of certain metals, such as FeSO₄, CuSO₄, CoSO₄ and 0.5 g cetyltrimethylammonium bromide (CTAB). This mixture is poured into 100 ml of mineral oil SAE10 with 10 ml hydrazine emulsion. All volume was mixed intensively during 5 minutes. This mixture with formed according nano-particles was used for tribological investigations. The concentrations of nanoparticles in suspensions using

single metal were 0.25 %, using double metal nanoparticles – 0.125 % of each metal in compound.

Four-ball type tribotester was used for wear and friction tests. The balls of 12.7 mm diameter were made of 100Cr6 bearing steel. The testing procedure was adapted from the standard DIN 51 350 [9].

The test oil sample of 22 cm³ was poured into the sample chamber, fully submerging the stationary balls. Under the applied load of 150 N, and rotation speed of 1420 rpm, the machine was run for 1 hour. Prior to each experiment, all the appropriate parts of the machine, i.e. bottom and upper ball holders, oil vessel and the test balls were washed in an ultrasonic bath with hydrocarbon solvents, and then dried.

The diameters of the circular wear tracks (wear scars) on three stationary balls were measured with an optical microscope. For each run the scar measurements were reported as an average of the Wear Scar Diameter (WSD) of the three balls in millimetres. Friction between the balls is represented by torque.

3. RESULTS AND DISCUSSIONS

The results of performed tests are presented in Figure 1. It shows that all used suspensions of nanoparticles decrease the wear and friction comparing to pure mineral base oil SAE 10. However the positive influence was not equal for all suspensions.

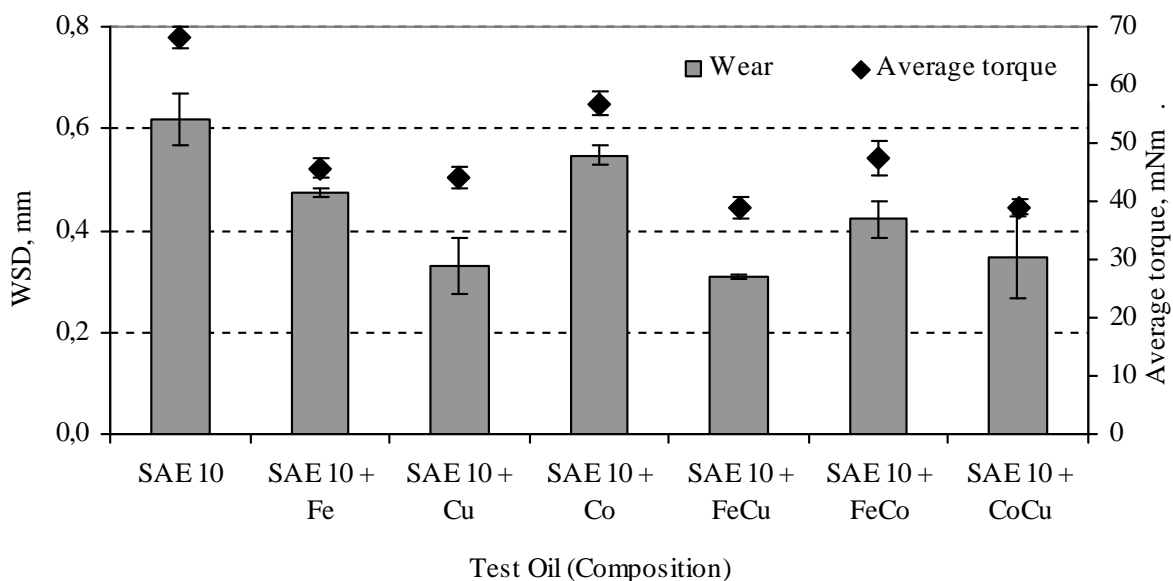


Figure 1. Wear and friction behaviour of base oil and metal nanosuspensions

The best result was obtained using copper nanoparticles when using single metal nanosuspension and the worst one when using cobalt nanoparticles.

Lubrication with copper nanosuspension reduces the wear 1.87 times and the friction – 1.54 times comparing to base oil. Wear reduction was less important when using iron nanosuspensions in comparison to copper. However the friction reduction was virtually the same for both those nanosuspensions. The wear and friction reduction of cobalt nanosuspension was almost negligible.

It is likely that wear and friction reduction properties of copper nanosuspension are related to its mechanical properties. The soft and ductile material can easily get between contacting surfaces and cover them making good protection against the wear.

Estimation of wear and friction behaviour of

double metal nanoparticles displays that the best result of all tested nanosuspensions shows iron – copper nanosuspension. Lubrication with iron – copper nanosuspension reduces the wear almost two times, and the friction – 1.76 times. Such a great increase in lubricity can be due to combination of two metals with different mechanical properties and of course different interaction mechanisms.

Despite that cobalt does not reduce the wear significantly in single metal nanosuspension tests, in combination with iron and copper it has much better lubricity. The suspension of cobalt–copper nanoparticles reduces the wear and friction respectively 1.78 and 1.75 times comparing to base oil.

Friction torque variation graphs during the entire test (Figures 2 and 3) were used for friction analysis. Figure 2 presents the friction torque when lubricating with single metal nanosuspension.

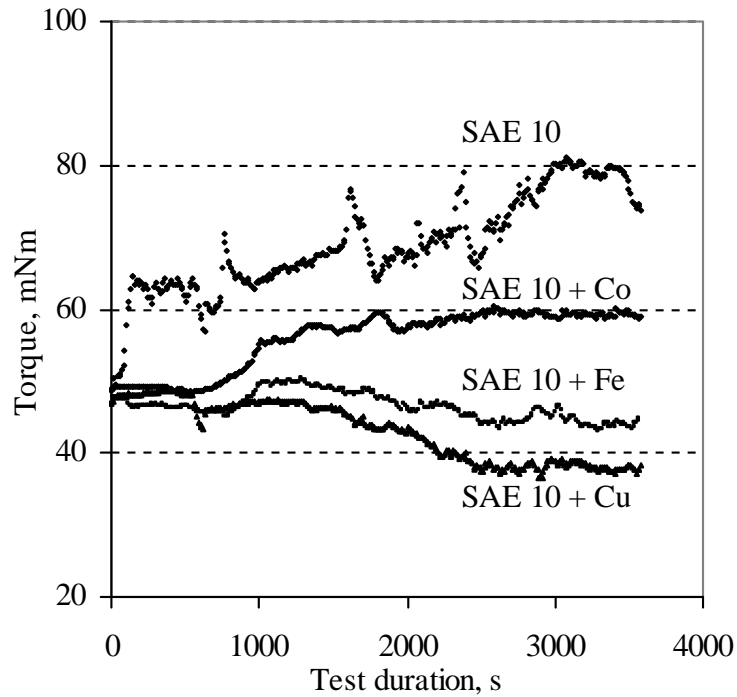


Figure 2. Friction torque variation during the test using the lubrication with pure base oil and single metal nanosuspensions

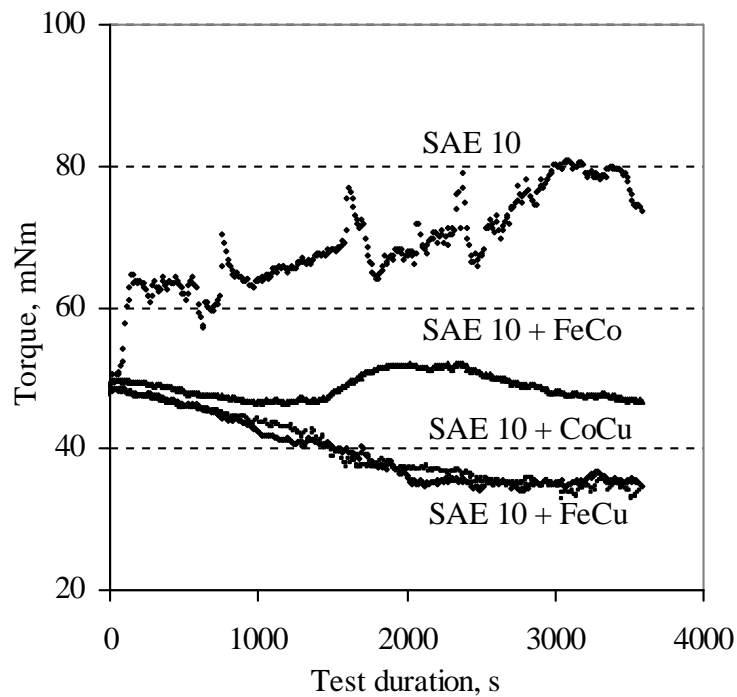


Figure 3. Friction torque variation during the test using the lubrication with pure base mineral oil and double metal nanosuspensions

Usually friction torque increases during the tests when using the pure base oil. Regardless some fluctuations it was also the case in our investigations. Using the nanosuspensions the

fluctuations almost disappear. Moreover, the friction value has decreasing trend during the test when using the nanosuspensions of single copper and iron.

Slightly different results were obtained when using double metal nanosuspensions (Figure 3).

Friction torque values are stable for those suspensions, but we have no friction decrease tendency for FeCo nanosuspension. It was almost no difference between the friction behaviour of CoCu and FeCu nanosuspensions. The reason for that could be much more important influence of copper on tribological properties of double metal nanosuspensions.

4. CONCLUSIONS

- Metallic nanoparticles' suspensions obtained by direct sintering in the lubricant are efficient for wear and frictions reduction. Moreover all used nanosuspensions help to increase friction stability.
- Copper and iron – copper nanoparticles' suspensions presented the best lubrication properties, Co nanosuspensions – the worst.

ACKNOWLEDGEMENT

This research was funded by Lithuanian State Science and Studies Foundation grant B-34/2008 "NanoTribo-Suspensions".

REFERENCES

1. **Wu Y. Y., Tsui W. C., Liu T. C.**, 2007, "Experimental Analysis of Tribological Properties of Lubricating Oils with Nanoparticle Additives," *Wear*, 262, p. 819 – 825.
2. **Hernández Battez A., González R., Felgueroso D.**, and other, 2007, "Wear Prevention Behavior of Nanoparticles Suspension under Extreme Pressure Condition," *Wear*, 263, p. 1568 – 1574.
3. **Hernández Battez A., González R., Felgueroso D.**, and other, 2008, "CuO, ZrO₂ and ZnO Nanoparticles as Antiwear Additive in Oil Lubricants," *Wear*, 265, p. 422 – 428.
4. **Rapoport L., Leshchinsky V., Lapsker I.**, and other, 2003, "Tribological Properties of WS₂ Nanoparticles under Mixed Lubrication," *Wear*, 255, p. 785 – 793.
5. **Rapoport L., Nepomnyashchy O., Lapsker I.**, and other, 2005, "Behavior of Fullerene – like WS₂ Nanoparticles under Severe Contact Conditions," *Wear*, 295, p. 703 – 707.
6. **Huang H. D., Tu J. P., Gan L. P., Li C. Z.**, 2006, "An Investigation on Tribological Properties of Graphite Nanosheets as Oil Additives," *Wear*, 261, p. 140 – 144.
7. **Peng D. X., Kang Y., Hwang R. M.**, and other, 2009, "Tribological Properties of Diamond and SiO₂ Nanoparticles Added in Paraffin," *Tribology International*, 42, p. 911 – 917.
8. **Padgurskas J., Rukuiža R., Kreivaitis R.**, and other, 2009, "Tribological Properties of Mineral Oils Modified with Metallic Nano-Particles," *Proceedings of 5th International Scientific Conference „BALTRIB 2009“*, Lithuanian University of Agriculture, Kaunas, p. 69-76.
9. DIN 51350-3, Testing of lubricants - Testing in the four-ball tester- Part 3: Determination of wearing characteristics of liquid lubricants, 1977 (In Germany).

Alexandru V. RADULESCU¹
e-mail: *varrav2000@yahoo.com*

Irina RADULESCU²
e-mail: *irena_sandu@yahoo.com*

¹ Department of Machine Elements and Tribology,
University POLITEHNICA Bucharest,
ROMANIA

² Mechanical Engineering and Research Institute
S. C. ICTCM S.A. Bucharest,
ROMANIA

INFLUENCE OF THE RHEOMETER GEOMETRY ON THE RHEOLOGICAL PROPERTIES OF INDUSTRIAL LUBRICANTS

The rheological properties of two transmission lubricants (75W90 and 75W140), in fresh and used state, were investigated using shear viscosity rheological measurements. It was found that the lubricants do not exhibit a yield stress and that, above a critical shear rate, they exhibit shear-thinning behavior, well described by the Cross model.

The rheological measurements were performed on a Brookfield viscometer CAP2000+ equipped with four cone-and-plate geometry, for a range of temperature between 20 ... 70°C, using the viscometer Peltier system. The experiments have shown that only two geometries are appropriate for testing the transmission lubricants. Another important conclusion refers to the influence of the wear degree of the lubricant on the rheological parameter of the model.

Keywords: viscosity, lubricants, shear-thinning, wear

1. INTRODUCTION

Rheological modeling of lubricants has always been a subject of great importance when working with oil from different fields of interest. The need for predicting the rheological behavior of the lubricants when experiencing conditions outside the available measuring range for the equipment designed in accordance with API specifications [1,2] has always been present.

Transmission lubricants behave in a non-Newtonian way. They are shear-rate dependent and normally termed as shear-thinning lubricants. Rheological measurements are normally performed in the laboratory within a given range of shear rates. Based on these measured values the models should be able to predict the shear-dependent behavior of the lubricants outside the measured interval of shear rates.

The rheological properties of two transmission lubricants (75W90 and 75W140), in fresh and used state, were investigated using shear viscosity rheological measurements. It was found that the lubricants do not exhibit a yield stress and that, above a critical shear rate, they exhibit shear-thinning behaviour, well described by the Cross model. Supplementary tests have been made, regarding the thermal behaviour of the lubricants. Three thermal models have been assumed, in order to determine the variation of the viscosity with the temperature, for lubricants in fresh and used state.

2. THEORY

The rheological model based on the Cross equation is one of the most popular in use today. It can be found on virtually every research rheometer software packages and it can be used to extract some meaningful numbers from the "full" viscosity versus shear rate profile (Fig. 1).

The mathematical expression of the the Cross model is described by the Eq. (1), [3]:

$$\eta = \eta_{\infty} + \frac{\eta_0 - \eta_{\infty}}{1 + (\lambda\dot{\gamma})^m}, \quad (1)$$

where $\dot{\gamma}$ is the shear rate and η is the viscosity at any given shear rate $\dot{\gamma}$.

The other parameters involved in eq. (1) are:

- η_0 is the zero shear viscosity and represents the magnitude of the viscosity at the lower Newtonian plateau. It is a critical material property and can prove valuable in making assessments of suspension and emulsion stability, estimating of comparative polymer molecular weight and tracking changes due to process or formulation variables etc.

- λ is the infinite shear viscosity. This signifies how the product is likely to behave in very high shear processing situations such as blade, knife and roller coating.

- m is known as the Cross time constant and has dimensions of time. The reciprocal, $1/m$, gives a

critical shear rate that proves a useful indicator of the onset shear rate for shear thinning.

- m is a dimensionless rate constant (Cross rate constant) indicating the degree of dependence of the

viscosity on shear rate in the shear-thinning region. A value of zero for m indicates Newtonian behavior with m tending to unity for increasingly shear thinning behavior.

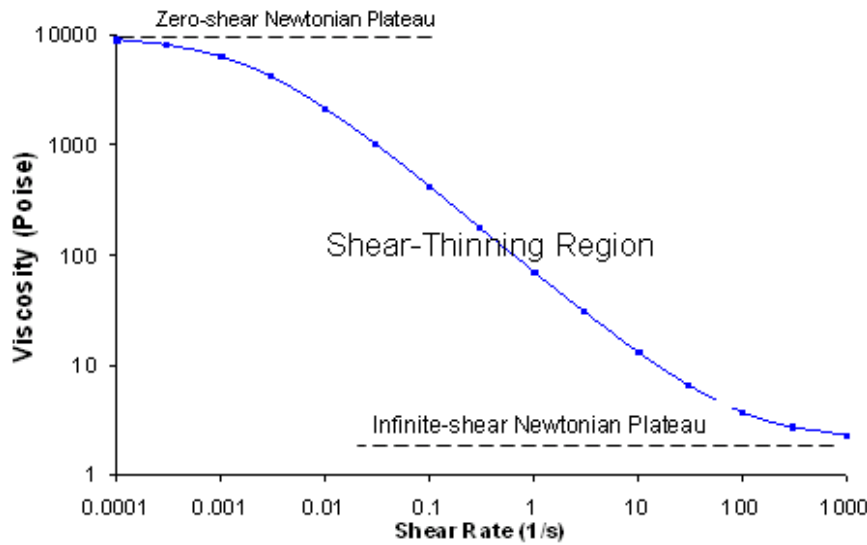


Figure 1. Graphical expression of Cross model

Concerning the thermal model assumed for the variation of the rheological parameters of the studied lubricants, three possibilities have been considered, [4]:

- Jarchoh and Theissen model:

$$\eta = \eta_{50} e^{\frac{B \cdot 50 - t}{95 + t}}, \quad (2)$$

where: η – lubricant viscosity; η_{50} – lubricant viscosity at 50 °C; B – non-dimensional parameter; t – temperature.

- Cameron model:

$$\eta = K e^{\frac{b}{95 + t}}, \quad (3)$$

where: η – lubricant viscosity; K – viscosity parameter; b – temperature parameter; t – temperature.

- Reynolds model:

$$\eta = \eta_{50} e^{m(t-50)}, \quad (4)$$

where: η – lubricant viscosity; η_{50} – lubricant viscosity at 50 °C; m – temperature parameter; t – temperature.

In order to obtain the main values of the characteristic parameters specific for Cross model (Eq. 1) and all three thermal models (Eqs. (2), (3) and (4)), the experimental data are numerically treated, using the regression analysis method, [5].

3. EXPERIMENTAL SET-UP

The rheological measurements were performed on a Brookfield viscometer CAP2000+ equipped with four cone-and-plate geometry and using a Peltier system for controlling the temperature. The CAP 2000+ Series Viscometers are medium to high shear rate instruments with Cone Plate geometry and integrated temperature control of the test sample material, [6]. A typical view of the viscometer is presented in Figure 2, with all the four cone and plate geometries.



Figure 2. Geometry of Brookfield viscometer

Concerning the technical parameters of the viscometer, rotational speed selection ranges from 5 to 1000 RPM. Viscosity measurement ranges depend upon the cone spindle and the rotational speed (shear rate). Viscosity is selectively displayed in units of centipoise (cP), poise (P), or Pascal seconds (Pa.s). Temperature control of sample is possible between either 5°C (or 15°C below ambient, whichever is higher) and 75°C or 50°C and 235°C depending on viscometer model. The viscometer uses a CAPCALC32 software for complete control and data analysis. The geometry of

testing cones and the viscosity range are presented in Table 1.

The lubricants used for testing are two transmission lubricants (75W90 and 75W140), in fresh and used state (2000 km), with physical and chemical properties presented in Table 2, [7]. These are 100% synthetic extreme pressure lubricants, characterized by an efficient anti wear protection, with a better resistance at high temperature and a longer life time. The lubricants are specially designed for racing vehicle gearboxes, synchronized or not synchronized gearboxes, gearbox/differential, transfer gearboxes and hypoid differentials.

Table 1. Geometry and viscosity range of testing cones

Cone number	Cone radius, mm	Cone angle, degree	Viscosity range, Pa.s
3	9.53	0.45	0.083 ... 1.87
5	9.53	1.8	0.333 ... 7.50
6	7.02	1.8	0.833 ... 18.7
8	15.11	3	0.312 ... 3.12

Table 2. Physical and chemical properties of tested lubricants, [7]

Lubricant Parameter	GEAR 300 75W-90	GEAR Competition 75W-140
Density at 15°C (59°F) ASTM D1298	900 kg/m ³	906 kg/m ³
Viscosity at 40°C (104°F) ASTM D445	72.6 mm ² /s	170 mm ² /s
Viscosity at 100°C (212°F) ASTM D445	15.2 mm ² /s	24.7 mm ² /s
Viscosity index VIE ASTM D2270	222	178
Flash point ASTM D92	200°C	212°C
Pour point ASTM D97	-60°C	-36°C

4. RESULTS

The first stage of the experiment was focused on the influence of the cone and plate geometry on the measured rheological properties. Figures 3 and 4 show the characteristic rheograms for 75W-90 and 75W-140 oils, in fresh state, with a detail for low values of the shear rate (0 ... 3500 s⁻¹). In the case of the used oils, the rheograms have the same shape, similar to those of the fresh oils; that is the reason why they are not presented in this paper.

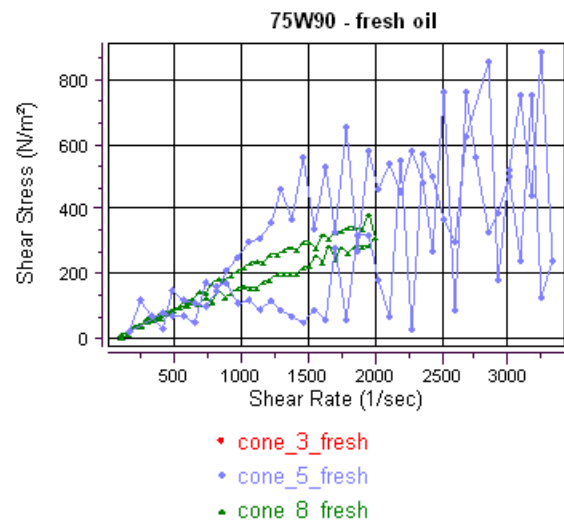
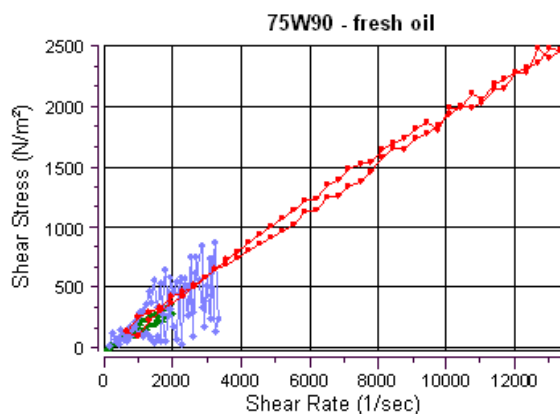


Figure 3. Rheograms for 75W-90 oil, in fresh state

By analyzing Figures 3 and 4 it can be observed that only the cones number 3 and 8 offer consistent measurements, with low dispersion of the experimental values. For the viscosity range of the two oils, cone number 5 is not appropriate for the experimental tests, due to the large dispersion of the values.

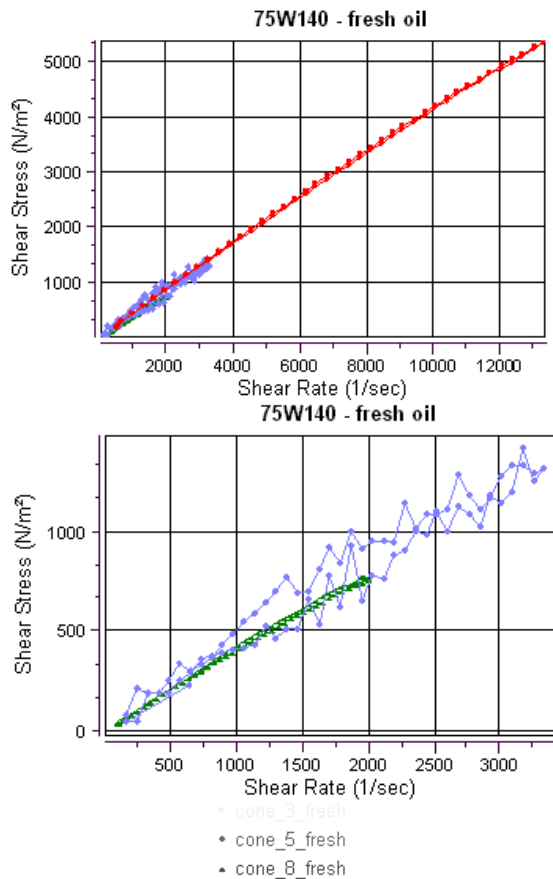


Figure 4. Rheograms for 75W-140 oil, in fresh state

The cone number 8 is characterized by a low shear rate range (0 ... 2000 s⁻¹), while the cone number 3 has a larger shear rate range, between 0 s⁻¹ and 13300 s⁻¹. The tests with this geometry offer results which can characterize the behavior of the lubricant for a vaster interest domain.

The experimental results obtained with cones number 3 and 8 have been treated with the regression analysis method, according to the Cross model (Eq. 1), in order to obtain the variation of the viscosity with the shear rate. The parameters of the Cross model are presented in Table 3, and the comparison between the experimental results obtained with cone number 3 and the theoretical model is shown in Figures 5 and 6.

It can be observed significant differences between cone 3 and 8, caused by the extended field of the shear rate values. Another important conclusion refers to the influence of the wear degree of the lubricant on the rheological parameter of the Cross model. For the 75W90 oil, there are almost no differences between fresh and used lubricant (Fig. 5) while the oil 75W140 presents important changes in used state comparative to fresh state (Fig. 6). The same observation can be made for the two oils regarding the variation of the viscosity with temperature.

The experimental results are presented in Figures 7 and 8 and Table 4 shows the values of the rheological parameters of the studied lubricants.

Table 3. Parameters of the Cross model for the transmission lubricants

Type of oil	Wear degree	Cone number	Cross model			
			η_{∞} , Pa·s	η_0 , Pa·s	λ , s	m
75W90	fresh	3	0.153	0.229	$7.595 \cdot 10^{-4}$	0.065
		8	0.068	0.275	$6.028 \cdot 10^{-3}$	0.147
	used	3	0.118	0.307	$3.057 \cdot 10^{-3}$	0.175
		8	0.061	0.263	$2.045 \cdot 10^{-3}$	0.111
75W140	fresh	3	0.257	0.628	$1.725 \cdot 10^{-3}$	0.104
		8	0.213	0.601	$1.212 \cdot 10^{-3}$	0.037
	used	3	0.220	0.574	$1.753 \cdot 10^{-3}$	0.095
		8	0.151	0.529	$7.362 \cdot 10^{-4}$	0.149

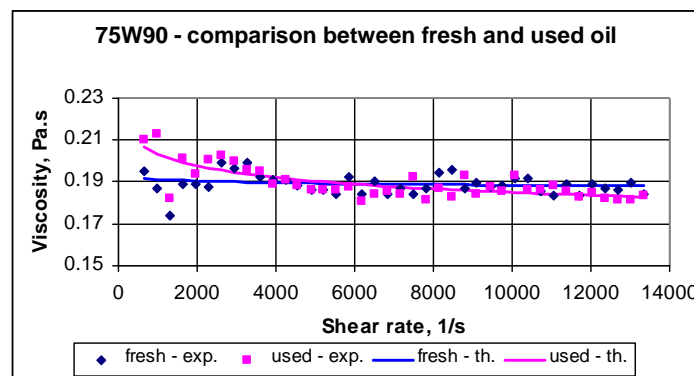


Figure 5. Comparison between the experimental results and the theoretical model for 75W-90 oil (cone no. 3)

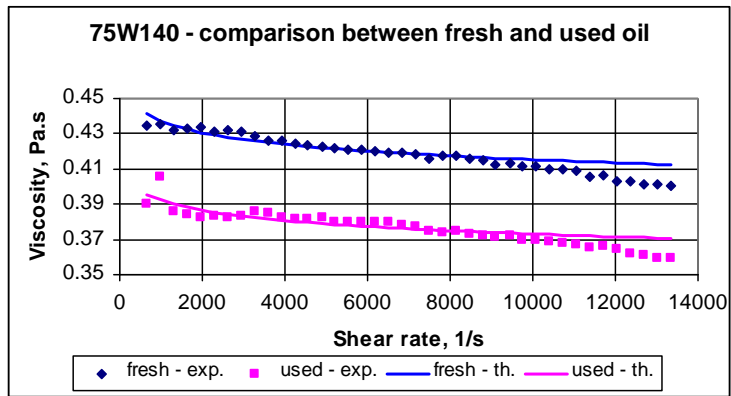


Figure 6. Comparison between the experimental results and the theoretical model for 75W-140 oil (cone no. 3)

Table 4. Variation of the rheological parameters of lubricants with temperature

Parameter		Jarchov and Theissen model			Cameron model			Reynolds model		
		η_{50} , Pa·s	B	Corr. coeff.	K, Pa·s	b, °C	Corr. coeff.	η_{50} , Pa·s	m, °C ⁻¹	Corr. coeff.
75W90	Fresh	0.0446	5.419	0.9981	$1.979 \cdot 10^{-4}$	785.75	0.9981	0.0435	-0.0473	0.9996
	Used	0.0446	5.517	0.9976	$1.776 \cdot 10^{-4}$	799.97	0.9976	0.0432	-0.0478	0.9995
75W140	Fresh	0.1043	5.232	0.9986	$5.572 \cdot 10^{-4}$	758.58	0.9986	0.1021	-0.0454	0.9995
	Used	0.0919	5.520	0.9994	$3.678 \cdot 10^{-4}$	800.46	0.9994	0.0899	-0.0477	0.9989

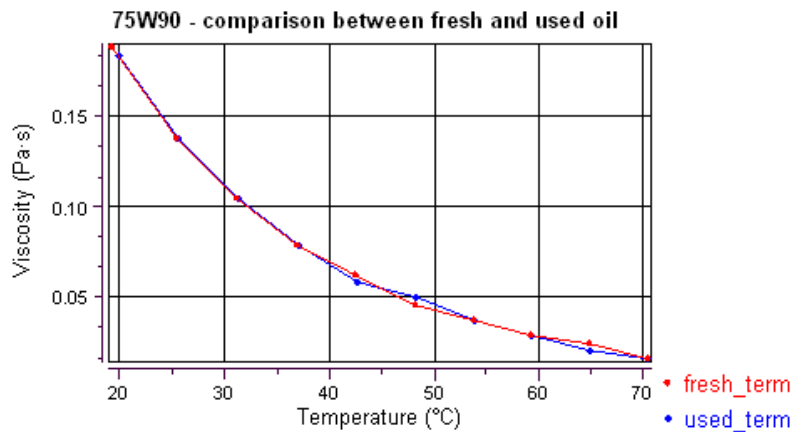


Figure 7. Variation of the viscosity with temperature for 75W90 oil

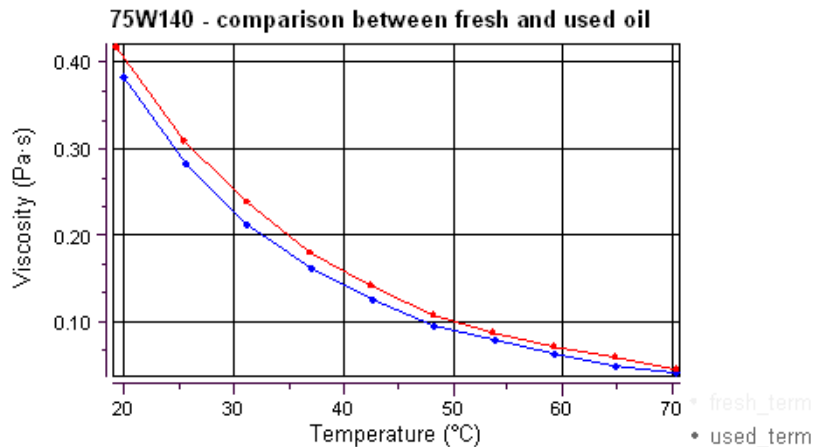


Figure 8. Variation of the viscosity with temperature for 75W140 oil

5. CONCLUSIONS

The experimental results were found to be well described by the Cross model, except for the viscometer geometries number 5 and 6. It can be observed also significant differences between cone 3 and 8, caused by the extended field of the shear rate values. Another important conclusion refers to the influence of the wear degree of the lubricant on the rheological parameter of the model, including the variation with temperature.

REFERENCES

1. **Qemada, D.**, 1998, "Rheological Modeling of Complex Fluids I. The Concept of Effective Volume

Fraction Revisited," *Eur. Phys. J., Appl. Phys.* 1, pp. 119–127.

2. *** , 1990, Specification for Materials and Testing for Well Cements, 5th edn., API Spec., vol. 10, American Petroleum Institute, Dallas, TX, USA

3. **Cross, M.M.**, 1965, "Rheology of Non-Newtonian Fluids: A New Flow Equation for Pseudoplastic Systems," *Journal of Colloid Science*, Vol. 20, No. 5, p. 417-437.

4. **Balan, C.** (compiled author), 2000, *The Rheology of Lubricating Greases*, ELGI, Amsterdam, 160 p.

5. **Crocker, D.C.**, 1983, "How to Use Regression Analysis in Quality Control," American Society for Quality Control, Vol. IX, 243 p.

6. *** Oil catalog MOTUL France, <http://www.motul.fr/fichestechniques/Transmission>.

Vlad – Flaviu ZEGREAN
email: zegrean@fim.usv.ro

Emanuel DIACONESCU

Department of Applied Mechanics,
University "Stefan cel Mare" of Suceava,
ROMANIA

MEASUREMENT OF LUBRICANT OIL MICROVISCOSITY BASED ON RESONANT FREQUENCY SHIFT OF AFM CANTILEVER

Experimental investigations on microviscosity of T90 lubricant oil were conducted using an atomic force microscope. The resonant frequency of the cantilever beams was measured in air, in pure water and in sample oil. Based on the resonant frequency shift the viscosity of the lubricant was calculated using the formula deduced by Papi [1] for uncalibrated cantilevers. The results obtained are in good agreement with those of Ionescu [2], measured with a Rheotest2 rheometer, for the same lubricant.

Keywords: microviscosity, atomic force microscopy, resonant frequency shift

1. INTRODUCTION

Since its invention by Binning et al. in 1986 [3], the atomic force microscope (AFM) gained ever-increasing importance in nanotechnology and biotechnology. The AFM is now widely used to obtain high-resolution surface topography images, to measure intermolecular forces or to characterize the mechanical properties of polymers. The capability of the AFM to take measurements with the cantilever and sample submerged in a liquid enhance the image resolution due to reduced capillary forces.

There are two operating modes for atomic force microscopy:

- Contact mode, when the cantilever tip is in permanent contact with the sample. Using this mode, the friction force between the tip and the sample can be measured. This imaging mode dramatically reduces the lifetime of the tip.
- Tapping mode, when the tip is kept above the sample by the feedback loop. In this operating mode, the cantilever is driven at resonant frequency, near the surface of the probe by acoustic, magnetic or Brownian methods. The amplitude and phase of tip oscillation are then used to extract information about the sample topography.

The frequency of cantilever vibration immersed in a fluid strongly depends on the fluid rheological properties. The drag forces acting on cantilever are directly related to kinematic viscosity and fluid density. Thus the viscosity of the fluid can be determined from the resonant frequency of the cantilever.

2. THEORETICAL CONSIDERATIONS

To our best knowledge, existing research did not provide a simple and general relationship between fluid viscosity and cantilever resonant frequency. The attempt to find a relationship to describe the dependence of fluid viscosity on cantilever resonant frequency can be classified on two broadly approaches.

Viscous model proposed by Sader [4] and experimentally validated by Chon et al. [5] accounts all the geometrical parameters of the cantilever. Sader assumed that the beam cross section is uniform over the entire length, the length of the beam greatly exceeds its width, b , the beam is an anisotropic linearly elastic solid and internal frictions effects are negligible, the amplitude of vibration is far smaller than any length scale of the beam geometry. The expression that correlates the normalized Reynolds number, \overline{Re} , on frequency response of the cantilever is:

$$\overline{Re} = \frac{\rho \omega_{vac,1} b^2}{4\eta}, \quad (1)$$

where ρ is the fluid density, $\omega_{vac,1}$ is the fundamental radial resonant frequency of the beam in vacuum and η is the fluid viscosity.

Classical model that draws a heuristic analogy with the dynamic motion of a sphere through viscous fluid was approached by Chen [6], Oden [7], and Ahmed [8].

The calculation of viscosity using this approaches rely on accurate values of cantilever thickness, coating thickness, mass, density and

elastic modulus. The calibration procedure of the cantilever is time consuming, presents the risk of damaging the cantilever, or has to be reinitiated when viscosity changes.

To overcome these difficulties, Papi [9] proposed a method for determining the absolute value of fluid viscosity by accounting for the cantilever resonant frequency measured in air or vacuum, in the sample solution and in a liquid of known viscosity as a standard.

Based on the classical model, Papi [1] finds the following mathematical expression to correlate the sample viscosity, η_s , to resonant frequencies:

$$\eta_s = \frac{Y_s}{Y_{H_2O}} \frac{\omega_s}{\omega_{H_2O}} \eta_{H_2O}, \quad (2)$$

where ω_s , ω_{H_2O} are the resonant frequencies of the cantilever submerged in sample solution, respectively in pure water (used as a standard liquid), and Y_s , Y_{H_2O} are two dimensionless parameters yielding from:

$$Y_{s,H_2O} = \left[\left(\frac{\omega_0^2 - \omega_{s,H_2O}^2}{\omega_{s,H_2O}^2} \right) - \beta \right]^2. \quad (3)$$

The parameter β is a combination of cantilever beam geometry and structure parameters and its value can be set as unity for the great majority of common commercial cantilevers.

3. EXPERIMENTAL PROCEDURE

To measure the resonant frequency of the cantilever, a Nanonics Imaging Multiview 1000 AFM, depicted in Figure 1, was used. The cantilever is acoustically driven in a range of frequencies set by user and the resonant frequency is detected by the optical device of the AFM.

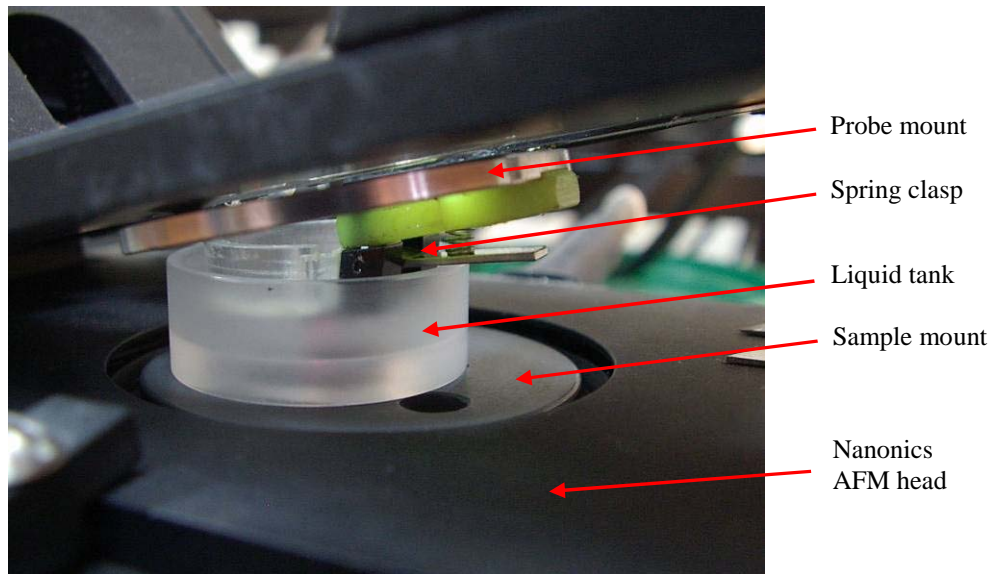
The Nanonics NWS software allows tracing the sweep curve, setting the oscillation amplitude of the cantilever and setting the input gains for the signal.



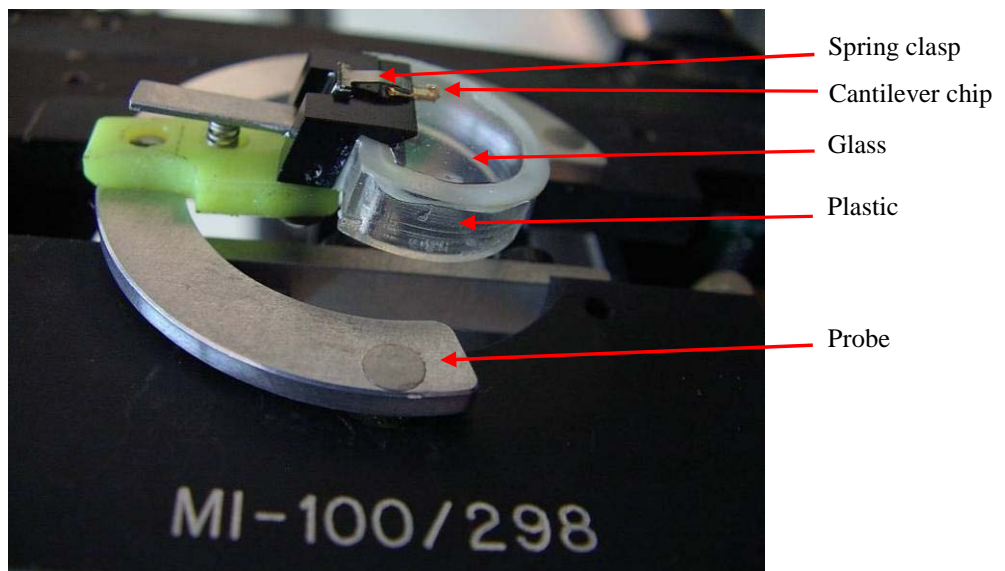
Figure 1. Nanonics Imaging Multiview 1000 AFM and Academia optical microscope

In order to submerge the cantilever, a Park Scientific Instruments Universal SPM liquid cell was modified to fit the Nanonics sample and probe mount, Figure 2. A small liquid tank was attached to a sample mount, Figure 2(a). A transparent thin flat glass window with a plastic collar was fitted to the probe mount, Figure 2(b). The probe mount is magnetically connected to the AFM head.

A spring clasp for standard silicon – nitride probes, Figure 2(b), was firmly attached under the glass window. The radius of the glass window is smaller than the interior radius of the tank and it submerges partially in the liquid along with the cantilever chip, Figure 2(a). Two mirrors are used to direct the laser beam from the source on the surface of the cantilever and the reflected beam to the photo-sensitive detector, Figure 2(b).



(a)



(b)

Figure 2. (a) Modified PSI liquid cell mounted on the Nanonics AFM head; (b) Detail on modified probe mount



Figure 3. Rectangular PSI cantilever

A rectangular shaped Park Scientific Instruments MicroMash cantilever was used in this experiment, Figure 3. The laser spot is reflected by the first mirror on the far edge of the rectangular cantilever for a maximum deflection angle. The rectangular cantilever was chosen to reduce the damping effect on the oscillation when the cantilever is immersed in the viscous lubricant oil.

This image was captured with a CCD camera mounted on an Academia optical microscope, Figure 1.

4. EXPERIMENTAL RESULTS

The first frequency sweep curve was traced in air with the liquid tank empty, Figure 4. The frequency range was set from 0 to 20 kHz and the measurements were made in 500 points across this range. The values displayed are averaged values of three consecutive measurements in each point. The maximum amplitude corresponds to the resonant frequency of the cantilever. The gain set for this measurement was 0.08. The maximum amplitude of 0.86751 V was reached at a frequency of 11.9038 kHz.

The liquid tank was then filled with pure water at 20°C, measured by a thermocouple and a

new frequency sweep curve, Figure 5, was traced after the laser was realigned. The realignment is necessary because refractive index of water modify the reflection angle of the laser beam. Results were averaged on ten consecutive measurements for a precise result. The frequency range was limited to 0 – 8 kHz because the resonant frequency is lower in a liquid than in air. The input gain was increased to 0.1 and the maximum amplitude of 1.2133 V at 6.6262 kHz resonant frequency.

After the tank was drained and dried, T90 lubricant oil at 30°C was poured into it and the laser was realigned. Because the lubricant is less transparent to laser than pure water the input gain was increased to 3.2. The frequency range was gradually reduced down to 0 – 3 kHz. Maximum amplitude of 3.08057 V was reached at 1.9697 kHz resonant frequency, Figure 6.

The resonant frequencies experimentally obtained in air, pure water and T90 lubricant oil are used in Papi's formula (2). Considering the water viscosity $\eta_{H_2O} = 0.00113 \text{ Pa}\cdot\text{s}$, the absolute value of lubricant kinematic viscosity is $\eta_{T90} = 0.265804 \text{ Pa}\cdot\text{s}$. The result is in good agreement with the values obtained by Ionescu, [2], on a Rheotest 2 rheometer on T90 lubricant oil in a range of temperatures from 17°C to 100°C.

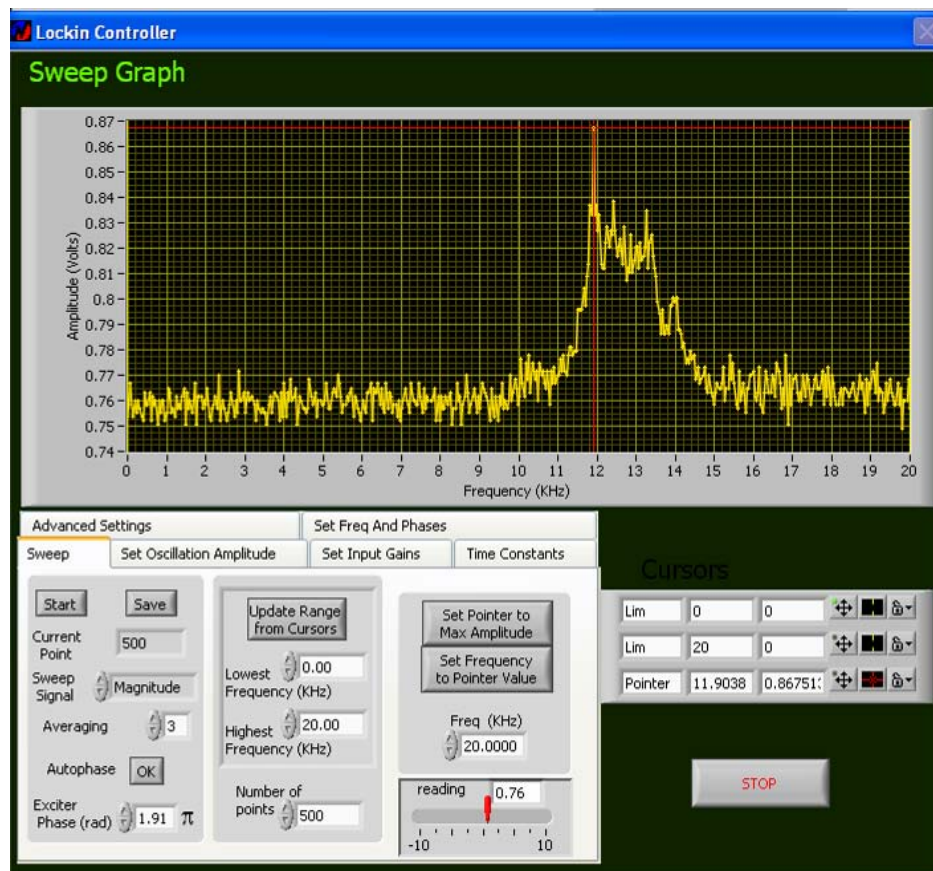


Figure 4. Frequency sweep curve of cantilever in air

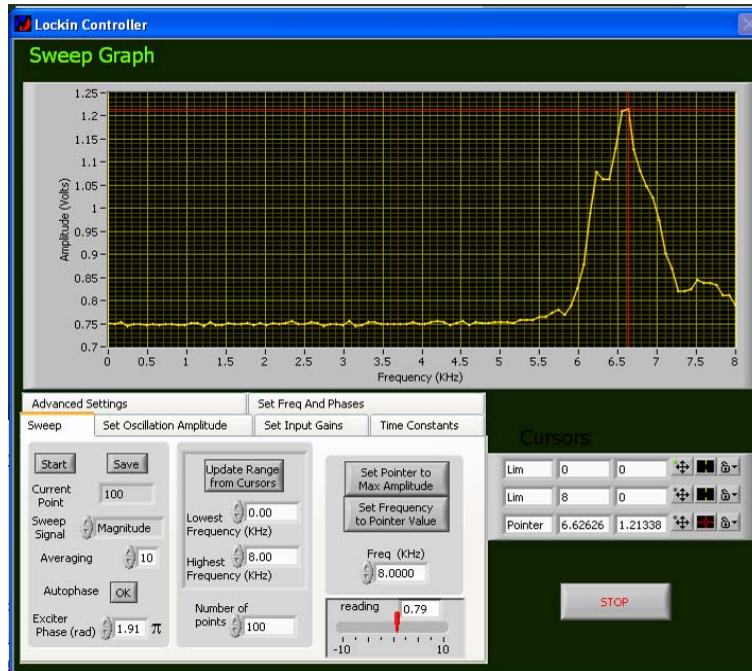


Figure 5. Frequency sweep curve of cantilever in pure water



Figure 6. Frequency sweep curve of cantilever in T90 lubricant oil

Table 1. Experimental viscosity of T90 measured with Rheotest 2, [2]

Temperature (°C)	Viscosity (Pa.s)
17	0.4807853
30	0.2726842
40	0.1506939
50	0.0896987
60	0.0574072
70	0.0358795
80	0.0215277
90	0.0143518
100	0.0107638

5. CONCLUSIONS

A Nanonics MultiView 1000 AFM from Laboratory of Micro and Nanotribology at the University of Suceava was used to determine the resonant frequency of a rectangular PSI MicroMash cantilever. To enable cantilever submersion, a Park Scientific Instruments Universal SPM liquid cell was modified to fit the Nanonics head.

The microviscosity of T90 transmission lubricant oil was measured at 30 °C, by means of resonant frequency shift of an AFM cantilever in three different mediums: air, pure water and oil.

The fundamental resonant frequency measured in air is 11.9038 kHz, decrease to 6.6262 kHz when measured in pure water and reached 1.9697 kHz resonant frequency if submerged in sample lubricant oil.

The obtained results were applied in Papi's formula for viscosity determination by means of uncalibrated atomic force microscopy cantilevers. The absolute value of viscosity, $\eta_{T90} = 0.265804 \text{ Pa} \cdot \text{s}$, is in good agreement with the results obtained by Ionescu with a Rheotest 2 rheometer.

REFERENCES

1. Papi, M., Arcovito, G., De Spirito, M., Vassalli, M., Tiribilli, B., 2006, "Fluid Viscosity Determination by Means of Uncalibrated Atomic Force Microscopy Cantilevers," *Applied Physics Letters*, 88, 194102.
2. Ionescu M., 2004, "A System for Viscosity Measurement in Variable Conditions of Temperature and Pressure," *MOCM 10*, Vol.1, 205 – 208.
3. Binning G., Quate C.F., Gerber Ch., 1986, "Atomic Force Microscope," *Phys. Rev. Lett.* 56, 930 – 933.
4. Sader, J.E., 1998, "Frequency Response of Cantilever Beams Immersed in Viscous Fluids with Applications to the Atomic Force Microscope," *Journal of Applied Physics*, 84, 64 – 76.
5. Chon, J.W.M., Mulvaney, P., Sader, J.E., 2000, "Experimental Validation of Theoretical Models for the Frequency Response of Atomic Force Microscope Cantilever Beams Immersed in Fluids," *Journal of Applied Physics*, 87, 3978 – 3988.
6. Chen, G.Y., Warmack, R.J., Thundat, T., Allison, D.P., Huang, A., 1994, "Resonance Response of Scanning Force Microscopy Cantilevers," *Rev. Sci. Instrum.*, 65(8), 2532 – 2537.
7. Oden, P.I., Chen, G.Y., Steele, R.A., Warmack, R.J., Thundat, T., 1996, "Viscous Drag Measurements Utilizing Microfabricated Cantilevers," *Applied Physics Letters*, 68, 3814 – 3816.
8. Ahmed, N., Nino, D.F., Moy, V.T., 2001, "Measurement of Solution Viscosity by Atomic Force Microscopy," *Rev. Sci. Instrum.*, 72(6), 2731 – 2734.
9. Papi, M., Maulucci, G., Arcovito, G., Paoletti, P., Vassalli, M., De Spirito, M., 2008, "Detection of Microviscosity by Using Uncalibrated Atomic Force Microscopy Cantilevers," *Applied Physics Letters*, 93, 124102.

M.C. CORNECI^{1,2}e-mail: magdalena-carla.corneci@insa-lyon.fr**A.-M. TRUNFIO-SFARGHIU¹****F. DEKKICHE^{3,4}****Y. BERTHIER¹****M.-H. MEURISSE¹****J.-P. RIEU³**

¹Laboratoire de Mécanique des Contacts et des Structures, INSA-Lyon, CNRS UMR5259, F69621 Villeurbanne Cedex, **FRANCE**

²Université Technique "Gh. Asachi", Faculté de Mécanique, 700050, Iasi, **ROUMANIE**

³Laboratoire de Physique de la Matière Condensée et Nanostructures, Université Claude Bernard Lyon 1, CNRS UMR5586, F69622 Villeurbanne Cedex, **FRANCE**

⁴Département de Chimie, Faculté de Sciences exactes, Université Mentouri Constantine (25000), **ALGERIE**

INFLUENCE OF LUBRICANT PHYSICO-CHEMICAL PROPERTIES ON THE TRIBOLOGICAL OPERATION OF FLUID PHASE PHOSPHOLIPID BIOMIMETIC SURFACES

Phospholipid bilayers appear to play a key role in joint lubrication in controlling and reducing frictional forces between biological surfaces. We have investigated the mechanical and tribological properties of Dioleoyl phosphatidylcholine (DOPC) bilayers prepared by the micelle and vesicle method in different solutions (ultrapure water and Tris buffer pH 7.2 with or without 150 mM NaCl). Friction forces are measured using a homemade biotribometer. Mechanical resistance to indentation is measured by AFM and lipid bilayer degradation is controlled in-situ during friction testing using fluorescence microscopy. This study confirms that mechanical stability under shear or normal load is essential to obtain low and constant friction coefficients. The major result is that the Tris buffer pH 7.2 improves mechanical and tribological stability of the studied bilayers. In ultrapure water, bilayers obtained by the micelle method are not resistant and spontaneously adsorb to the other contacting surface. Bilayers prepared by the vesicle method show slightly better lubricant properties than those prepared by the micelle method. Additional salt (150 mM NaCl) has existing but secondary effects on the mechanical and tribological properties of the bilayers.

Keywords: supported phospholipid bilayers, biolubrication, atomic force microscopy, friction coefficient, nanomechanics

1. INTRODUCTION

Phospholipids, together with proteins, are the major components of biological membranes and play vital roles in many biological processes. In particular, phospholipid layers are found in the synovial fluid and appear to play a key role in joint lubrication [1-4]. Other physiological lubricating sites where lipids are claimed to have a beneficiary lubricating function include pleura, pericardium, the ocular surface and the gut where sliding occurs during gastric motility [5].

Supported phospholipid bilayers (SPB) composed of phospholipids adsorbed to a planar solid support are widely used as models to investigate the properties of these membranes and associated processes such as molecular recognition, enzymatic catalysis, cell adhesion and membrane fusion [6-8]. SPB are also important for a number of applications including biosensors design, solid surfaces and biomaterials biofunctionalization, protein crystallization and DNA immobilization [7,9,10].

The physical and chemical properties of biological membranes are of critical importance to understand specific membrane function. The stability of SPB is a major concern for the use of such layers in these various applications. The atomic force microscopy (AFM) provides an important way to measure this stability and to observe the nature of bilayer defects. There have been several reported studies concerning the effect of various physicochemical parameters on the SPB integrity by AFM: pH dependence [11], deposition pressure of the outer lipid layer [12] or temperature [13]. AFM has become a major tool to measure forces between surfaces and colloidal particles [14-15]. It has also been used to study the interaction between bilayers and silicon nitride or silicon oxide tips [16-24].

Besides imaging, force spectroscopy allows us to obtain valuable experimental information about the interaction forces and mechanical behavior of the studied systems with nanometric and nanonewton resolution through the force-distance curves. Jumps have been described on the approaching curve on

lipid bilayers, this breakthrough being interpreted as the penetration of the AFM tip through the lipid bilayer [25]. The force at which this jump in the force plot occurs is the maximum force the bilayer is able to withstand before breaking. Thus, a quantitative measurement of the force at which the jump occurs can shed light on basic information concerning cell membrane nanomechanics as well as interaction forces between neighboring lipid molecules in the membrane. Therefore, the force value at which this jump takes place is closely related to membrane stability [26].

Recently, we observed a clear correlation between membrane stability (probed by AFM force curves) and the tribological properties of lipid bilayers. Our homemade biotribometer allows the simultaneous measurement of friction coefficient and the visualization of surface degradation by light and fluorescence microscopy [27]. We have shown that it is possible to reduce the friction coefficient of model surfaces by nearly 2 orders of magnitude, to a very reproducible value $\mu=0.002$ when both surfaces are covered by a DPPC (Dipalmitoyl phosphatidylcholine) bilayer (solid phase). With only one bilayer in the contact region, the friction coefficient was much higher than with two bilayers and it increased during prolonged friction while the bilayer degraded as evaluated by fluorescence microscopy. When two DOPC bilayers were deposited, the friction coefficient was higher than with DPPC, it increased during prolonged friction while the bilayer degraded to an extent visibly depending on the bilayer preparation method [28].

In order to better understand the molecular mechanisms responsible for the lubricating ability of SPB it is essential to vary physico-chemical parameters (temperature and phase of the lipid bilayer, ions, pH, viscosity of the buffer...) and to measure the structure and the mechanical properties of the contact (lipid packing, water layers, resistance of the bilayers to friction or normal load, lipid mobility and mobility of the fluid around the bilayer...). Our ambition for this study is more restricted: we aim to measure whether pH, ions and bilayer method of preparation are changing the mechanical and tribological properties of SPB. Resistance to nano-indentation is measured with an AFM (force spectroscopy mode) while friction and bilayer degradation under shear are measured with our biotribometer. The important conclusion of this study is that DOPC bilayers in an unbuffered solution (ultrapure water pH 5) are intrinsically less resistant and lubricant than those in Tris buffer pH 7.2.

2. MATERIALS AND METHODS

2.1 Materials

All chemicals were of analytical grade and were used without further treatment. 1,2-dioleoyl-sn-

glycero-3-phosphatidylcholine (DOPC) and 1-palmitoyl-2-{6-[(7-nitro-2-yl)-3-benzoxadiazol-4-yl]amino]hexanoyl}-sn-glycero-3-phosphocholine (NBD-PC) were purchased from Avanti Polar Lipids, and used without further purification. NBD-PC whose ends are fluorescent in blue light was used to visualize the bilayer homogeneity by fluorescent microscopy. The buffer beneath the bilayers was 15 mM Tris-HCl buffer pH 7.2 (Sigma Aldrich) containing or not 150 mM NaCl, prepared in ultrapure water (MilliQ, 18.2 M \cdot cm resistivity) and filtered with a PES membrane 0.20 μ m before use. The non-ionic sugar-based surfactant n-dodecyl- β -maltoside (DDM) was purchased from Sigma Aldrich.

2.2 Preparation of SPB

We used a 8 mm radius convex soft HEMA lens (Corneal Industrie, Annecy, France) and a flat borosilicate glass plate as the surfaces on which lipid bilayers were deposited for tribological measurements. When swollen in saline solution (150 mM NaCl, actual pH 7.2), the HEMA lens contains 25% water (wt %) and has mechanical and physicochemical properties similar to those of articular cartilage [26]. Borosilicate glass was also used for AFM nano-indentation experiments. Glass surfaces were sonicated twice for 20 min at 60°C in aqueous detergent MicroSon (Fisher-Bioblock, France) and once for 20 min at 60°C in ultrapure water, then rinsed copiously with ultrapure water immediately before bilayer deposition. HEMA was gently cleaned by hand and rinsed copiously with ultrapure water. SPB were prepared using both vesicle fusion [29] and micelle [30, 31] methods. DOPC was solubilized to 1-20 mg/ml depending on the employed method together with 1% NBD-PC (wt%) in chloroform/ethanol (9/1, v/v). An appropriate aliquot was poured in a glass tube and the solvent was evaporated under a stream of nitrogen. The resulting lipid film was then kept under high vacuum overnight to ensure the absence of organic solvent traces.

To obtain supported phospholipid bilayers from vesicles (SPBv), we used the following classical protocol. Multilamellar vesicles (MLV) were obtained by hydrating the dry lipid film in 15 mM Tris buffer pH 7.2 at room temperature to a final concentration of 20 mg/ml. MLV were vortexed for 10 min, frozen for 5 min in liquid nitrogen and then thawed for 10 min in a water bath, the whole procedure being repeated six times and in between each cycle MLV were vortexed for 1 min. The vesicles were then extruded using a miniextruder (Avanti Polar Lipids). Samples were successively subjected to 19 passages through 0.4 and 0.2 μ m pore diameter polycarbonate membranes (Avanti Polar Lipids) respectively. The resulting unilamellar vesicles (LUV) were diluted ten times in 15 mM TRIS buffer pH 7.2 and stored at 4°C under

nitrogen. Glass and HEMA surfaces were incubated for 1 hour with the LUV solution diluted ten times, to which 2 mM of Ca^{++} ions were added to stimulate vesicles fusion and bursting on the surfaces. The lipidic surplus was then eliminated by rinsing.

Supported phospholipid bilayers were also produced from mixed micellar solutions (SPBm) [30, 31]. The dry lipid film was solubilized in micelles using DDM surfactant and ultrapure water at 0.114 g/l lipid solution (lipid/DDM = 1/6, wt/wt) and co-adsorbed on the glass and HEMA surfaces for 5 minutes in 2 mM of Ca^{++} . DDM was eliminated by slow rinsing with ultrapure water at 3 ml/min for 90 min. A second adsorption from a less concentrated solution (0.0114 g/l) was sometimes performed. SPBv or SPBm were conserved in ultrapure water or 15mM Tris buffer pH 7.2 and used within a day. 150 mM NaCl was eventually added to Tris buffer for experiments.

2.3 Atomic force spectroscopy

Measurements were carried out with a commercial AFM (NanoScope III, Veeco Instruments, Santa Barbara, CA) equipped with a liquid J-scanner. Force plots were acquired using V-shaped Si_3N_4 tips NP (Veeco) and OMCL TR400PSA (Olympus, Japan) with a nominal spring constant of $K=0.06\text{-}0.12$ N/m and $K=0.08$ N/m respectively. Individual spring constants were calibrated using the thermal noise method with a MFP-3D Asylum Stand Alone AFM. Tip radii of curvature R were measured by imaging a silicon grating (TGT1, NT-MDT, Zelenograd, Moscow) and individual radii were found to be 20-40 nm. Thousands of approach-retraction cycles were performed at several locations of the lipidic bilayer and the cantilever deflection was recorded versus the position of the Z-piezo of the AFM. These data can be converted into force-distance curves where the force F was calculated from the measured cantilever deflection Δz as $F=K \cdot z$, where K is the cantilever spring constant and subtracting the cantilever deflection from the height position to obtain the distance. The tip-sample approaching velocity was set for all force curves at $400 \text{ nm}\cdot\text{s}^{-1}$ so that the effect of the velocity on the breakthrough force could be totally neglected. Jump distances, breakthrough and adhesion forces (Figure 1) were automatically measured using our own C++ code.

2.4 Tribological measurements

A homemade biotribometer permitting in situ visualization of the contact was used to measure the frictional forces between a compliant soft HEMA lens and a flat borosilicate glass plate, each surface being covered with one DOPC bilayer as previously described. An upright epifluorescence microscope (Leica DMLM) equipped with a fluorescence camera (Leica DC350F) was used to view the contact through the opposing glass body. This

observation was performed in situ during friction and under white and blue light to visualize the centering of the contact area and the bilayer integrity respectively. An eddy current position sensor measured the deformation of the flexible blades holding the tank, and permitted calculating the tangential force. An average normal load of 0.3 MPa was imposed, resulting in a contact area diameter of about 2 mm independent of the bilayer type. The friction coefficient μ was defined as the ratio between the tangential force (once the surfaces slide against each other) and the normal load. Several series of friction tests were performed, each lasting 50 min (about 150 back and forth cycles). Mean and min-max (for the error bar) values of both initial and final friction coefficient (i.e., just after the beginning and after 50 min of friction) were calculated.

3. RESULTS

3.1 Nano-mechanical properties of SPBm

We first present experimental results on the nano-mechanical resistance to indentation of DOPC bilayers prepared by micelle method (SPBm). Two typical AFM approaching-retracting (AR) curves are displayed in Figure 1 in raw data (i.e., deflexion vs. Z piezo displacement). The AR curve 1 exhibits a breakthrough feature in the approaching curve occurring at a deflexion of about 10 nm corresponding to a breakthrough force $F_B \sim 0.88$ nN (black arrow).

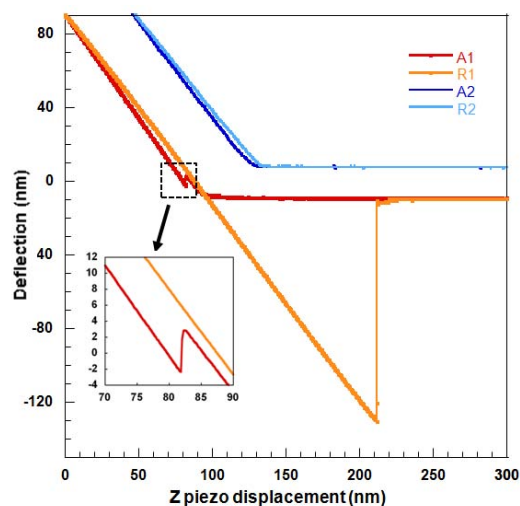


Figure 1. Typical deflection-distance curves recorded on DOPC SPBm with one incubation. The cantilever spring constant value is $K=0.08$ N/m.

Legend: A and R refers as approaching and retracting curves respectively, numbers as successive deflection-distance cycles. Cycles 1 exhibit a breakthrough feature with jump of about 4.6 nm in the approaching curve at a force level of about 0.88 nN and large adhesion peak of about 9.4 nN in the retracting curves (see the enlarged region in the inset). Cycle 2 on the other hand does not display either jump or adhesion.

As previously reported [26,28,32,33] the lipid bilayer is unable to withstand the force exerted by the tip and the breakthrough feature corresponds to the penetration of the bilayer by the apex of the tip. The jump distance is about 4.6nm. The corresponding retracting curves show a large adhesion force ($F_{Ad} \sim 10$ nN). On the other hand, when the tip does not penetrate the bilayer (curve 2 in Figure 1), the retracting curve does not present any adhesion.

We have recorded thousands of AR curves up to a maximal load of 20 nN in water and Tris buffer pH 7.2 with or without 150 mM NaCl. In ultrapure water, SPBm (one or two incubations) were punctured in 100% of the cases. However, one can note a clear difference between the two conditions: the distribution of breakthrough forces is peaked at about 0.3 nN in the case of one incubation (Figure 2A) while breakthrough forces are higher with a second histogram peak around 2 nN in the case of two incubations (Figure 2D). The jump distance and adhesion force histograms are similar for each condition (Figures 2B-C, E-F). They are broad and range between 2 and 10 nm, and between 0 and 20 nN respectively. They are slightly depending on the sample or on the tip used (each plain bar style corresponds to a different experiment in Figures 2-3). We never observed on glass two successive jumps in the force plots.

When using 15 mM Tris pH 7.2 buffered solution, the force curves are drastically changing and very few penetrations are observed either with one (Figure 2G) or two incubations (not shown). The penetration frequency is nearly zero when 150 mM NaCl is added to the Tris buffer with one (Figure 2H) or two incubations (not shown).

Nano-mechanical properties of SPBv. DOPC bilayers prepared by the vesicle method (SPBv) do not show any clear dependence on the buffer type (Figure 3A-F) contrary to SPBm. Nearly 50% of the AR cycles present no breakthrough feature and the other are penetrated by the tip under a mean force of about 10 nN in water or in a Tris buffer pH 7.2 (Figure 3A-D). The associated jump distance distribution is much more peaked around 3 nm (Figure 3B-E) than the corresponding distribution for SPBm (Figure 2B-E). This mean jump distance corresponds therefore to the thickness of a single DOPC bilayer³⁴. Another change due to the method of preparation of bilayers concerns the adhesion force distribution. When there is penetration of the bilayer, the mean adhesion value is centered around 3~5 nN for SPBv (Figure 3C, F) instead of 5~10 nN for SPBm (Figure 2C, F).

3.2 Friction coefficients and degradation of DOPC bilayers

We have measured the friction coefficient μ between hydrophilic surfaces (a convex lens in soft HEMA articulated against a flat borosilicate glass plate)

each covered or not with a DOPC bilayer. We have also investigated the effect of buffer and bilayer method of preparation. Results are summarized in Figure 4A. In water, as previously found [28], we have confirmed that as compared to bare surfaces, μ is reduced when surfaces are covered with SPB. However, after 20 min of friction, the value of the friction coefficient for bare or SPBm covered surfaces reached the same very high value $\mu=0.165$ which may induce glass degradation.

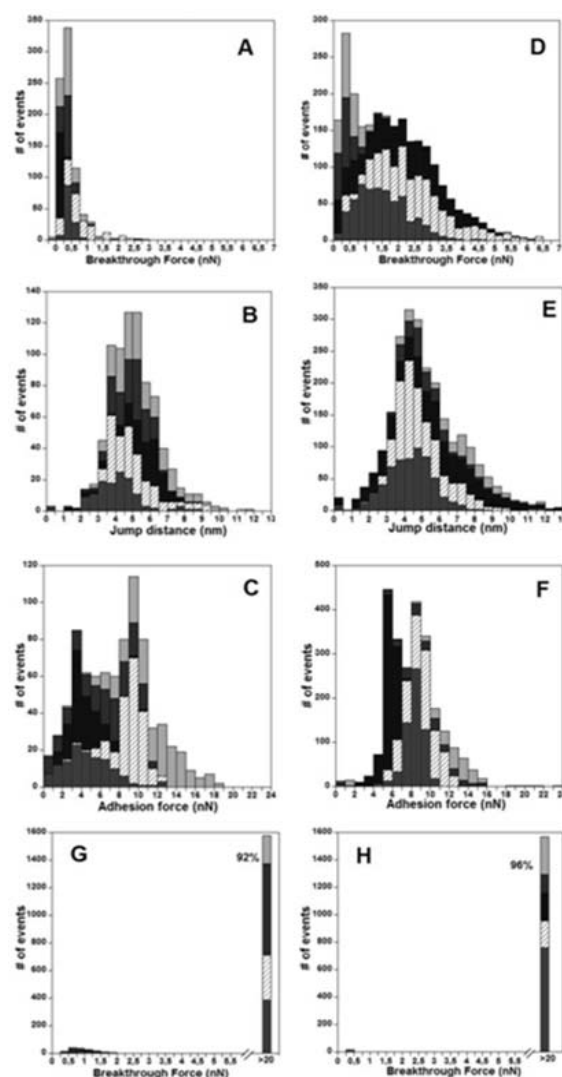


Figure 2. Histograms corresponding to the breakthrough force (A,D,G,H), the jump distance (B,E) and the adhesion force (C,F) measured by AFM for DOPC bilayers prepared by the micelle methods in different solutions: (A-C) ultrapure water, one incubation; (D-F) ultrapure water, two incubations; (G) Tris buffer pH 7.2, one incubation; (H) Tris buffer pH 7.2, 150 mM NaCl, one incubation. Colors correspond to different experiments with different samples and different tips

In Tris buffer pH 7.2, the situation is drastically changed: on bare surfaces (with or

without 150 mM NaCl) the friction coefficient is stabilized to a lower value $\mu=0.1$; when surfaces are covered with SPB, the friction coefficient is surprisingly low and stable during prolonged friction (i.e., $\mu=0.035$ for SPBm and $\mu=0.022$ for SPBv) with little effect if any of salt (150 mM NaCl). This stability of the friction coefficient value in Tris buffer is accompanied by very little bilayer degradation if any at the end of the 50 min friction period as seen by the fluorescence images of the bilayer (Figures 4B-E) This stability is a really new result as we previously obtained a large increase of μ and an important degradation in water or in a non-buffered saline solution both by the micelle and vesicle method [28].

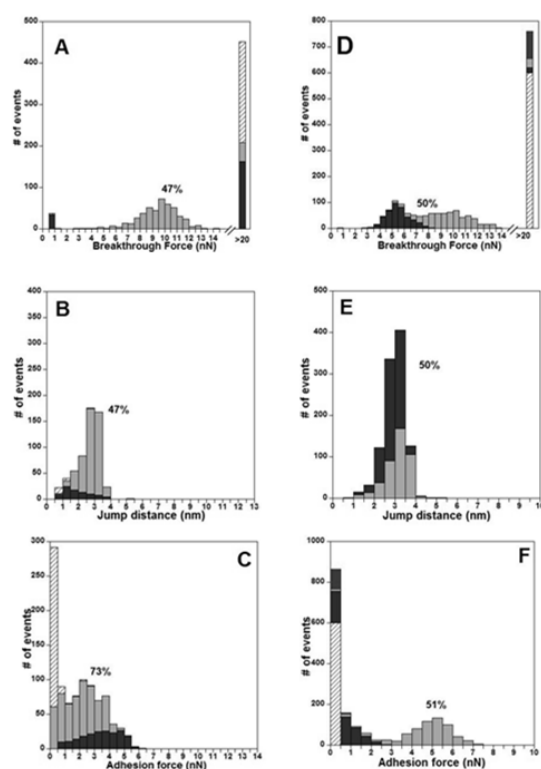


Figure 3. Histograms corresponding to the breakthrough force (A, D), the jump distance (B, E) and the adhesion force (C, F) measured by AFM for DOPC bilayers prepared by the vesicle method in different solutions: (A-C) pure water; (D-F) pH 7.2 Tris buffer. Colors correspond to different experiments with different samples and different tips

4. DISCUSSION

In this report, we have found a strong pH dependence of the mechanical and tribological properties of DOPC bilayers prepared by the micelle or vesicle method.

First, SPBm are easily punctured in water but not in a Tris buffer pH 7.2. Such a buffer influence does not hold for SPBv. Secondly, the distribution of jump distances (penetration lengths) is peaked

around 3-4 nm for SPBv but ranges up to 10 nm for SPBm. The first value compares well with the bilayer thickness [34,21] while a distance of 7-8 nm agrees with the thickness of two DOPC bilayers. It strongly suggests that, in water and when using the micelle method of preparation, a bilayer is also present on the surface of the AFM tip and that two bilayers are interacting together in the recorded force-distance curves. This result is in agreement with previous observations of spontaneous bilayer adsorption on an initially bare hydrophilic AFM tip [21,28] or on the glass sphere of a surface force apparatus when these surfaces are approached to a DOPC SPBm. Interestingly, such an adsorption was never reported for the vesicle method to our best knowledge.

We never observed two successive jumps in the force plots on glass. The two bilayers are therefore punctured simultaneously as found for surfaces covered by surfactant bilayers [36]. The fact that the adhesion force in the retracting curves after a penetration is twice larger for the micelle method reflects probably that a larger force is needed to separate two adsorbed bilayers (micelle case) than a bilayer from a bare surface (vesicle case).

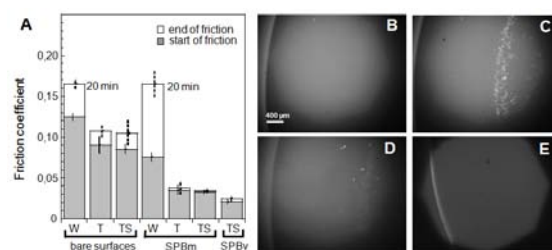


Figure 4. Effect of the bilayer preparation method and of the buffer on the tribological behaviour of DOPC supported bilayers. (A) Average values of friction coefficient are calculated from at least 2 independent experiments. Gray bars represent the initial value and white bars the final value after 50 min of friction (except two measurements stopped after 20 min because of too large friction coefficient degrading the glass surface). Error bars indicate minimum and maximum measured values. Abbreviations: W, water; T, Tris buffer pH 7.2; TS, Tris buffer pH 7.2 with 150mM NaCl; SPBm and SPBv. (B)-(E) In situ fluorescence visualisations of the recorded border of the contact zone showing some eventual bilayer degradation; (B) is the initial control image (before starting sliding the surfaces) of a SPBm; the same type of bilayer in water shows a strong degradation in water after 20 min of friction (C) and slight degradation in Tris buffer pH 7.2 within 50min of friction (D); a bilayer prepared with the vesicle method after 50 min of friction in Tris buffer pH 7.2 with 150 mM NaCl is not degraded (E)

In water, the lower resistance to tip indentation and the propension to spontaneously adsorb to other surfaces during contact for SPBm are certainly related to the presence of traces of detergent DDM. First, because these phenomena are not observed in the absence of detergent (vesicle method) and as secondly because the number of incubations increased significantly the mean bilayer breakthrough force. A possible scenario is that detergent-lipids interactions in water (but not in Tris buffer) induce a spontaneous curvature and a destabilization of the bilayer. DOPC is normally considered to form particularly stable flat bilayers but in the presence of cholesterol, its spontaneous radius of curvature is drastically reduced [37]. Cholesterol can even lead to the formation of nonbilayer structures [38]. The formation of defects on DLPE SPB during repeated scanning of the AFM tip was also reported to be highly pH-dependent and was explained by the increasing bending energy or frustration due to the high spontaneous curvature of DLPE monolayers at low pH [11]. We believe that such an effect is likely to occur here because of a pH dependence of residual DDM-lipids interactions.

In Tris buffer pH 7.2, SPBm seem more resistant to normal indentation than SPBv (Figures 2G,H, 3D). Actually, the distribution of breakthrough forces for SPBv is similar to previously reported values on mica with the same method of preparation [26,33]. The great resistance of SPBm at pH 7.2 is on the other hand a surprising result. However, both kind of SPB are not punctured by forces equivalent to those used in friction experiments (i.e. 0.3 MPa in a normal joint which corresponds to about 1nN in AFM experiments)[28]. This resistance to nano-indentation is again correlated with a weak if any bilayer degradation during prolonged friction and with a low and stable friction coefficient. SPBv have slightly better lubricant properties at pH 7.2 than SPBm, perhaps again due to the presence of traces of DDM in the latter case. The friction coefficient with DOPC bilayers remains however nearly an order of magnitude larger than DPPC bilayers in the solid phase previously measured [28]. This indicates that fluid bilayers are intrinsically less lubricant than solid ones even if they resist to shear and normal stress. Understanding the coupling between lipid mobility and surrounding buffer mobility, along with localizing precisely the slip plane seems to be the key steps toward the understanding of mechanisms of biolubrication by lipid layers.

5. CONCLUSION

We have examined the role of the buffer (pH, ions) and the bilayer preparation method on SPB mechanical resistance and tribological properties. The method of preparation gives very different

properties in water but not in Tris buffer pH 7.2. In water, SPBm are especially weak and spontaneously adsorb to the other contacting surface. In a buffer pH 7.2, bilayers are more resistant to nano-indentation and more stable to prolonged periods of friction than those in water. They present also better lubricant properties. Additional salt (150 mM NaCl) have existing but secondary effects on the mechanical and tribological properties of the bilayers.

ACKNOWLEDGEMENT

The authors would like to thank Mr. R. Bougaran of CORNEAL Industrie which provided us the manufactured HEMA lenses, Mrs. Piednoir from LPMCEN Lyon and Mr. C. Godeau, from INSA Lyon for their helpful participation in this work. The LPMCEN team belongs to CellTiss consortium. F.D. was supported by a PROFAS fellowship.

REFERENCES

1. Hills, B.A., 1995, *Ann. Biomed. Eng.*, 23, 112–115.
2. Johnston, S.A., 1997, *Vet. Clin. North Am. Small Animal Pract.*, 27, 699.
3. Schwarz, I.M., Hills, B.A., 1998, *Br. J. Rheumatol.*, 37, 21–26.
4. Hills, B.A., 1989, *J. Rheumatol.*, 16, 82–91.
5. Hills, B. A., 2000, *Proc. Inst. Mech. Eng. H., J. Eng. Med.*, 214, 83–94.
6. McConnell, H.M., Watts, T.H., Weis, R.M., Brian, A., 1986, *Biochim. Biophys. Acta*, 864, 95–106.
7. Sackmann, E., 1996, *Science*, 271, 43–48.
8. Richter, R.P., Bérat, R., Brisson, A.R., 2006, *Langmuir*, 22, 3497–505.
9. Mou, J, Czajkowsky, D.M., Zhang, Y., Shao, Z., 1995, *FEBS Lett.*, 371, 279–282.
10. Brisson, A., Bergsma-Schutter, W., Oling, F., Lambert, O., Reviakine, I., 1999, *J. Cryst. Growth*, 196, 456–470.
11. Hui, S.W., Viswanathan, R., Zasadzinski, J.A., Israelachvili, J.N., 1995, *Biophysical Journal*, 68, 171–178.
12. Benz, M., Chen, N., Israelachvili, J., 2004, *J Biomed Mater Res A*, 71, 6–15.
13. Fang, Y., Yang, J., 1997, *J. Biochim Biophys Acta, Biomembranes*, 1324, 309–319.
14. Butt, H.-J., 1991, *Biophys.J.*, 60, 1438–1444.
15. Ducker, W.A., Senden, T.J., Pashley, R.M., 1991, *Nature*, 35, 239–241.
16. Dufrêne, Y.F., Boland, T., Schneider J.W., Barger, W.R., Lee, G.U., 1998, *Faraday Discuss.*, 111, 79–94.
17. Mueller, H., Butt, H.-J., Bamberg, E., 2000, *J. Phys. Chem.*, 104, 4552–4559.

- 18. Schneider, J., Dufrene Y.F., Barger W.R., Lee G.U.,** 2000, *Biophys. J.*, 79, 1107–1118.
- 19. Schneider, J., Barger, W., Lee, G.U.,** 2003, *Langmuir*, 19, 1899–1907.
- 20. Butt, H.-J., Franz, V.,** 2002, *Phys. Rev. E.*, 66, 031601.
- 21. Grant, L.M., Tiberg, F.,** 2002, *Biophys. J.*, 82, 1373–1385.
- 22. Loi, S., Sun, G. X., Franz, V., Butt, H.-J.,** 2002, *Experiment. Phys. Rev. E.*, 66, 031602.
- 23. Richter, R.P., Brisson, A.,** 2003, *Langmuir*, 19, 1632–1640.
- 24. Künnecke, S., Krüger, D., Janshoff, A.,** 2004, *Biophys. J.*, 86, 1545–1553.
- 25. Franz, V., Loi, S., Muller, H., Bamberg, E., Butt, H.,** 2002, *J. Colloids and Surfaces B: Biointerfaces*, 23, 191–200.
- 26. Garcia-Manyes, S., Oncins, G., Sanz, F.,** 2005, *Biophysical Journal*, 89, 1812–1826.
- 27. Trunfio-Sfarghiu, A.-M., Berthier, Y., Meurisse, M.-H., Rieu, J.P.,** 2007, *Tribology International*, 40, 1500–1515.
- 28. Trunfio-Sfarghiu, A.-M., Berthier, Y., Meurisse, M.-H., Rieu, J.P.,** 2008, *Langmuir*, 24, 8765–8771.
- 29. Schönherr, H., Johnson, J. M., Lenz, P., Frank, C. W., Boxer, S. G.,** 2004 *Langmuir*, 20, 11600–11606.
- 30. Tiberg, F., Harwigsson, I., Malmsten, M. Eur.,** 2000, *Biophys. J.*, 29, 196–203.
- 31. Vacklin, H.P, Tiberg, F., Thomas, R.K.,** 2005, *Biochimica et Biophysica Acta*, 1668, 17–24.
- 32. Oncins, G., Garcia-Manyes, S., Sanz, F.,** 2005, *Biophysical Journal*, 89, 7373–7379.
- 33. Pera, I., Stark, R., Kappl, M., Butt, H.-J., Benfenati, F.,** 2004, *Biophys. J.*, 87, 2446–2455.
- 34. Liu, Y., Nagle, J.F.,** 2004, *Phys. Rev. E*, 69, 040901.
- 35. Leroy, S., Steinberger, A., Cottin-Bizonne, C., Trunfio-Sfarghiu, A.-M., Charlaix, E.,** 2009, *Soft Matter*, 5, 24 p.4997–5002.
- 36. Grant, L.M., Ederth, T., Tiberg, F.,** 2000, *Langmuir*, 16, 2285–2291.
- 37.(37). Chen, Z., Rand, R.P.,** 1997, *Biophysical Journal*, 73, 267–276.
- 38. Coorssen, J.R., Rand, R.P.,** 1990, *Biochem Cell Biol.*, 68 (1), 65–9.

Simon LE FLOC'H^{1,2}
e-mail: *simon.lefloch@imag.fr*

M.C. CORNEC^{2,3}
A.-M. TRUNFIO-SFARGHIU²
M.-H. MEURISSE²
J.-P. RIEU⁴
J. DUHAMEL²
C. DAYOT²
F. DANG²
M. BOUVIER²
C. GODEAU²
A. SAULOT²
Y. BERTHIER²

¹ Université Joseph Fourier, Ecole doctorale EDISCE, Laboratory TIMC-IMAG, DynaCell Team, **FRANCE**

² Laboratoire de Mécanique des Contacts et des Structures, INSA-Lyon, CNRS UMR5259, F69621 Villeurbanne Cedex, **FRANCE**

³ Université Technique "Gh. Asachi", Faculté de Mécanique, 700050, Iasi, **ROUMANIE**

⁴ Laboratoire de Physique de la Matière Condensée et Nanostructures, Université Claude Bernard Lyon 1, CNRS UMR5586, F69622 Villeurbanne Cedex, **FRANCE**

IMAGERIE MEDICALE POUR EVALUER LES CONDITIONS DU FONCTIONNEMENT TRIBOLOGIQUES DES ARTICULATIONS SYNOVIALES

Le but de ce travail est d'évaluer avec précision les conditions tribologiques macroscopiques subies par l'articulation du genou au cours de la marche en essayant de considérer les interactions entre elles. Le contexte plus global est la compréhension du fonctionnement tribologique de l'articulation saine lui permettant de durer 70 ans. Dans une première partie, les vitesses relatives tangentielles entre les surfaces en contact ont été évaluées au cours de la marche. L'étude a été consacrée aussi à l'évaluation des conditions géométriques du contact lorsque le pied subit un effort de compression de l'ordre de 300 N (patiente de 29 ans pesant 60 kg ayant subi une méniscectomie).

Les résultats sur la déformée sont validés qualitativement par des éléments bibliographiques. Ils permettent d'émettre une hypothèse quant à la capacité du cartilage à se déformer de quelques dixièmes de mm suivant son épaisseur sans que la pression locale de contact soit importante, permettant une répartition de la pression très efficace.

L'étude a été complétée par l'évaluation de l'influence des efforts musculaires sur la réaction de contact et sur les déplacements relatifs des os (patient de 36 ans et de 62 kg (avec une lésion des ménisques) a subi une compression du membre inférieur). Il est conclu que l'action des muscles augmente énormément la pression moyenne de contact, mais que cette action peut aussi permettre d'optimiser les conditions de contact en déplaçant le tibia par rapport au fémur.

Keywords: articulation synoviales, conditions du contact, compression de cartilage

1. INTRODUCTION

L'articulation saine du genou est un système tribologique performant car elle peut fonctionner normalement plus de 70 ans. La compréhension de son fonctionnement tribologique a particulièrement été étudiée dans les dernières décennies car les maladies ostéo-articulaires prennent de plus en plus d'ampleur et les traitements ne s'avèrent souvent pas assez efficaces.

De nombreuses études ont montré le fonctionnement complexe des différentes composantes articulaires prises individuellement (cartilage, synovie et ensemble musculaire) mais le fonctionnement réel d'une articulation dépend non seulement des propriétés individuelles de chaque composant articulaire mais aussi des interactions et

de l'arrangement structurel entre tous ces composants.

D'où notre intérêt de comprendre le fonctionnement tribologique de l'ensemble de l'articulation.

Pour cela des études récentes ont permis de définir un modèle expérimental *ex-vivo* prenant en compte les caractéristiques physico-chimiques et mécaniques de l'ensemble in vivo cartilage – synovie.

Ce modèle permet de comprendre à l'échelle microscopique le fonctionnement tribologique de l'interaction cartilage – synovie.

En revanche ce modèle comporte des paramètres qu'il faut fixer par rapport aux conditions réelles du contact (pressions de contact, aires de contact, déformée du cartilage, vitesses relatives tangentielles) qui font l'objet de cette étude.

2. ETUDE IN VIVO DU MECANISME ARTICULAIRE DU GENOU

Ce travail a été réalisé avec la collaboration avec le Laboratoire de Biomécanique et Modélisation humaine (LBMH, Université Lyon 1) et le service d'Arthroscanner de l'Hôpital Lyon Sud.

L'objectif de ce travail est d'évaluer in vivo les conditions tribologiques macroscopiques (pressions de contact, vitesses relatives entre les cartilages articulaires) subies par une articulation du genou au cours de la marche.

Dans ce domaine, la bibliographie n'apporte en effet que des informations souvent incomplètes, et manquantes d'inter cohérence.

Pour obtenir ces conditions tribologiques, nous avons entrepris une étude englobant:

- la détermination de la cinématique du contact (vitesses tangentielles relatives),
- la mesure de la géométrie du contact (dimensions et courbures, conformité des corps en contact, aires de contact),
- la détermination de la dynamique du contact:
 - mesures quasi statiques de la déformée des cartilages articulaires et de la variation de l'aire de contact en fonction du chargement articulaire ;
 - calculs des efforts musculaires et de la réaction du contact, estimation de la pression,
 - l'évaluation du rôle musculaire dans l'optimisation des conditions de contact (diminution de la pression de contact par un déplacement relatif des os).

3. STRATEGIE

Nous avons évalué les conditions cinématiques locales, lors de la marche d'une personne saine : à partir de données issues de la bibliographie (Kapandji), et d'une base de données sur la marche construite au sein du LBMH, des simulations ont été effectuées en dynamique inverse afin de calculer la « réaction de contact ».

Par imagerie médicale (arthroscanner), nous avons évalué les conditions géométriques locales in vivo (courbure des corps en contact, aires de contact) Ces essais ont également permis une analyse quasi-statique de la phase d'appui de la marche, dans le but final d'évaluer la répartition de pression en contact.

Deux patients bénévoles ont participé à nos essais quasi-statiques en arthroscanner. Au cours de ces essais, nous avons mesuré l'effort extérieur appliqué sur le pied de chaque patient. Nous avons également pu enregistrer l'activité électrique des muscles de l'un des deux patients à l'aide d'un dispositif électromyographique.

Ces éléments ont permis de calculer les efforts développés par les muscles articulaires du genou, grâce à une évaluation in vivo des bras de levier des muscles et à l'utilisation d'un code de calcul développé au sein du LBMH (thèse en cours d'Alice Bonnefoy).

La mesure du déplacement relatif des os a permis d'étudier le rôle des muscles pour l'optimisation des conditions tribologiques de contact.

Une brève description anatomique du genou est présentée ci-dessous, ainsi qu'un résumé de résultats obtenus dans le cadre de ce travail.

4. ANATOMIE DE GENOU

L'articulation du genou est une diarthrose, c'est-à-dire une articulation mobile, qui comporte (Figure 1):

- Deux segments osseux, présentant des surfaces articulaires. Dans le cas du genou, une des extrémités osseuses est représentée par les condyles fémoraux et l'autre extrémité par le plateau tibial;
- Deux cartilages articulaires recouvrant les surfaces osseuses (cartilage fémoral et cartilage tibial);
 - La capsule articulaire, fibreuse;
 - La membrane synoviale, qui tapisse intérieurement la capsule;
 - Des ligaments, reliant les deux segments osseux (pour le genou il y a 4 ligaments : deux ligaments croisés et deux ligaments latéraux);
 - Des petites structures fibro-cartilagineuses, les ménisques, qui viennent s'insérer sur les surfaces articulaires pour assurer une meilleure conformité des surfaces. L'articulation du genou présente deux ménisques (l'un interne et l'autre externe) attachés au plateau tibial par des petits ligaments;
 - Une poche graisseuse et des bourses séreuses, sortes de petits coussins hydrauliques constitués d'une enveloppe membranaire contenant un liquide similaire au liquide synovial.

Enfin, les tendons des muscles qui s'insèrent à proximité d'une articulation entourent l'ensemble de ces structures. Le rôle principal des muscles est de mobiliser l'articulation, mais ils ont aussi une importance pour maintenir la cohésion de l'articulation (coaptation).

De nombreux travaux consacrés à l'anatomie par imagerie médicale ont permis de définir avec exactitude la géométrie des extrémités osseuses en contact. Ainsi, les deux condyles fémoraux forment des cycloïdes avec des rayons maximaux de 38mm pour le condyle interne et 60 mm pour le condyle externe (Figure 2.).

En ce qui concerne le plateau tibial, il présente deux cavités (glènes) correspondant aux deux contacts avec les condyles fémoraux. Les deux glènes ont des rayons d'environ 70mm. Elles se

distinguent par leur courbure, la glène interne étant concave et la glène externe convexe (Figure 3). Cela génère un contact conforme pour le condyle interne et un contact non conforme pour le condyle externe.

5. CINEMATIQUE DU GENOU

5.1. Modèle de calcul des vitesses

Pour étudier la cinématique du genou, nous avons utilisé l'hypothèse classique de rattachement ferme des ménisques au plateau tibial. Ainsi, la cinématique simplifiée du genou, consiste en la composition de deux mouvements entre le condyle fémoral et la glène tibiale :

- du roulement, influencé par les courbures des corps en contact,
- du glissement correspondant à des translations relatives entre les deux extrémités osseuses.

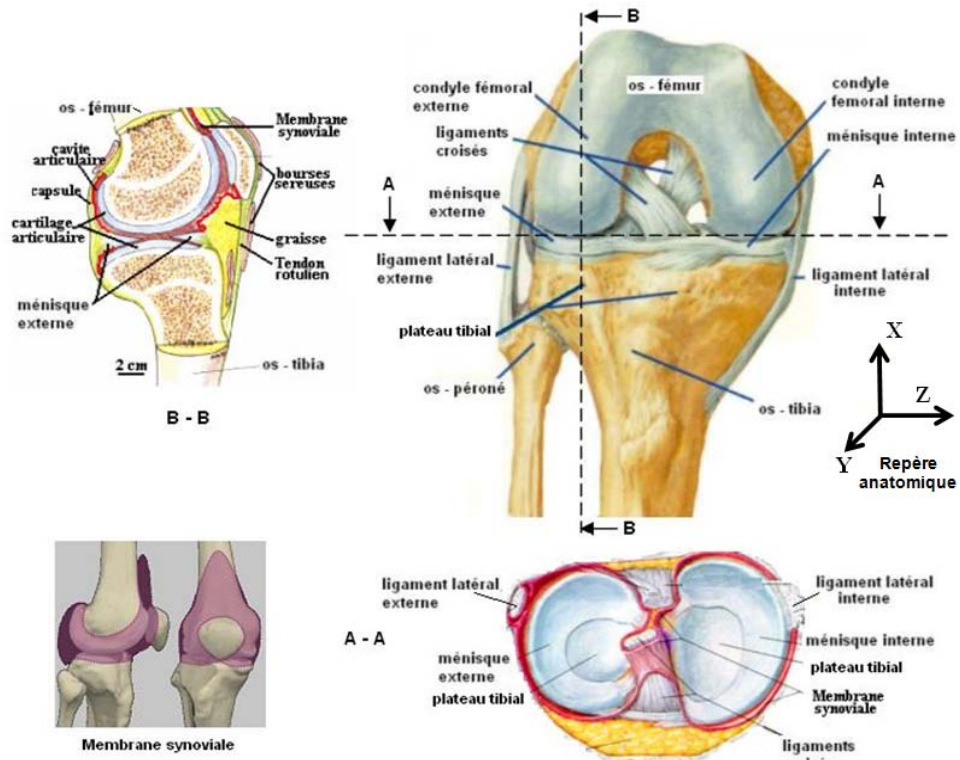


Figure 1. Représentation anatomique de l'articulation du genou

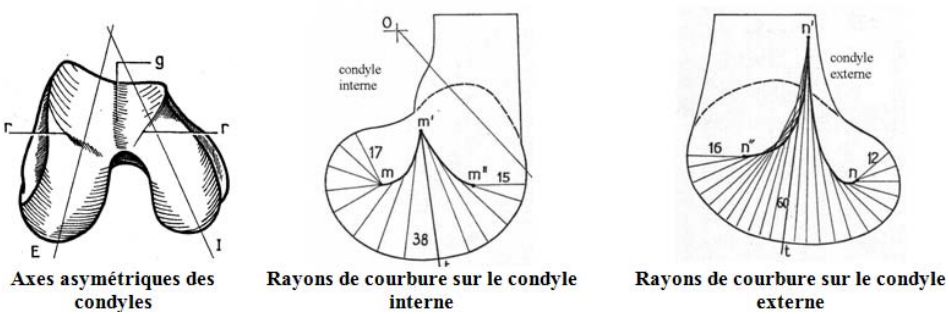


Figure 2. Géométrie des condyles fémoraux

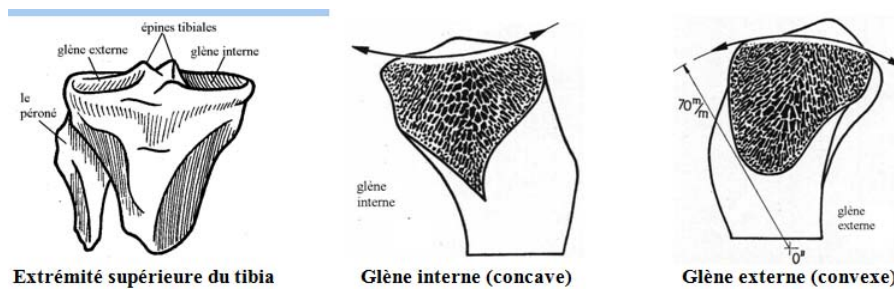


Figure 3. Géométrie des glènes tibiales

Un modèle géométrique simple a été utilisé pour les condyles. Ils sont représentés chacun par un arc de cercle. Le plateau tibial est représenté par deux segments de droite (Figure 4). Ce modèle, de type cylindre sur plan, permet de quantifier rapidement les vitesses tangentielles entre les surfaces.

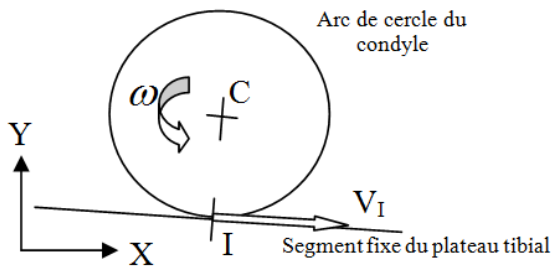


Figure 4. Modèle géométrique de condyle pour le calcul des vitesses

Selon les conventions de signe utilisées (vitesses positives selon les X positifs), la vitesse relative au point de contact de la surface du cartilage d'un condyle du fémur par rapport à la surface du cartilage du tibia est donnée en prenant le tibia comme solide fixe de référence. La vitesse relative tangentielle au point de contact du fémur par rapport au tibia est la somme de la vitesse du fémur en ce point avec la vitesse du point géométrique de contact:

$$V_{\text{fémur/tibia}}(I) = V_I + \omega \cdot R \quad (1)$$

ou R est le rayon du condyle considéré, V_I la vitesse du point de contact I, ω la vitesse angulaire.

Les valeurs de rayons de courbure retenues correspondent à 10° de flexion du genou, et sont issues de l'ouvrage de référence de Kapandji [2]: 55 mm pour le condyle externe et 35mm pour le condyle interne.

Le déplacement des points de contact en fonction de l'angle de flexion, est donné par Li et al. [4] pour le cas des genoux sains en flexion passive. La bibliographie démontre, malgré tout, que les déplacements des condyles sont modifiés suivant que le pied est chargé ou non.

Deux vitesses tangentielles sont calculées aux deux « points de contact ». Enfin, une idée de la réaction du contact artriculaire du genou est donnée par les calculs de dynamique inverse. Cet effort n'est qu'une estimation qualitative de l'effort de contact, permettant d'avoir une idée des conditions interactionnelles entre la cinématique et la pression de contact.

5.2. Résultats

Les résultats des essais sur la cinématique du genou sont présentés dans la Figure 5.

Les vitesses relatives de roulement entre les surfaces au niveau du contact du condyle interne varient cycliquement de 0 mm/sec à 200 mm/s au cours d'une marche effectuée à 5 km/h. Pendant la phase d'appui, la vitesse relative change deux fois de signe et sa valeur maximale dans cette phase est de 80 mm / s pour le contact interne et de 130 mm / s pour le contact externe. Pendant la phase d'oscillation (faibles pressions de contact), les vitesses relatives sont plus importantes (interne : 200 mm / s ; externe : 300 mm / s) et changent également deux fois du signe.

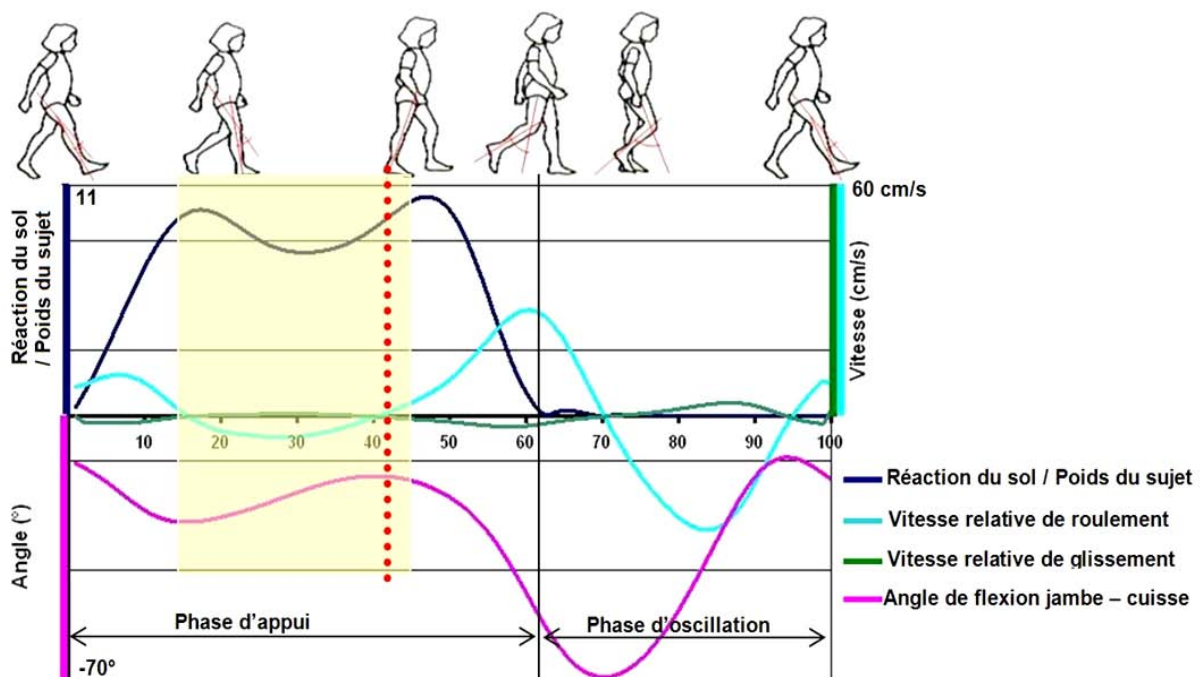


Figure 5. Résultats des essais sur la cinématique du genou

Les vitesses de glissement du contact vers l'arrière du plateau tibial (25 mm / s au maximum) ne compensent pas les vitesses relatives induites par la rotation du fémur par rapport au tibia car les rayons de courbure des condyles sont assez importants. Le condyle externe, dont la surface de contact se déplace plus vers l'arrière que le condyle interne, a un rayon de courbure supérieur, ce qui augmente la vitesse relative tangentielle entre les surfaces en contact à 300 mm/s au maximum.

Ces résultats sont très sensibles aux rayons des condyles retenus. Par contre, l'amplitude de la translation des points de contact vers l'arrière du plateau tibial (de 0° à 60° de flexion), n'influence pas significativement le calcul. Cette translation a une valeur maximale de 10 mm.

6. DINAMIQUE DU GENOU

6.1. Modèle de calcul des déformées des cartilages articulaires (fémur et tibia)

La stratégie consiste à évaluer la déformée in vivo du cartilage des deux condyles fémoraux en faisant une différence entre les épaisseurs de cartilage mesurées avant et après la compression de l'articulation.

Pour obtenir les épaisseurs de cartilage in vivo nous avons utilisé le scanner (rayons X) du CHU de Lyon Sud. La technique de scanner utilisée est nommée « arthro scanner ». Elle comporte l'injection intra articulaire d'un produit à base d'iode qui permet de faire ressortir sur des images radiologiques les parties cartilagineuses de l'articulation. Le volume scanné par les rayons X est de 15 x 23 x 20 cm³ et il permet d'avoir 44 + 77 + 66 coupes de genou dans les trois plans du repère anatomique (Figure 6).

Un montage a été réalisé pour comprimer le membre inférieur du sujet lors de la prise d'images par irradiation X.

Le traitement des deux lots d'images (chargé/non-chargé) a consisté tout d'abord en une reconstitution des volumes du cartilage du fémur. Cette reconstruction a été réalisée en utilisant le logiciel AutoCAD (Figure 7), et a permis de repérer les zones de contact et mesurer les aires de contact extérieurement chargé ou non. Un recalage spatial, a été nécessaire pour superposer le volume du cartilage comprimé sur le volume du cartilage non comprimé, en faisant coïncider des points de repère définis sur l'os.

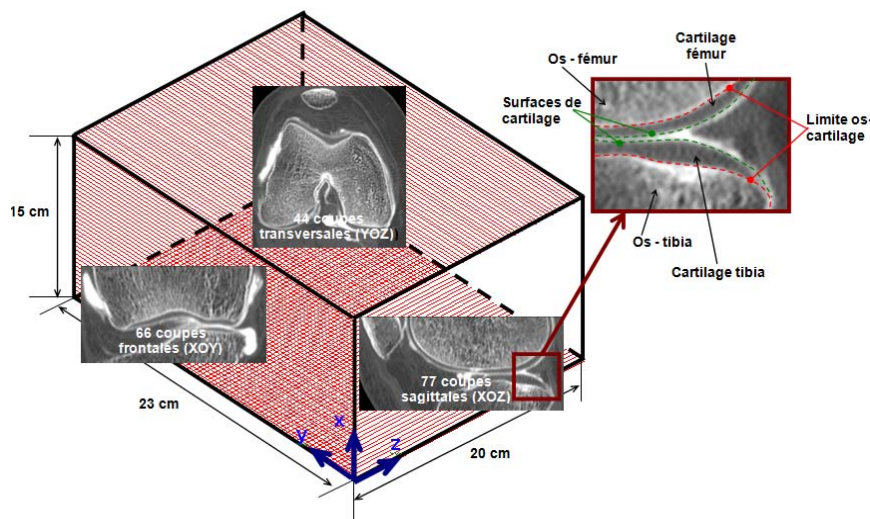


Figure 6. Reconstitution du volume de cartilage en ArthroScanner

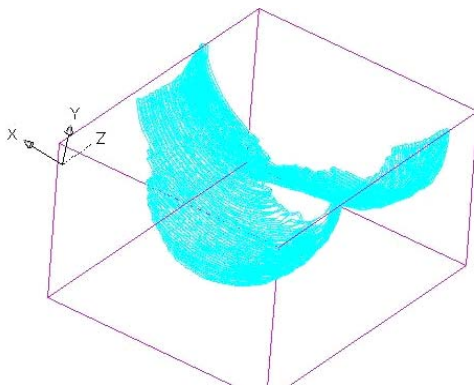


Figure 7. Volume du cartilage comprimé, (AutoCAD)

Une carte de la déformée du cartilage du fémur a été ainsi réalisée.

Le calcul de l'effort de contact a été fait en adaptant le modèle de dynamique inverse à notre étude. Ainsi, dans le cadre de notre étude, les accélérations sont nulles (quasi statique), et le torseur au niveau du pied se limite à une force à deux composantes (F impact). Un capteur force permet de mesurer les deux composantes de cette force sur le pied (suivant X et Y). Le problème est donc plan, et ne permet que le mouvement de flexion – extension au niveau du genou. Les quatre groupes de muscles inter articulaires du genou les plus importants pour la flexion – extension sont

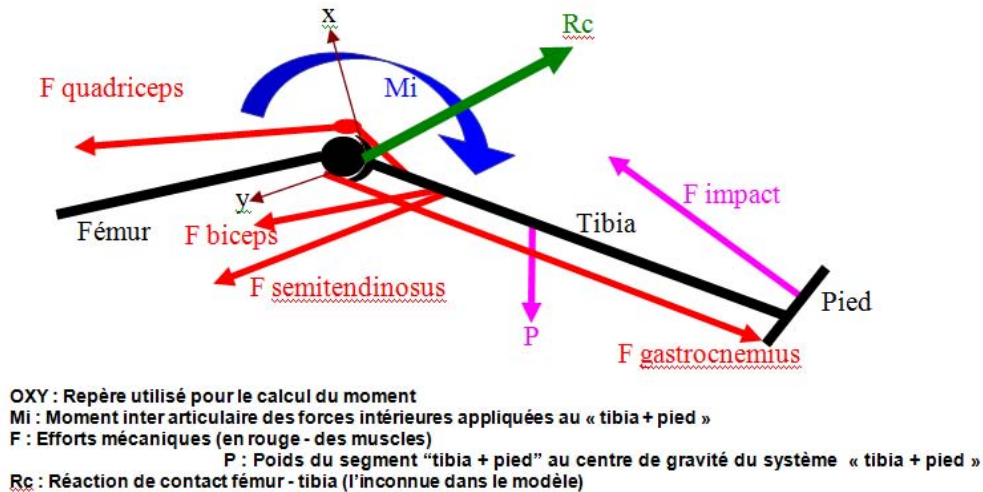


Figure 8. Modèle de dynamique inverse pour calculer les efforts musculaires et la réaction de contact

inclus dans le modèle : le quadriceps, le biceps femoris, le semitendinosus et le gastrocnemius. Les bras de leviers articulaires sont mesurés in vivo grâce aux images d'arthroscanner. Ces données sont introduites dans le modèle de calcul en dynamique inverse qui évalue les efforts musculaires développés par le membre inférieur. (Figure 8)

Pour le calcul en dynamique inverse, deux critères physiologiques ont été retenus : on minimise la réaction de contact, ainsi que la norme quadratique des contraintes des muscles.

Pour vérifier de manière expérimentale si les muscles sont contractés ou non, un dispositif électromyographique a été utilisé.

Par contre, ce dispositif permet seulement d'évaluer de manière qualitative la contracture musculaire.

Deux patients ont participé à notre étude :

- Une patiente de 29 ans, pesant 60 kg. Elle n'a plus de ménisques sur le genou droit, duquel est effectué le scanner. Le fait qu'elle n'ait plus de ménisques augmente les déformations. L'effort de compression a été de 300 N. Nous avons réalisé une carte de déformées du cartilage du fémur, une analyse d'aires de contact fémur - tibia (avant et après compression).
- Un patient de 36 ans qui pèse 62 kg. Il a une lésion au niveau des ménisques sur le genou gauche où est effectué le scanner, en revanche, les ménisques sont en très grande partie sains. L'effort de compression a été de 310 N. Pour cette étude, nous avons effectué un calcul d'effort de contact en prenant en compte l'action musculaire.

6.2. Résultats

Les efforts extérieurs au niveau du pied qui ont été considérés dans ce travail, avec des vitesses nulles entre les surfaces articulaires et un angle

presque nul entre le fémur et le tibia correspondent à la fin de la phase d'appui de la marche (points rouges de la Figure 5).

Dans ces conditions, la pression moyenne au niveau du contact articulaire du genou avec ménisques, a été évaluée entre 10^5 et 10^6 MPa. On a constaté que cette pression est augmentée de 50% s'il n'y a pas de ménisques.

De plus, cette étude nous a permis de montrer l'influence des muscles sur les conditions de contact articulaire, cela est schématisé dans la Figure 6. Ainsi :

- Le rôle principal des muscles au niveau d'une articulation est de générer des couples internes permettant d'assurer le mouvement et/ou l'équilibre. Il a été montré que les efforts externes (poids propre de 40 N et effort de 330 N au bout du pied) appliqués au membre inférieur tendent à réduire la flexion au niveau du genou. Dans ce cas, les fléchisseurs développent un effort de l'ordre de 1200 N pour compenser les efforts externes. Grâce à un enregistrement des efforts musculaires au cours de la compression de la jambe (électromyogramme), il a été conclu que le quadriceps est également actif. L'activité musculaire du quadriceps n'est cependant pas nécessaire en terme de couple. Cette activité, qu'il nous est impossible de quantifier grâce au code de calcul utilisé pour évaluer l'activité musculaire des autres muscles, doit probablement permettre de « stabiliser » l'articulation. Ainsi, la valeur de 200 N indiquée Figure 9 (en opposition à 0 N), pour l'action du quadriceps est totalement arbitraire. Plus l'effort du quadriceps est important, plus l'effort des fléchisseurs doit être important pour compenser le couple interne développé par le quadriceps. Ainsi, si un effort de 200 N est considéré au niveau du quadriceps, l'effort développé par l'ensemble des muscles fléchisseurs est de 1500 N.

- Un rôle secondaire des muscles est de modifier les positions relatives du tibia par rapport

au fémur, ce qui provoque une tension du ligament croisé postérieur et une compression de la partie antérieure des ménisques. Ce mouvement modifie la répartition de pression et donc les conditions du contact.

Pour cette étude nous nous sommes placés dans les conditions de fonctionnement défavorables

pour la lubrification articulaire par effets de type hydrodynamique, qui correspondent à la phase située entre 15% et 45% du cycle de marche (rectangle jaune de la Figure 5).

Dans cette phase, on peut considérer que les pressions de contact atteignent entre 10^5 et 10^6 MPa, avec des vitesses relatives variant de 0 à 5 cm/s.

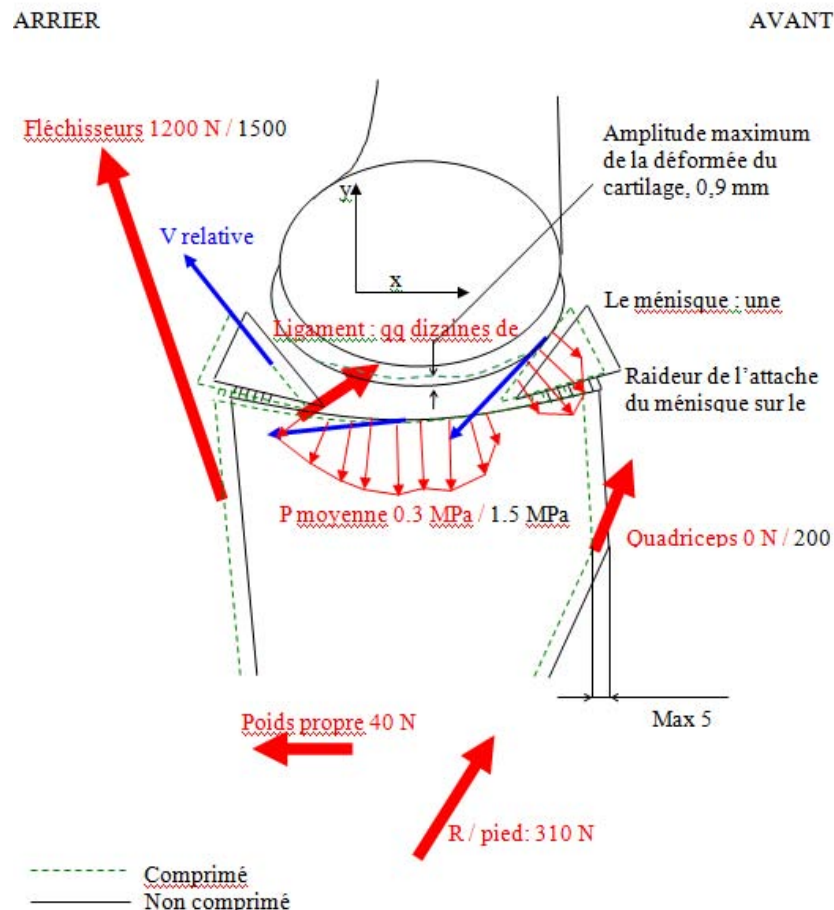


Figure 9. Schéma d'ensemble du rôle du mécanisme dans les conditions du contact articulaire du genou (Avec ménisques / sans ménisque)

7. CONCLUSIONS

La bibliographie apporte de manière séparée et de façon incomplète les informations nécessaires à l'étude de la tribologie au niveau de l'articulation saine du genou. Deux grands buts ont donc été poursuivis tout au long de cette étude. Le premier but était de mieux spécifier les conditions de contact telles que les vitesses de frottement entre les surfaces de contact, les aires de contact, la pression de contact, la déformée du cartilage et les efforts musculaires.

Le second but était de mettre en relation ces éléments qui sont considérés séparément dans la bibliographie. En effet, les échelles considérées pour comprendre et analyser les différents phénomènes vont du mètre (analyse du mouvement d'ensemble comme la marche), au μm (étude tribologique du mécanisme de l'articulation).

Pour synthétiser les apports majeurs de ce travail, trois schémas ont été créés.

Le premier schéma (Figure 9) présente le rôle des différents éléments mécaniques, principalement le rôle des muscles, dans le système tribologique constitué des cartilages et des ménisques (les premiers corps), du liquide synovial (le troisième corps) et l'ensemble des muscles, des os et des ligaments (le mécanisme). Il souligne l'importance du mécanisme de l'articulation sur les conditions tribologiques du contact.

En effet, le premier rôle des muscles au niveau d'une articulation est de générer des couples internes permettant d'assurer le mouvement et/ou l'équilibre. Ce premier rôle influe sur la pression de contact qui est augmentée de manière considérable. Ainsi, la pression moyenne au niveau du contact entre les cartilages est évaluée à 1,5 MPa. Cette pression est en grande partie issue de l'action des

muscles qui compriment l'articulation. Si les actions des muscles ne sont pas considérées dans le calcul de la pression moyenne, cette pression moyenne n'est plus évaluée qu'à 0,33 MPa. Un rôle secondaire mais très probable des muscles est de modifier les positions relatives du tibia par rapport au fémur, ce qui provoque une tension du ligament croisé postérieur et une compression de la partie antérieure des ménisques (ces efforts ne sont pas évalués au cours de cette étude). Ce mouvement modifie la répartition de pression et donc les conditions du contact. Dans le cadre de notre étude, les efforts externes (poids propre de 40 N et effort de 330 N au bout du pied) appliqués au membre inférieur tendent à réduire la flexion au niveau du genou. Les fléchisseurs développent un effort de l'ordre de 1200 N pour compenser les efforts externes. Grâce à un enregistrement des efforts musculaires au cours de la compression de la jambe (grâce à un électromyogramme), il est conclu que le quadriceps est aussi actif. L'activité musculaire du quadriceps n'est pas nécessaire en terme de couple. Cette activité, qu'il nous est impossible à déterminer grâce au code de calcul utilisé pour évaluer l'activité musculaire des autres muscles, doit probablement permettre de « stabiliser » l'articulation. Ainsi, la valeur indiquée de 200 N (en opposition à 0 N), pour l'action du quadriceps est totalement arbitraire. Plus l'effort du quadriceps est important, plus l'effort des fléchisseurs doit être important pour compenser le couple interne développé par le quadriceps. Ainsi, si un effort de 200 N est considéré au niveau du quadriceps, l'effort développé par l'ensemble des muscles fléchisseurs est de 1500 N. La pression moyenne de contact est alors réévaluée à 2 MPa. La tension dans le ligament croisé postérieur et la compression de la partie antérieure des ménisques sont alors moins importantes que lorsque le quadriceps est relâché.

Les efforts extérieurs appliqués au niveau du pied sont analogues à ceux rencontrés à la fin de la phase d'appui de la marche. La flexion de la jambe n'est alors pas la même, modifiant toutes les conditions tribologiques étudiées en statique au cours de ce travail. Les vitesses relatives tangentielles exposées sur le schéma (Figure 9) sont celles de la fin de la phase d'appui, ne donnant qu'une indication des sollicitations en cisaillement que le gel synovial subit en fin de phase d'appui. La répartition de la pression de contact est influencée par l'action des muscles, mais aussi par les vitesses tangentielles relatives entre les surfaces en contact. En effet, l'étude sur les vitesses relatives tangentielles au niveau des points de contact permet de conclure à un régime de lubrification de type « squeeze » allié à un régime de type « palier » en fin de la phase d'appui, ces régimes modifiant la répartition de pression en contact. Alliée à la génération de pression par le cisaillement et l'écrasement du gel synovial, la déformée du

cartilage influe elle aussi sur la répartition de pression. Avec une amplitude de 0,9 mm pour des efforts extérieurs proches de ceux rencontrés en fin de phase d'appui, la déformée du cartilage ne peut être négligée lors de l'étude de la répartition de pression.

Les muscles précédemment cités sont activés par le système nerveux qui détient des informations sur les conditions de contact. Le second schéma (Figure 10) expose les possibles retours d'informations (jusqu'au système nerveux) sur les conditions tribologiques du contact exposées précédemment. Ainsi, la tension des ligaments articulaires (internes et externes), la tension de chaque muscle, l'effort subit par les ménisques (par l'intermédiaire de la membrane articulaire) et la pression de contact (par l'intermédiaire de la pression sanguine des vaisseaux de l'os sous le cartilage) sont connus par le système nerveux. Le système nerveux peut en retour contrôler certains paramètres (déplacements, efforts, douleur si il y a des lésions) grâce à des critères physiologiques qu'il se fixe. Ce contrôle vient influencer les mesures effectuées et surtout vient influencer les conditions précédemment exposées. Nous l'avons vu dans cette étude, les muscles, contrôlés par le système nerveux, peuvent modifier de manière importante les conditions de contact, pour une même position macroscopique enregistrée. Pour une même position statique (il est sûrement possible d'étendre cette observation au cas du mouvement), il est ainsi possible de réduire la pression de contact ou d'annuler les efforts dans les ligaments croisés et la pression de contact sur la partie antérieure des ménisques.

Ces informations engrangées par l'organisme peuvent aussi avoir des conséquences sur les propriétés mécaniques du cartilage (module d'Young, coeff. de Poisson, épaisseur), mais à plus long terme. Dans la période embryonnaire la transformation du tissu cartilagineux (le modèle d'os embryonnaire) en tissu osseux est déterminée par l'invasion des capillaires sanguins dans le tissu cartilagineux (processus d'ossification). Ce processus est stoppé au niveau articulaire par l'équilibre entre la pression mécanique exercée au niveau articulaire (par des mouvements articulaires) et la pression de perfusion des capillaires sanguins (exercée dans le processus d'ossification). Cette zone d'équilibre des pressions marque la zone du contact entre l'os et le cartilage articulaire. Cette zone est spécifique pour chaque individu et elle peut évoluer au cours de la vie en fonction de l'intensité de l'effort mécanique transmis dans l'articulation (condition physique de chaque individu). Ainsi, le manque de mouvement diminue l'épaisseur du cartilage articulaire et peut même produire une ossification complète de l'articulation dans le cas de manque de mouvement dans la période embryonnaire.

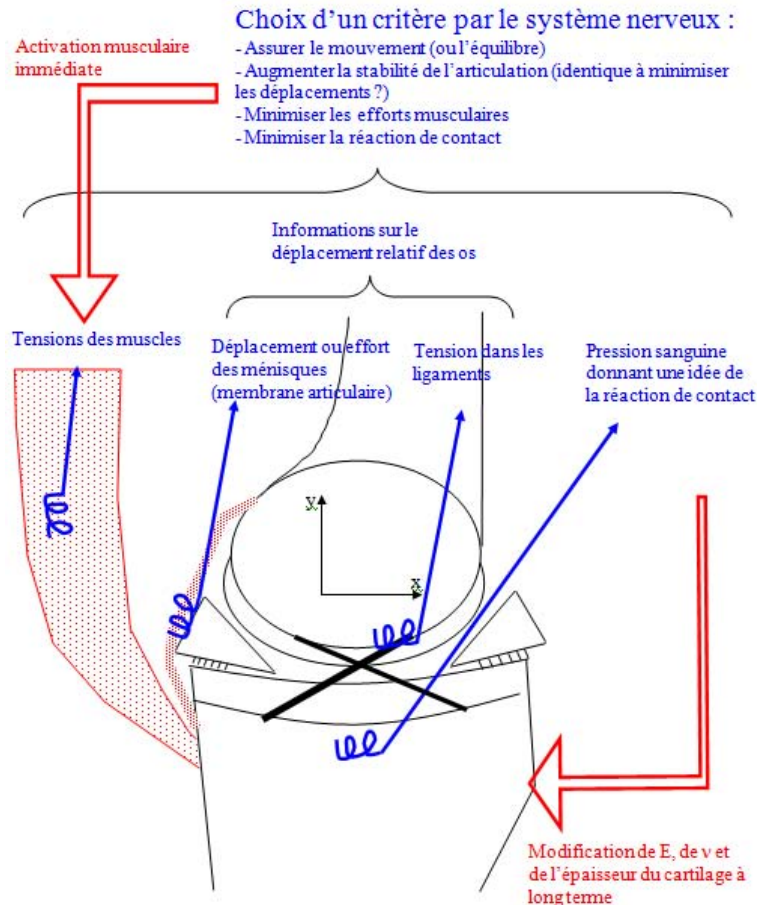


Figure 10. Schéma des retours d'informations possibles vers le système nerveux concernant les paramètres du mécanisme de l'articulation. Hypothèses sur les conséquences mécaniques possibles

De part ses ménisques et les formes complémentaires des surfaces de contact du fémur et du tibia, l'articulation du genou a une bonne conformité à l'échelle du cm. En effet, les ménisques et les formes complémentaires des os (surtout pour le condyle interne), permettent d'avoir une très bonne répartition de la pression. Les courbures des surfaces de contact sont alors de l'ordre de quelques cm (4 à 8 cm). L'étude du contact entre les cartilages doit s'intéresser à des échelles plus petites. A ce niveau, il a été montré au que le cartilage se déforme de manière importante, jusqu'à 0,9 mm de diminution de l'épaisseur lors d'une compression de l'ordre de 1500 N sur l'articulation.

Une hypothèse qui peut expliquer ces fortes déformations calculées est la structure même du cartilage qui pourrait se déformer de manière importante sans développer des pressions importantes au niveau de sa surface. Cette hypothèse permettrait d'accommoder les différences de géométrie entre les surfaces en opposition jusqu'à quelques dixièmes de mm, toujours dans le but de répartir au mieux la pression. Par exemple, au niveau des bords internes des ménisques, le cartilage du fémur peut se déformer pour s'accommoder à la

marche que représente le bord du ménisque (marche de quelques dixièmes de mm).

A l'échelle du μm , prise en compte grâce au travail en cours au sein du LaMCoS sur la compréhension du fonctionnement tribologique d'une articulation saine (Ana-Maria Sfarghiu), la conformité du contact est assurée par la formation de « sacs ou de poches » de gel synovial permettant d'assurer une continuité de la pression malgré la rugosité du cartilage.

Ces trois échelles différentes concernant la conformité du contact permettent une répartition très efficace de la pression de contact, limitant à long terme l'usure (Voir Figure 11).

Un autre aspect de cette étude a été l'exploration de techniques permettant de retirer des informations grâce aux images du scanner (ou de l'IRM). Grâce à ces images, les bras de levier des muscles, pour une certaine position du membre inférieur, ont été évalués in vivo avec une bonne précision. L'amplitude de la déformée maximale du cartilage a elle aussi été évaluée in vivo : Cette technique permettra dans les années à venir, avec l'amélioration de la résolution des images, de connaître in vivo et sans perturber le contact les déformations de chaque élément de l'articulation.

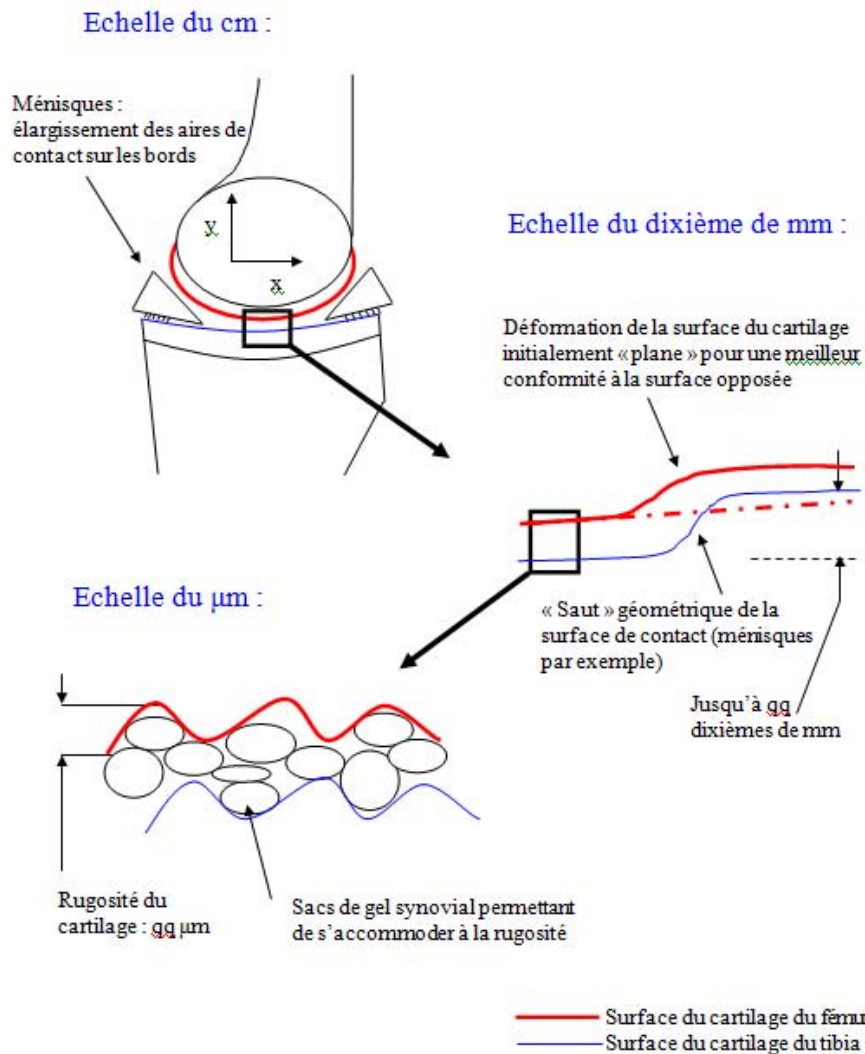


Figure 11. Les trois échelles importantes assurant la conformité du contact pour une articulation saine

ACKNOWLEDGEMENT

Les auteurs remercient vivement Mme Laurence Chèze (LBMH), Monica Cretan, Alice Bonnefoy, dr. Xavière Rivière et son équipe de radiologie (Hôpital Lyon Sud), Lionel Lafarge (INSA de Lyon) pour l'aide précieux apporté à cette étude.

REFERENCES

1. **Adriacchi, O. Dyrby**, 2005, "Interactions Between Kinematics and Loading During Walking for the Normal and ACL Deficient Knee," *Journal of Biomechanics*, Vol. 38.
2. **Adriacchi, O. Dyrby**, 2004, "Secondary Motions of the Knee During Weight Bearing and Non-Weight Bearing Activities," *Journal of Orthopaedic Research*, Vol. 22.
3. **Ahmed, Burje**, 1983, "In-vitro Measurement of Static Pressure Distribution in Synovial Joints--Part I: Tibial Surface of the Knee," *J Biomech Eng.*
4. **Bassey et al.**, 1997, "Relations Between Compressive Axial Forces in an Instrumented Massive Femoral Implant, Ground Reaction Forces, and Integrated Electromyographs from Vastus Lateralis During Various 'Osteogenic' Exercises," *Journal of Biomechanics*, Vol. 30.
5. **Beillas et al.**, 2004, "A New Method to Investigate In Vivo Knee Behaviour Using a Finite Element Model of the Lower Limb," *Journal of Biomechanics*, Vol. 37.
6. **Bergmann et al.**, 2001, "Hip Contact Forces and Gait Patterns from Routine Activities," *Journal of Biomechanics*, Vol. 34.
7. **Brewer Robin**, 2002, *Reconstitution du fonctionnement du genou naturel et artificiel*, DEA au LaMCoS / CHU Lyon Sud.

8. **Cheng et al.**, 2001, "The Influence of Inserting a Fuji Pressure Sensitive Film Between the Tibiofemoral Joint of the Knee Prosthesis on the Actual Contact Characteristics," *Clinical Biomechanics*, Vol. 16.
9. **Clair David**, 2000, *Analyse et modélisation des effets mécaniques dans le processus d'usure par impacts / glissements. Application à des contacts de géométrie conforme*. Thèse au LMC (actuel LaMCoS).
10. **Colloud Floren**, 2003, *Modélisation dynamique du rameur lors d'exercices réalisés sur ergomètres d'aviron. Implications pour l'entraînement*, thèse dirigée par Laurence Chèze UCB 1.
11. **Doriot Nathalie**, 2001, *Modélisation dynamique du membre inférieur pour l'estimation des forces articulaires et musculaires mises en jeu pendant la phase d'appui de la marche*, Thèse UCBL 1 sous la tutelle de Laurence Chèze.
12. **Duda and Taylor et al.**, 2004, "Tibio-Femoral Loading During Human Gait and Stair Climbing," *Journal of Orthopaedic Research*, vol. 28.
13. **Fleisig et al.**, 1998, "An Analytical Model of the Knee for Estimation of Internal Forces During Exercise," *Journal of Biomechanics*, vol. 31.
14. **Freeman et al.**, 2005, "The movement of the normal tibio-femoral joint," *Journal of Biomechanics*, Vol. 38.
15. **Gautier Thomas**, 1997, *Adaptation du modèle d'analyse quantifiée de la marche à l'étude clinique des IMC*, Laboratoire LBMH – UCB Lyon 1, 2004.
16. **Glitsch et al.**, "The Three-Dimensional Determination of the Internal Loads in the Lower Extremity," *J. Biomechanics*, Vol. 30.
17. **Haut Donahue et al.**, 2002, "How the Stiffness of Menisci Attachments and Meniscal Material Properties Affect Tibio-Femoral Contact Pressure Computed Using a Validated Finite Element Model of the Human Knee Joint," *Journal of Biomechanics*, Vol. 36.
18. **Hobatho et al**, 1998, "In Vivo Determination of Contact Areas and Pressure of the Femorotibial Joint Using Non-Linear Finite Element Analysis," *Clinical Biomechanics*, Vol. 13.
19. <http://catalog.nucleusinc.com>: site commercial d'images d'anatomie.
20. **Huiskes et al.**, 1997, "An Inverse Dynamics Modelling Approach to Determine the Restraining Function of the Human Knee Ligament Bundles," *J. Biomechanics*, Vol. 30.
21. **Iwaki et al.**, 2000, Tibio-Femoral Movement 1: The Shapes and Relative Movements of the Femur and Tibia in the Unloaded Cadaver Knee: Studied by Dissection and MRI," *Journal of Bone and Joint Surgery*, Vol. 82B.
22. **Johal et al.**, 2004, "Tibio-Femoral Movement in the Living Knee. A Study of Weight Bearing and Non-Weight Bearing Knee Kinematics Using 'Interventional' MRI," *Journal of Biomechanics*, Vol. 37.
23. **Kapandji**, 1965, *Physiologie articulaire: schémas commentés de mécanique humaine*. 2; Membre inférieur. Maloine.
24. **Komistek et al.**, 2004, "Knee Mechanics : A Review of Past and Present Techniques to Determine In Vivo Loads," *J. Biomechanics*, Vol. 38.
25. **Kurosawa, Fukubayashi, Nakajima**, 1980, "Load-Bearing Mode of the Knee Joint: Physical Behaviour of the Knee Joint With or Without Menisci," *Clin Orthop*, Jun.
26. **Li et al.**, 2004, "In Vivo Tibiofemoral Contact Analysis Using 3D MRI-Based Knee Models," *Journal of Biomechanics*, Vol. 37.
27. **Lu et al.**, 1998, "Validation of a Lower Limb Model With In Vivo Femoral Forces Telemetered from Two Subjects," *Journal of Biomechanics*, Vol. 31.
28. **Mahfouz et al.**, "In Vivo Determination of the Normal and Anterior Cruciate Ligament-Deficient Knee Kinematics," *Journal of Biomechanics*, 2004
29. **Majumbar et al.**, 2004, "A Three Dimensional MRI Analysis of the Knee Kinematics," *Journal of Orthopaedic Research*, Vol. 22.
30. **Maquet, Van de Berg, Simonet**, 1975, "Femorotibial Weight-Bearing Areas. Experimental Determination," *J Bone Joint Surg Am.*, Sep.
31. **McCarthy et al.**, 1999, "Knee Cartilage Topography, Thickness, and Contact Areas from MRI: In-Vivo Calibration and In-Vivo Measurements," *Osearthristis and Cartilage*, Vol. 7.
32. **McPherson et al.**, 2004, "Imaging Knee Motion Using MRI, RSA/CT and 3D digitalization," *Journal of Biomechanics*, Vol. 37.
33. **Pandy et al.**, 1997, "A Musculoskeletal Model of the Knee for Evaluating Ligament Forces During Isometric Contractions," *J. Biomechanics*, Vol. 30.
34. **Pinskerova et al.**, 2001, The Shapes and Relative movements of the Femur and Tibia in the Unloaded Cadaver Knee: A Study Using MRI as an Anatomic Tool. Chapter 10. In: Insall, J. Scott, W.N. (Eds), "Surgery of the Knee", Edition Saunders.
35. **Ramsey et al.**, Tibiofemoral contact points relative to flexion angle measured with MRI, *Clinical Biomechanics*, Vol. 17, 2002.
36. **Rotat François**, 2005, Rapport de projet de fin d'étude effectué au sein du département de l'INSA génie mécanique et conception.
37. **Scarvell et al.**, 2004, "Comparison of Kinematics in the Healthy and ACL Injured Knee Using MRI," *Journal of Biomechanics*, Vol. 38.
38. **Scarvell et al.**, 2004, "Evaluation of a Method to Map Tibiofemoral Contact Points in the Normal Knee Using MRI," *Journal of Orthopaedic Research*, Vol. 22.
39. **Shelburn et al.**, 2004, "Pattern of Anterior Cruciate Ligament Force in Normal Walking," *Journal of Biomechanics*, Vol. 37.

- 40. Shirazi-Adl et al.**, 1995, "Biomechanics of the Human Knee Joint in Compression: Reconstruction, Mesh Generation and Finite Element Analysis," *The Knee*, Vol. 2.
- 41. Shrive, O'Connor, Goodfellow**, 1978 ;
- 42. Taylor S.J.G.** et al., 2001, "Forces and Moments Telemetred from Two Distal Femoral Replacements During Various Activities," *Journal of Biomechanics*, Vol. 34,.
- 43. Thambyah et al.**, 2004, "Contact Stresses in the Knee Joint in Deep Flexion," *Medical Engineering and Physics*.
- 44. Thambyah et al.**, 2005, "Estimation of Bone-on-Bone Contact Forces in the Tibiofemoral Joint During Walking," *The Knee*.
- 45. Walker PS, Erkman MJ.**, 1975, The Role of the Menisci in Force Transmission Across the Knee, *Clin Orthop*.
- 46. Walsh et al.**, 1999, "An Improved Method for Measuring Tibiofemoral Contact Areas in Total Knee Arthroplasty: A Comparison of K-Scan Sensor and Fuji Film," *Journal of Biomechanics*, Vol. 32.
- 47. Wang et Walker**, 1974 ;
- 48. Wo et al.**, 1991, Tibial meniscal dynamics using three-dimensional reconstruction of magnetic resonance images.
- 49. Woo et al.**, 1997, "Biomechanics of the ACL: Measurements of In Situ Force in the ACL and Knee Kinematics," *The Knee*, vol. 5.
- 50. You et al.**, 2001, "In Vivo Measurement of 3D Skeletal Kinematics from Sequences of Biplane Radiographs: Application to Knee Kinematics," *IEEE Transactions on Medical Imaging*.

M.C. CORNECI^{1,2}e-mail: magdalena-carla.corneci@insa-lyon.fr**A.-M. TRUNFIO-SFARGHIU¹****F. DEKKICHE^{3,4}****Y. BERTHIER¹****M.-H. MEURISSE¹****J.-P. RIEU³****M. LAGARDE⁵****M. GUICHARDANT⁵**

¹Laboratoire de Mécanique des Contacts et des Structures, INSA-Lyon, CNRS UMR5259, F69621 Villeurbanne Cedex, **FRANCE**

²Université Technique "Gh. Asachi", Faculté de Mécanique, 700050, Iasi, **ROUMANIE**

³Laboratoire de Physique de la Matière Condensée et Nanostructures, Université Claude Bernard Lyon 1, CNRS UMR5586, F69622 Villeurbanne Cedex, **FRANCE**

⁴Département de Chimie, Faculté de Sciences exactes. Université Mentouri Constantine (25000), **ALGERIE**

⁵Institut Multidisciplinaire de Biochimie des Lipides, INSERM / INSA de Lyon, UMR870, F69621, Villeurbanne, **FRANCE**

PHOSPHOLIPIDES DANS LE FLUIDE SYNOVIAL - INFLUENCE SUR LE FONCTIONNEMENT TRIBOLOGIQUE DES ARTICULATIONS SYNOVIALES PATHOLOGIQUES

Des études récentes ont montré le rôle des assemblages lipidiques associées à la structure discontinue du fluide synovial dans les performances du fonctionnement tribologique d'une articulation saine. Dans le cas des pathologies articulaire, ce fonctionnement est modifié. Ce travail cherche ainsi à identifier l'influence de la variation en composition lipidique des fluides synoviaux pathologiques sur le fonctionnement tribologique des articulations synoviales atteintes de différentes pathologies (arthrite, arthrose)

Keywords: biotribology, synovial joints, phospholipids, lipidomic analysis

1. INTRODUCTION

Les recherches de ces dernières années ont proposé différents types de substances en tant que responsables (seules ou ayant une action synergique) pour la lubrification au niveau des articulations synoviales caractérisées par un frottement bas et une usure réduite. On peut mentionner : l'acide hyaluronique (HA) [1], la lubricine [2-4], le cartilage, qui attire les têtes hydrophiles des phospholipides [5] (en utilisant la chromatographie sur couche mince (CCM), Hills avait conclu que la phosphatidyl-choline (PC) est le plus abondant phospholipide qu'on trouve sur la surface du cartilage articulaire en y format des structures empilées [6,7]), les proteoglycans de type PRG4 [8], les SAPLs [2]. Ces composants sont synthétisés au niveau de fluide synovial par les synoviocytes : PGL4 [9], SAPL [2], HA [10], les chondrocytes [11].

En tant que fluide biologique, le fluide synovial est un ultrafiltrat de plasma, concentrée à travers la membrane synoviale.

L'équilibre (l'homéostasie) entre la production des composants de fluide synovial et leur filtration au niveau de la membrane synoviale assure le comportement tribologique remarquable des articulations saines, constituant des systèmes ayant une usure réduite et un frottement bas au niveau du contact articulaire.

Pourtant, dans le cas des pathologies articulaires (l'arthrite, l'arthrose ainsi que le remplacement d'une articulation non fonctionnelle par un implant articulaire) on constate une augmentation du frottement au niveau du contact articulaire ainsi que l'usure des surfaces de cartilage qui est accompagnée par une altération des caractéristiques biochimiques du fluide synovial, notamment de sa composition lipidique.

Dans le cas de l'arthrose, l'usure des cartilages a été corrélée entre autre avec des dysfonctionnements biologiques dus à l'activation de la phospholipase A2 qui modifie la structure macromoléculaire du fluide synovial en détruisant ses assemblages lipidiques, ce qui modifie leur

comportement mécanique et par conséquent celui de l'articulation synoviale.

D'autres marqueurs des dysfonctionnements biologiques (ex. léucotriène de type LTB4 et prostaglandine de type 5-HETE dans les cas d'inflammation) ont été identifiés dans l'articulation arthrosique.

Même si les études ont montré que les phospholipides sont les composants majeurs contribuant à la lubrification au niveau de cartilage articulaire [14,15], il n'y a pas beaucoup d'étude s'intéressant à la nature des différentes classes de phospholipides présents au niveau des articulations synoviales (liées à la surface de cartilage articulaire ou bien dans la composition du fluide synovial). Cette étude est donc menée afin d'analyser le contenu en phospholipides présentes dans différentes classes de fluides synoviaux pathologiques. Des contraintes d'éthique médicale nous ne permettent pas d'avoir accès pour ces études à des échantillons de fluide synoviaux sains.

Les différentes classes de phospholipides ont été identifiées et quantifiées en utilisant la chromatographie gazeuse (GC) en couplage avec la chromatographie sur couche mince (CCM).

En vingt ans, la pratique médicale a constaté un accroissement des maladies articulaires de plus de 30%. Leurs traitements supposent soit l'utilisation de médicaments soit l'intervention chirurgicale pour mettre en place des prothèses articulaires dont la durée de vie in vivo est au maximum de 10 ans, alors que la durée de vie d'une articulation saine est d'environ 70 ans.

Des études récentes [12] considèrent que cette différence peut-être due aux conditions d'essais ex vivo, qui généralement ne respectent pas suffisamment la réalité biologique complexe. En effet la plus parte des pathologies articulaires sont traitées en essayant d'améliorer les constats cliniques. Si cette démarche donne des résultats assez satisfaisants pour les pathologies simples, les

résultats satisfaisants sont en nombre limité pour le cas des pathologies complexes au niveau des contacts frottants biologiques et cela parce que dans ces cas il y a plusieurs composants qui doivent être considérés.

Lors d'une pathologie articulaire, c'est tout le triplet tribologique qui est soumis à des dysfonctionnements biologiques. Si ces dysfonctionnements sont à nos jours de mieux en mieux diagnostiqués individuellement, ils en restent encore des difficultés expérimentales in vivo qui rendent assez difficile la prédiction de leurs effets couplés ainsi que l'identification des éléments du triplet tribologique qu'ils affecteront. Cette situation fait que souvent un traitement n'intervient que sur un effet intermédiaire sans même parfois traiter le bon élément du triplet. Pour remédier cette situation, il faut donc optimiser les traitements pour cibler l'élément du triplet tribologique dans lequel il faut contrôler la libération du bon principe actif. Pour ce faire, dans cet étude on cherche à reproduire ex vivo les pathologies articulaires afin d'optimiser leurs traitements. Pour cela, on utilise le modèle tribologique *ex-vivo* réaliste [13] qui prend en compte le comportement biologique complexe d'une articulation (cartilage et fluide synovial) (Figure 1).

Ce modèle a permis de mettre en évidence le rôle des assemblages lipidiques, associés à la structure discontinue du fluide synovial (Figure 2), qui assurent les performances tribologiques du fonctionnement articulaire sain. De plus, il respecte les structures moléculaires et les interactions entre les éléments du triplet tribologique - cet à dire le mécanisme (le fonctionnement articulaire saine, simplifié avec une vitesse de glissement très faible, permettant d'exacerber le rôle de 3^{ème} corps), les 1er corps (reproduisant ex vivo les caractéristiques du cartilage articulaire sain (hydrogels type HEMA), et le 3ème corps (reproduisant d'une manière réaliste la structure et la composition du fluide synovial sain).

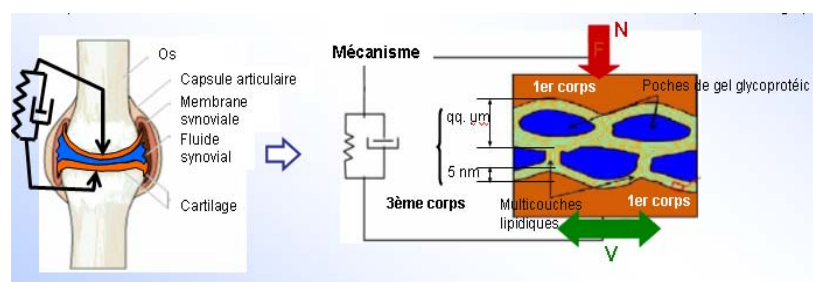


Figure 1. Modèle ex vivo réaliste de la lubrification articulaire [12]

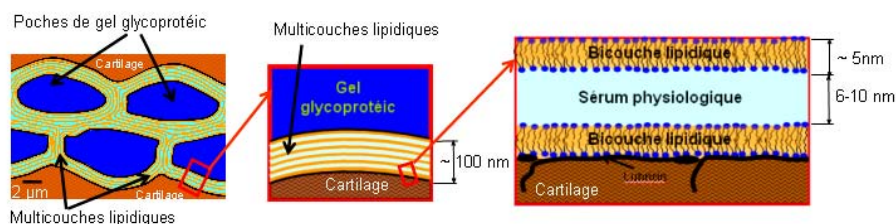


Figure 2. Assemblages lipidiques dans la structure discontinue du fluide synovial [12]

Dans le cas d'une pathologie articulaire de type arthrite on a une inflammation du fluide synovial accompagnée d'une baisse locale de pH, ce qui favorisent l'augmentation du coefficient de frottement et des endommagements locale qui détermineront l'usure du cartilage, la principale caractéristique d'une arthrose qui nécessite pour son traitement la mise en place d'une prothèse. Vu ces changements au niveau d'une articulation pathologique on peut distinguer des paramètres des dysfonctionnements pathologiques à introduire dans le modèle *ex vivo* existant: mécaniques, physicochimiques et biologiques.

Dans ce contexte, l'objectif de ce travail est d'adapter le modèle *ex vivo* existant en y introduisant les paramètres biologiques, physicochimiques et mécaniques des pathologies afin de simuler le fonctionnement pathologique et de comprendre le bon enchaînement cause/conséquence responsable d'une pathologie et donc de cibler son traitement aussi bien médicamenteux (pharmacologie articulaire) que prothétiques (surfaces frottantes des implants articulaires).

Il faudra donc apporter des solutions d'optimisation des traitements pour différentes pathologies articulaires et pour un meilleur fonctionnement tribologique des articulations prothésées.

2. MATERIEL ET METHODE

Pour arriver à proposer des solutions d'optimisation des traitements des pathologies articulaires il est nécessaire de faire des études biologiques pour déterminer les variations de la composition lipidique [13] et la destruction d'assemblages lipidiques par des actions enzymatiques associés aux pathologies articulaires.

Pour cela, la composition lipidique/biologique « réelle » de ces assemblages lipidiques, dans le cas de pathologies articulaires ou en présence d'une prothèse ont été déterminées en utilisant des analyses lipidomiques de fluides synoviaux caractéristiques pour différentes pathologies articulaires (collaboration avec l'Institut Multidisciplinaire de Biochimie des Lipides, INSA de Lyon, France) [16].

a. Lipides analysés : phosphatidylcholine (PC), phosphatidyléthanolamine (PE) et phosphatidylinositol + phosphatidyl sérine (PI + PS)

Extraction lipidique : On a fait la séparation des lipides en différentes classes : phospholipides, mono- et di-glycérides, cholestérol, acides gras libres, triglycérides et esters de stérol par chromatographie sur couche mince (CCM) ensuite la séparation des différentes classes de phospholipides : PE, PC, PI, PS. Ensuite, par transestérification de ces fractions on a fait l'analyse de

leur contenu en acides gras par chromatographie gazeuse couplée à la spectrométrie de masse.

b. Lipides médiateurs de l'inflammation

L'infiltration des leucocytes entraîne la formation de leucotriènes et en particulier du leucotriène B₄ (LTB₄) formé à partir de l'acide arachidonique (20:4n-6). Ce dernier est libéré par activation de la phospholipase A₂ lors de l'inflammation et devient substrat de la 5-lipoxygénase pour former les leucotriènes et l'acide 5-hydroxy-eicosatétraénoïque (5-HETE). LTB₄ et 5-HETE ont été extraits du liquide synovial, puis mesurés par chromatographie liquide à haute performance (HPLC).

Ces deux marqueurs ont été validés dans de nombreux modèles inflammatoires [15-17]. Ils permettront dans les études cliniques de déterminer si la prothèse est bien acceptée par le patient. Ils pourront aussi être utilisés pour vérifier l'efficacité de médicaments anti-inflammatoires.

Quatre types de fluides synoviaux pathologiques ont été analysés :

- fluide synovial suite au décèlement et remplacement d'un implant articulaire (I) ;
- fluide synovial dans le cas d'une arthrose « localisée » (AL) ;
- fluide synovial dans le cas d'une arthrose « localisée » accompagnée d'une infection (ALI) ;
- fluide synovial dans le cas d'un patient manifestant une arthrose « généralisée » (AG).

c. Préparation des échantillons biologiques (dans chaque éprouvette on a 1 ml fluide synovial)

À l'hôpital, des précautions s'imposent : il faut utiliser seulement des récipients en verre, jamais de « plastique » ; de plus la solubilisation de la synovie se fait « sur place » dans des éprouvettes en verre contenant chaque une : 3 ml éthanol, 0.15 ml deferoxamine (agent hémolytique, 15 μmol final, M=656.79g/mol), 0.5 ml butylhydroxytoluène - BHT (antioxydant, 5mmol final, M=220.35g/mol) et ensuite le transport au laboratoire se fait dans les plus brefs délais dans une boîte de glace carbonique (-20°C). Une fois arrivé au laboratoire on ferme sous azote et on stock les échantillons à -20°C jusqu'au moment quand on continue l'analyse lipidomique, c'est à dire l'extraction et quantification des lipides;

Extraction lipidique

Les lipides sont extraits [18] à l'aide d'un mélange éthanol/chloroforme (3/6, v/v) contenant du BHT à la concentration finale de 5.10⁻⁵ M, en milieu acide (pH = 3) (à l'aide d'acide acétique glaciale). On utilise comme standard interne du 100 μl PC (10mg/ml) et 50 μl PE (1mg/ml) ajoutés dans chaque tube.

Les lipides sont extraits selon la méthode de Bligh et Dyer (1959) par le mélange

chloroforme/méthanol (1/2 ; v/v) en présence de BHT (5.10-5M). Après fermeture sous azote, vortex et centrifugation (5 min, 25°C, 1800torr/min) le mélange se sépare en deux phases. La phase aqueuse est récupérée et transférée dans un autre tube, ensuite évaporée sous jet d'azote ; une deuxième extraction est effectuée et les phases organiques obtenues sont réunies puis évaporées à sec et conservées sous azote à -20°C. On ajoute de nouveau 3ml éthanol et 6 ml de chloroforme et l'échantillon est de nouveau centrifugé ensuite le surnageant (la phase supérieure) est récupéré et la phase restante est ré extraite 2 fois comme précédemment.

Séparation par CCM (en phospholipides totaux, marqueurs d'oxydation)

Les extraits lipidiques (évaporées à sec sous azote) sont reprises dans un faible volume du mélange méthanol/chloroforme (1/2, v/v) (250µl) pour être déposées sur une plaque de silice de chromatographie en couche mince (CCM). Les standards de migration sont déposés simultanément à raison de 10µl LTB4 et 8 µl 9-HODE. La séparation des lipides est effectuée par migration dans le système de solvants : n-héxane : diéthyl éther : acide acétique glaciale (25 :75 :1, v/v/v). Après la séparation, et le séchage des plaques, la révélation des standards de migration se fait par vaporisation de phosphomolibdate puis chauffage de la plaque à 50°C.

La zone de silice correspondant au dépôt est située à la même hauteur que le standard de migration plus 1 cm au dessus et au dessous. Les bandes de silice correspondant aux phospholipides totaux et aux marqueurs d'oxydation sont grattées et récupérées dans des tubes en verre à vis. La silice est réhydratée par un mélange de 2 ml méthanol : chloroforme (2/1) et ensuite 2 fois avec 2 ml chloroforme, pour les phospholipides totaux et 2 fois avec 3 ml méthanol pour les marqueurs d'oxydation afin d'extraire ces composants de la silice. Les échantillons sont centrifugés (5min, 25°C, 1800torr/min). La phase supérieure est récupérée pour préparer la séparation CCM des phospholipides totaux [19] et de l'autre coté pour préparer les échantillons pour HPLC (identification des marqueurs de stress oxydant). Les phases d'intérêt sont rassemblées et évaporées à sec sous azote.

Séparation par CCM (des phospholipides)

Les extraits de phospholipides totaux (évaporées à sec sous azote) sont reprises dans un faible volume du mélange méthanol/chloroforme (1/2, v/v) (400µl) pour être déposées sur une plaque de silice de chromatographie en couche mince (CCM). Les standards de migration sont déposés simultanément à raison de 30µl PE (1mg/ml) et 3µl PC (10mg/ml). La séparation des lipides est effectuée par migration dans le système de solvants : chloroforme : méthanol : méthyle amine aqueuse 40% (61 :19 :5, v/v/v). Après la séparation, et

séchage des plaques, la révélation des standards de migration se fait par vaporisation de dichlorofluoresceine, puis repos 5 min et puis visualisation en UV. La zone de silice correspondant au dépôt est située à la même hauteur que le standard de migration plus 1 cm au dessus et au dessous. Les bandes de silice correspondant aux phospholipides d'intérêt (PE, PC, PI+PS) sont grattées et récupérées dans des tubes en verre à vis.

Transmethylation et GC (chromatographie gazeuse)

Les acides gras sont trans méthylés en présence de 750µl mélange toluène : méthanol (2/3, v/v), 750 µl BF₃ 14% suite une fermeture sous azote, à 100°C dans une cuve thermostatique pendant 90 min. La réaction est arrêtée en plongeant les tubes dans la glace et en ajoutant 1.5 ml de carbonate de potassium (K₂CO₃) 10% afin de neutraliser le milieu. Les esters méthyliques d'acides gras ainsi obtenus sont extraits par 2ml isoocane pestipur ensuite fermeture sous azote. On applique une centrifugation (5min, 1800torr/min) et on obtient une séparation tri phasique. La phase organique supérieure est récupérée dans des tubes en verre puis évaporation à sec sous jet d'azote.

Les extraits sont repris dans un volume d'isoocane puis analysés par chromatographie gazeuse (GC) (Système de chromatographie en phase gazeuse couplée à la spectrométrie de masse (GC Hewlett Packard Séries 6890, colonne capillaire silice HP-5MS 30m x 0.25mm, gaz vecteur – hélium 0.5 bar) [20, 21].

La quantification (en nanomoles) des acides gras composants les queues hydrophobes de phospholipides est faite à l'aide des standards internes (type 17 :0 PC et respectivement 17 :0 PE) qui sont ajoutés dans les échantillons au moment de l'extraction lipidique.

3. RESULTATS

Dans le cas de pathologies articulaires, on a des changements locaux qui favorisent les ruptures par actions enzymatiques au niveau des structures lipidiques du fluide synovial donnant ainsi l'oxydation de phospholipides (PLs) qui entraîne ainsi des modifications de la composition de fluide synovial en fonction de différents types de PLs. Ces modifications ont été étudiées par une analyse lipidomique quantitative.

De l'autre coté, l'oxydation des lipides génère des marqueurs d'oxydation lipidique avec des modifications de la structure (notamment due à la perte des propriétés hydrophiles-hydrophobes des PLs qui assurent la structure discontinue du fluide synovial sain). La présence de ces marqueurs d'oxydations liée à une modification de la structure a été étudiée par une analyse lipidomique quantitative.

Les analyses sur les échantillons de fluide synovial pathologique nous ont permis d'établir par chromatographie gazeuse (GC) la composition lipidique du fluide synovial (en fonction du type de PLs ainsi que pour la composition en acides gras, saturés et non saturés, pour chaque PL identifié) (Tableau 1).

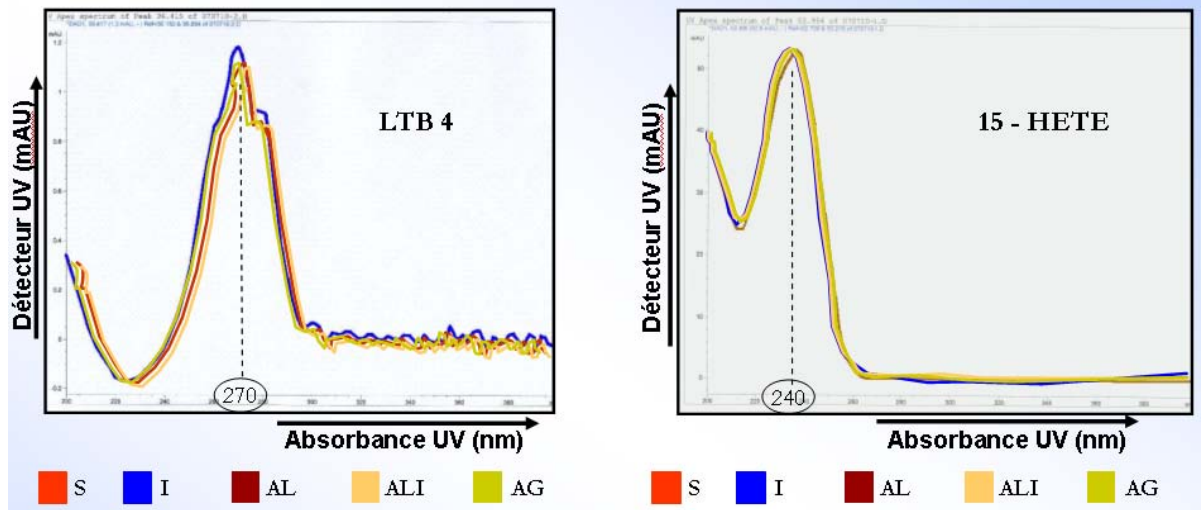


Figure 3. Médiateurs lipidiques d'inflammation (HPLC, pics caractéristiques d'adsorption)

Pour les échantillons de fluides synoviaux analysés, trois classes majeures des PLs ont été identifiées : PC, PE, PI+PS. Les quantités moyennes concernant la composition en acides gras des PLs analysés sont présentées dans le Tableau 2. En utilisant les résultats obtenus par GC, on peut constater que pour les acides gras non saturés l'acide oléique (C18 :1) est le plus abondant acide gras.

Pour le comportement tribologique articulaire, la conséquence de cette variabilité de la composition chimique des fluides synoviaux étudiés peut être identifiée d'un côté, en fonction de type de phospholipides (ayant des petites ou grosses têtes, chargés ou neutres) quand on peut avoir une modification de l'accrochage au niveau des assemblages lipidiques et de l'autre côté, en fonction de type d'acides gras constituant les queues phospholipidiques. Dans ce cas on distingue une faible (cas d'acides gras saturés, en phase solide) ou une forte (pour les acides gras non saturés, en phase fluide) mobilité des lipides à l'intérieur de ces structures et donc une modification de leur rhéologie. Ces modifications locales peuvent entraîner des modifications du comportement tribologique pour le cas des articulations synoviales pathologiques.

L'analyse des résultats obtenus ne permet d'identifier les variations pathologiques dans le cas des échantillons étudiés :

- pour le phospholipide de type PE

Par chromatographie liquide à haute performance (HPLC) de mettre en évidence la présence dans le fluide synovial de deux médiateurs lipidiques d'inflammation (Figure 3), associés aux différentes pathologies articulaires (ces médiateurs produisent la destruction enzymatique des assemblages moléculaires du fluide synovial).

On remarque une quantité plus élevée dans le cas « ALI », on a donc + des charges au niveau des assemblages lipidiques du fluide synovial ce qui entraîne une modification de l'accrochage ;

De plus, un % supérieur en acides gras non saturés (pour « ALI » et « AG ») indique une plus grande mobilité des structures lipidiques et donc une modification de la rhéologie

- pour le PC

On remarque qu'il est le phospholipide le plus abondant dans la composition de fluide synovial ; sa structure (têtes petites et neutres) ne détermine pas des modifications significatives de l'accrochage

Il y a un équilibre entre le % en acides gras saturés et celui en acides gras non saturés donc, on n'observe pas plus de changements nets des phases des assemblages lipidiques et non plus de leur rhéologie

- pour les PI+PS

On remarque une quantité plus élevée dans le cas « ALI », on a donc + des têtes + volumineuses au niveau des assemblages lipidiques du fluide synovial ce qui entraîne une modification de l'accrochage ;

Pour tous les échantillons analysés on a obtenu un % supérieur en acides gras saturés, ce qui caractérise une faible mobilité des assemblages lipidiques et donc pas de changements nets de leurs phases et leur rhéologie.

Tableau 1. Variation de la composition lipidique des fluides synoviaux pathologiques

a. en fonction de type de phospholipide

Phospholipides	« I »	« AL »	« ALI »	« AG »
PE (nanomoles)	37	53	84	78
PC (nanomoles)	434	546	588	472
PI+PS (nanomoles)	234	347	356	272

b. en fonction des acides gras saturés ou non saturés composant les phospholipides

Phospholipides	Acides gras	« I »	« AL »	« ALI »	« AG »
PE	Saturés (w%)	42	37	27	23
PE	Non saturés (w%)	53	59	68	70
PC	Saturés (w%)	52	50	48	45
PC	Non saturés (w%)	46	49	50	53
PI+PS	Saturés (w%)	62	59	61	51
PI+PS	Non saturés (w%)	37	40	38	49

Tableau 2. Composition en acides gras de principales classes de PLs présentes dans les fluides synoviaux pathologiques analysés

Acides gras	% PC total	% PE total	%PI+PS total
12:0	0,00	0,00	0,00
14:0	0,17	0,40	0,10
16:0 DMA	3,95	0,66	0,96
16:0	16,33	34,22	25,94
16:1	1,10	1,20	0,70
17:0	0,00	0,00	0,00
18:0 DMA	3,83	0,21	0,55
18:1 DMA	1,23	0,08	0,15
18:0	14,55	16,30	15,63
18:1 n-9	11,82	14,29	6,03
18:1 n-7	2,46	0,28	0,17
18:2 DMA	0,00	0,00	0,00
18:2 n-6	8,05	15,17	4,05
20:0	0,09	0,05	2,05
18:3 n-6	0,16	0,03	0,01
18:3 n-3	0,14	0,05	0,04
20:1 n-9	0,21	0,15	0,07
20:2n-6	1,55	0,35	1,17
20:3n-9	0,00	0,01	0,00
20:3 n-6	1,10	3,45	0,40
22:0	0,17	0,05	6,18
20:4 n-6	18,49	9,11	4,48
22:1	0,06	0,02	0,19
20:5 n-3	0,52	0,46	0,08
24:0	0,76	0,13	7,75
22:2n-6	1,83	0,06	1,65
22:4n-6	3,73	0,43	0,43
24:1 n-9	0,08	0,04	16,66
22:5n-6	0,33	0,11	0,01
22:5 n-3	1,93	0,48	0,75
22:6 n-3	5,38	2,23	3,82
TOTAL acides gras saturés (%)	32,06	51,15	57,65
TOTAL acides gras non saturés (%)	58,92	47,90	40,69

Le fluide synovial fait l'objet de nombreuses études cherchant à identifier les composants qui assurent la lubrification en régime limite (boundary lubrication) [5]. Il est montré dans la littérature que les PLs sont impliquées dans le mécanisme de la lubrification au niveau des articulations [2,12], des poumons [22], du péricarde [5].

Pour le comportement tribologique il est donc fort important d'analyser la lubrification en fonction des différents paramètres comme: la longueur des chaînes des acides gras, leurs orientation, les tailles des têtes hydrophiles des PLs, l'accrochage au niveau des surfaces au niveau du contact etc.

Cette étude se concentre sur la composition lipidique en PLs, par rapport à leurs chaînes d'acides gras (longueur et saturation) en utilisant des échantillons de fluide synovial pathologiques et les têtes hydrophiles (PC, PE, PI et PS).

Les principales classes de PLs identifiées étaient : PC (32 %) le composant majoritaire, et PE (20%) et Pi+PS (20%) présentes en quantités significantes. Sarma et al ainsi que Wüthier et al ont mentionnée des résultats similaires [13, 23].

Les objectifs étaient d'étudier les éventuelles modifications en composition en fonction de l'état pathologique du fluide synovial ainsi que de mettre en évidence la présence des marqueurs de stress oxydant dans la composition de fluide synovial pathologique (différentes cas cliniques ont été étudiés).

Les résultats de cet étude nous ont montré les variations de la composition lipidique de différentes fluides synoviaux pathologiques en fonction du type de phospholipide contenu ainsi qu'en fonction des acides gras formant leurs queues phospholipidiques (par analyse en GC et HPCL).

Cela nous permet maintenant de reproduire *ex-vivo* les variations de ces compositions et donc d'étudier par la suite l'influence de ces variations sur l'accrochage et sur la rhéologie dans le cas des fluides synoviaux pathologiques, afin de déterminer les modifications du fonctionnement tribologique articulaire pathologique.

Par la suite ces résultats nous permettront de reproduire *ex-vivo* et de manière réaliste, les pathologies articulaires afin de comprendre au cours des essais tribologiques utilisant ce modèle les différents comportements et l'évolution tribologique des assemblages lipidiques en fonction des pathologies.

4. CONCLUSIONS ET PERSPECTIVES

L'analyse lipidomique nous a permis d'identifier les variations de la composition et les modifications de la structure pour le cas des fluides synoviaux pathologiques ; on connaît donc maintenant les paramètres de dysfonctionnements pathologiques qui caractérisent le modèle *ex vivo* des

pathologies articulaires. L'exploitation de ce modèle au cours des études *ex vivo* nous permettra de comprendre l'enchaînement causes (pathologies) conséquences (symptômes) dans le but de proposer des solutions d'optimisation des traitements pour les pathologies articulaires (médicaments et/ou implants)

En conclusion, PC (32%), PE (20%), PI+PS (20%) sont les trois principales classes de PLs présentes dans le fluide synovial pathologique. Avec le PC en tant que constituant prédominant. De plus, cette étude a montré la présence d'un mélange des acides gras au niveau des queues lipidiques des PLs analysées, avec un % supérieur pour les acides gras non saturés (59%) par rapport aux acides gras saturés (32%).

En pratique, pour traiter efficacement l'arthrose après avoir identifié chaque dysfonctionnement biologique, il faut en connaître les effets mécaniques et physicochimiques afin de pouvoir développer des médicaments capables:

- d'agir principalement sur l'élément du triplet tribologique qui est la cause de la pathologie,
- d'être efficaces dans des conditions physicochimiques variables, imposées par l'évolution de la maladie.

Des études supplémentaires seraient nécessaires pour avoir une caractérisation détaillée de l'interaction des phospholipides au niveau de la surface de cartilage, permettant ainsi une meilleure compréhension sur la lubrification et les mécanismes de frottement. Cela pourrait inclure la quantification séparément des autres espèces moléculaires de type PL, la quantification de la sphingomyéline et du cholestérol, sachant que leur présence influence la mobilité des assemblages moléculaires contenant les lipides, l'orientation des lipides dans les liposomes pour avoir une information sur l'orientation au niveau des surfaces d'accrochage, l'étude des interactions lipides –protéines et la modélisation moléculaire pour estimer l'assemblage ainsi que l'orientation des PLs au niveau des bicouches.

5. REMERCIEMENTS

Les auteurs veulent remercier au collectif du bloc opératoire « Orthopédie adultes » de l'Hôpital Edouard Herriot (Lyon), pour nous avoir fourni les échantillons de fluides synoviaux pathologiques tant nécessaires pour mener à fin cette étude.

REFERENCES

1. Hills, B.A., 1998, "Enzymatic Degradation of the Load Bearing Boundary Lubricant in Joint," *Br J Rheumatol*, 37, pp. 137-142.
2. Schwartz, I.M. and Hills B.A., 1998, "Surface-Active Phospholipide as the Lubricating Component of Lubricin", *Br J Rheumatol*, 37, pp. 21-26.

3. Furey, M. J., and Burkhardt, B. M., 1997, "Biotribology: Friction, Wear and Lubrication of Synovial Joints", *Lubr. Sci.*, 9, pp. 255–271.
4. Furey, M. J., 1997, "Exploring Possible Connections Between Tribology and Osteoarthritis," *Lubr. Sci.*, 9, pp. 273–281.
5. Hills, B.A., 1984, "Surfactants Identified in Synovial Fluid and Their Ability to Act as Boundary Lubricants", *Ann Rheum Dis*, 43, pp. 641-648.
6. Hills, B.A., 1990, "Oligolamellar Nature of the Articular Surface", *J Rheumatol*, 17, pp. 349-356.
7. Hills, B.A., 1989, "Oligolamellar Lubrication of Joints by Surface Active phospholipid", *J Rheumatol*, 16, pp. 82-91.
8. Schmid, R. et al, 2001, "Alteration of Fatty Acid Profiles in Different Pulmonary Surfactant Phospholipids in Acute Respiratory Distress Syndrome and Severe Pneumonia, *Am. J. Crit. Care Med.*, 163, pp. 95-100.
9. Jay, G.D, Britt, D.E., Cha, D.J., 2000, "Lubricin is a Product of Megakaryocyte Stimulating Factor Gene Expression by Human Synovial Fibroblasts", *J Rheumatol*, 27, pp.594-600.
10. Momberger, T.S., Levick, J.R., and Mason, R.M., 2005, "Hyaluronan Secretion by Synoviocytes is Mechanosensitive", *Matrix Biol*, 24, pp.510-519.
11. Schumacher, B.L., Block, J.A., Schmid, T.M., 1994, "A Novel Proteoglycan Synthesized and Secreted by Chondrocytes of the Superficial Zone of Articular Cartilage", *Arch Biochem Biophys*, 311, pp. 144-152.
12. Trunfio-Sfarghiu, A.-M., Berthier, Y., Meurisse, M.-H., Rieu, J.-P., 2007, "Multiscale Analysis of the Tribological Role of the Molecular Assemblies of Synovial Fluid. Case of a Healthy Joint and Implants", *Tribology International*, 40, pp. 1500-1515.
13. Sarma, A. V., and Powell G. L., 2001, "Phospholipid Composition of Articular Cartilage Boundary Lubricant", *Journal of Orthopaedic Research*, 19, 671-676.
14. Blewis, M. E. et al, 2007, "Model of Synovial Fluid Lubricant Composition in Normal and Injured Joints", *European Cells and Materials*, 13, pp. 36-39
15. Gale, L.R., Chen, Y., Hills, B.A., Crawford R., 2007, "Boundary Lubrication of Joints", *Acta ortopedica*, 78, pp. 309-314.
16. Bordet J.-C., Guichardant M., Lagarde M., 1990, "Modulation of Prostanoid Formation by Various Polyunsaturated Fatty Acids During Platelet-Endothelial Cell Interactions", *Prostaglandins Leukot Essent Fatty Acids*, 39, 197-202.
17. Corneci M.C. et al., 2007, "Optimisations des surfaces frottantes des implants articulaires pour favoriser la lubrification par les assemblages lipidiques", 34TH LEEDS-LYON SYMPOSIUM ON TRIBOLOGY – SUMMER SCHOOL, Lyon.
18. <http://www.cyberlipid.org/>
19. Wolff, J.P., 1968, "Analyse des lipides et séparation des acides gras par CCM"
20. Benzaria, A., 2006, *Etude biochimique et nutritionnelle de l'effet immunomodulateur des huiles de poisson, d'olive et d'argan. Effets comparés de leurs acides gras*, Thèse : Institut National des Sciences Appliquées de Lyon, [26/02/2007], p. 105-106.
21. Goerke J, 1998, "Pulmonary Surfactant: Functions and Molecular Composition", *Biochim. Biophys. Acta*, 1408, pp. 79–89.
22. Soares, A.F., 2005, Effets du stress oxydant sur le fonctionnement des adipocytes : adiponectine et prostaglandines [En ligne]. Thèse : Institut National des Sciences Appliquées de Lyon, 2005 [04/05/2006], 130 p. Disponible sur : <http://docinsa.insa-lyon.fr/these/pont.php?id=soares>
23. Wüthier, R.E., 1968, "Lipids of Mineralizing Epiphyseal Tissues in the Bovine Fetus", *Journal of lipid research*, 9, pp. 68-78.

Ionut Cristian ROMANU
email: ionutromanucristian@yahoo.com

Emanuel DIACONESCU
email: emdi@fim.usv.ro

Department of Applied Mechanics,
University "Stefan cel Mare" of Suceava,
ROMANIA

BIOARTICULAR FRICTION

The present paper illustrates experimental investigations of bioarticular friction. The first set of experiments was conducted on a pig synovial joint and the second one investigates the friction between a spherical cap made out of cartilage and an elastic half-space. For the experimental investigations, a device was conceived and built that ensures rolling and sliding movements of the joint.

Keywords: bioarticular friction, friction coefficient, synovial joints

1. INTRODUCTION

The human body contains 143 joints that connect skeletal bones [1]. Most of these joints are synovial and represent the object of present study. Human synovial joints are subjected to various and large forces under static and dynamic loading, while executing sliding and rolling movements [2].

A joint represents the connection between two or more bones, via a fibers and ligaments. Viewed from the mechanical engineer's perspective, joints can be treated as cinematic couplings. A healthy joint must ensure a series of functions such as [3]:

- allowing bone movements in particular directions;
- ensuring low friction between contacting surfaces;
- receiving and transmitting forces;
- shock and vibration damping.

2. JOINT TYPES

The first to classify the joints into categories was Bichat [1]. Using physiological characteristics as a criterion, Bichat suggested that joints are either mobile joints (later named diarthrosis by Galien) or fixed joints (also named synarthrosis). Another type of joint can be distinguished, having less mobility, also called amphiarthrosis.

3. EXPERIMENTAL SET-UP

Experimental investigations were conducted on a joint from an approximately 250 days old pig. For preservation, the joint was kept in a container filled with 0.98% saline solution, at constant temperature and in darkness.

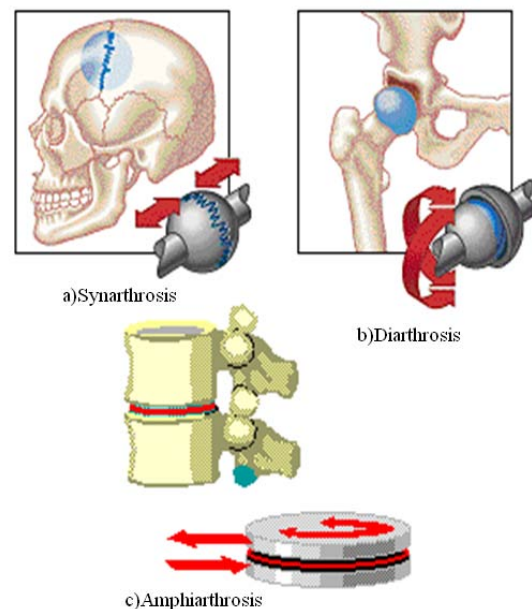


Figure 1. Types of joints: a) Synarthrosis, [2];
b) Diarthrosis, [2]; c) Amphiarthrosis, [4]

Mechanically, the joint was clamped on an adjustable arm at one end and to a stiff enough elastic lamella at the other. The elastic lamella is rigidly bound to the mobile core of an electrodynamic actuator. Once the actuator is turned on, the joint is subjected to both rolling and sliding movements.

Besides the mechanical part, ensuring joint movements, as shown in Figure 2, the experimental set-up consists of the following auxiliary components: signal generator, audio amplifier, strain indicator, oscilloscope and PC.

The devices used in the experimental installation are connected one to another as illustrated in Figure 3.

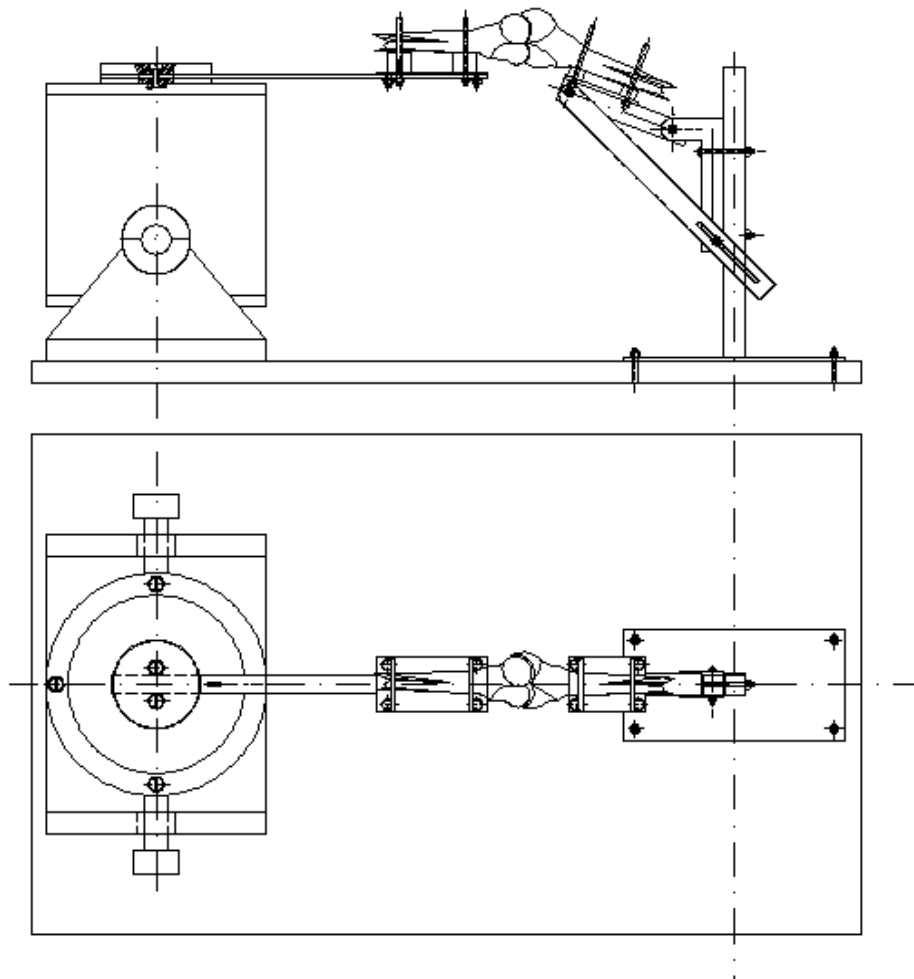


Figure 2. Experimental set-up [6]

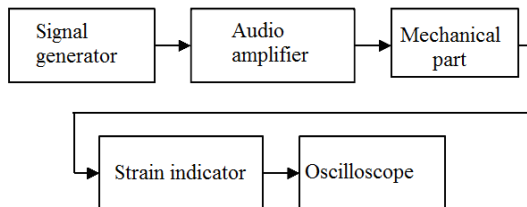


Figure 3. The connections between devices

The first step of presented experimental investigations was calibration of the measuring devices. To this end, the strain indicator was first set to indicate „0” when subjected no load, and a sinusoidal signal with a frequency of 3 Hz and an amplitude of 0.8V was programmed at the signal generator’s output. In order to quantitatively assess forces transmitted in joints, the elastic lamella was loaded using dead weights of known mass. The values indicated by the strain indicator are presented in Table 1.

After calibrating the measuring apparatus, the joint was fixed into position on the device as described before, and measurements were taken under different conditions.

Table 1. Loading device calibration values

Weight [g]	Strain indicator value [mV/V]	Equivalent load [N]
5	0.002	0.05
10	0.004	0.1
20	0.007	0.2
25	0.008	0.25
30	0.01	0.3
50	0.016	0.5
100	0.031	1
150	0.046	1.5
200	0.061	2

Experimental measurements of friction were made for several different frequencies, in the form of oscilloscope graphical charts, as the one illustrated in Figure 5.

In order to calculate joint friction, the 2Hz chart was considered. This frequency corresponds to a 1.80m tall man having an average step width of 0.8m / step, at a frequency of 2 steps / s. This means he would walk at a speed of 1.6m / s or 5.7 km / h, which represents the average speed at which a normal human is moving most of the time.



Figure 4. Joint clamped on the experimental apparatus [6]

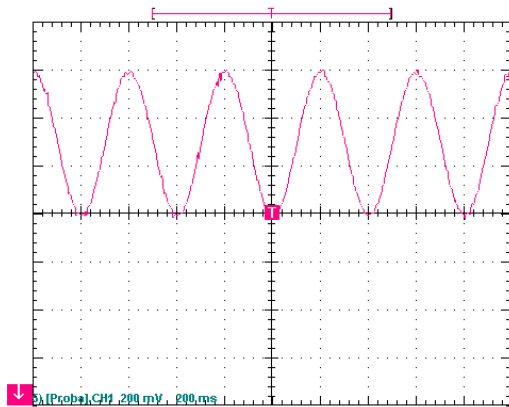


Figure 5. Friction curve at 2Hz

The graph in Figure 5 indicates that peak to peak signal amplitude is 410mV, and 205mV for a half alternation respectively. By comparing the charts with values obtained when the device was statically loaded for calibration, it is shown that for a 1N load, an output voltage of 220 mV is generated. In this manner, it is possible to graphically conclude that maximum joint friction occurs when the signal reaches a maximum. For such maximum the force can be evaluated as shown in eq. (1):

$$F_f = \frac{1 \cdot 205}{220} = 0.931N. \quad (1)$$

Thus, for a 2 Hz frequency, the friction force evaluated at 0.931N. This measured force is the result of both cartilage friction and loss due to friction between articular tissue linings.

To better assess friction force between bone ends in a joint, a second experimental rig described in [6, 7] was employed to study the contact between a bone end and a flat glass surface. The investigations are based on contact mechanics theory, according to which the contact between two spherical punches (bone ends in this case) can be replaced by the contact of an equivalent punch pressed against a half-space (represented by the glass plate).



Figure 6. Second experimental set-up [7]

The second experimental set-up consists of a mechanical part that ensures loading and movement of the bone pressed against a glass plate, strain indicator, oscilloscope and PC.

As before, the test rig was first calibrated, obtaining for the elastic lamella used in friction measurements a calibrating curve as the one shown in Figure 7.

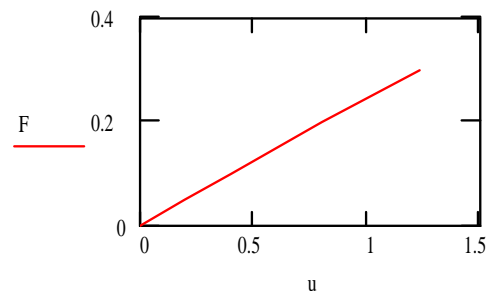


Figure 7. Elastic lamella calibration curve

In the experimental investigations, the following steps were covered:

- Cleaning the glass disc;
- Connecting the experimental device to the power supply and strain indicator;
- Interfacing oscilloscope and strain indicator;
- Calibrating strain indicator;
- Equipment functionality was checked before fixing bone end;
- Fixing bone end on the support by screw;
- Lowering the glass disc until contact with bone end is established.
- Operating the test rig, thus creating bone end movements, and recording friction charts as the one depicted in Figure 8.

The chart in Figure 5 indicates a peak to peak signal amplitude of 0.8V, value obtained during calibrations at a 20 g weight, which corresponds to a 0.2N applied force.

In order to validate the experiments, friction coefficient was calculated and compared against literature values.

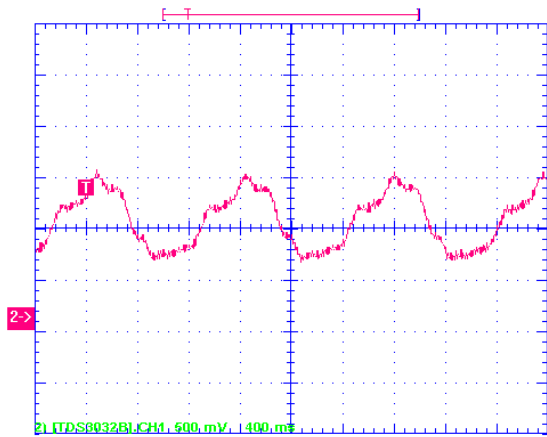


Figure 8. Friction curve at 15 N loading

Thus, for a friction force of $F_f = 0.02$ N at a $N = 15$ load, the resulting friction coefficient is:

$$\mu = \frac{F_f}{N} = 0.013. \quad (2)$$

This value was found to be close to friction coefficient values from literature.

Another set of tests involved placing water between the bone end and glass plate, thus better modeling real life lubrication conditions. A typical resulting friction curve is shown in Figure 9.

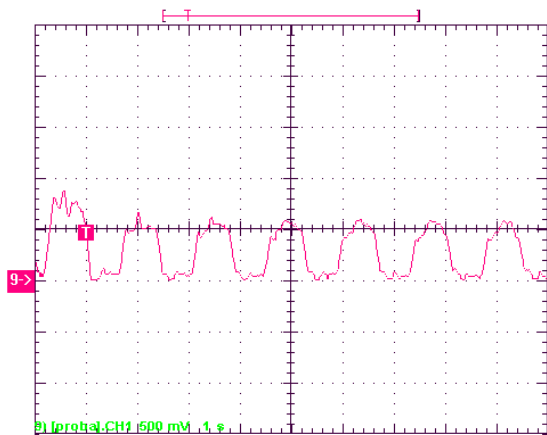


Figure 9. Friction curve (with water lubrication)

According to the chart, signal amplitude is 0.6V, which corresponds to a static load of 0.15N, leading to a friction coefficient value as follows:

$$\mu = \frac{F_f}{N} = 0.01. \quad (3)$$

From these results it can be concluded that, in the presence of a lubricating layer (in this case water), friction decreases up to 70% from its initial value. Water was chosen as lubricant because synovial fluid is 90% water.

4. CONCLUSIONS

The work reported here can be summarized by a few conclusions listed below.

- The first experiment aimed to determine joint friction without separating joint elements. Several measurements were taken at different frequencies and friction force was calculated at 2 Hz, frequency corresponding to a 1.8 m tall man walking at 5.7km per hour. For these conditions, a friction force of 0.931N was determined in the joint.

- At first glance, such friction value may seem high, but this value includes the friction between cartilage covered bone ends and that between tissues lining the joint.

- Graphical results show an increase in friction with frequency, which can be attributed to intra-articular fluid viscosity.

- For a better assessment of friction, a second test rig was employed, in which cartilage covered bone ends moves against a flat glass surface. From this second experiment, friction forces were evaluated at 0.2 N for dry contact and at 0.15N when a liquid (water) was used as lubricant respectively.

- On the second rig, measurements were taken at the same frequency (given by the motor drive of the device), but contact load varied.

- A linear dependence of friction to load was observed.

- In order to validate obtained results, friction coefficients were calculated and found to be in good agreement with literature values.

REFERENCES

1. Bichat, X., 1829, Anatomie descriptive, JS Chaudé, Paris, tome II, pp 41-44
2. Merkher, Y., Sivan, S., Etsion, I., Maroudas, A., Halperin, G., Yosef, A., 2006, A Rational Friction Test Using a Human Cartilage on Cartilage Arrangement, Parma.
3. Diaconescu, E., Glovnea, M., Bejinariu, B., 2008, "Experimental Evidence Upon Contact Behavior of Cartilage Covered Bone Ends," *Proceedings of VAREHD 14*, Suceava;
4. Furey, M.J., 1996, "Friction Wear and Lubrication of Natural Synovial Joints," *Proc. Of 12th int. Colloquium on Tribology*, 1421-1430, Esslingen.
5. Diaconescu, E., Glovnea, M., Frunza, G., 2007, Metode inovative de bio-ortopedie pentru reconstruc ia articular , (in Romanian), contract CEEX BIOART Nr. 70 / 2006, Suceava.
6. Romanu, I., 2009, *Bioarticular friction*, (in Romanian), Graduation Paper, University of Suceava.
7. Brîndu a, B., 2008, *Experimental modeling of bioarticular contacts*, (in Romanian), Graduation Paper, University of Suceava.

A.-M. TRUNFIO-SFARGHIU¹
e-mail: *ana-maria.sfarghiu@insa-lyon.fr*

M.C. CORNECI^{1,2}
Y. BERTHIER¹
M.-H. MEURISSE¹
J.-P. RIEU³

¹Laboratoire de Mécanique des Contacts et des Structures, INSA-Lyon, CNRS UMR5259, F69621 Villeurbanne Cedex, **FRANCE**

²Université Technique "Gh. Asachi", Faculté de Mécanique, 700050, Iasi, **ROUMANIE**

³Laboratoire de Physique de la Matière Condensée et Nanostructures, Université Claude Bernard Lyon 1, CNRS UMR5586, F69622 Villeurbanne Cedex, **FRANCE**

MECHANICAL AND PHYSICO-CHEMICAL ANALYSIS OF THE TRIBOLOGICAL OPERATION OF JOINT REPLACEMENTS

The aim of this work is to identify the coupled role of the biological components of synovial fluid in the remarkable tribological operation of a healthy natural joint, as well as in the friction of steel and polythene implants. It uses a realistic ex-vivo model capable of reproducing the mechanical and physicochemical characteristics of the entire tribological triplet of the joint, whether healthy or implanted. It particularly focuses on the lipidic bilayers and vesicle structures associated with synovial fluid. The analysis of the friction measurements and fluorescence microscopy images confirm the role of lipidic bilayers in maintaining a very low friction coefficient. In addition, we observe that the substitute cartilage favours the formation and maintenance of these bilayers, which is not the case of implant materials.

Keywords: synovial joint, biolubrication, molecular assemblies, lipidic bilayers, articular cartilage

1. INTRODUCTION

Over the years the growing number of osteo-articular diseases has led to the development of joint implants whose lifetimes depend on their tribological performances. In spite of sustained efforts to develop new biomaterials, the in-vivo lifetime of implants has often proven to be most deceptive when set against extrapolations performed on the basis of ex-vivo simulations. This discordance can be imputed mainly to ex-vivo tribological test conditions that are insufficiently realistic in comparison with the mechanical and physicochemical conditions of biological environments.

This is why interest has grown over the last few decades in attempting to identify and characterise the biomolecular interfaces formed during the tribological operation of healthy and implanted joints. Thus four biological components of synovial fluid have been identified as being decisive in the tribological performances of joints and certain works have attributed separate roles to them:

- albumin protects against wearing of artificial cartilage [1] and the metal surfaces of joint implants [2],
- hyaluronic acid tends to increase the viscosity of healthy synovial fluid [3] at low shear rate. But at the high shear rates encountered in synovial joints, the effect of hyaluronic acid on apparent viscosity is not significant [4].

- lubricin and other polyelectrolytes attach to the surface of healthy cartilage and modify tribological conditions under boundary regime [5,6].

- phospholipids multilayers play also an important role in the boundary lubrication regime [7,8].

However, these works have neglected the role of the multiple interactions between the components of the synovial fluid and the bodies in contact during the tribological operation of the joint. Recent research has suggested the essential tribological role of such interactions.

Under tribological stress the albumins create reticulations with the hyaluronic acid that modify the rheology of the synovial fluid [9].

The association of hyaluronic acid with lipids can form pocket and tube-like structures filled with hyaluronic acid and surrounded by lipidic multilayers [10]. Furthermore, it has been shown that such structures reduce the rheothinning effect of aqueous solutions of hyaluronic acid [11].

The "vitonectin" part of lubricin can fix lipidic bilayers on articular cartilage while its "hemopexin" part protects them against oxidation [12-14].

The healthy joint is an ultra-high performance tribological system and an essential reference for understanding the tribological operation of synovial fluid and thus aiding research aimed at improving the treatment of joint diseases and optimising implant design. Consequently, this work is based on a realistic ex-vivo model to understand the coupled role of the molecular

components of synovial fluid involved in the remarkable tribological performances of natural joints. It also examines the potential capacities of these components to improve the tribological performances of joint implants.

The ex-vivo model proposed here, and presented in section 2, is designed to reproduce the mechanical and physicochemical characteristics of the whole tribological triplet, either healthy or implanted, composed of first bodies in contact (articular cartilage and implant materials), the third body (the synovial fluid with its real biomolecular structure) which separates the first bodies, and obviously the mechanism (muscle and ligament system) which imposes local loadings. This article focuses on the boundary regime under which the effects of hydrodynamic load carrying capacity are completely negligible, and which exacerbates the role played by the interfaces.

The tribological analysis proposed in section 3 is based on optical microscopy observation of lipidic interfaces performed under white and fluorescent light, in situ through a transparent first body, and after opening the contact. The changes in the lipidic structures are correlated with the changes of the friction coefficient.

2. EX VIVO MODEL TRIBOLOGICAL TRIPLET

This section presents a model of an ex-vivo tribological triplet of a natural and implanted joint, with realistic mechanical and physicochemical parameters. We successively describe the elements making up the tribological triplet: the "first bodies" (substitute cartilage and implant material), the "third body" (substitute synovial fluid), and the "mechanism" (experimental device providing contact pressures and kinetics). The entire procedure used to define this experimental model is presented in [15].

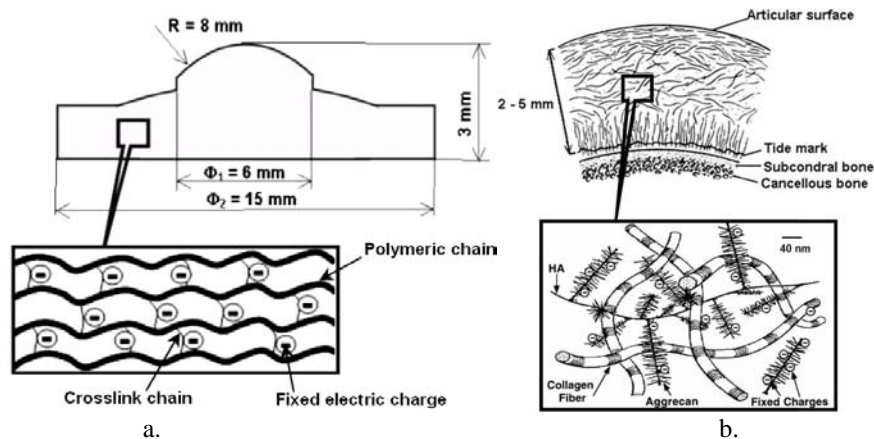


Figure 1. Schematic representation of hydrogel and cartilage structure: a) hydrogel HEMA (at macroscopic and molecular scales), b) cartilage (at macroscopic and molecular scales) from [11]

2.1 First bodies

2.1.1 Substitute cartilage

Taking samples of cartilage affects the complexity of its structure and in particular destroys the collagen membrane on its surface. What is more, it loses its living properties when subjected to long-term tribological tests, thereby leading us to seek non-living materials capable of forming a substitute joint cartilage that corresponds as much as possible to the mechanical and physicochemical properties of real cartilage. Consequently, we turned to highly hydrophilic polymeric materials like hydrogels, since cartilage contains 80% water in volume. These materials are used to repair cartilage injuries: polyalcohol vinyl (PVA) and hydroxyethyl methacrylate (HEMA) [16,17,18]. Of the latter we opted for the hydrogel HEMA used for corneal lenses, since its structure and mechanical properties are very close to those of cartilage:

HEMA hydrogel has large methacrylate polymeric chains reticulated by hydroxy-ethyl groups (Figure 1a) that are hydrophilic due to their negative HO- charges. This structure is comparable to that of cartilage which has collagen fibres reticulated by glucidic chains (aggrecan, see Figure 1b), that are hydrophilic due to their negative SO₃⁻ and COO⁻ charges..

Table 1 highlights the similitude between the mechanical properties of HEMA hydrogel after 48 hours in physiological solution and articular cartilage.

The first bodies used as substitute for joint cartilage are semi-rigid blanks of HEMA lenses (Corneal, France) whose macro-geometry has a domed part (cf. Figure 1a.), making it possible to localise the contact during the friction tests. The roughness of this contact zone is very low (Ra of a few nanometres), comparable to the one of natural cartilage compressed and flattened to nanometer levels under the pressures in human hip and knee joints [19].

Table 1. Mechanical properties of hydrogel HEMA and cartilage listed from literature values

	Hydrogel HEMA [21]	Cartilage [22]
Equilibrium compressive modulus (MPa)	0.2 – 0.9	0.5 - 1
Permeability ($m^4/N.s$) measured for a gradient of hydrostatic pressure of 21 MPa through 1 mm	$\sim 10^{-16}$	$10^{-16} - 10^{-15}$
Water content (% mass)	$\sim 25\%$	External layer $\sim 20\%$ Internal layer $\sim 70\%$

Since this hydrogel reproduces only partially the structure and some mechanical properties of the real cartilage, further on it will be called “artificial cartilage”, following the term of Murakami [20].

2.1.2 Joint implants

Two types of material used in joint implants were considered: polyethylene (UHMWPE) and stainless steel (316L). Cylindrical test pieces 15 mm in diameter and 3 mm thick had an RMS roughness of 0.1 μm for UHMWPE and 0.05 μm for stainless steel, representative of the roughness of the rubbing surfaces of joint implants.

2.2 Model of synovial third body

The model of the synovial fluid used in this study is based on histological and biophysical observations showing that synovial fluid forms vesicles (or "pockets") [23] several micrometers in diameter filled with a gel composed of hyaluronic acid and albumins (Figure 2a). According to [10], these "vesicles" are “coated” with lipidic multilayers formed by the stacking of lipidic bilayers and layers of physiological solution that can also be found at the interface between the synovial gel and the cartilage [8] (Figure 2b).

This type of structure has been reproduced ex-vivo by using recent technology derived from nanostructural physics and described below.

2.2.1 Formation of synovial gel vesicles

Synovial gel was synthesised from DPPC lipids (1,2-Dipalmitoyl-sn-Glycero-3- Phospho-

choline, 850355CP Avanti Polar Lipids), hyaluronic acid (H7630 Sigma-Aldrich) and serous albumin (A1653 Sigma-Aldrich), acquired in powder form, then placed in physiological solution, in order to obtain concentrations equivalent to those of synovial fluid.

Accumulations of lipids due to their very low solubility in aqueous solutions were eliminated by using a technique specific to the fabrication of liposomes [24]. They first consist in generating two solutions with identical volumes:

- a solution of 3 g/l lipids in a solvent composed of 90% chloroform and 10% ethanol in volume,
- a solution of 3 g/l hyaluronic acid and 20 g/l serous albumin in physiological solution.

The gel vesicles are then formed by following the procedure schematized in Figure 3, whose successive steps are as follows:

- evaporation of the solvent in nitrogen (Figure 3a) and centrifugation of the first solution causes the lipids to spread over the internal wall of a glass test tube.
- the hyaluronic acid and serous albumin solution is then added to the test tube and the resulting mixture is subjected to ultrasound for 2 minutes to trigger the formation of the vesicles, before leaving them to incubate for 48 hours at 45°C so that the vesicles incorporate the synovial gel (Figure 3b).

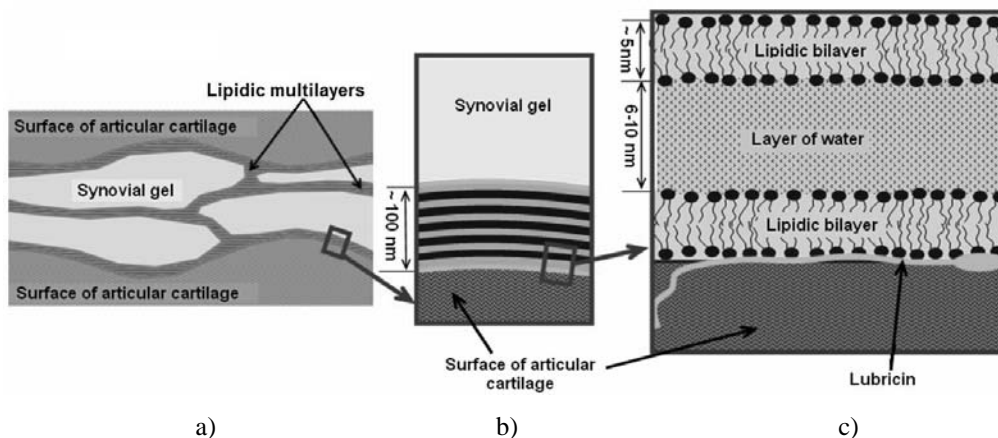


Figure 2. Schematic view of the synovial fluid : a) discontinuous structure made up of lipidic pockets filled of synovial gel (hyaluronic acid + albumine), b) lipidic multilayered structures at the interface between synovial gel and cartilage, c) detail of the lipidic multilayered structures fixed on articular cartilage by lubricin

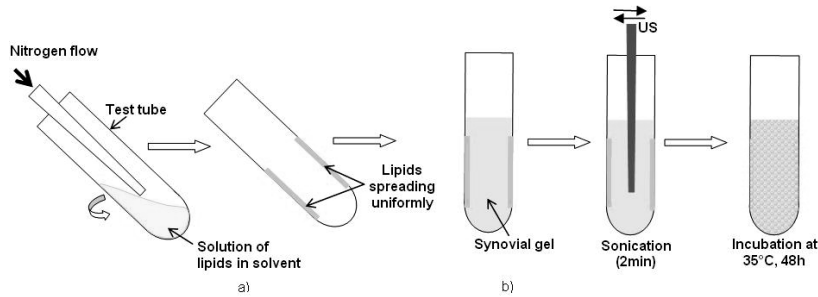


Figure 3. Procedure of formation of vesicles of synovial gel: evaporation of solvent to cover lipids on the surface of the test tube, suspension in synovial gel (hyaluronic acid + albumine), sonication to form small unilamellar vesicles and incubation to form lipid pockets filled with synovial gel (see methods for more details)

2.2.2 Adhesion of lipidic bilayers on the surface of the first bodies

To stimulate ex-vivo the multilayer properties of the interface between the first and third bodies in a healthy joint as well as possible (Figure 2b), we initiated the adhesion of lipidic bilayers on the first bodies by using a lipidic vesicle fusion method [25,26].

This first entails forming lipidic bilayers several hundred nanometres in diameter, by subjecting an aqueous suspension of 2 g/l lipids to ultrasound (at 50W power) for 5 minutes. This suspension, diluted ten times, is then used to produce the lipidic deposit.

As shown in the diagram in Figure 4, the deposit technique consists in:

- leaving the surfaces of the first bodies to incubate for 5 minutes in a diluted suspension of small lipidic vesicles, to which 2mmol/l of Ca^{++} ions were added to stimulate the vesicles to adhere and burst on the surfaces of the first bodies (Figure 4a),
- eliminating the lipidic surplus by rinsing (Figure 4b).

This technique permits obtaining model lipidic bilayers containing Ca^{++} ions. The work done by Hills [18, 22] has shown that these ions are also present in in-vivo lipidic bilayers where they stiffen the bilayer by forming ionic links with the negative parts (phosphate group) of the lipidic heads (Figure. 4c).

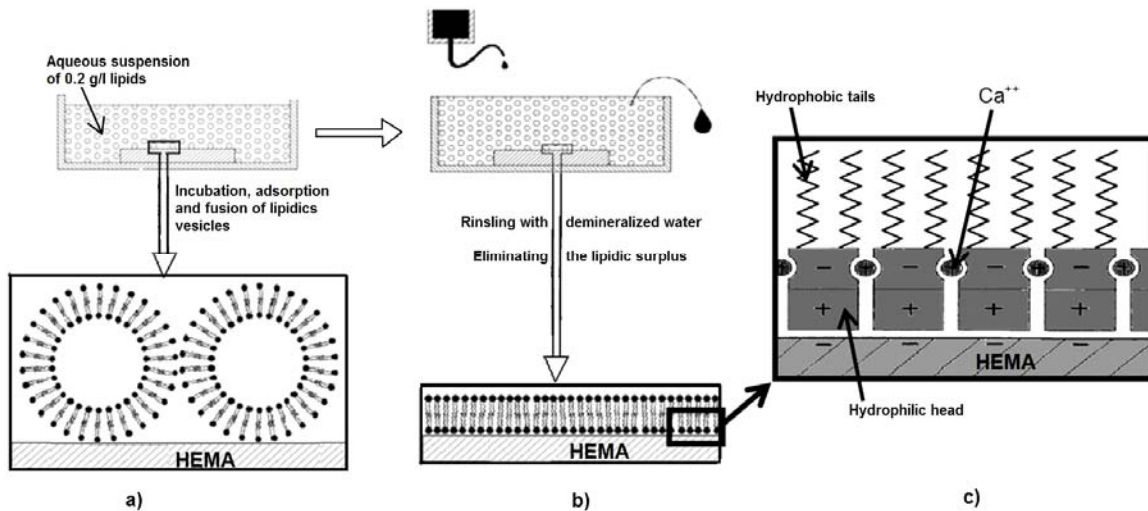


Figure 4. Formation of lipidic bilayers by the vesicle fusion method: a) incubation, adsorption and fusion of vesicles, b) elimination of the lipidic surplus by rinsing, c) internal structure of lipidic bilayers (from [27])

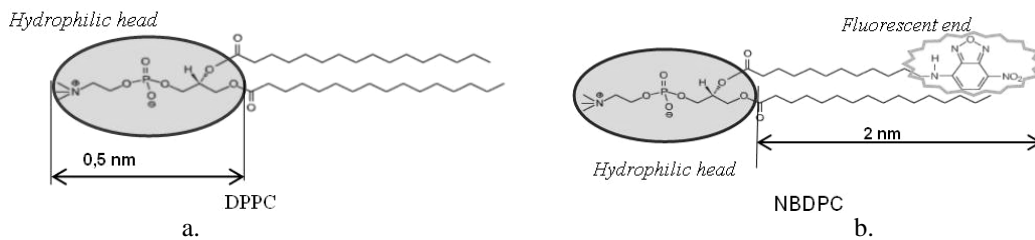


Figure 5. Chemical-molecular structure of lipids: a) 1,2-Dipalmitoyl-sn-Glycero-3-Phosphocholine (DPPC), b) 1-Palmitoyl-2-[12-[(7-nitro-2-1,3-benzoxadiazol-4-yl)amino]dodecanoyl]-sn-Glycero-3-Phosphocholine (16:0-12:0 NBD PC)

2.2.3 Viewing lipidic structures

Molecular markers were added at 1% molar concentration in DPPC lipidic powder in order to view the initial structure of the third body and its evolution during the friction tests. These are NBDPC lipids (Avanti Polar Lipids), whose ends are fluorescent under blue light (Figure 5).

In order to focus the microscope on a transparent interface (lipidic bilayer, glass surface, free surface of a solution of synovial vesicles), focusing was done in white light on the projection on this surface of the octagonal contour of the microscope's field diaphragm. This focusing was then kept when changing to blue light to view the fluorescent elements of this interface [28].

Several situations can be observed under blue light:

- If the third body does not contain any fluorescent elements under blue light, the diaphragm does not appear in the image. This is, for example, the case of a glass surface without a lipidic bilayer, or of the free surface of physiological solution (Figure 6a).
- If the third body contains fluorescent elements, the images obtained under blue light are composed of a clear zone bordered by the octagon of the diaphragm. This clear zone can be uniform, as in the case of a glass surface with an intact lipidic bilayer (Figure 6b), or an aqueous solution of small lipidic vesicles, or reveal details as in the case of a solution of large vesicles of synovial gel (Figure 6c).

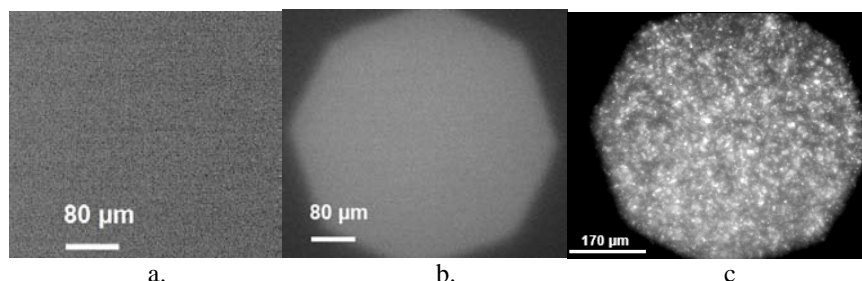


Figure 6. Fluorescence microscopy images of various lipidic structures containing 1% of fluorescent NBDPC using blue light. a) glass surface without any lipidic bilayer. b) glass surface with an intact lipidic bilayer (the projection on the surface of the octagonal contour of the microscope's field diaphragm is seen). c) solution of synovial gel vesicles without any lipidic bilayer near a glass surface

2.3 Experimental set-up

An experimental set-up permitting the in-situ visualisation of the contact was developed (Figure 7) to simulate the tribological operation of the model articular contact.

The model first bodies (HEMA, PE and steel samples) were fixed to the bottom of a tank containing the third body to be tested. The tank was linked to a translation stage by a system of flexible blades. The translation stage imposed cyclic translation movements forwards and backwards.

A transparent opposing first body formed the contact with the upper surface of the model first body. Normal load was applied by gravity. An upright microscope (Leica DMLM) linked to a camera (Leica DC350F) for fluorescent analytical imaging permitted viewing the contact through the opposing first body. This observation was done in-situ, during friction and could be done under white and blue (fluorescence) light. Exactly the same camera acquisition parameters were used under blue light to compare the different quantities of fluorescent lipids in the contact.

An eddy current position sensor measured the deformation of the flexible blades holding the tank, and permitted calculating the tangential force and the friction coefficient. The sensitivity, linearity range and sensor position were set-up so that the uncertainty on the force measurements between -1N and 1N was 0.0005N.

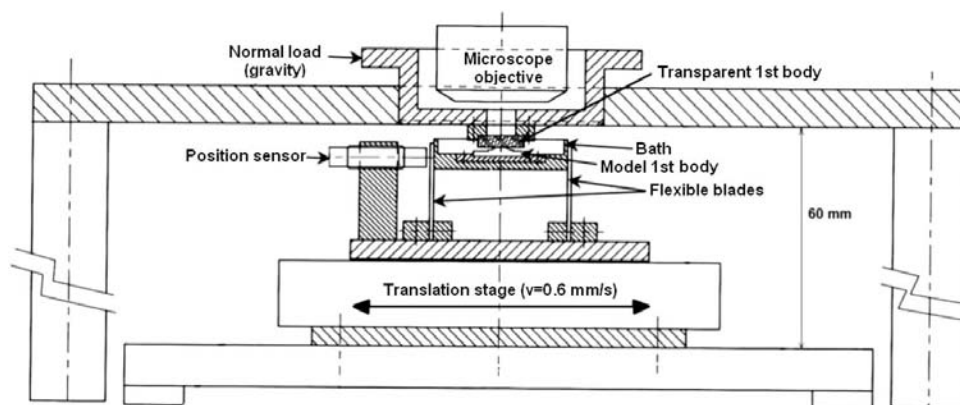


Figure 7. Schematic view of the experimental device

2.4 Experimental procedure

For the tests presented in this text, normal load was applied at 2.5N, which, by using the curve radii of the test pieces, permitted imposing realistic pressure conditions. The position sensor thus allowed the indirect measurement of friction coefficients up to 0.4, with an uncertainty in the region of 0.0002.

Back and forth displacements were made at a constant speed of 0.6 mm/s. On the one hand, this low value permitted good visualization of the contact by the optical microscope and, on the other, a boundary type lubrication regime. The back and forth movements were of equal duration, in the region of ten seconds, which, given the speed, permitted the successive visualization of the whole length of the contact.

Several series of friction tests, each lasting 1h (about 180 back and forth cycles), were performed. They included 3 types of first body and 4 types of third body.

The different combinations of first body, aimed at simulating natural articulations and the different types of implant, were the following:

A contact between a convex sample (curve radius 8mm) in soft HEMA (Young modulus of about 1.5 MPa) hydrated for 48h in physiological solution and a flat glass (borosilicate) opposing surface (Figure 8a). Given the load applied, the contact, which had a diameter of 2mm, was subjected to an average pressure of 0.3 MPa, whose order of magnitude seems realistic in comparison to the operating healthy knee joint in normal gait [29,30]. In what follows, this contact is called "artificial cartilage contact model".

A contact between a flat sample in steel 316L and a transparent convex opposing surface (curve radius 8mm) made of non-hydrated rigid HEMA (Young modulus of about 1 GPa) (Figure 8b). This circular contact of 0.8 mm in diameter was subjected to an average pressure of 5 MPa, which is realistic for the operating knee joint implant in normal gait [31]. This contact is referred in what follows as "steel joint implant contact model".

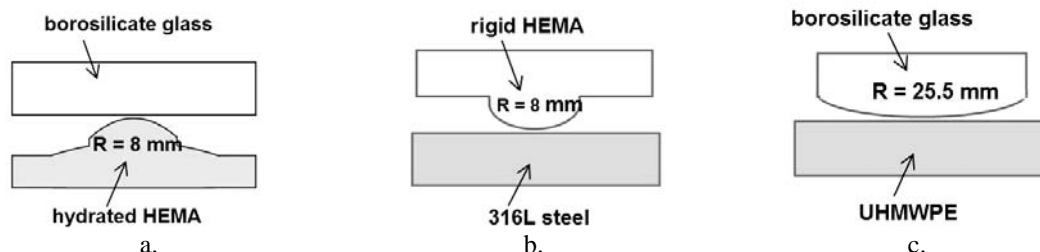


Figure 8. Model first bodies considered in this study:

- a) model of natural joint (model 1st body = hydrated HEMA, transparent 1st body = borosilicate glass),
- b) polyethylene joint implant contact model (model 1st body = 316L steel, transparent 1st body = rigid HEMA),
- c) polyethylene joint implant contact model (model 1st body = UHMWPE, transparent 1st body = borosilicate glass)

A contact between a flat polyethylene UHMWPE sample and a transparent convex glass (borosilicate) opposing surface (curve radius 25.5 mm) (Figure 8c). This circular contact of 0.8 mm diameter bore an average pressure of 5 MPa, which is realistic for the operating knee joint implant in normal gait [31]. This contact is referred to in what follows as "polyethylene joint implant contact model".

The following 4 types of third body and interfaces were used in order to study in uncoupled mode the tribological role of the different constituents of synovial fluid:

- physiological solution between the first bodies not covered with lipidic bilayers, referred to hereafter as "3rd body A", considered as the reference 3rd body with respect to the friction values,
- a suspension of 2 g/l of small lipidic vesicles (several hundred nm in diameter) in physiological solution, fluorescent under blue light (cf. 2.2.2) and referred to hereafter as "3rd body B" (fig 9a),
- physiological solution between the first bodies initially covered with lipidic bilayers (cf. 2.2.2), referred to hereafter as "3rd body C", (fig 9b),
- lipidic pockets filled of synovial gel (cf 2.2.1) between the first bodies initially covered with lipidic bilayers, referred hereafter as "3rd body D" (fig 9c).

3. EXPERIMENTAL RESULTS

3.1 Friction measurements

Figure 10 shows the evolution of the friction coefficient, at the start of the test and after one hour of operation for the artificial cartilage contact model in the presence of 3rd body A (physiological solution). The friction coefficient was observed to be very stable, in the region of 0.035. The rate of variation of the friction coefficient during a cycle is representative of the curves obtained for each of the combinations between the first and third bodies. However, in other configurations, the friction value changed through time.

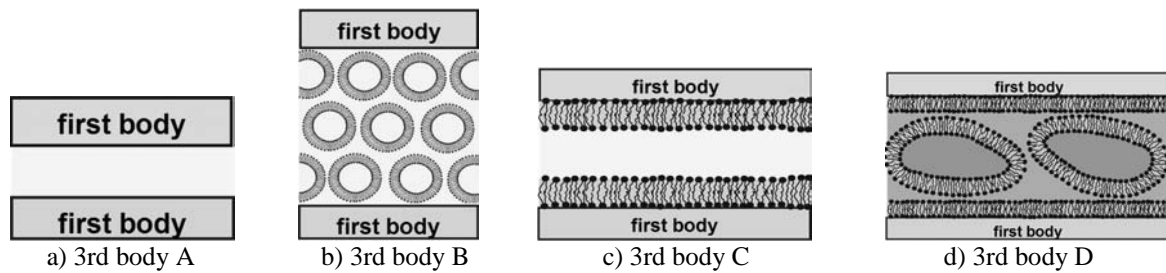


Figure 9. Schematic view of the third bodies and interfaces considered in the experiments
 a) 3rd body A (physiological solution), b) 3rd body B (suspension of small lipidic vesicles in physiological solution; c) 3rd body C (physiological solution between the first bodies initially covered with lipidic bilayers, d) 3rd body D (lipidic pockets filled of synovial gel between the first bodies initially covered with lipidic bilayers)

In the case of the artificial cartilage contact model, the friction tests were repeated five times, the dispersion on the friction force being 4% of the average value. For the implant models, each of the tests was performed twice, resulting in a maximum variation of 7% on the friction measurement.

All the average values of the friction coefficients obtained in this way for the 12 test configurations corresponding to the 3 model contacts and 4 third bodies (cf. 2.4.) at the start and end of the tests are grouped in Figure 11.

It can be seen that the combination of lipids with hyaluronic acid and albumins (3rd body D) gives a higher friction coefficient (0.12), whatever the model contact studied, than 3rd body A.

On the other hand, the comparison of 3rd bodies B and C, in which only lipids are present, without hyaluronic acid or albumin, with 3rd body A gives results as a function of the model contact and operating time. The following can be observed:

- a significant decrease of the friction coefficient for the artificial cartilage contact model (0.035 for 3rd body A, 0.005 for 3rd body B after 1h and 0.0015 for 3rd body C);
- an initial decrease of the friction coefficient for the steel joint implant contact model (0.07 for 3rd body A, 0.03 for 3rd bodies B and C), but a return to the initial value after 1h of friction;

- an initial increase of the friction coefficient for the polyethelene implant contact model (0.06 for 3rd body, 0.07 for 3rd bodies B and C), followed by a reduction to 0.05 after 1h of friction. However, this fall is probably not directly correlated with the presence of lipids in the third body, since it can also be observed with 3rd body A.

3.2 Visualization

The microscopy images of the first bodies before friction are shown in Table 2. These show that:

- the soft hydrated HEMA surfaces and rigid non-hydrated HEMA surfaces, as well as those in steel and glass, permitted the physicochemical adhesion of a fluorescent uniform lipidic bilayer (cf. 2.2.2)
- however, the polyethelene surface did not adsorb the lipidic bilayer.

The in-situ images taken during friction are shown respectively in the first two columns of Tables 3, 4 and 5. The images show:

- a zone including the border of the contact for the artificial cartilage contact model (Table 3).
- the central zone of the contact for the implant contact models (Tables 4 and 5), the experimental set-up and the contact configuration (Figure 8b and 8c) did not permit access to the edge of the contact.

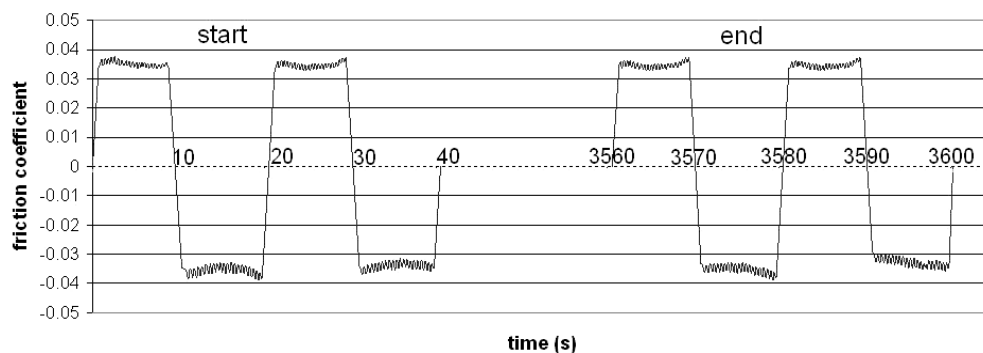


Figure 10. Typical shape of friction curves recorded with artificial cartilage in the presence of 3rd body

Table 2. Visualisation using different lights of the different first bodies (1-6) with or without lipids before contact. First bodies were immersed in water to keep the lipidic bilayer integrity. 1a-6a: Visualisation in white light of the surfaces. 1b-6b: Visualisation in blue light of the surfaces without any lipidic bilayer. 1c-6c: Visualisation in blue light of the surfaces with lipidic bilayer

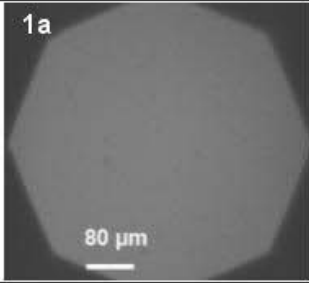
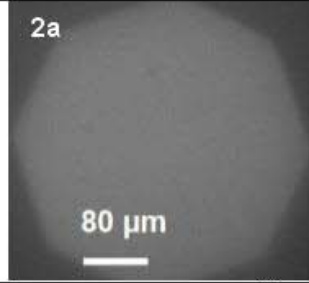
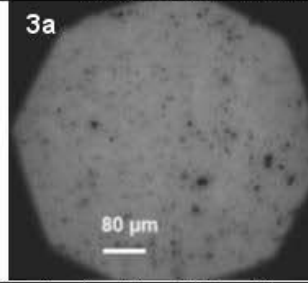
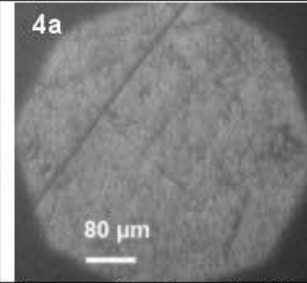
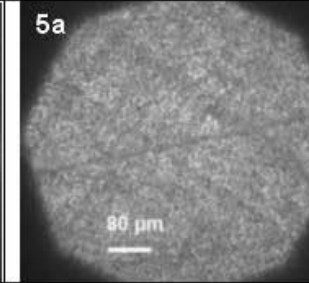
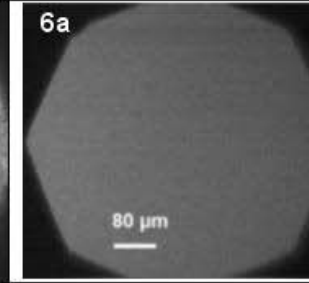
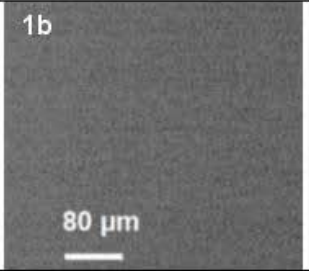
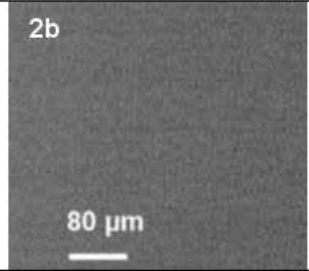
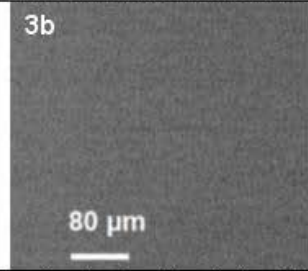
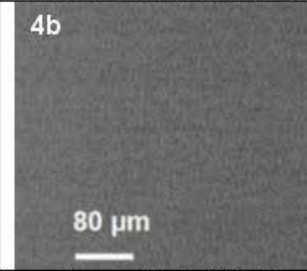
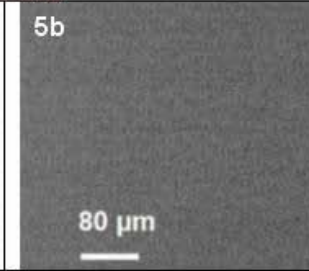
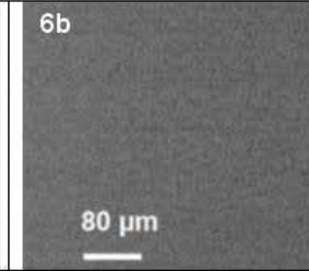
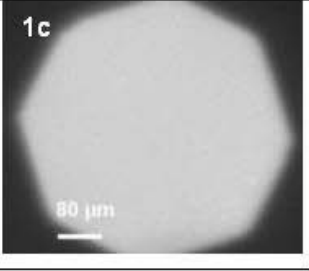
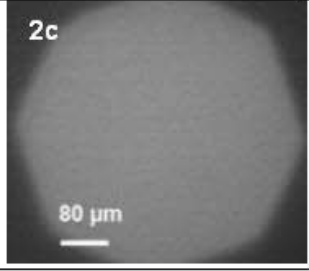
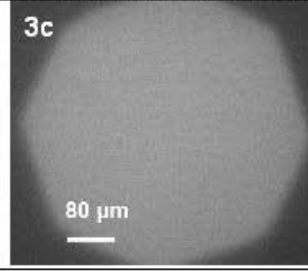
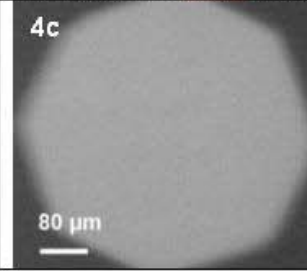
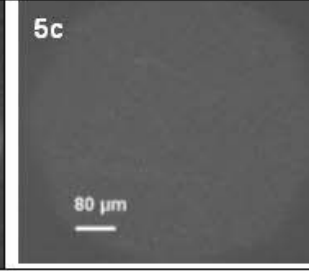
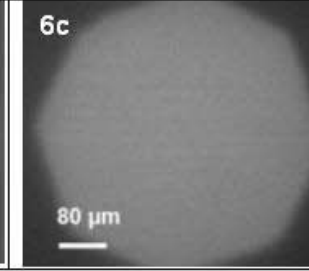
Model of articular cartilage		Model of steel joint implant		Model of polyethylene joint implant	
Hydrated HEMA	Borosilicate glass	316L steel	Rigid HEMA	UHMWPE	Borosilicate glass
Visualisation in white light of the surfaces					
					
Visualisation in blue light of the surfaces without any lipidic bilayer					
					
Visualisation in blue light of the surfaces with lipidic bilayers					
					

Table 3. Visualisation of artificial cartilage contact model; 1-2: in situ before and after friction; 3-4: after contact on both first-body (hydrated HEMA and borosilicate glass). Different third-bodies were investigated: a-b: third body B (suspension of small lipidic vesicles in physiological solution); c-d: third-body C (physiological solution between the first bodies initially covered with lipidic bilayers); e-f: third-body D (lipidic pockets filled of synovial gel between the first bodies initially covered with lipidic bilayers). Images were performed with white light (a,c,e) or with blue light (b,d,f)

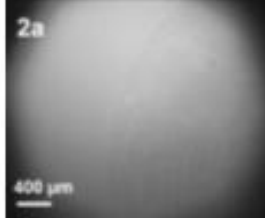
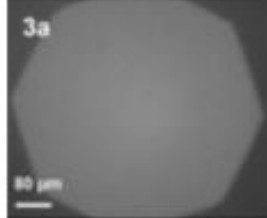
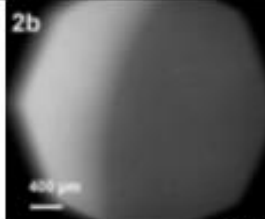
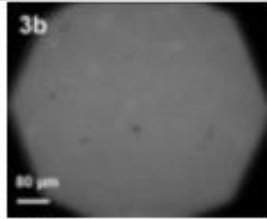
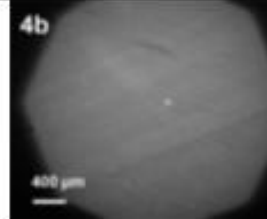
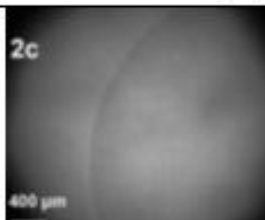
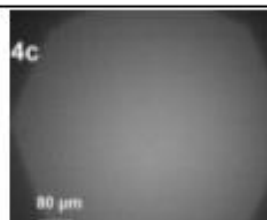
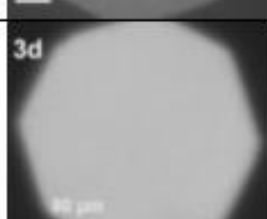
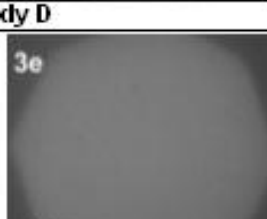
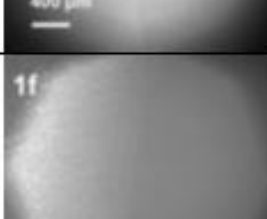
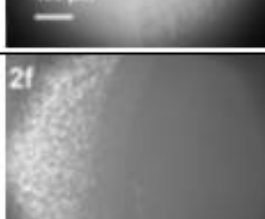
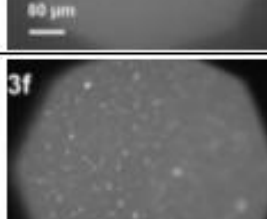
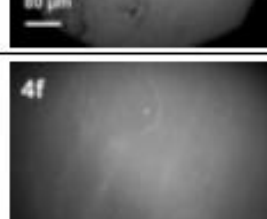
		In situ visualisation of the contact (zone including the border of the contact)		Visualisation of the 1 st bodies after contact	
		Before friction	After 1h of friction	Hydrated HEMA	Borosilicate glass
3rd body B					
white light					
blue light					
3rd body C					
white light					
blue light					
3rd body D					
white light					
blue light					

Table 4. Visualisation of steel joint implant contact; 1-2: in situ before and after friction; 3-4: after contact on both first-body (316L steel and rigid HEMA). Different third-bodies were investigated: a-b: third body B (suspension of small lipidic vesicles in physiological solution); c-d: third-body C (physiological solution between the first bodies initially covered with lipidic bilayers); e-f: third-body D (lipidic pockets filled of synovial gel between the first bodies initially covered with lipidic bilayers). Images were performed with white light (a,c,e) or with blue light (b,d,f)

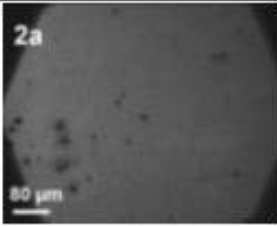
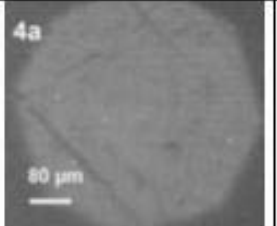
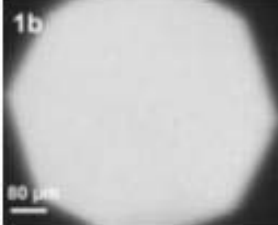
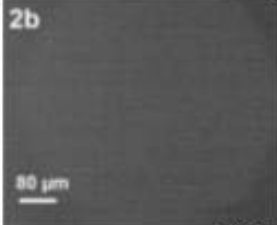
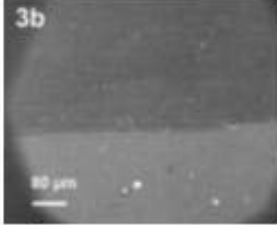
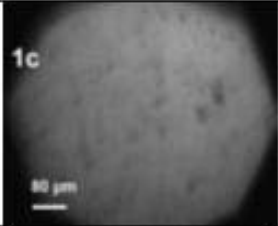
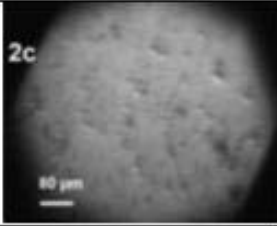
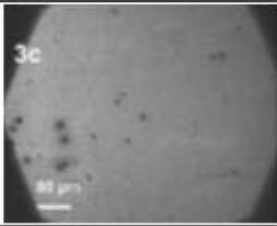
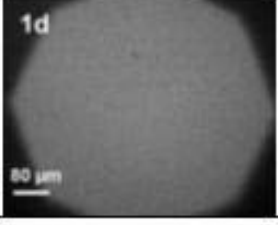
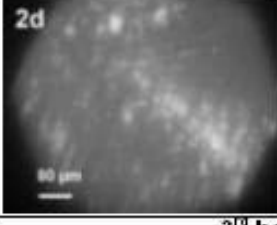
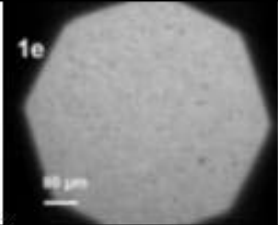
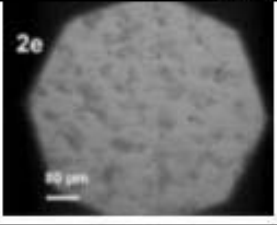
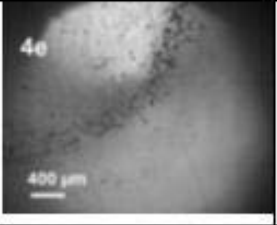
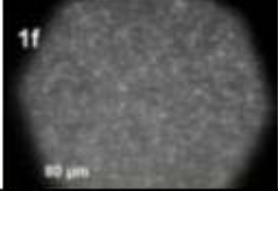
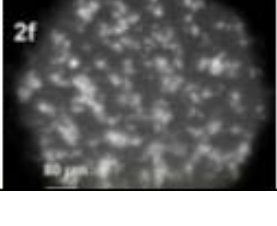
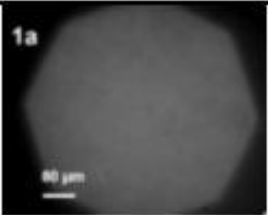
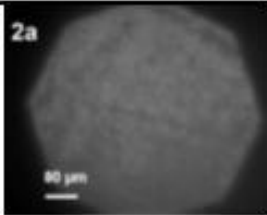
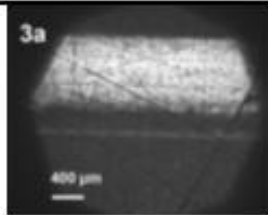
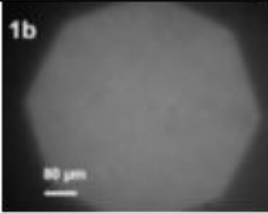
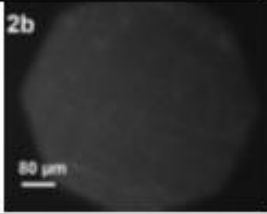
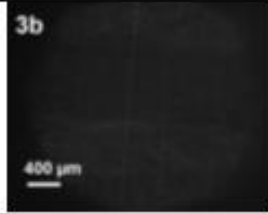
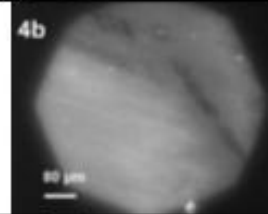
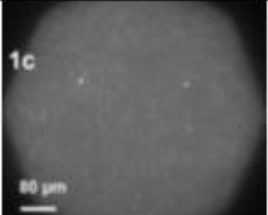
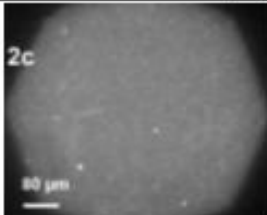
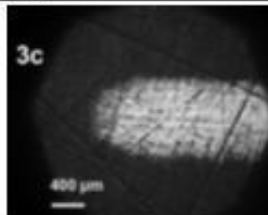
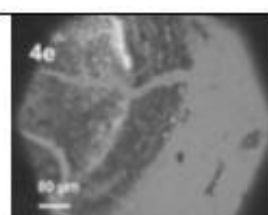
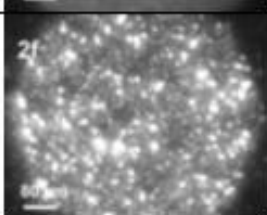
		In situ visualisation of the contact (contact area)		Visualisation of the 1 st bodies after contact	
		Before friction	After 1h of friction	316L steel	Rigid HEMA
3rd body B					
white light					
blue light					
3rd body C					
white light					
blue light					
3rd body D					
white light					
blue light					

Table 5. Visualisation of polyethylene joint implant contact; 1-2: in situ before and after friction; 3-4: after contact on both first-body (UHMWPE and borosilicate glass). Different third-bodies were investigated: a-b: third body B (suspension of small lipidic vesicles in physiological solution); c-d: third-body C (physiological solution between the first bodies initially covered with lipidic bilayers); e-f: third-body D (lipidic pockets filled of synovial gel between the first bodies initially covered with lipidic bilayers). Images were performed with white light (a,c,e) or with blue light (b,d,f)

	In situ visualisation of the contact (contact area)		Visualisation of the 1 st bodies after contact	
	Before friction	After 1 h of friction	UHMWPE	Borosilicate glass
3rd body B				
white light				
blue light				
3rd body C				
white light				
blue light				
3rd body D				
white light				
blue light				

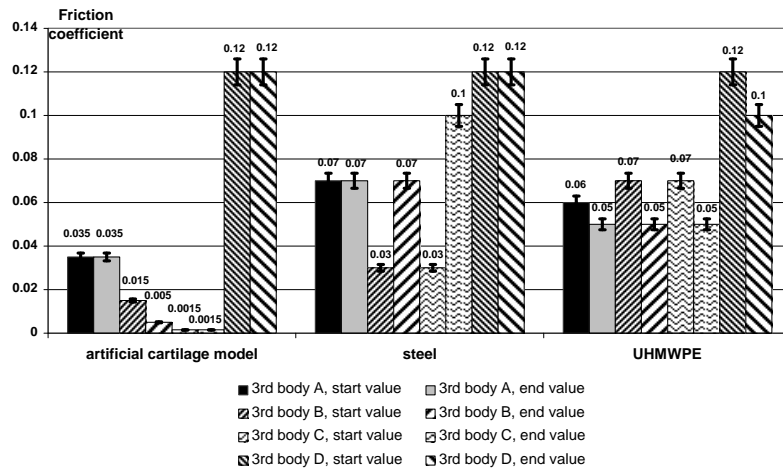


Figure 11. Friction coefficients at starting and end of each test

They permit observing changes in the distribution of fluorescence in the contact and possibly the exterior during friction.

The last two columns of these tables concern the images of the first bodies at the end of the tests, after opening the contact and rinsing with distilled water.

In section 3.3 we propose an analysis of the tribological role of the components of the different third bodies tested, in each of the model contacts, by using the correlations between the values and evolutions of the friction coefficients and the evolution of the images in white and blue light.

3.3 Interpretation

3.3.1 Artificial cartilage contact model

3rd body B (physiological solution, small lipidic vesicles)

The presence of small lipidic vesicles (approximately 200 nm in diameter) solution within 3rd body B generated quite significant fluorescence (Table 3, image 1b, part on right) provided by vesicles confined in the contact. This fluorescence was a little less significant than that recorded outside the contact (Table 3, image 1b, part on left) since the lipidic vesicles here were not confined in the contact and thus the thickness of the volume visualized was greater. After friction of 1h, the contact zone appeared much less fluorescent (Table 3, image 2b).

The reduction of fluorescence in the volume of the 3rd body occurred along with the appearance of fluorescence on the surface of first bodies: uniform fluorescence on the HEMA surface (Table 3, image 3b), and accentuated fluorescence on the friction trace on the glass surface (Table 3, image 4b). The lipidic vesicles present in the third body at the beginning of friction burst under the effect of tribological stresses leading to a lipidic deposit on the surfaces of the first bodies. This evolution occurs with a reduction of the friction coefficient from 0.015 to 0.005.

3rd body C (physiological solution, lipidic bilayers)

As in the case of 3rd body B, the fluorescence inside the contact before friction was the same as that observed outside the contact (Table 3, image 1d). But contrary to case B, the fluorescence did not evolve significantly during friction (Table 3, image 2d).

Visualisation of the rubbing surfaces of the first bodies after friction showed that the lipidic surfaces initially present remained intact (Table 3, images 3d and 4d).

Correlation of these observations with the measurement of the very low friction coefficient (0.0015) from the beginning to the end of friction showed that the lipidic bilayers adsorbed on the first bodies resisted friction well and were responsible for the significant reduction of the friction coefficient in comparison to 3rd body B.

These results demonstrated that the presence of two lipidic bilayers separated by a physiological salt solution layer in the contact area leads to very low friction. Our very low friction coefficient values contradict the hypothesis that lipids layers only reduce wear but not significantly friction in the healthy joints [6]. Low friction could be due to the location of velocity accommodation, in the physiological salt solution layer. This type of accommodation mode was also suggested by Briscoe et al. [32], but in their experiments, velocity accommodation was located in the hydration water layer at the substrate/surfactant monolayer interface. In this study the hydration layer located between two lipidic bilayers is probably thicker resulting in a much lower friction coefficient (by a factor of 10).

3rd body D (substitute synovial fluid, lipidic bilayers)

The presence of large lipidic vesicles (a few dozen micrometers in diameter) filled with hyaluronic acid and albumin gel ("synovial gel") in 3rd body D generated uniform fluorescence inside the contact, but much weaker than outside the

contact where it was not uniform (Table 3, image 1f). Therefore the large lipidic vesicles of 3rd body D did not remain inside the contact, and the fluorescence observed inside the contact was mainly caused by the lipidic bilayers adsorbed on the first bodies.

After 1h of friction, we observed the presence of fluorescent roller-like structures inside the contact (Table 3, lower part of image 2f). The roller-like appearance of this structure could be favoured by the presence of “free” synovial gel (not incorporated in the lipidic vesicles) and, due to the modification of the velocity accommodation mode, be responsible for the high friction coefficient (0.12). This value is similar to those obtained by Benz and Israelachvili [33] who studied the friction of a hyaluronic acid gel fixed (chemically and physically) by a lipidic bilayer on the surfaces in contact of a surface force apparatus, and show that synovial gel leads to a high friction coefficient (0.1 – 0.3) in a boundary lubrication regime.

Visualizations of the surfaces of first bodies after friction show the presence of fluorescent lipidic vesicles on the HEMA surface (Table 3, image 3f) and slightly fluorescent non-uniform deposits on the glass surface (Table 3, image 4f).

Therefore all the experiments carried out on the artificial cartilage contact model show that the lipidic bilayers, adhering physicochemically and uniformly to the rubbing surfaces of the first bodies led to a very low friction coefficient (in the region of 0.0015). Although the lipidic bilayers adhere during friction, they do not adhere uniformly (more visible fluorescent trace of friction in image 4b) which may explain why the friction coefficient is slightly higher (0.005). However, a much higher friction coefficient (0.12) is obtained if the friction is localised inside a layer of synovial gel and not in the layer of physiological solution that separates the lipidic bilayers deposited on the rubbing surfaces.

3.3.2 Steel joint implant contact model

3rd body B (physiological solution, small lipidic vesicles)

The fluorescence inside the contact before friction was uniform (Table 4, image 1b) but had completely disappeared after 1h of friction (Table 4, image 2b). The small lipidic vesicles (several hundred nanometres) of 3rd body B were therefore in the contact before rubbing, in the same way as for the artificial cartilage contact model.

Visualisation of the friction surfaces of the first bodies after friction showed that:

- the trace of friction on the steel surface did not contain lipids whereas a uniform bilayer was observed only outside the friction trace (Table 4, image 3b),
- the lipids adhered to the HEMA surface uniformly (Table 4, image 4b).

The steel surfaces therefore allowed the physicochemical adhesion of the lipids, but the lipidic bilayers did not resist the tribological stress, explaining the increase in the friction coefficient from 0.03 to 0.07 from the start to the end of the tests (Figure 11).

3rd body C (physiological solution, lipidic bilayers)

As expected, the fluorescence inside the contact before rubbing was uniform (Table 4, image 1d), due to the lipidic bilayers deposited on the first bodies.

The fluorescence lost its uniformity during the test (Table 4, image 2d), since the lipidic bilayers loosened from the first bodies and accumulated in fluorescent agglomerations inside the contact. Visualisations of the surfaces of the first bodies after friction also showed the destruction of the lipidic bilayers after friction and the formation of clusters in the friction traces on the steel (Table 4, image 3d) as on the HEMA (Table 4, image 4d).

The correlation with a variation from 0.03 to 0.1 of the friction coefficient during the tests (Figure 11) showed that the lipidic bilayers adhering on the steel surfaces did not resist tribological stress, and their destruction caused the friction to increase.

3rd body D (substitute synovial fluid, lipidic bilayers)

The presence of large lipidic vesicles filled with hyaluronic acid gel and albumin in 3rd body D generated non uniform fluorescence (Table 4, image 1f), which shows that the vesicles remain in the contact, as opposed to the case of artificial cartilage. After 1h friction these vesicles were seen to merge in the contact and form fluorescent clusters (Table 4, image 2f).

Furthermore, the images of the surfaces of the first bodies after friction showed:

- the presence of a non uniform fluorescent deposit on the steel surface over the entire friction surface (Table 4, images 3e and 3f),
- the presence of fluorescent and non fluorescent clusters at the border of the contact on the HEMA surface (Table 4, images 4e and 4f).

These clusters and the deposit could be caused by the presence of synovial gel not incorporated in the lipidic vesicles during the fabrication of the substitute synovial fluid. Velocity accommodation by shearing of these residues could be the source of the high friction coefficient (0.12), as in the case of the artificial cartilage model (Figure 11).

3.3.3 Polyethylene joint implant contact model

3rd body B (physiological solution, small lipidic vesicles)

The fluorescence inside the contact zone before friction was uniform (Table 5, image 1b), but

lessened substantially after 1h friction (Table 5, image 2b). The small lipidic vesicles were therefore present inside the contact before friction and were mostly ejected from the contact during friction.

The reduction of fluorescence in the contact zone during the test occurred with the appearance of fluorescence over the entire surface of the glass contact, at a level higher than that of the friction trace (Table 5, image 4b). On the other hand, the fluorescence of the polyethylene surface remained negligible (Table 5, image 3b).

This shows that the lipidic vesicles contained in the volume of 3rd body B and not ejected from the contact, burst due to tribological stress, with the lipids adhering only to the glass surface, both spontaneously and due to the effect of friction.

However, the polyethylene surface did not permit adhesion by the lipids by spontaneous physicochemical effects or by tribological stress effects. This appears to result in a high friction coefficient comparable to that obtained with 3rd body A (pure physiological solution). The reduction of the friction coefficient at the end of the test (a reduction from 0.07 to 0.05) can be explained by the smoothing of the polyethylene, resulting in increased shininess of the friction trace (Table 5, image 3a).

3rd body C (physiological solution, lipidic bilayers)

The presence of lipidic bilayers on the surface generates fluorescence of the contact (Table 5, image 1d), but this fluorescence is less uniform than in the case of the articular contact model (Table 3, image 1d) or the steel joint implant contact model (Table 4, image 1d). This is due to the difference of wettability between the two surfaces in contact (glass, polyethylene) which caused faults in the lipidic bilayers. During friction, the lipids loosened from the surfaces, to form fluorescent clusters inside the contact (Table 5, image 2d).

Visualisations of the friction surfaces of the first bodies after friction showed, as in the case of 3rd body B:

- the absence of lipids adhering to the polyethylene surface (Table 5, image 3d) and the smoothing of the friction trace detectable under white light due to the shininess of the friction trace (Table 5, image 3c).
- The presence of a high inhomogeneous lipidic bilayer on the glass (Table 5, image 4d), with lipidic clusters that did not exist before friction (Table 2, image 6c).

Thus, in the case of the polyethylene joint implant contact model, the evolution of the contact was the same, whether the lipids were initially in the volume of the 3rd body in the form of small vesicles, or in bilayers on the surface of the first bodies, thereby explaining why the change in the friction coefficient was the same (Figure 11).

3rd body D (substitute synovial fluid, lipidic bilayers)

The presence of large lipidic bilayers filled with synovial gel in the third body generated non-uniform fluorescence of the contact (Table 5, image 1f), which shows that these vesicles exist initially inside the contact zone. After 1h of friction, fusion of the vesicles into fluorescent clusters was observed (Table 5, image 2f).

Visualisations of the friction surfaces of the first bodies after friction showed:

- the absence of fluorescence for the polyethylene surface (Table 5, image 3f), and less pronounced shininess in the friction trace (Table 5, image 3e) than in the two previous cases, thereby showing the start of surface smoothing.
- the presence of clusters of non-uniform fluorescence in the contact zone on the glass surface (Table 5, image 4f).

In this configuration, it therefore seems that the accommodation of velocity between the surfaces was mainly ensured by free synovial gel between fluorescent clusters within the 3rd body, which explains why the same high level of friction was found (Figure 11) as for the artificial cartilage and steel joint implant contacts models. The polythene was also seen to smoothen during the test, leading to an apparent reduction of the friction coefficient.

4. CONCLUSIONS

An experimental model was used for the ex-vivo reproduction of the tribological triplets associated in, respectively, a healthy joint, a steel implant, and a polyethylene implant. In particular the aim was to analyse the tribological role of the biological components of the natural lubricant provided by synovial fluid, by specifically focusing on lipidic structures.

In order to exacerbate the role played by the interfaces, experimental conditions were chosen so as to eliminate any hydrodynamic load carrying capacity effect; therefore third bodies were considered, making it possible to study the influence of different lipidic structures on friction separately.

The analysis proposed relied on friction force measurements associated with optical microscopy images of the contact and surfaces. This microscopy made use of fluorescent and white light to detect the lipidic structures.

The study demonstrated that the presence of two lipidic bilayers separated by a physiological salt solution layer in the contact area leads to low friction, clearly shown in the case of the artificial cartilage, where it led to a friction coefficient in the region of a thousandth. On the contrary, it was not sensitive in the case of the model implants:

- In the case of the artificial cartilage, the lipidic bilayers resisted realistic tribological stresses. In addition, these stresses favoured their formation in the presence of lipidic vesicles. This beneficial effect of the lipidic bilayers was not observed in the implant models.

- The steel surfaces also favoured the adhesion of the lipidic bilayers, which tends to reduce friction. However, they did not resist tribological stress and were totally eliminated from the contact after one hour. Also the friction coefficient returned to a high value.

- The polyethylene surfaces did not permit any adhesion of the lipidic bilayers. This result appears to contradict the literature, which states that the presence of lipids in a steel-polyethylene contact reduces the friction coefficient [24]. A fall in the friction coefficient during the tests was observed, though it is only correlated to the smoothing effect on the polyethylene surface.

Furthermore, the addition of hyaluronic acid and albumin in the substitute synovial fluid resulted in an increase of the friction coefficient in all the tests performed. This was probably due to the presence of hyaluronic acid and albumin “free” gel, i.e. not incorporated in the lipidic vesicles. It was proposed to explain the increase of the friction coefficient that large molecules of hyaluronic acid may bridge the gap between surfaces [6] even in the presence of lipidic bilayers [34]. Within the framework of this study, we correlated the increase of the friction coefficient to the formation of the rollers containing lipids, which have been visualized in fluorescence microscopy (Table 3, image 2f).

However, it is probable that the presence of free synovial gel was due to our method of preparing the initial synovial gel - lipidic vesicle solution, which did not permit the complete incorporation of the gel. Indeed, it appears that the process of incorporating the gel in the vesicles greatly depends on physicochemical conditions (temperature, pH, osmotic pressure, etc.) [19]. Also, the pharmaceutical synthesis of the liposomes includes a final filtration step aimed at eliminating the free gel. This filtration was not performed in the framework of this work.

What is more, it is probable that there is no free gel in a healthy joint, in which the presence of lubricin ensures the correct formation of lipidic structures (bilayers, vesicles), by providing an adhesive interface between the lipidic surfaces of the cartilage and the synovial gel.

The situation is perhaps quite different in implants. This study suggests that the lipidic bilayers are destroyed by friction, thereby permitting the existence of free gel and increasing friction. Nonetheless, it should be noted that in spite of an increase in the friction coefficient, the presence of free gel may have a beneficial effect in protecting the steel surfaces against wear [1].

This study therefore shows that molecular structures, such as lipidic bilayers, hyaluronic acid and albumin gel, and their interactions have a decisive influence on the tribological performances of the artificial cartilage and the joint implant materials operating under boundary regime. Thus it appears vital to take them into account in implant lifetime tests and not use a lubricant composed only of physiological solution and albumin, as is most often the case.

A means of optimising the rubbing surfaces of joint implants requires improving the compatibility of the materials with the lipidic bilayers, in order to obtain a low friction coefficient and a lubrication mode similar to that of a healthy joint. These conclusions agree with the works of Hills [25] which show a stack of 3 to 7 lipidic bilayers on the surfaces of articular cartilage and suggest that most implant surfaces do not permit the formation of this stacking.

Our results with lipidic multilayers show very low friction coefficients similar to those obtained for polyelectrolyte experiments [Klein]; thus future experiments should be done in order to properly identify the tribological role of these molecules. Also, it was shown that polyelectrolytes such as lubricin have a role of adhesion on the lipidic membranes ([34,13]) which could modify their tribological performance. Therefore, future experiments should be performed in presence of lubricin and lipidic multilayers.

ACKNOWLEDGEMENT

The authors would like to thank in particular:

- Mr. G. Vitaly of CORNEAL Industrie which provided the HEMA samples,
- Pr. L. Cheze, Pr. J.-P. Carret of the Laboratoire de Biomécanique et Modélisation Humaine (LBMH) of Université Claude Bernard, Lyon 1 for their help in providing understanding of joint dynamics, anatomy and articular histology.
- Pr. D. Hartmann of the Institut des Sciences Pharmaceutique et Biologique de Lyon, UMR MA, for his help in providing understanding of the biochemistry and morphology of articular molecular structures.
- M. C. Godeau for his helpful participation in this work.

REFERENCES

1. Sawae Y., Murakami T., 2006, “An Experimental Investigation of Boundary Lubrication Mechanism with Protein and Lipid in Synovial Joint Using Total Internal Reflection Fluorescence Microscopy”, *Journal of Biomechanics*; Vol. 39 (Suppl 1).

2. **Wimmer MA, Sprecher C, Hauert R, Täger G, Fischer A.** 2003, "Tribochemical Reaction on Metal-on-Metal Hip Joint Bearings. A Comparison Between In-Vitro and In-Vivo Results," *Wear*; 255 : 1007–1014.
3. **Schurz J, Ribitsch V.,** 1987, "Rheology of synovial fluid," *Biorheology*, 24(4): 385-99
4. **Dowson, D., and Jin, Z.M.,** 1987, "An Analysis of Micro-Elastohydrodynamic Lubrication in Synovial Joints Considering Cyclic Loading and Entraining Velocities," *Fluid Film Lubrication—Osborn Reynolds Centenary, Proc. 23th Leeds–Lyon Symposium on Tribology*, edited by D. Dowson et al., Elsevier, Amsterdam, 1986, pp. 375–386.
5. **Swann D.A., Silver F.H., Slayter H.S., Stafford W., Shore E.,** 1985, "The Molecular Structure and Lubricating Activity of Lubricin Isolated from Bovine and Human Synovial Fluids," *Biochem J*; 225: 195-201.
6. **Jay G.D., Harris D.A. and Cha C.-J.,** 2001, "Boundary Lubrication by Lubricin is Mediated by O-linked (1-3)Gal-GalNAc Oligosaccharides," *Glycoconjugate Journal* 18, 807–815
7. **J. Klein,** 2006, "Molecular Mechanisms of Synovial Joint Lubrication", *Proc. IMechE* Vol. 220 Part J: J. Engineering Tribology, 220, 691-710.
8. **Schwarz IM, Hills BA.,** 1998, "Surface-Active Phospholipid as the Lubricating Component of Lubricin," *British Journal of Rheumatology*; 37: 21-26.
9. **Hills BA.,** 1989, "Oligolamellar Lubrication of Joints by Surface-Active Phospholipid". *J Rheumatol*;16: 82-91.
10. **Oates KMN, Krause WE, Jones RL and Colby RH.,** 2005, "Rheopexy of Synovial Fluid and Protein Aggregation." *Journal of the Royal Society Interface*; 1-8.
11. **Pasquali-Ronchetti,** 1997, "Hyaluronan–Phospholipid Interactions," *Journal of structural biology*; 120: 1–10.
12. **Crescenzia V, Taglienti A, Pasquali-Ronchetti I.,** 2004, "Supramolecular Structures Prevailing in Aqueous Hyaluronic Acid and Phospholipid Vesicles Mixtures: An Electron Microscopy and Rheometric Study," *Colloids and Surfaces A: Physicochem. Eng. Aspects*; 245: 133–135.
13. **Rhee DK, Marcelino J, Baker MA, Gong Y, Smits P, Lefebvre V, Jay GD, Stewart M, Wang H, Warman ML, Carpten JD.,** 2005, "The Secreted Glycoprotein Lubricin Protects Cartilage Surfaces and Inhibits Synovial Cell Overgrowth of Synovial Cell Growth," *The Journal of Clinical Investigation*; 115(3): 622–631.
14. **Schvartz I, Seger D, Shaltiel S.,** 1999, "Molecules in Focus: Vitronectin," *The International Journal of Biochemistry & Cell Biology*; 31: 539-544.
15. **Tolosano E, Altruda F.,** 2002, "Hemopexin: Structure, Function, and Regulation," *DNA and Cell Biology*; 21(4): 297-306.
16. **Trunfio-Sfarghiu AM, Berthier Y, Meurisse MH, Rieu JP.** "Operation Function of a Healthy Synovial Joint. Part I: Design of a Tribological Model by Multiscale Analysis of the Role of Biological Components", submitted for publication.
17. **Broom ND, Oloyede A.,** 1998, "The Importance of Physicochemical Swelling in Cartilage Illustrated with a Model Hydrogel System," *Biomaterials*; 19: 1179-1188.
18. **Freeman ME, Furey MJ, Love BJ, Hampton JM.,** 2000, "Friction, Wear, and Lubrication of Hydrogels as Synthetic Articular Cartilage," *Wear*; 241: 129-135.
19. **Covert RJ, Ott RD, Ku DN.,** 2003, "Friction Characteristics of a Potential Articular Cartilage Biomaterial," *Wear*; 255: 1064–1068.
20. **Dowson, D., and Jin, Z. M.,** 1992, "Microelastohydrodynamic Lubrication of Low-Elastic-Modulus Solids on Rigid Substrates," *J. Phys. D*, 25, pp. A116–A123.
21. **K. Nakashima, Y. Sawae, T. Murakami,** 2005, "Study on Wear Reduction Mechanisms of Artificial Cartilage by Synergic Protein Boundary Film Formation," *JSME International Journal*, series C, vol 48, nr. 4, p 555-561
22. **Migliaresi C, Nicodemo L, Nicolais L, Passerini P.,** 1981, "Physical Characterisation of Microporous Poly (2-Hydroxyethyl Methacrylat) Gels," *Journal of Biomedical Materials Research*; 15: 307-317.
23. **Mow VC, Ratcliffe A.,** 1992, "Cartilage and diarthrodial joints as paradigms for hierarchical materials and structures." *Biomaterials*; 13(2): 67-97.
24. **Watanabe M, Leng CG, Toriumi H, Hamada Y, Akamatsu N, Ohno S.,** 2000, "Ultrastructural Study of Upper Surface Layer in Rat Articular Cartilage By "In-Vivo Cryotechnique" Combined with Various Treatments," *The Clinical Electron Microscopy Society of Japan*; 33: 16-24.
25. **Torchillin V, Weissig V.,** 2003, *Liposomes: A Practical Approach*, Oxford University Press, USA.,
26. **He L, Dexter A, Middelberg A.,** 2006, "Biomolecular Engineering at Interfaces," *Chemical Engineering Science*; 61: 989 – 1003.
27. **Bayerl TM, Bloom M.,** 1990, "Physical Properties of Single Phospholipids Bilayers Adsorbed to Micro Glass Beads: A New Vesicular Model System Studied by 2H-Nuclear Magnetic Resonance," *Biophys. J.*; 58(2): 357–362.
28. **Hills BA, Crawford RW.,** 2003, "Normal and Prosthetic Synovial Joints Are Lubricated by Surface-Active Phospholipid. A Hypothesis," *The Journal of Arthroplasty*; 18(4): 499-505.
29. see the Olympus microscopy resource center, <http://www.olympusmicro.com/primer/anatomy/reflectkohler.html>

- 30. Gale LR, Coller R, Hargreaves DJ, Hills BA, Crawford R.,** 2006, "The Role of SAPL as a Boundary Lubricant in Prosthetic Joints." *Tribology International*; Available online 18 January.
- 31. Perie D., Hobatho M.C.,** 1998, "In Vivo Determination of Contact Areas and Pressure of the Femorotibial Joint Using Non-Linear Finite Element Analysis," *Clinical Biomechanics* 13, 394-402
- 32. Johnson T.S., Laurent M.P., Yao J.Q., Blanchard C.R.,** 2003, "Comparison of Wear of Mobile and Fixed Bearing Knees Tested in a Knee Simulator," *Wear* 255, 1107–1112
- 33. Briscoe et al.,** 2006, "Boundary Lubrication Under Water," *Nature* 444, 191-194.
- 34. Benz M, Chen N, Istraelachvili J.,** 2004, "Lubrication and Wear Properties of Grafted Polyelectrolytes, Hyaluronan and Hyalan, Measured in the Surface Forces Apparatus." *Journal of Biomedical Materials Research Part A*; 71A(1): 6-15.
- 35. Bruno Zappone, Marina Ruths, George W. Greene, Gregory D. Jay, Jacob N. Israelachvili,** "Adsorption, Lubrication and Wear of Lubricin on Model Surfaces: Polymer Brush-Like Behavior of a Glycoprotein," *Biophysical Journal*, 2006

D. N. OLARUe-mail: dolaru@mail.tuiasi.ro**C. STAMATE
A. DUMITRASCU
Gh. PRISACARU**Department of Machine Elements and
Mechatronics,
Technical University "Gheorghe Asachi" – Iasi
ROMANIA**ROLLING FRICTION TORQUE IN
MICROSYSTEMS**

To determine the rolling friction torque in the micro rolling systems, the authors developed an analytical model based on the dissipation of the inertial energy of a rotating microdisc in three rolling microballs. Using an original microtribometer with two steel rotating discs and three steel micro balls the rolling friction torque in dry conditions was determined for contacts loaded with normal forces of 8.68 mN to 33.2 mN and with rotational speed ranging between 30 to 210 rpm. The experimental results confirm the hypothesis that the rolling friction torque in dry contacts is not depending of the rotational speed.

Keywords: rolling friction torque, microtribometer, dynamic modeling

1. INTRODUCTION

The use of the rotating microball bearings in MEMS applications (micromotors, microgenerators, microactuators, micropumps) implies the simplification in construction, low level friction, low level wear, high stability. Thus the microball bearings seem to be a promising solution for future MEMS applications.

Recently, some experimental evaluations of the global friction in the rotating microball bearings was realized. Ghalichechian et al. [1] determined experimentally the global friction torque in an encapsulated rotary microball bearing mechanism using silicon micro fabrication and stainless steel microballs of 0.285 mm diameter. The global friction torque was indirectly obtained by measuring the transient response of the rotor in the deceleration process from a constant angular velocity until it completely stops due to friction. Using a high – speed camera system, the angular position of the rotor in the deceleration process was determined. The authors introduced the hypothesis that the global friction torque in the microball bearing is proportional with rotational speed. In this circumstances, the measured angular positions $\phi(t)$ was fitted to an exponential function of the form $\phi(t) = a \cdot e^{-bt} + c \cdot t + d$, where t is the time (in seconds) and a , b , c and d are constants. The acceleration of the rotor was obtained by differentiation of the function $\phi(t)$. The global friction torque obtained varied between 5.62 μNm and 0.22 μNm for the rotational speed of the rotor decreasing from 20.5 rad/s to zero, under an axial load of 48 mN. McCarthy et al. [2] experimentally

investigated the influence of the speed and of the normal load on the friction torque in a planar-contact encapsulated microball bearing having 0.285 mm diameter steel balls and silicon races. Using the spin-down testing and the hypothesis of the linear dependence between global friction torque and rotational speed, the authors determined the global friction torque for rotational speed between 250 rpm and 5000 rpm and for axial loads between 10 mN and 50 mN. Based on the experimental results, the authors obtained following empirical power-law model for the global friction torque in the microball bearing [2]: $M = 9 \cdot 10^{-5} \cdot F_N^{0.444} \cdot n$, where M is the global friction torque in μNm , F_N is the axial load acting on the microball rolling, in mN, and n is rotational speed in rot/min. Tan et al. [3] propose a viscoelastic model for friction force developed in a rolling contact between a microball and a plane. This viscoelastic model includes material parameters, ball diameter, normal load and linear speed and was applied for a steel microball having 0.285 mm diameter, loaded with a normal force of 2 mN and rolling on a silicon plane with a linear speed between zero to 0.03 m/s. The rolling friction torque obtained by this viscoelastic model varied between zero and $2.2 \cdot 10^{-3} \mu\text{Nm}$.

Using the integration of the free oscillations equations of a steel microball on a spherical glass surface, Olaru et al. [4] evaluated the rolling friction torque on the basis of the number and amplitude of the experimentally determined microball oscillations. For a steel microball having a diameter of 1 mm, Olaru et al. [4] obtained in dry conditions values for rolling friction torque of $0.7 \cdot 10^{-3} \mu\text{Nm}$ at a normal load on microball of 0.04mN.

The experimental results obtained in [1] and [2] refer to the global rolling friction torque in a rotary microball bearing. It is important to notice that in a rotary microball bearing the global friction torque is a result of both rolling and sliding friction caused by the pivoting motion of the microballs and by the direct contact of the microballs.

To determine only the rolling friction torque in the micro rolling systems the authors developed an analytical model based on the dissipation of the inertial energy of a rotating microdisc in three rolling microballs. Using an original microtribometer with two steel rotating discs and three steel microballs, the rolling friction torque in dry conditions was determined for normal contact loads of 8.68 mN to 33.2 mN and for rotational speed varying between 30 to 210 rpm.

2. ANALYTICAL MODEL

Figure 1 presents the new micro tribometer. The driving disc 1 is rotated with a constant rotational speed and has a radial groove race. Three microballs are in contact with the race of the disc 1 at the equidistance position (120 degrees). All three microballs sustain an inertial disc 2 and are normal loaded with a force $Q = \frac{G}{3}$, where G is the weigh of the disc 2. When the disc 1 start to rotate with a constant angular speed ω_1 , the balls start to rolls on the raceway of the disc 1 and start to rotate the inertial disc 2, as a result of rolling friction forces between the balls and the disc 2. As a result of inertial effect the disc 2 is accelerated from zero to the synchronism rotational speed (when $\omega_2 = \omega_1$) in a time t, after that the rotational speed of the disc 1 is stopped. The disc 2 has a deceleration process from the constant rotational speed $\omega_{2,0}$ to his completely stop as a result of the friction in the rolling of the three microballs over the two discs.

In the deceleration process of the disc 2 when

ω_2 decreases from a constant value to zero, following differential equation can be used:

$$J \cdot \frac{d\omega_2}{dt} - 3 \cdot F_2 \cdot r - M_f = 0, \quad (1)$$

where J is inertial moment for the disc 2, F_2 is the tangential force developed in the contact between a microball and disc 2, r is the radius and M_f is the friction torque developed between the rotating disc 2 and air.

For a disc with inner radius R_i , outer radius R_e and a mass m_d , the inertial moment J is determined by following relation:

$$J = 0.5 \cdot m_d \cdot (R_i^2 + R_e^2). \quad (2)$$

For a disc having a rotational speed ω_2 in a fluid with a kinematics viscosity ν_f and a density ρ_f , the friction torque M_f can be determined by relation [5]:

$$M_f = 0.5 \cdot K_M \cdot \rho_f \cdot R^5 \cdot \omega^2, \quad (3)$$

where K_M is a coefficient depending on the Reynolds parameter. When the rotational speed of the disc 2 have maximum values between 30 and 210 rpm and the radius R is 0.012 m, the Reynolds parameter have values between 30 and 200 (the kinematics viscosity of the air was considered $\nu_f = 15 \cdot 10^{-6} \text{ m}^2/\text{s}$ and the density of the air was considered $\rho_f = 1.18 \text{ kg/m}^3$). For these values of the Reynolds parameter it can be approximated the K_M coefficient by a constant value of 0.5 and equation (3) can be approximated as follows:

$$M_f = c_f \cdot \omega^2, \quad (4)$$

where the coefficient c_f have an approximate value of $7.3 \cdot 10^{-11} \text{ N} \cdot \text{m} \cdot \text{s}^2$.

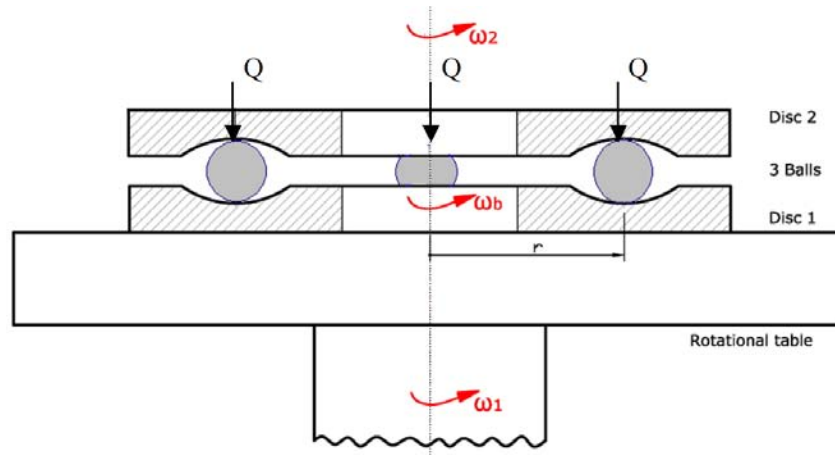


Figure 1. General view of the microtribometer

As presented in Figure 2, in the deceleration of the disc 2, following forces act on a microball in the rotational plane: the tangential contact forces F_1 and F_2 and the inertial force F_{ib} . Also, in the two contacts we consider two rolling friction torques M_{r1} and M_{r2} .

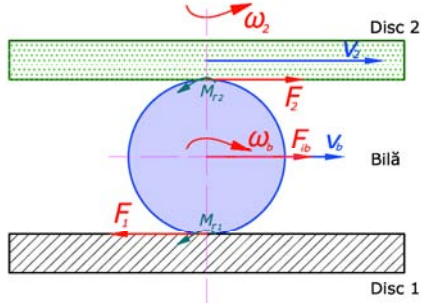


Figure 2. The forces and the moments acting on a microball in deceleration process

The tangential force F_2 was determined using force and moment equilibrium equations for a microball, resulting:

$$F_2 = \frac{(M_{r1} + M_{r2})}{d} - \frac{F_{ib}}{2}, \quad (5)$$

where d is the microball diameter.

The inertial force acting in the center of the microball is determined by relation:

$$F_{ib} = m_b \cdot \frac{d\omega_b}{dt} \cdot r, \quad (6)$$

where m_b is the mass of the microball and ω_b is the angular speed of the microball in the revolution motion around the center of the two discs. Considering the pure rolling motion of the microballs, the angular speed ω_b can be expressed as $\omega_b = 0.5 \cdot \omega_2$ and the equation (6) can be written as follows:

$$F_{ib} = \frac{m_b \cdot r}{2} \cdot \frac{d\omega_2}{dt}. \quad (7)$$

According to the equations (1), (4), (5) and (7), following differential equation in the deceleration process of the disc 2 is obtained:

$$\frac{d\omega_2}{dt} = a \cdot (M_{r1} + M_{r2}) + b \cdot \omega_2^2, \quad (8)$$

where a and b are constants defined by:

$$a = \frac{3 \cdot r}{d \cdot (J + \frac{3}{4} \cdot r^2 \cdot m_b)}, \quad b = \frac{c_f}{(J + \frac{3}{4} \cdot r^2 \cdot m_b)}.$$

To integrate the differential equation (8), two hypotheses were made:

i) it is considered that the rolling friction torques M_{r1} and M_{r2} are not depending on the rotational speed;

ii) the rolling friction torques M_{r1} and M_{r2} have a linear dependence on rotational speed.

i) Considering that the rolling friction torques M_{r1} and M_{r2} are constants, equation (8) leads to the following solution for ω_2 as function of time:

$$\omega_2(t) = \frac{c}{b} \cdot \text{tg} \left[-c \cdot t + \text{arctg} \left(\frac{b}{c} \cdot \omega_{2,0} \right) \right], \quad (9)$$

where $c = \sqrt{a \cdot b \cdot (M_{r1} + M_{r2})}$ and $\omega_{2,0}$ is angular rotational speed of the disc 2 at the moment of the stopped the rotation of the disc 1.

Considering that $\omega_2(t) = \frac{d\phi_2(t)}{dt}$, where

$\phi_2(t)$ is the variation of the angular position of the disc 2 in deceleration process, equation (9) can be integrated and following solution for $\phi_2(t)$ results:

$$\phi_2(t) = \frac{-\ln \left[1 + \text{tg} \left[-c \cdot t + \text{arctg} \left(\frac{b}{c} \cdot \omega_{2,0} \right) \right] \right]}{2b} + \frac{\ln \left[1 + \left(\frac{b}{c} \cdot \omega_{2,0} \right)^2 \right]}{2b}. \quad (10)$$

ii) Considering that the rolling friction torques M_{r1} and M_{r2} have a linear dependence on rotational speed it can be written that $(M_{r1} + M_{r2}) = k \cdot \omega_2$ and differential equation (8) becomes:

$$\frac{d\omega_2}{dt} = a \cdot k \cdot \omega_2 + b \cdot \omega_2^2. \quad (11)$$

Equation (11) leads to the following solutions:

$$\omega_2(t) = \frac{a \cdot k \cdot \exp(-a \cdot k \cdot t + k1)}{1 - b \cdot \exp(-a \cdot k \cdot t + k1)}; \quad (12)$$

$$\phi_2(t) = \frac{1}{b} \cdot \ln(1 - b \cdot \exp(-a \cdot k \cdot t + k1)) - \frac{1}{b} \cdot \ln(1 - b \cdot \exp(k1)). \quad (13)$$

$$\text{where } k1 = \ln \left(\frac{\omega_{2,0}}{a \cdot k + b \cdot \omega_{2,0}} \right).$$

For given dimensions of the microballs and of the two discs, by monitoring the angular position

and angular speed of the disc 2 in the deceleration process it is possible to determine the sum of the rolling friction torques ($M_{r1} + M_{r2}$).

Also, having determined the sum of these friction torques, the tangential force F_2 can be determined by equation (5) and the friction coefficient in the rolling contact μ_r by equation:

$$\mu_r = \frac{F_2}{Q}. \quad (14)$$

3. EXPERIMENTAL INVESTIGATION

Using the new microtribometer presented in Figure 1 a set of experimental investigations was performed. The microtribometer was mounted on the rotational table of the CETR-UMT Tribometer as shown in Figure 3.

To determine the angular acceleration of the disc 2 a high – speed camera Philips SPC900NC/00 VGA CCD with 90 frames/seconds was used to capture the angular position of the disc 2 from the rotational speed $\omega_{2,0}$ to his completely stop. Also, the angular positions of the disc 1 are captured by camera. In Figure 4, the registered positions of the disc 2, and of the disc 1, at a short time t after the stop of the disc 1 are presented.

The images captured by the camera was processed, frame by frame, in a PC using Virtual Dub soft and was transferred in AutoCAD to measure the angular positions θ_2 corresponding to every frame. The camera was installed vertically

150 mm above the disc 2, to minimize the measurement errors. A white mark was placed both on disc 2 and on disc 1 as it can be observed in the Figure 4 and the angular positions $\theta_2(t)$ was measured according to the reference position of the mark on the disc 1 (position at $t = 0$). The discs 1 and 2 are the steel rings of an axial ball bearing (series 51100) having a rolling path at a radius $r = 8.4\text{mm}$ and a transversal curvature radius of 2.63 mm. The inertial disc 2 was machined on external surface by electro erosion to reduce the weight to a minimum of $G = 26.05\text{ mN}$, and it has the following dimensions: $R_i = 5\text{ mm}$, $R_e = 12\text{ mm}$, which means a minimum normal load on every microball $Q = 8.68\text{ mN}$. To increase the normal load on the microball a lot of new discs similar to the disc 2 was attached on the disc 2 obtaining following values for the normal load: 8.68 mN, 15 mN, 22.3 mN, 27 mN, 33.2 mN. Three stainless steel microballs having the diameter of 1.588 mm (1/16 inch) was used in the experiments. The roughness of the active surfaces of the two discs and of the balls was measured by Form Talysurf Intra System. Following values of R_a were obtained: rolling path of the disc 1 and 2, $R_a = 0.030\text{ }\mu\text{m}$, and ball surface, $R_a = 0.02\text{ }\mu\text{m}$. The tests were realized for the following rotational speed of the disc 2: 30 rpm, 60 rpm, 90 rpm, 120 rpm, 150 rpm, 180 rpm, 210 rpm.

All measurements are performed in steady room environment at a temperature of $(18-20)^\circ\text{C}$ and a relative humidity of $(40 - 50)\%\text{RH}$. All the tests were realized in dry conditions (without lubricant or condensed water on contact surfaces).

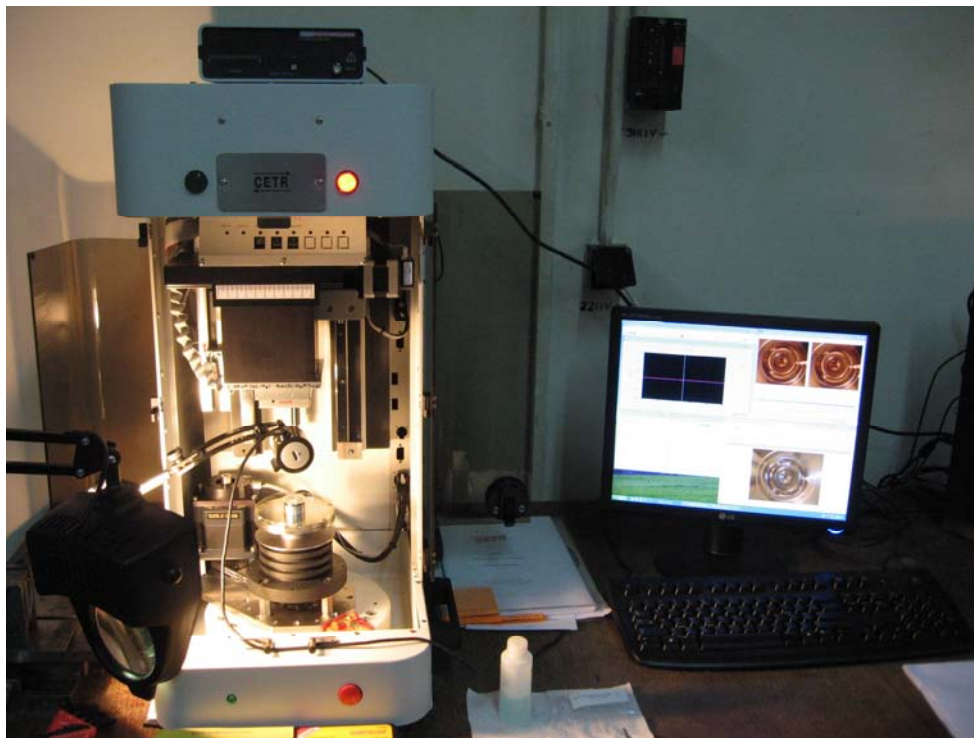


Figure 3. General view of the experimental equipments

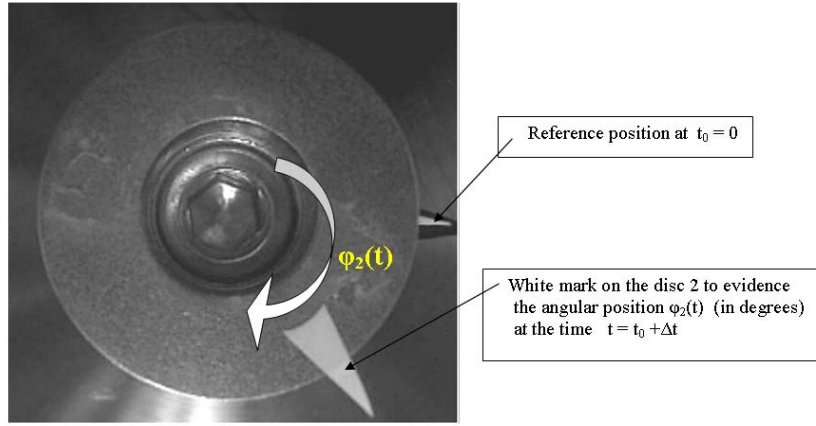


Figure 4. Determination of the angular position $\varphi_2(t)$ of the disc 2

4. VALIDATION OF THE ANALYTICAL MODELS

Two experimental data were obtained for each experiment: the variation of the angular position $\varphi_2(t)$ from the moment of beginning the deceleration process of the disc 2 to its completely stop and the time of the deceleration process. A typical variation of the angular position $\varphi_2(t)$ for a rotational speed of 120 rpm and a normal load $Q = 8.68$ mN experimentally determined, is shown in Figures 5 and 6. For all experiments, the variations of the angular position of the disc 2, $\varphi_2(t)$ are similar, but other time of deceleration and other maximum values were obtained, depending of the initial angular speed $\omega_{2,0}$ and the normal load Q acting on the microballs. Both hypotheses were used to validate the experimental results.

i) The hypothesis of constant torque friction was applied for all experiments and a good validation with experiments was obtained. Using equation (10) it was determined the value of the sum of friction torques ($M_{r1} + M_{r2}$) imposing the condition that at the stop of the disc 2, the angular position of this disc cumulates the experimentally determined value. With the above sum ($M_{r1} + M_{r2}$), it was verified by equation (9) if the angular speed of the disc 2 was stopped after the experimentally determined time.

Figure 5 shows the numerical variation of the angular position of the disc 2 given by equation (10) for a rotational speed of the disc 2 of 120 rpm and a normal load $Q = 8.68$ mN.

The maximum differences between the numerical values obtained by equation (10) and the experimental values do not exceed 5%. In Figure 5-b it can be observed the numerical variation of the angular speed $\omega_2(t)$ obtained by equation (9) with a quasi linear variation from $\omega_{2,0} = 12.4$ rad/s to $\omega_{2,0} = 0$, in a time $t = 41$ seconds. This deceleration time corresponds to the experimental determined value.

ii) The hypothesis of the linear variation of the friction torque with rolling speed was applied for all experiments. Using equation (13), the value for the sum of friction torques ($M_{r1} + M_{r2}$) was determined by imposing the condition that at the stop of the disc 2 the angular position of this disc cumulates the experimentally determined value. With the above sum ($M_{r1} + M_{r2}$) equation (12) yields the variation of the angular speed of the disc 2.

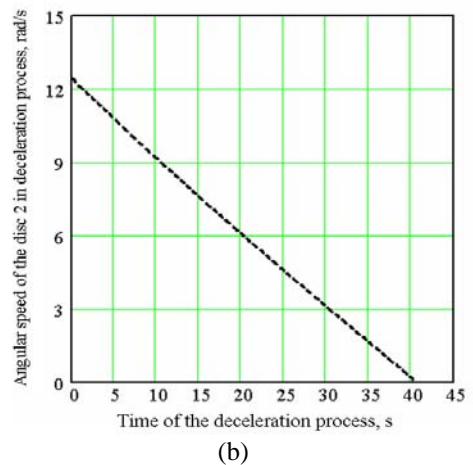
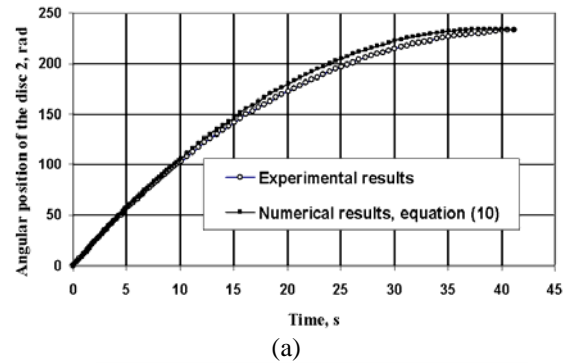
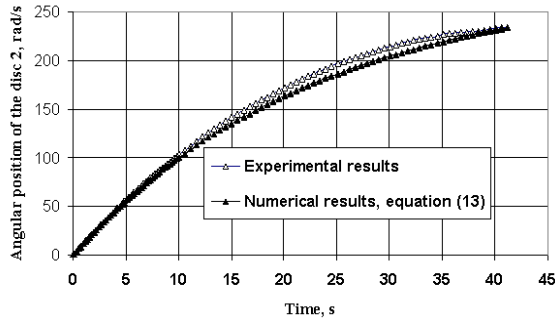
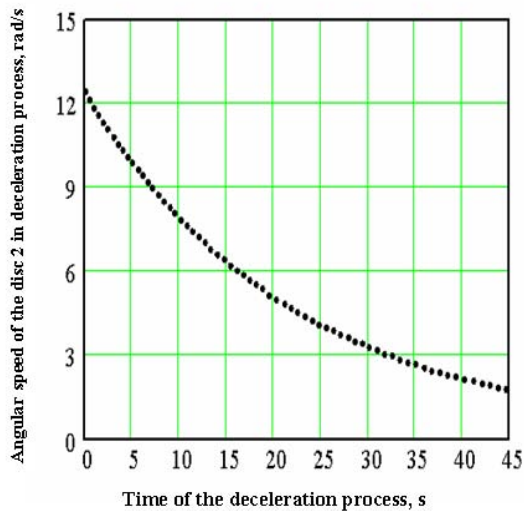


Figure 5. Variation of the numerical and experimental values for $\varphi_2(t)$ - (a) and variation of the angular speed $\omega_2(t)$ - (b) for a rotational speed of the disc 2 of 120 rpm and normal load $Q = 8.68$ mN (constant friction torque's hypothesis)

Figure 6 shows the numerical variation of the angular position of the disc 2 given by equation (13) for a rotational speed of the disc 2 of 120 rpm and a normal load $Q = 8.68 \text{ mN}$. The maximum differences between the numerical values obtained by equation (13) and the experimental values do not exceed 8%. Figure 6-b shows the numerical variation of the angular speed $\omega_2(t)$ obtained by equation (12). It can be seen that the angular speed of the disc 2 is not zero at a time $t = 41$ seconds.



(a)



(b)

Figure 6. Variation of the numerical and experimental values for $\varphi_2(t)$ –(a) and variation of the angular speed $\omega_2(t)$ –(b) for a rotational speed of the disc 2 of 120 rpm and normal load $Q = 8.68 \text{ mN}$ (variation of friction torque's hypothesis)

By comparing the two analytical variations of the angular position $\varphi_2(t)$ given by equations (10) and (13) and presented in Figure 7, it can be observed that the equation (10) leads to a variation of angular position with a maximum around of the time $t = 41$ seconds while the equation (13) leads to a continuum increasing of the angular position $\varphi_2(t)$. This means theoretically a continuous rotation over the time of experimentally stopping of the disc 2.

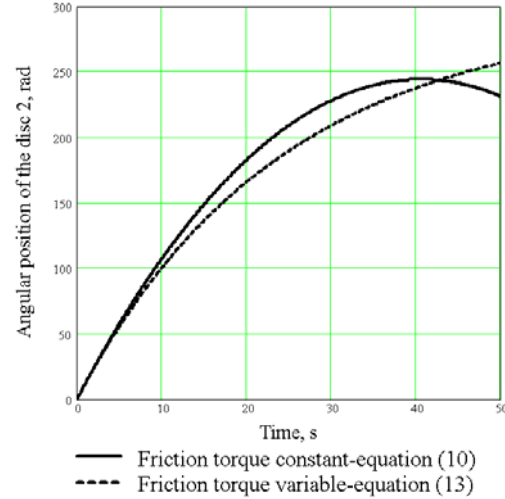


Figure 7. The theoretical variation of the angular position $\varphi_2(t)$ for the two hypothesis applied for rotational speed of 120 rpm and normal load of 8.68 mN

Our conclusion is that the hypothesis of the constant friction torque can be accepted and leads to a good theoretical model in the interval of the rotational speed between 30 rpm to 210 rpm.

5. EXPERIMENTAL RESULTS

The sum of the friction torques for all experiments was determined in the hypothesis of the constant friction torque using equations (9) and (10). Considering that the geometry of the contact between microball and the two discs is the same and neglecting the influence of the microball weight (the mass of a microball leads to an additional force $Q_b = 0.165 \text{ mN}$ in the contact between microball and the disc 1) we can consider that the friction torque between a microball and the disc 1 or 2 is given by relation $M_r = 0.5(M_{r1} + M_{r2})$. In Figure 8 are presented the rolling friction torques M for all rotational speeds and normal loads used in the experiments.

It can be observed that between 30 rpm and 150 rpm the friction torque M depends only on the normal load and is not depending on the speed. By increasing the speed from 150 rpm to 210 rpm the friction torque increases with rotational speed, especially when increasing the normal load. The increasing of the friction torque with rotational speed above 150 rpm, can be explained by increasing of the rotating disc's vibration with a supplementary loss of energy. It is important to notice that increasing of the normal load is realised by adding supplementary discs on the initial disc 2. Geometrical imperfections of the supplementary discs increase the vibration level of the rotating disc, and vibrations of the rotating disc were observed experimentally.

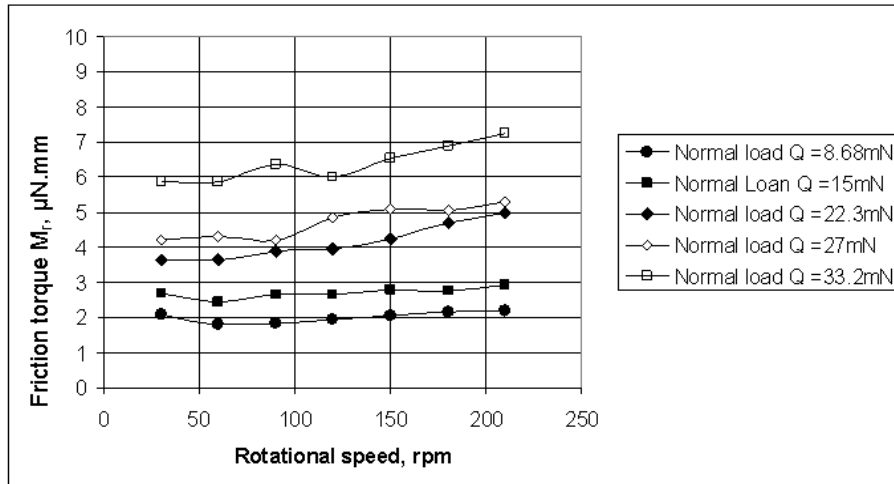


Figure 8. The rolling friction torques M_r determined by equation (10) applied to the experiments

The friction coefficient determined by equation (14) has values between 0.0002 and 0.0004 which means a dominance of the rolling friction between the microballs and the two discs.

6. CONCLUSIONS

Two analytical models to determine the rolling friction in an original microtribometer were elaborated. The two models are based on the integration of the differential equation of a rotating disc sustained only by three microballs. Two hypothesis were considered : i) the friction torque is not depending on the rotational speed in dry contacts and ii) the friction torque has a linear variation with rotational speed.

To validate these hypotheses, a set of experiments was performed for a variation of rotational speed between 30 rpm to 210 rpm and a normal load in the rolling contact between 8.68 mN to 33.2 mN. The hypothesis based on the constant friction coefficient was validated as a good hypothesis in dry conditions.

The friction torques for all experiments was determined by the analytical model based of the constant friction torque. The numerical values are between 1.8 $\mu\text{N}\cdot\text{mm}$ to 7.2 $\mu\text{N}\cdot\text{mm}$.

The rolling friction coefficient obtained in all experiments ranges between 0.0002 and 0.0004.

ACKNOWLEDGEMENTS

This paper was realised with the support of Grant CNCSIS ID_607 No. 381/1.10.2007 and BRAIN “Doctoral scholarships as an investment in intelligence” project, financed by the European Social Found and Romanian Government.

REFERENCES

1. Ghalichechian, N., Modafe, A., Beyaz, M. I., Ghodssi, R., 2008, “Design, Fabrication, and Characterization of a Rotary Micromotor Supported on Microball Bearings,” *Journal of Microelectromechanical Systems*, 17, p. 632-642
2. McCarthy, M., Waits, C. M., Ghodssi, R., 2009, “Dynamic Friction and Wear in a Planar-Contact Encapsulated Microball Bearing Using an Integrated Microturbine,”. *Journal of Microelectromechanical Systems*, 18, p. 263-273
3. Tan, X., Modafe, A., Ghodssi, R., 2006, “Measurement and Modeling of Dynamic Rolling Friction in Linear Microball Bearings,” *Journal of Dynamic Systems, Measurement, and Control*, 128, p. 891-898
4. Olaru, D. N., Stamate, C., Prisacaru, Gh., 2009, “Rolling Friction in a Microtribosystem,” *Tribology Letters*, 35, p. 205-210
5. Czichos, H. ed. HÜTTE - *Die Grundlagen der Ingenieurwissenschaften*, Springer Verlag, Berlin, 1989.

Lorena DELEANU
e-mail: lorena.deleanu@ugal.ro

Sorin CIORTAN

Machine Design and Graphics,
University Dunarea de Jos – Galati,
ROMANIA

EVALUATING TRIBOLOGICAL DAMAGES BY 3D PROFILOMETRY

The authors present a study on using 3D roughness parameters for assessing the quality of worn surfaces of polymeric composites. A set of three plates was tested under water lubrication in contact with a steel disc, being tested at 2.5m/s (the sliding speed at plate center) and average pressure 2.02 MPa. The plates (6 x 20 x 30 mm) were made of PTFE composites with glass fibers (0% for the polymer, 15%, 25% and 40%, respectively).

Keywords: polymeric composites, wear, roughness

1. INTRODUCTION

Polymeric composites are expected to give solutions for tribological applications as manufacturing technology and test results offer the opportunity of an easy adapting to the design requirements. PTFE composites are still used even if there are some other fluoropolymers trying to challenge it, as this polymer offers, especially in composites, the possibility of friction reduction. The new tendency is to use PTFE as adding material as solid lubricant and less as matrix, but there are several applications including those requiring chemical resistance in which PTFE could be an efficient matrix [2,5,6,8] or an adding material [3,7] for improving tribological behavior.

This paper investigated the surface quality of triboelements made of PTFE and PTFE + glass fibers when sliding in water against steel in order to evaluate 3D roughness parameters and to point out correlations among the analyzed parameters and the constituent percentage.

2. MATERIALS AND TESTING METHODOLOGY

Tests were done on four materials and their mechanical properties are given in Figure 1. Testing machine has an original design in order to allow a large range for sliding speed but low variations ($\pm 5\%$) and loading ($0 \dots 10 \text{ kN} \pm 3\%$) (Fig. 2, [2]). Each test involved a set of three plates (6x20x30 mm), introduced in a steel support disc. The mating disc was made of stainless steel (40 HRC and $R_a = 0.6 \dots 0.8 \mu\text{m}$). Plates were made of PTFE and PTFE composite with different glass fiber concentration. Testing conditions were: sliding speed $v = 0.7, 1.5, 2.5 \text{ m/s}$, values for average pressure being $p = 0.22, 0.77, 1.46$ and 2.02 MPa ,

respectively, open-circuit water temperature $\theta = 18 \pm 1^\circ\text{C}$. Average pressure was calculated as

$$p = \frac{F}{3A_{\text{plate}}} \text{ [MPa]}, \quad (1)$$

where F is the normal load [N], $n=3$ is the number of tested plates in one set and A_{plate} – the nominal area of one plate [mm^2].

Friction coefficient was calculated based on the outputs from the torsion gauge 6,

$$\mu = \frac{F}{F_f} = \frac{F}{M_r / r_a}, \quad (2)$$

where F is the normal load, F_f – the friction force, M_r – the resistant torque as measured by the gauge 6 (fig. 2) and r_a – the radius from the rotation axle of the steel disc to the center of the plate, during a sliding distance of 5,000 m (rate sampling being 1/sec). Plates' position may be changed in order to obtain different sliding speed, allowing also to calculate average wear if $r_{a1} = r_{a2} = r_{a3}$.

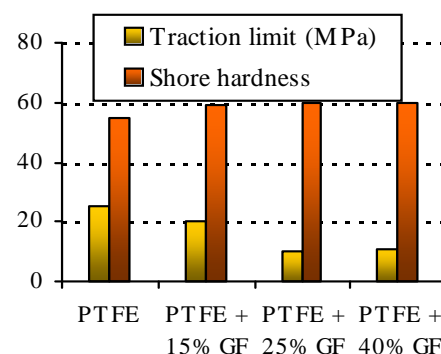


Figure 1. Tested materials (gf – glass fibers)

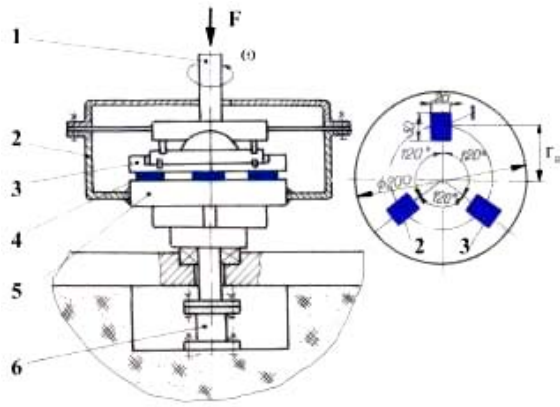


Figure 2. Testing device and samples' placement:
 1 - driving shaft, 2 - enclosure,
 3 - mobile triboelement, 4 - fixed triboelement (with plates 1, 2 and 3), 5 - base board, 6 - torsion gauge

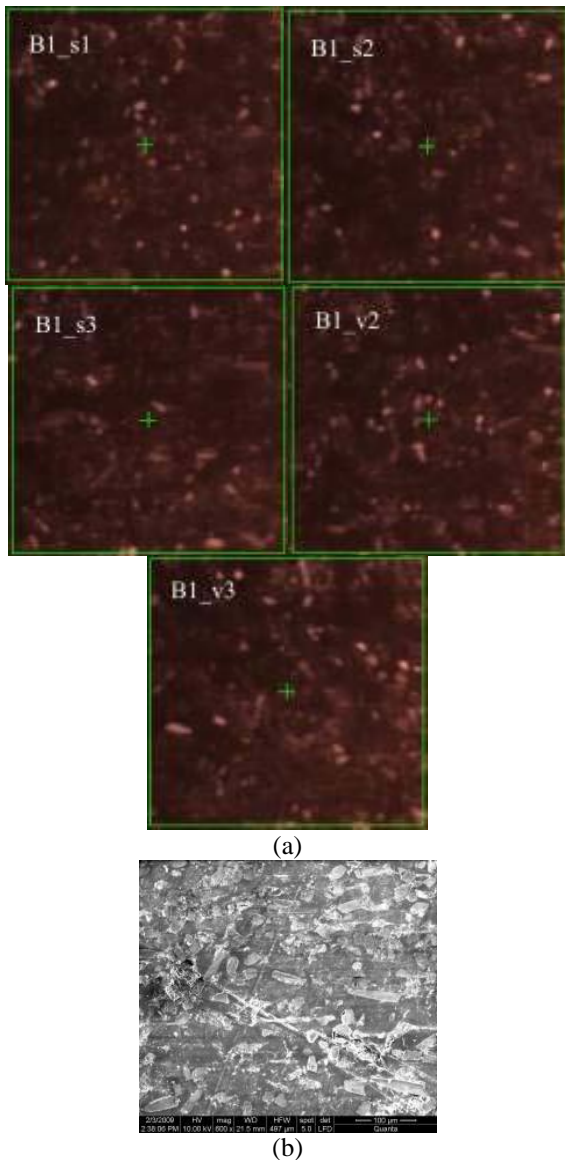


Figure 3. a) investigated surfaces on the same sample, for 5 measurements; b) SEM image of B1 sample

For each material and for the testing conditions ($v=2.5$ m/s, $p=2.02$ MPa), a plate from each set of three, was the subject of this investigation, using a CETR contact profilometer and its dedicated soft for analysis [9]. There were recorded the topography of 5 zones of $500 \mu\text{m} \times \mu\text{m}$ in the central region of the plate, one next to the other, 3 in the sliding direction and 2 in the radial direction, coded as in Figure 3 [10].

Figure 3 presents the investigated zones for the composite with 40% GF. The results of the analyzed parameters for one of the three plates that forms a tested set for each of the studied materials are given in Figures 5 and 6.

A reduced number of measurements could induce evaluation errors as 3D investigations the authors having access to, are small ($500 \mu\text{m} \times 500 \mu\text{m}$), especially on S_q and S_{sk} as they point out local topography disturbance. S_a seems to be unaffected by the number of measurements and also S_k , but S_{ku} , S_{vk} have high maximum values above the obtained average. The only parameters having the spread of values around 16% as recommended by [10], are S_a and S_k .

3. RESULTS AND DISCUSSIONS

3.1. Tribological behavior

Wear as average mass loss of a plate after 5,000 m of sliding in water in open circuit, is given in Figure 4a for the test regime and Figure 4b presents the evolution of friction coefficient for the same regime. In this paper quality investigation is done only for the sliding regime characterized by an average pressure of $p=2.02$ MPa and a sliding speed of $v=2.5$ m/s. Negative values for wear are possible because of continuous process of fragmenting and embedding of wear debris together with small water droplets and water solid impurities that remain insulated into the superficial layers, increasing the plate mass.

SEM images in Figure 6 reveal mechanical processes characterizing the superficial layers of the polymer and composites and they were done after testing under the conditions ($v=2.5$ m/s, $p=2.02$ MPa, water lubrication in open circuit):

- the polymer has a different behavior when tested in contact with steel counterpart, including abrasion, localized flows, transfer on the steel surface, material detaching as rolled particles, re-embedding of wear particles etc.,
- for composites the processes differ in intensity and aspects: the polymeric matrix has lower displacements and reveal neither deep plough traces, nor overlapping. the random fiber net allows reducing the polymer flow and detaching, but glass fibers on the surface are bearing enough load to be worn, fractured at medium glass fiber concentration (15...25%wt); statistically, fibers remained on the

surface have been fractured at their end situated on/out the surface, the fragments being embedded near-by and, thus, “consolidating” the polymer in the fiber neighborhoods, but at higher concentration (40% GF), many fibers are totally fractured, around the length middle, the process of fiber agglomeration being the result of wearing (tearing) out the polymer, the external load being now supported by a rigid structure, formed by the random arrangement of fibers within the superficial layer, a similar process being analyzed in [4, 5].

For the tested composites, at $v=2.5$ m/s, the friction coefficient becomes stable for all the composites, except for the polymer that varies within the range 0.008...0.02; there is a general tendency that friction coefficient has greater values at starting, but it becomes stable after $\sim 2,500$ m of sliding (Fig. 4b).

By analyzing the wear diagram (Fig. 4a), the following aspects may be pointed out:

- composites have a better tribological behavior as their wear is four, even ten times or less than the polymer wear, under similar testing conditions;
- for the set of three plates involved in each test, results are spread in a large range ($\pm 10...15\%$ around average value, calculated as $\Delta m = (\Delta m_1 + \Delta m_2 + \Delta m_3) / 3$, the spread being larger for the polymer and the composite with the highest concentration, 40% GF);
- comparing only these four tested materials, the composites should be recommended for similar applications instead of the polymer;
- for two composites (15% and 25% GF), results pointed out specific processes characterizing composites with short fibers: wear decreases when average pressure increase as a result of compressing the tribolayer, PTFE remaining kept in a non-arranged fiber net. Also, small changes in the fiber net allow capturing water drop or impurities, so sample mass may increase (see Fig. 4a and [5]).

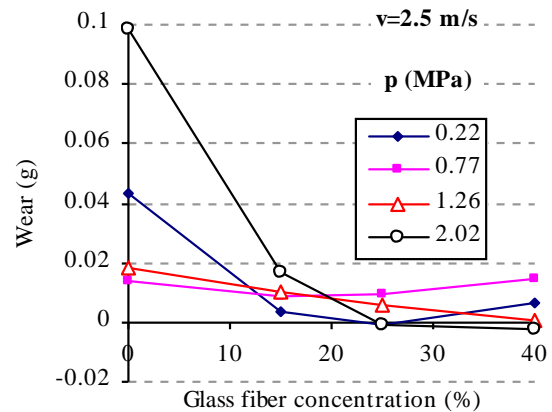
Tribological parameters as friction coefficient and wear of composites with PTFE matrix depend on tribotesters by geometrical shape and dimensions [4,8], but processes within the superficial layers are similar, fact proved by SEM images or 3D profilometry analysis, even if for polymeric composites the studies are still a few [1,4,6].

3.2 Analysis of several 3D parameters of surface topography

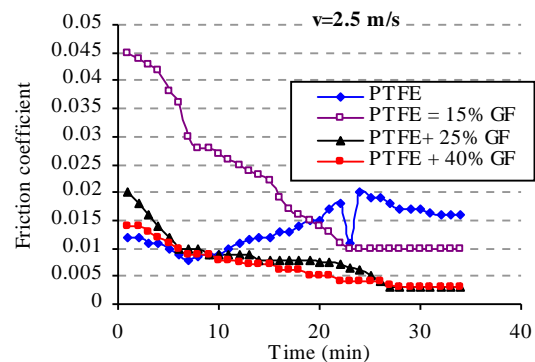
Profilometer PRO500 3D (with stylus) was used to measure the surface topography [16] assisted by a dedicated soft [9]. The selection of area size is important since this should be large enough to characterize a representative part of the surface or at least to generate stable parameter values. Here there were chosen zones in the plate center. The vertical range was set at $500 \mu\text{m}$ and the scan speed was selected as $35 \mu\text{m/s}$. All records have been done

with 200 points on each line. Pitch between lines was set at $5 \mu\text{m}$. All 3D parameters were calculated for raw profiles because they offer the possibility of pointing out extreme values [10], this being one of the aim of the paper: to detect extreme values of the analyzed parameters and, as it is written in [1, 9] the raw profiles help „building” a virtual image closer to the actual one. The equivalent contact force of the stylus was set for polymeric surfaces, at 16 mg.

There were analyzed here only some of 3D amplitude parameters: the roughness average S_a [μm], the root mean square (RMS) parameter, S_q [μm], the surface skewness, S_{sk} [-], the surface kurtosis, S_{ku} [-], the peak-peak height [μm] and three parameters obtained based on the bearing area curve: the reduced summit height, S_{pk} [μm], the core roughness depth, S_k [μm], the reduced valley depth, S_{vk} [μm], as defined in [9]. The wear value has a minimum for $\sim 25\%$ GF, but only S_{sk} has an evolution that could be related to the wear one: S_{sk} seems to be a “mirror” of wear evolution as it has a maximum in the same range where the wear is minimum. S_{ku} plot has a similar shape as for wear, but the point obtained for 40% glass fiber does not confirm this tendency (Fig. 5).



a) Wear as function of glass concentration



b) Friction coefficient

Figure 4. Tribological behavior of tested materials

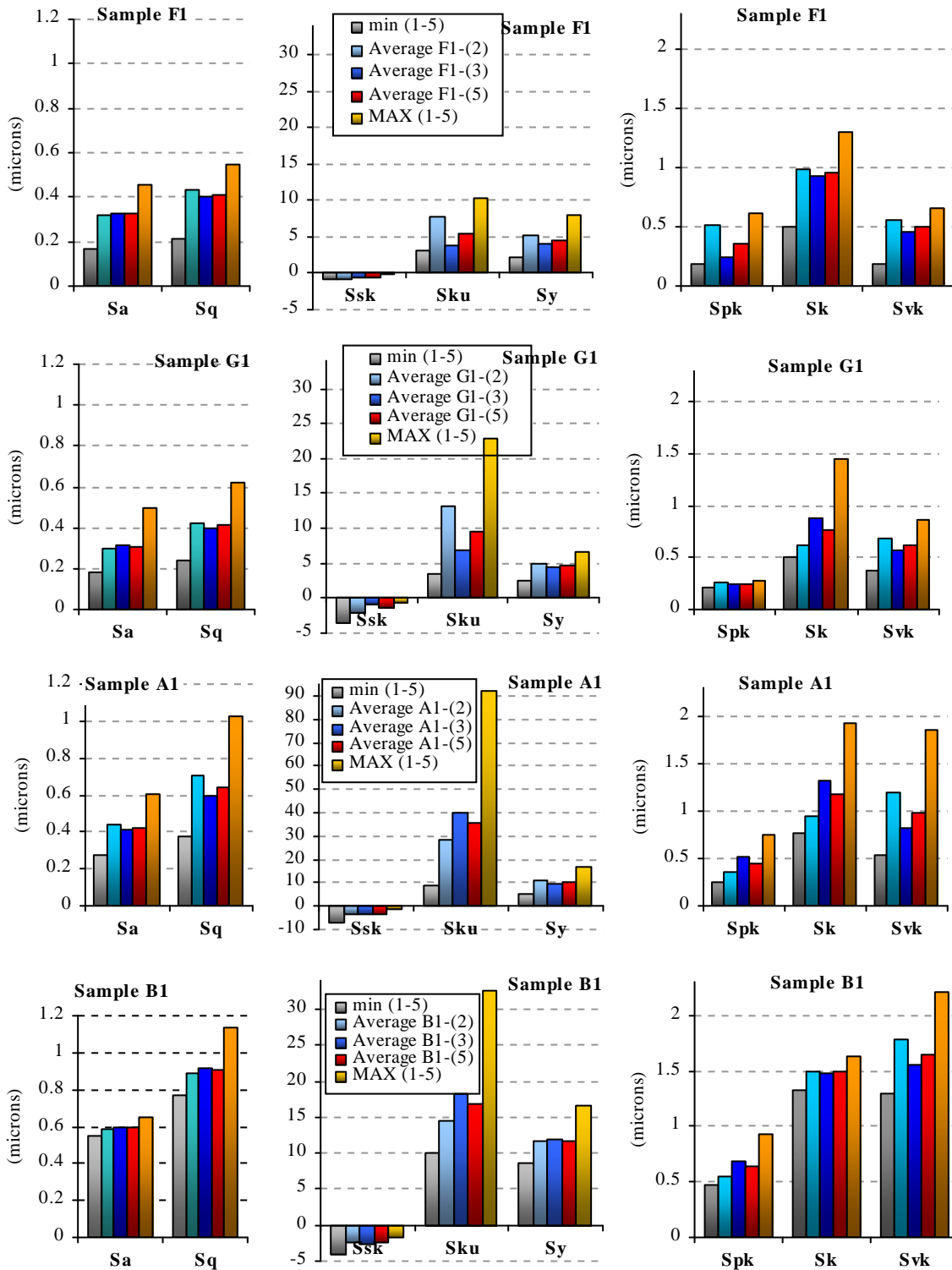


Figure 5. 3D parameters for the studied plates: F – PTFE, G – PTFE + 15% GF, A – PTFE + 25% GF, B – PTFE + 40% GF; GF – glass fibers

As $S_{sk} < 0$, it may be a bearing surface with holes and its high values may indicate extreme holes or peaks on the surface. S_{ku} being higher than 3, reflects a surface with high centered distributions of peaks. Average values and up and down deviations for the 5 measurements on the studied samples are given in Table 1.

By analyzing values of 3D parameters for the tested materials and conditions it could be concluded that surface is still smooth enough to continue the tribosystem functioning, but there are insulated micro-zones with higher maximum values, which could reveal the fibers' fracturing (see values for S_y , S_{pk}).

It could be concluded that for assessing the quality of worn surfaces there is not possible to apply rules and recommendations given in [10] and each research should be adapted taking into account

the tribosystem, including materials in contact, triboelements' shapes, regime (dry, lubricated, boundary lubricated), movement type, environment requirements.

Table 1. Average values and up and down deviations for the 5 measurements

Material	Range of deviations for studied parameters
PTFE	$Sa=0,32_{-88,6\%}^{+41,0\%}$; $Sq=0,41_{-80,1\%}^{+31,9\%}$; $Ssk=-0,58_{+133,1\%}^{-76,0\%}$; $Sku=5,4_{-132,2\%}^{+90,4\%}$; $S_y=4,5_{-132,2\%}^{+78,1\%}$; $Svk=0,49_{-94,6\%}^{+32,7\%}$; $Sk=0,95_{-83,4\%}^{+36,0\%}$; $Spk=0,35_{-119,9\%}^{+73,0\%}$
PTFE + 15% glass fibres	$Sa=0,30_{-104,5\%}^{+62,3\%}$; $Sq=0,41_{-91,4\%}^{+50,3\%}$; $Ssk=-1,43_{+196,9\%}^{-49,9\%}$; $Sku=9,46_{-203,5\%}^{+140,7\%}$; $S_y=4,65_{-90,1\%}^{+44,0\%}$; $Svk=0,61_{-79,6\%}^{+39,6\%}$; $Sk=0,77_{-121,9\%}^{+88,0\%}$; $Spk=0,26_{-30,1\%}^{+13,5\%}$
PTFE + 25% glass fibres	$Sa=0,42_{-78,8\%}^{+43,2\%}$; $Sq=0,63_{-103,0\%}^{+61,2\%}$; $Ssk=-3,33_{+170,5\%}^{-66,4\%}$; $Sku=35,45_{-234,9\%}^{+159,4\%}$; $S_y=10,2_{-108,2\%}^{+60,9\%}$; $Svk=0,97_{-135,2\%}^{+91,0\%}$; $Sk=1,17_{-98,2\%}^{+64,3\%}$; $Spk=0,45_{-110,1\%}^{+66,7\%}$
PTFE + 40% glass fibres	$Sa=0,59_{-16,3\%}^{+8,5\%}$; $Sq=0,90_{-40,6\%}^{+25,8\%}$; $Ssk=-2,50_{+97,5\%}^{-31,5\%}$; $Sku=16,80_{-133,7\%}^{+93,9\%}$; $S_y=11,77_{-68,5\%}^{+46,6\%}$; $Svk=1,64_{-54,8\%}^{+33,5\%}$; $Sk=1,48_{-20,6\%}^{+9,6\%}$; $Spk=0,69_{-73,6\%}^{+46,6\%}$

4. CONCLUSIONS

For tested sliding speeds, the wear tendency is similar for the tested material, but values for mass loss are almost one order less for the composites as compared to PTFE. For higher speed (2.5 m/s) composites' wear are reduced due to a synergetic effect of at least a partial water film and the polymer compression into the non-uniform fiber net. The high wear gradient between 0% GF (the polymer) and 6...10% GF suggests that at a lower speed, the composites offer conditions for a partial EHD regime. The presence of a fluid film is proved by both the very reduced wear, even if using a poor lubricant as water [4, 7] and the very low values of the friction coefficient.

Wear has been strongly influenced by fiber concentration (see Fig. 4a). Without fibers, the thin micro-bands of polymer are detached with high rate, the water, especially at higher pressure, promoting tearing of the material, rolling and rapid movement of this debris outside the contact. Even a rare and random net of fiber keep the polymer of being peeled, rolled and detached from the surface.

By analyzing the variation of average values as a function of the measurement number (fig. 5) it is obvious that 2...3 measurements are not representative at least for the studied surfaces, but 5 measurements have given a good indication of the surface quality, especially if this assessment is not reduced to studying Sa parameter. Comparing the average and extreme values for the analyzed amplitude 3D parameters, one may notice two distinct groups (see also Table 1):

- the group of Sa , Sq and Sy that have a slight

tendency to increase when the GF concentration increases, but with measured values spread in a not so large range around the average value,

- the group of Sku and Ssk that spread on a large range.

By analyzing the functional parameters the following conclusions could be drawn:

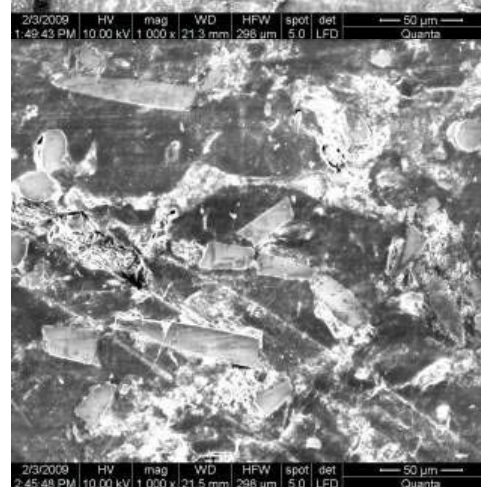
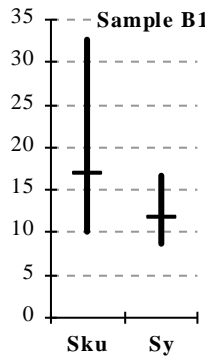
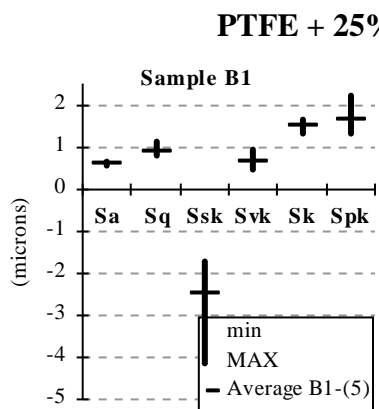
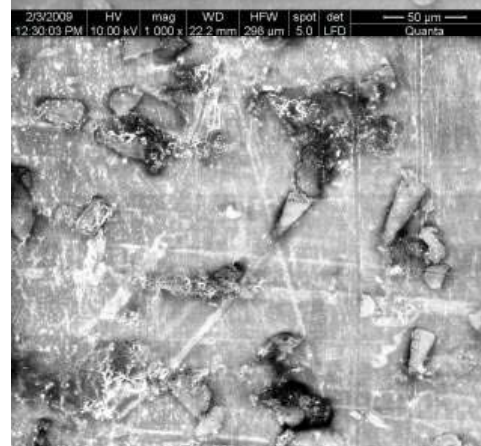
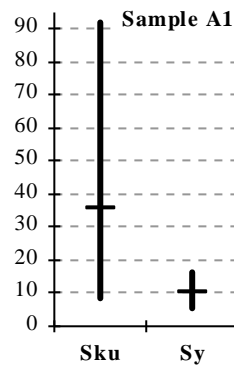
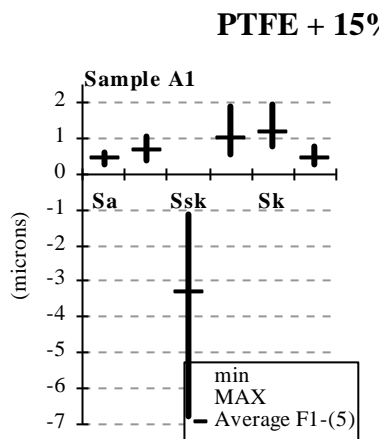
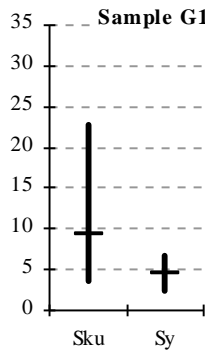
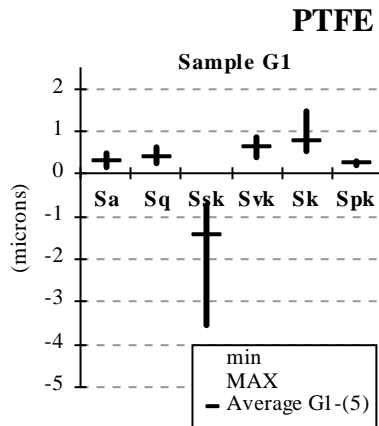
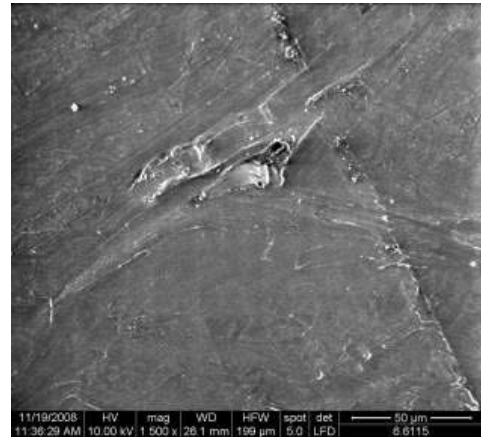
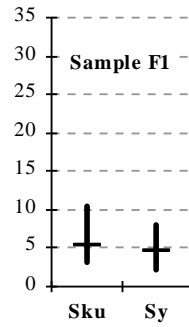
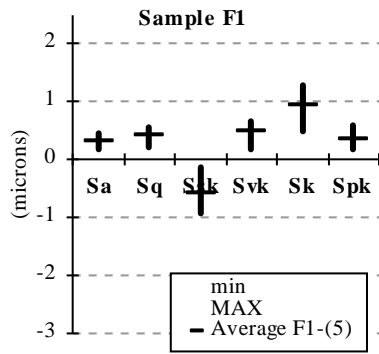
- Svk is slightly increasing when the GF concentration increases, but the value of 1.6 μm for the composite with 40% GF means that many glass fibers could remain outside the matrix being sources of micro-abrasions;

- Sk is the functional parameter with higher values as compared to other ones, Spk and Svk , meaning a good bearing core zone of the superficial layers for all tested materials, the lowest values being obtained for the composite with 15% GF;

- Spk has a large variation for the polymer, logically because of tearing off the polymer and of re-“bonding” of the polymeric debris, but when adding glass fibers this parameters becomes lower, especially for 15% and 25% GF;

- the highest values for these parameters were obtained for the composite with the highest glass fiber concentration (40%wt), but wear of this composite (see Figure 4a) still recommends it for actual applications with water lubrication, high speed and average pressure around 2 MPa.

These results underline the possibility of relating 3D roughness parameters to the tribological ones (wear, friction coefficient etc.) for polymeric composites, too. But data should be enough numerous in order to estimate with high degree of confidence the surface quality with the help of 3D roughness parameters.



PTFE + 40% GF

Figure 6. Amplitude and hybrid parameters for one plate from a three-plate set: average of all 5 measurements and the up and down deviations from this average value

REFERENCES

1. **Blunt L., Jiang X.**, 2003, *Advanced techniques for assessment surface topography*, Elsevier.
2. **Bratcu O., Tomescu (Deleanu) L., Bologa O.**, 2002, "Tribological Behaviour of PTFE + Glass Fibber Composites Used for Axial Bearings under Water Lubrication," *Analele Universit ii "Dun rea de Jos" din Gala i*, Fascicle VIII, Tribology, pp. 61-65.
3. **Burris L.D., Sawyer G.W.**, 2006, "A Low Friction and Ultra Low Wear Rate PEEK/PTFE Composite," *Wear*, 261, pp. 410-418.
4. **Dasari A., Zu Z.-Z., Mai Z.-W.**, 2009, "Fundamental Aspects and Recent Progress on Wear/Scratch Damage in Polymer Nano-Composites," *Materials Science and Engineering R*, 63, pp. 31-80.
5. **Deleanu L., Birsan I.G., Andrei A., Rîp M., Diaconu N.**, 2008, "PTFE Composites and Water Lubrication. II. Surface Characterisation," *Revista de Materiale plastice*, vol. 4, pp. 332-338.
6. **Khedkar J., Negulescu I., Meletis E.I.**, 2002, "Sliding wear behavior of PTFE composites," *Wear*, 252, pp. 361-369.
7. **Larsen T., Andersen T.L., Thorning B., Horsewell A., Vigild M.E.**, 2008, "Changes in the Tribological Behavior of an Epoxy Resin by Incorporating CuO Nanoparticles and PTFE Microparticles," *Wear*, vol. 265, n°1-2, pp. 203-213.
8. **Sawyer G.W., Freudenberg K.D., Bhimaraj P., Schadler L.S.**, 2003, "A Study on the Friction and Wear Behavior of PTFE Filled with Alumina Nanoparticles," *Wear*, 254, 573-580
9. **** The Scanning Probe Image Processor SPIP™, Version 4.7 (2008).
10. **** SR SR EN ISO 4288:2002 Geometrical product specifications (GPS) - Surface Texture: Rules and Procedures for the Assessment of Surface Texture.

Minodora RÎP
e-mail: *minodora.ripa@ugal.ro*

Simona BOICIUC

University "Dunarea de Jos" of Galati,
ROMANIA

CHARACTERISATION OF LASER CLADDING WITH NI-Cr-B-Fe- Al ALLOY BY PROFILOMETRIC STUDY OF THE SCRATCH TRACKS

The sliding indentation test have good results for characterizing metals and alloys, polymers, ceramics, composites and a great range of coatings, and often it is connected with wear tests and modeling and simulation techniques. This paper presents research results on several multi-layer claddings achieved by powder injection of Ni alloy from the Ni-Cr-B-Fe-Al system, in the bath melt by CO₂ laser in continuous wave. The comparisons of the geometrical characteristics of the different digital depth profiles confirm the better scratch behavior of the laser cladding layers.

Keywords: laser cladding, sliding indentation, wear track

1. INTRODUCTION

Laser surface treatments have become a profitable alternative to conventional surface processing technologies in many applications, and the laser has become a valuable and cost – effective tool. Laser surfacing offers a clean and reliable method of depositing coatings onto substrates, especially in order to increase wear and corrosion resistance.

Laser cladding is a high precision technique to generate desired surface properties, whilst retaining the mechanical properties of the substrate [1-4]. The most frequently used cladding materials are the powders in the single step processed (blown powder). The two step process has the advantage of very low dilution, but its use is limited to almost flat surfaces. The blown powder process is used more by industry, due to its better flexibility with respect to surface geometry. It is also easier to blend powders for a required chemical composition.

In order to maintain the genuine properties of the clad material, only a very thin layer of the substrate must be melted to obtain the minimum dilution (0,5 - 3%) of the metallurgical bond of the additional material with the substrate. The structure and the properties depend on the melting temperatures of both the support and clad material, their chemical composition and they may vary by applying various thermal regimes and granulation of the powder added [5,6].

This paper presents research results on several multi-layer claddings achieved by powder injection of Ni alloy from the Ni-Cr-B-Fe-Al system, in the bath melted by CO₂ laser in continuous wave.

Wear and friction of sliding components are highly related to their resistances to contact deformation and damage [7].

A scratch test combined with an instrumented indentation test is a very useful tool in examining the microscopic surface deformation mechanisms and processes that are taking place under mechanical contact/sliding. The scratch test was first suggested for coating adhesion measurements more than thirty years ago. The scratch testing method is today widely used, especially by the coating industry and coating development laboratories, as well as in research for evaluating the tribological properties of coatings and other hard surfaces [8]. Different standard were elaborated in Europe and USA.

The scratch test gives good results for characterizing metals and alloys, polymers, ceramics, composites and a great range of coatings [7-9,10] and often it is connected with wear tests [9, 11-13] and modeling and simulation techniques [8,11,13].

2. LASER CLADDING EXPERIMENTAL RESEARCHES

The powder used for laser cladding, "Alliages Speciaux 7569 Alliages Frites", has the following chemical composition (wt.%): 8.9%Cr; 4.5%Fe; 5.1%B; 2.4%Al; 0.6% Cu; balance Ni [2,3]. Grain fractions from 80-90 μm range were separately screened in order to be used as addition material. Powder had a spherical shape, which provided a fluid flow of addition material through the injection system. Before the addition of the material feeding

into the system tank, powder was dried at 110°C temperature for 15 minutes [3].

Cladding was performed on a 1C45, SR EN 10083-1:1994 steel specimen, by a Laser GT 1400W (Romania) type CO₂ continuous wave equipment, with x-y-z coordinate running table and computer programmed running. This equipment, provided by powder injection system on the laser melt surface, was updated at UZINSIDER Engineering, Gala i, Romania.

After adjusting the power level of laser radiation and laser beam diameter on the specimen surface, claddings were carried out under the form of parallel strips partly overlapping, with a transverse advance step of 1,5 mm. Final layer thickness was the result of overlapping 4-5 layers.

To determine the optimum laser cladding, the flow rate of material added, the surface scanning speed and the initial specimen temperature were varied. Researches on different working regimes

(working conditions and the thickness of the clad layers) were performed.

Table 1 shows the characteristics of the optimal cladding regime, which provides the highest hardness and thickness of the surface layer.

In order to characterize the exploitation behavior of the clad layers, for applications requiring wear and corrosion resistant surfaces [4-6,13] the following tests were performed: determination of the thermal stability; wear test on rotary disk with abrasive paper (STAS 9639-81 – Romanian Standard); corrosion tests; scratch test; profilometric studies of the scratch tracks.

The specimens realized with this regime were characterized as follows: macro and microstructural analyses (fig. 1); hardness (HV₅); microhardness (HV_{0,1}); phase quality analysis by X ray diffractometry (DRON 3 Diffractometer); EDX microanalysis of the clad Ni alloy composition (SEM – XL 30ESEM TMP - Phillips, spectrometer EDS - EDAX Sapphire).

Table 1. Working regime used in laser cladding

Added material rate [mg/s]	No. of overlapping runs	Working regime					
		P [W]	v [mm/s]	d _s [mm]	P _{av} [mm]	g [mm]	Hardness HV ₅ [MPa]
105	4	1150	7,5	1,8	1,5	2,07	11450

NOTE: P - laser radiation power , v – scanning speed of the laser beam on the processed surface, d_s – diameter of the laser beam; p_{av} - transversal advance step, g - thickness of clad layers; m_p - flow rate of added material.

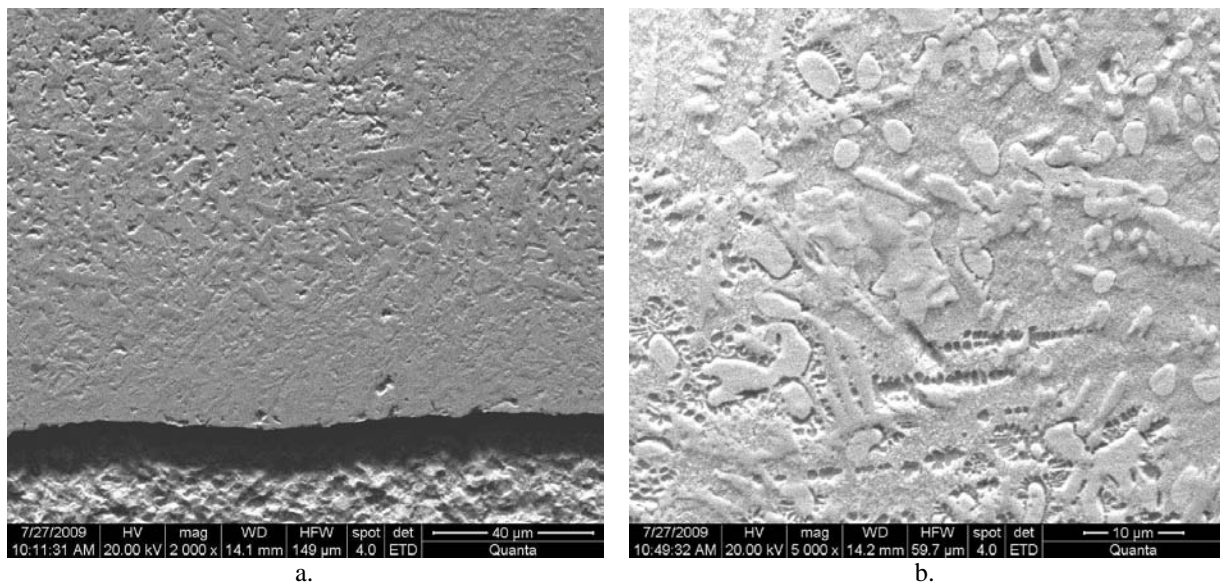


Figure 1. Microstructure of clad nickel – based alloy ($v = 7,5 \text{ mm/s}$, $m_p = 105 \text{ mg/s}$)
a) base of clad layer; b) surface layer . Electrolyte attack, solution 50% HNO₃ [1,3,14]

3. SCRATCH TEST

The scratching is a physical process during which a sharp object is pressed onto, and drawn over the surface of the coating simultaneously. The normal load is either kept constant or progressively increased, depending on the purpose of the test and machine availability. During constant load scratch testing, the normal force on the scratch indenter is maintained at a constant level. Multiple tests at increased constant load levels can be used to determine the critical scratch load or scratch hardness. The constant load scratch requires more tests to find the critical point of damage, but it can be carried out in a less costly test rig compared to the progressive loading scratch test. It can also be used to detect non-uniformity of the coating over the entire surface. In a scratch test, as a result of friction, a

tangential load is added to the normal load. This friction traction superposes a compressive stress at the front edge of the contact and a tensile stress at the trailing edge [15].

3.1. Scratch rig and methodology

The scheme of the rig for scratching tests (sliding indentation) is presented in Figure 2. It has the following components: 1-frame, 2-ABB frequency converter, 3-electric engine, 4-elastic coupling, 5, 6, 7, 8-mechanical transmission, 9-horizontal column, 10-balls guiding, 11-vertical column, 12-balls guiding, 13-force transducer, 14-elastic system, 15-loading screw, 16- specimen, 17-sustenance surface, 18- specimen fixing device, 19-balls guiding, 20-force transducer, 21-screw for transversal movement, 22- indenter.

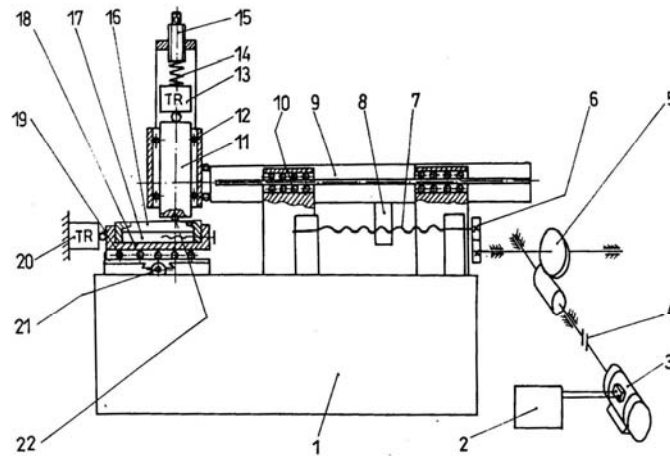


Figure 2. The components of the rig for scratching tests (sliding indentation) [16,17]

Because of the components of the mechanical transmission and the presence of the frequency converter, the speed of the column 9 is very slow and varies between 0 and 17 mm/min. In this experiment, the speed is set at 0.2 mm/s. Under this speed condition, the deformations are quasi-steady. The measuring system is composed by two force transducers (0...50 kN) and a data acquisition system. The indenter is a steel ball with a diameter of 12.675 mm. The normal forces used for indentation were: F1 = 2.886 kN; F2 = 4.330 kN; F3 = 5.773 kN; F4 = 7.216 kN.

3.2. Specimens

The substrate material used in this study is 1C45 steel grade with the following chemical compositions (wt.%): 13.75Ni, 2.72Mo, 0.019C, 0.50Si, 1.87Mn, 0.012S, 0.022P, 17.43Cr, 0.002Ni, 0.002Al.

Hardness differences between the center and edge of the laser clad layer were found. The center has higher hardness and the margins slightly lower

hardness. This is due to more intense heating of the edges, thus increasing the specimen surface temperature and increased evaporation processes.

Three specimens were tested: 1. code MB – specimen made of substrate material; code A – specimen from the center; B – specimen from the margins.

The presence of the intermetallic components (borides, carbides) cause the adherence inhibition. Their amount increases from the substrate material containing precipitates of cementite, for the specimen A, possessing a larger amount of borides. The maximum will be reached in the case of the specimen B, which has the highest hardness. Thus, the deformation behavior of the three specimens will be different.

The specimen surfaces were manufactured by grinding, perpendicular to the length. Experimental observations confirmed that this leads to an appropriate asperities orientation, in order to obtain very accurate wear scars. This is due to the plastic deformation (Figure 3) which could be measured with greater precision.

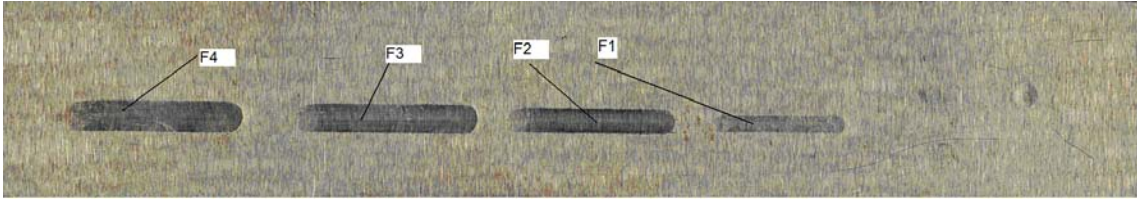


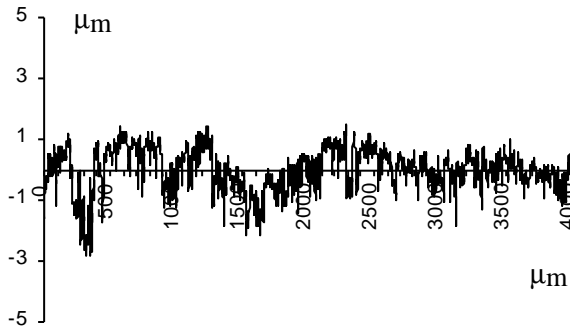
Figure 3. Picture of specimen MB with the scratch tracks

4. PROFILOMETRIC STUDY OF THE SCRATCH TRACKS

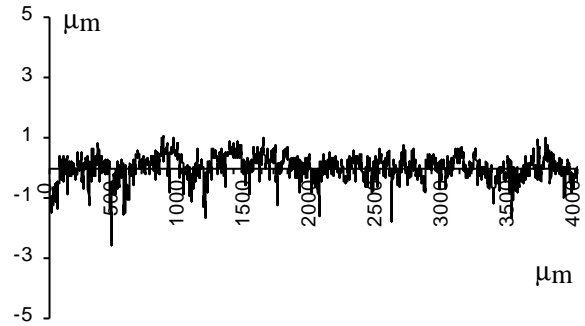
A stylus digital profilometer “SURTRONIC 3+” (Taylor-Hobson®) was used to assess the topography changes caused by scratching on laser cladding layer. For all the specimens, the average surface roughness was about $Ra \approx 0.210\mu\text{m}$. Figure

4 shows relevant roughness profiles for each specimen.

The specimen with scratching tracks is put on a support and guiding element (fig. 5) and could have a translation movement along its own axis. The stylus of the profilometer has a transversal movement over the track. As a result of this guiding, the cross-sections are parallel.



a) substrat material (code MB)



b) cladded specimen (code A)



b) cladded specimen (code B)

Figure 4. Roughness profile of specimens, before scratch test

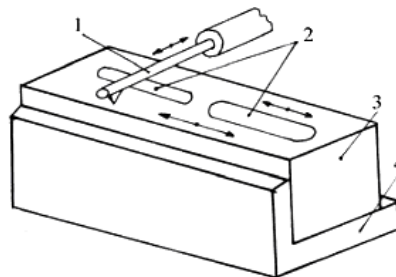


Figure 5. The support and guiding element: 1 – stylus of the profilometer, 2 - sliding indentation tracks, 3 - specimen, 4 - support and guiding element

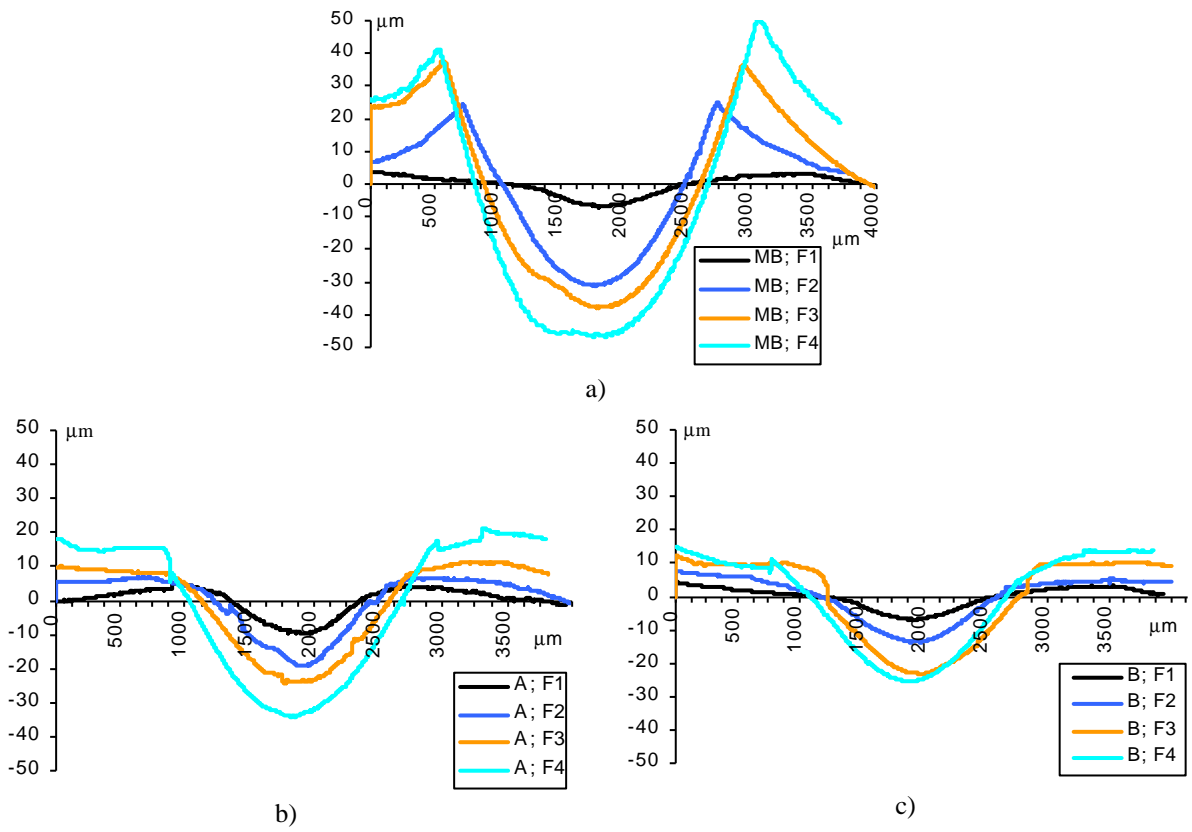


Figure 6. Comparison of the wear track depth profiles, (for the same specimen four plots are compared).
 Normal forces: F1=2.886 kN, F2=4.330 kN, F3=5.773 kN, F4=7.216 kN

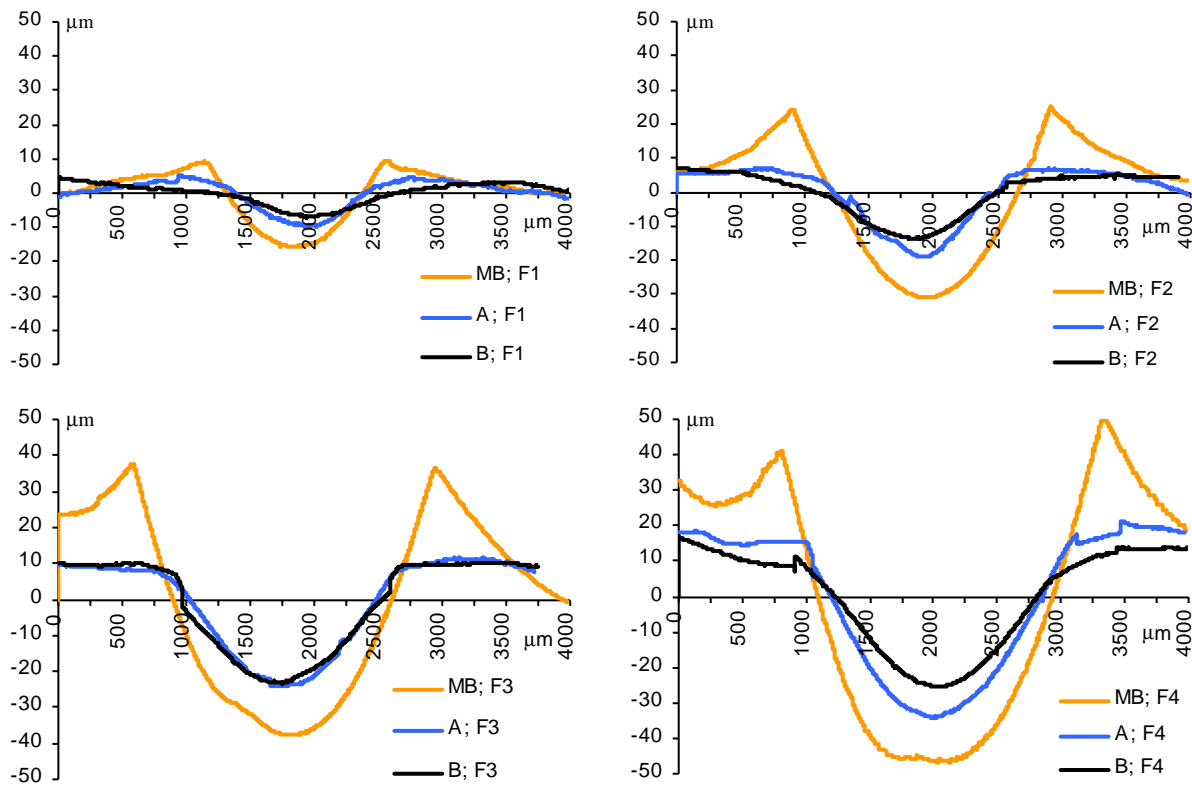


Figure 7. Comparison of the wear track depth profiles for the same force.
 Normal forces: F1=2.886 kN, F2=4.330 kN, F3=5.773 kN, F4=7.216 kN

The shape of the scratch tracks was obtained by measuring six depth profiles across each track with the stylus digital profilometer “SURTRONIC 3+”.

For the specimen code MB, the material is advanced plastically deformed, the indenter is in deep penetration; as consequence the friction surface is large and the adhesion tendency is high. Thus, for the basic material the increasing of normal force could lead to the increasing of the coefficient of friction. Analyzing the specimen A, it can be seen that plastic strain ratio is lower due to higher amounts of precipitates comparing to the case of the substrate material, resulting a lower penetration of the indenter and a lower friction surface associated with a lower adhesion trend.

In the case of the specimen B, it appears that high hardness, due to the large amount of borides make the plastic deformation to be minimal. The indenter penetration into the material is the lowest of the three cases.

Analyzing the depth profiles presented in fig. 6 some observations may be made:

- for the substrate material MB, the increasing of lateral ridges occurs with the increasing of normal force.

- due to the increasing of the normal force, material A is deforming less under the action of the ball, on both width and depth as comparing with substrate material and lateral ridges are more flattened.

- the specimen material code B, which has a higher hardness and yield limit than the specimen A, shows a lower deformation on both depth and width, lateral ridges being lower.

Depth profiles plotted in Figure 7 present a comparison of the plastic deformations of the investigated materials, on the same normal load. Due to the increasing hardness layer, the profile depth reduces, as well as the height of the lateral ridges.

This fact indicates that the clad laser surface has a higher resistance related to plastic deformation than the substrate material.

Figure 8 presents the geometrical characteristics of a depth profile, computed by the software of the profilometer.

Table 2 shows the values of the width, the maximum depth and the cross-sectional area of the wear track for the specimen code A.

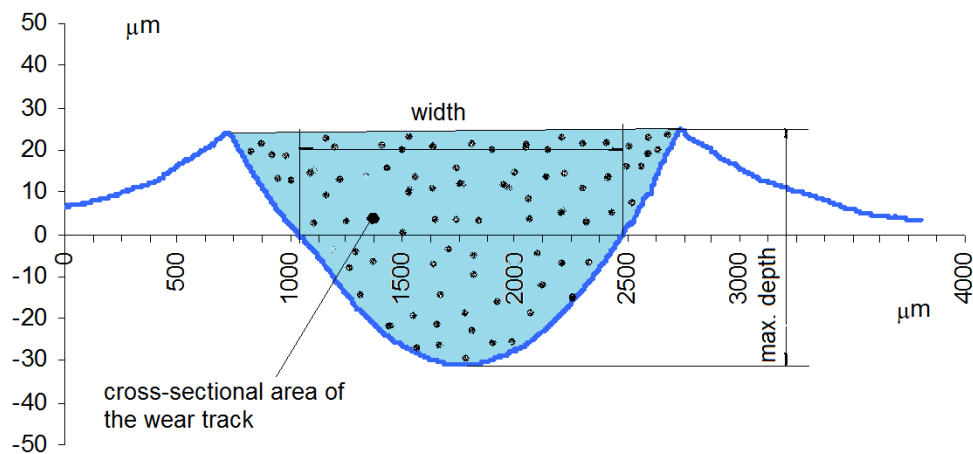


Figure 8. Geometrical characteristics of a depth profile

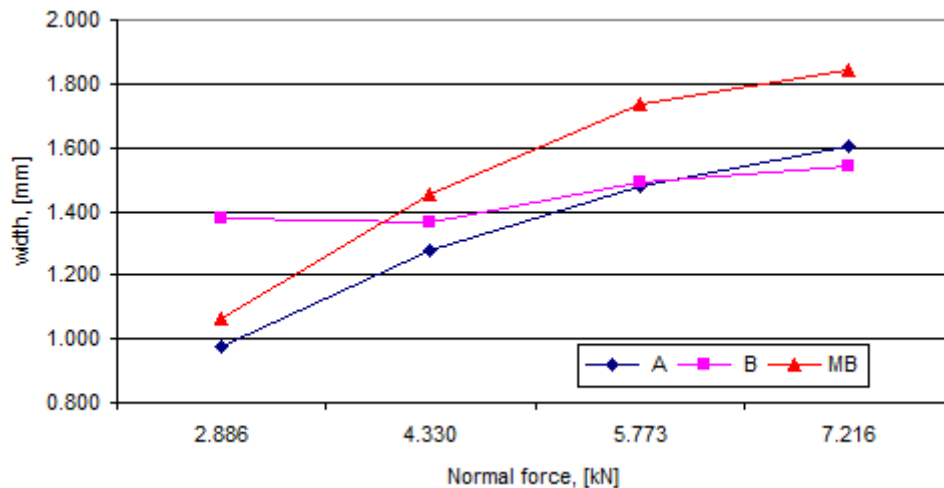


Figure 9. Track depth variation versus normal force

Table 2. Example: values of geometrical characteristics of the depth profile, specimen code A

Profile code	Normal force	Width [mm]	Maximum depth [μm]	Cross-sectional area of the wear track [μm^2]
A1_u_1	F1	1	10.1	5953
A1_u_2		1.01	10.7	6045
A1_u_3		1.01	9.91	6193
A1_u_4		1	11.1	7357
A1_u_5		1.11	9.88	6857
A1_u_6		0.86	6.72	3437
A1_u_7		0.93	9.16	5278
A1_u_8		0.94	7.28	3827
A1_u_9		0.95	8.14	4087
A2_u_1	F2	1.33	17.5	14342
A2_u_2		1.33	18.3	13849
A2_u_4		1.25	19.7	14963
A2_u_5		1.23	20.2	14158
A2_u_6		1.24	15.5	11266
A2_u_7		1.29	20.2	15605
A2_u_8		1.33	17.3	12532
A2_u_9		1.27	19.1	13180
A2_u_10		1.28	14.8	11196
A3_u_1	F3	1.5	23.5	22101
A3_u_2		1.46	24.2	22265
A3_u_3		1.47	23.3	21020
A3_u_4		1.51	24.6	22941
A3_u_5		1.46	22.8	21298
A3_u_6		1.46	25.3	22218
A4_u_1	F4	1.64	34	35704
A4_u_2		1.58	36	36262
A4_u_3		1.6	33.2	33981
A4_u_4		1.539	36.3	35830
A4_u_5		1.62	38.7	39123
A4_u_6		1.64	39.5	39129

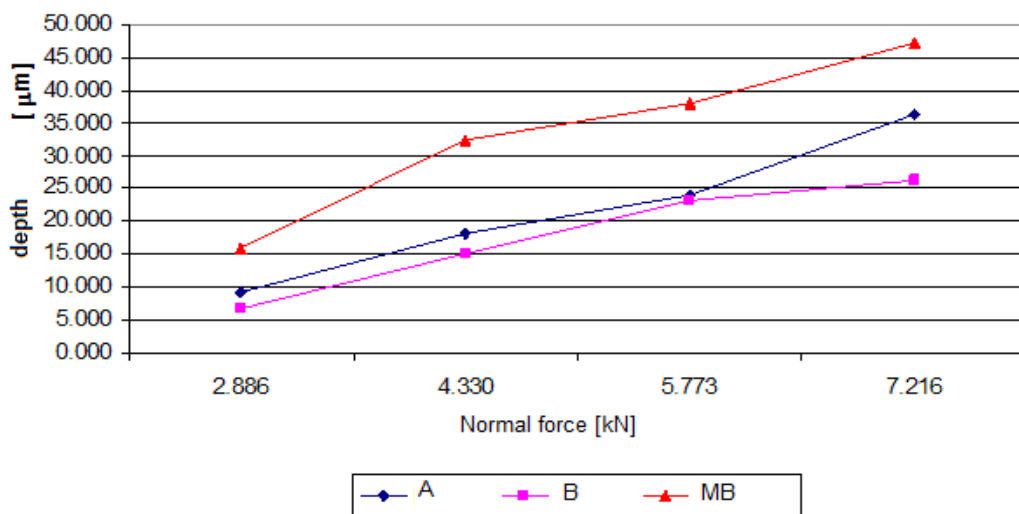


Figure 10. Track width variation versus normal force

Figure 9 presents track depth variation with normal force and Figure 10 shows track width variation with normal force. In Figure 9 it could be noticed that for small normal forces the deformation depth of specimen code B is reduced but the zones near to the track begin to participate at the deformation process, recording a maximum width, in good correspondence with fig. 6.

With the increasing of the normal force, in depth deformation becomes prevalent and for the force F4 the width for specimen B get less than the width of the specimen A.

Analyzing the track width variation with the normal force (fig. 10), it appears that trace depth growth occurs due to normal force increasing and to the arising of plastic deformation, a fact more visible for the substrat material.

5. CONCLUSIONS

This paper presents the first step in the complex characterization of laser cladding with Ni-Cr-B-Fe-Al alloy by profilometric study of the scratch tracks. The comparisons of the geometrical characteristics of the different digital depth profiles confirm the better scratch behavior of the laser cladding layers. The researches will continue with more complex tribological investigations, in order to succeed a complete characterization of the properties of the hard surfaces.

REFERENCES

1. **Boiciuc, S.** et al., 2009, "EDX Analysis of Laser Cladding Layers with Ni-Cr-B-Fe-Al Alloy," *Conference UGALMAT 2009*, Galati, Romania.
2. **Levcovici, D.T., Boiciuc, R., Levcovici, S.M., Gheorghie, C.**, 2006, "Laser cladding of M2 Steel on a steel substrate, The Intern," *Thermal Spray Conf. and Exposition (ITSC 2006)* Seattle, Washington, U.S.A, ASM Seattle 2006, Procs on CD.
3. **Levcovici, S.M., Levcovici, D.T., Gheorghie, C., Boiciuc, S.**, 2006, "Laser Cladding of Ni-Cr-B-Fe-Al Alloy on a Steel Support," *The International Thermal Spray Conference and Exposition (ITSC 2006)* May 15th-17th, 2006, Seattle, Washington, U.S.A, Proceedings on CD.
4. **Liu, X.-B., Wang, H.-M.**, "Microstructure and Tribological Properties of Laser Clad /Cr₇C₃/TiC Composite Coatings on -TiAl Intermetallic Alloy," *Wear* 262 (5-6), pp. 514-521.
5. **Gedda H.**, 2000, "Laser Surface Cladding - A Literature Survey," Lulea University of Technology, Division of Materials Processing, Sweden.
6. **Schneider, M.F.**, 1998, *Laser Cladding with Powder*, Ph. D. Thesis, University of Twente, Enschede, Holand/
7. **Futami T.**, et al., 2009, "Contact/Scratch-Induced Surface Deformation and Damage of Copper-Graphite Particulate Composites," *Carbon* 47 (2009), pp. 2742-2751.
8. **Holmberg K.** et al., 2006, "Tribological Contact Analysis of a Rigid Ball Sliding on a Hard Coated Surface. Part I: Modelling Stresses and Strains," *Surface & Coatings Technology* 200, pp. 3793 - 3809.
9. **Berns, H., Saltykova, A.**, 2009, "Wear resistance of in situ MMC produced by supersolidus liquid phase sintering (SLPS)," *Wear*, 267, pp. 1791-1797.
10. **Wang, Z.Z., Gu, P., Zhang, Z.**, 2010, "Indentation and Scratch Behavior of Nano-SiO₂/Polycarbonate Composite Coating at the Micro/Nano-Scale," *Wear* 269, pp.21-25.
11. **Avril L.**, 2003, *Elaboration de revetements sur acier inoxydable. Simulation de la fusion par irradiation laser. Caracterisation structurale, mecanique et tribologique*, PhD Thesis, Ecole Nationale Supérieure d'Arts et Métiers, Centre d'Angers.
12. **Emmerlich, J.** et al., 2008, "Micro and Macroscale Tribological Behavior of Epitaxial Ti₃SiC₂ Thin Films," *Wear* 264, pp. 914-919.
13. **Martukanitz, R.P., Babu S.S. and Vitek J.M.**, 2004, "Development of Advanced Wear and Corrosion Resistant Systems through Laser Surface Alloying and Materials Simulation," Applied Research Laboratory, State College, PA 16804, Oak Ridge National Laboratory.
14. **Boiciuc, S., Levcovici, S., Levcovici, D.T.**, 2007, "Structural Modifications in Laser Cladding Layers Heating up at Different Temperatures," *Metalurgia International*, nr.8, 2007, pp.14-19, Ed. Editura Stiintifica F.M.R.Bucharest, Romania.
15. **Friedrich, k., Schlarb, A.K.**, 2008, "Tribology of Polymeric Nanocomposites. Friction and Wear of Bulk Materials and Coatings," *Tribology and Interface Engineering Series*, 55. Editor: B.J. Briscoe, 2008.
16. **Spânu C.**, 2002, *Studii i cercet ri pe tribomodel privind deformatiile plastice in stratul superficial la rostogolire si la alunecare*, PhD Thesis, University Dun rea de Jos of Galati (in Romanian).
17. **Spânu, C.** et al., 2009, "Sliding Indentation Behaviour of The X 65 Hydrogenated Steel Grade," *The Annals of University "Dun rea de Jos" of Gala i*, Fascicle VIII, Tribology, XV (2), pp. 109-114.

Monica VLASE¹
e-mail: monica_utcb@yahoo.com

Andrei TUDOR²
e-mail: tudor@meca.omtr.pub.ro

¹ Technical University of Civil Engineering of
Bucharest, ROMANIA

² University POLITEHNICA of Bucharest,
ROMANIA

AN ANALYTICAL WEAR MODEL OF THE PIPES FOR CONCRETE TRANSPORTATION

The flow of fresh concrete in the pipe can be realized only when the concrete is saturated. The tribological solutions are formulated to obtain the saturation of concrete. The effect of flow in pipe is evaluated by the friction with the wall and the pipe wear. It is defined a critical angle of concrete impact in transition between horizontal and vertical pipe as a function to the friction coefficient, the velocity and the mean radius of solid particle in fresh concrete. The erosion wear model is proposed for inner wall pipe in contact with concrete.

Keywords: fresh concrete friction, erosion, wear model, fatigue

1. INTRODUCTION

Fresh concrete is a viscous two phases mixture, in which the solid phase, (sand, gravel) is suspended in the liquid phase, (cement binder and water). The binder is the slurry (suspension medium) of the solid phase and has a great importance in the rheological behavior of fresh concrete [1–3].

In order to be pumped through the metallic pipes, that is being pump able, fresh concrete must fulfill the following conditions:

- All the aggregates must be surrounded by the cement slurry which has also the role of binder, and to move freely in this liquid phase. That means the mixture must be saturated.
- To be able to form, near the solid wall of the pipe, a lubricant layer of cement slurry and aggregate with thin granulation.
- Under the concrete pumping pressure through pipes, to avoid the appearance of the segregation phenomenon, that is to avoid the separation of the solid and liquid phases or the aggregate deposition.

The levels of saturated and unsaturated concrete are suggestively presented in Figure 1. As it is shown in Figure 1, segregated concrete is an unsaturated mixture. The aim of this paper is to define the condition of flow of the fresh concrete in pipe and to analyze the effect of flowing on the wear of wall.

2. UNSATURATED CONCRETE VELOCITY

Concrete flow through a circular, curved pipe is different from a circular, straight-lined one. In order to analyze the flow average speed, it is suggested a model of the concrete flow under the action of weight forces and friction forces that

appear in the curved zone. Thus, it is considered an horizontal, circular pipe with d_i inner diameter, with R_k curvature radius under a ϕ_e angle, (Figure 2).

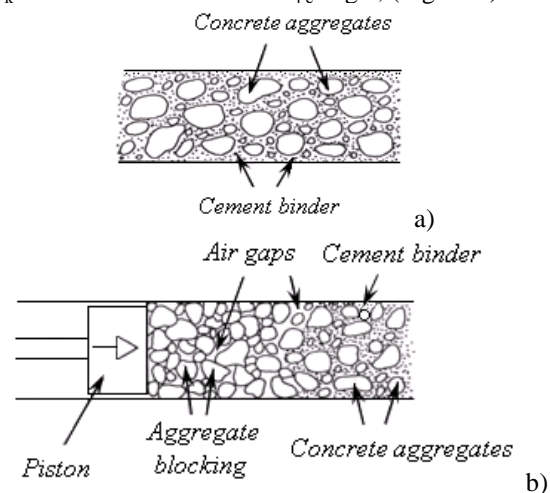


Figure 1. The saturation level of the concrete:
a) - saturated mixture; b) - segregated concrete
(unsaturated mixture), [3]

Regarding the concrete flow, the case of the horizontal pipe with vertical curvature is the most difficult one [4].

For a certain ϕ angle, it is considered an infinite small volume of concrete between the $d\phi$ elementary angle. The elementary concrete quantity (dG) in this infinite small volume is:

$$dG = \frac{Q_g}{v_m} R_k d\phi, \quad (1)$$

where Q_g is the gravimetric flow rate (N/s) of the pumped concrete, and v_m is the average speed of the concrete flow.

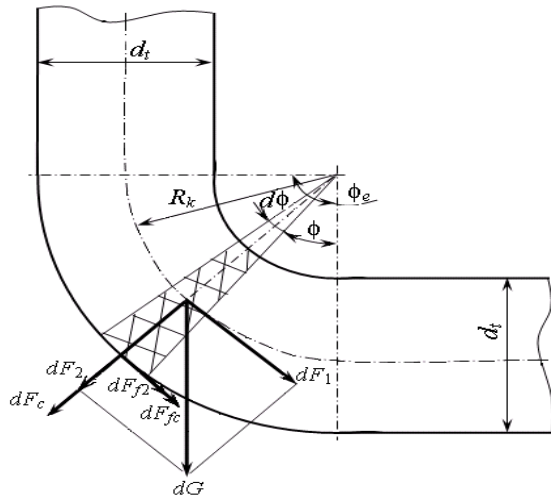


Figure 2. Concrete flow through quartered bond (angle pipe)

The elementary concrete quantity (dG) induces a certain pumping force in the flow direction, corresponding to the ϕ angle, and a friction force (dF_2) on the exterior or the interior pipe surface, depending on the position of the quartered bond (angle pipe) with the horizontal direction

Regarding the circular displacement of the concrete it will also appear centrifugal forces that will determine friction in the contact zone:

$$dF_{fc} = \frac{dG}{g} \frac{v_m^2}{R_k} \mu_e, \quad (2)$$

where: g is the gravitational acceleration; μ_e is the friction coefficient of the „concrete plug” with the pipe wall, at the exterior of the curvature.

Considering the mechanical equilibrium conditions, it can be deduced the average speed of the axial displacement of the „concrete plug” (v_m) and also, the angular speed of rotation of the „concrete plug” (ω_m) into the pipe, under the form of two differential equations of the first order:

$$\frac{dv_m}{d\phi} + \mu_e v_m + g R_k (\sin \phi + \mu_i \cos \phi) v_m^{-1} = 0; \quad (3)$$

$$\frac{d\omega_m}{d\phi} + 6\mu_e v_m - \frac{6g R_k}{v_m} \mu_i \cos \phi = 0. \quad (4)$$

The solution of the differential equation (3) (Bernoulli equation type, reducible to a linear equation) is under the form:

$$v_{am} = \frac{v_m}{v_{mi}} = e^{-2\mu_e \phi} - \frac{1}{v_{mi}^2 (1 + 4\mu_e^2)} [(2\mu_i + \mu_e) \sin \phi + 2\mu_i \mu_e \cos \phi + (1 - 2\mu_i \mu_e) e^{-2\mu_e \phi} - \cos \phi] \quad (5)$$

where: v_{mi} is the average speed of the „concrete plug” displacement at the entrance of the curvature zone (quartered bond), v_{rmi} is the average relative speed of the „concrete plug” at the entrance, comparing with the average speed in gravitational field of the „concrete plug” from a height equal with the quartered bond height, $v_{rmi} = v_{mi} / \sqrt{2g R_k}$.

The solution of the differential equation (4) (linear, first order differential equation) is:

$$\omega_{am} = \frac{\omega_m}{\omega_i} = \frac{6R_k \mu_i}{d_t v_{rmi}} \int_0^\phi \frac{\cos \phi}{(v_m/v_{mi})} d\phi - \frac{12\mu_e R_k}{d_t} \int_0^\phi \left(\frac{v_m}{v_{mi}} \right) d\phi. \quad (6)$$

By replacing the expression of the average speed (v_m/v_{mi}) from (5) into (6) it is obtained the angular rotation speed of the „concrete plug” in the quartered bond zone, in which $\omega_i = v_{mi}/R_k$ is the angular speed at the entrance of the curvature zone.

In Figure 3 it is presented the average speed change of the „concrete plug” for a horizontal up to a vertical curvature, upright (upwards).

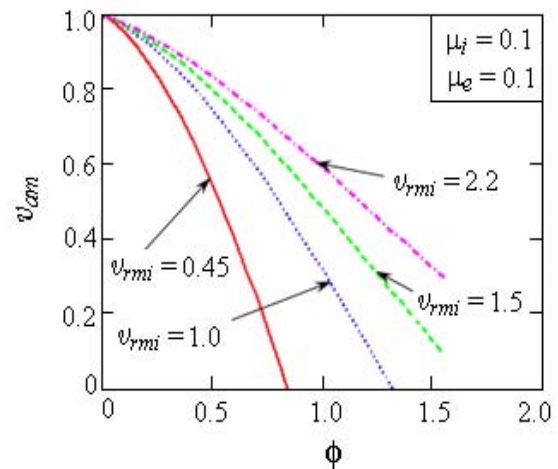


Figure 3. Nondimensional average speed of the „concrete plug”

The relative rotation of the concrete „concrete plug” during the displacement into the quartered bond is presented in Figure 4.

By analyzing the diagrams regarding the average speed decrease in the curvature zone, it is concluded the possibility of pipe blockage, meaning that the concrete can not be pumped any more. Thus, the necessary condition for a pumpable concrete is that for a saturated concrete.

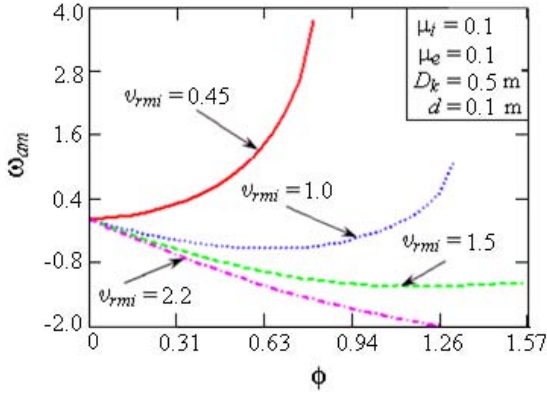


Figure 4. The relative rotation of the concrete „concrete plug” in the pipe’s quarter bond

3. TRIBOLOGICAL CONDITIONS FOR SATURATED CONCRETE

For a correct displacement of the concrete into the pipe it is necessary to respect the continuity and, implicit, a constant flow in any section. Thus, the concrete, as a liquid phase in a solid phase mixture, must flow in pipes with constant inner diameter with constant average speed [4].

In order to establish the necessary pressure gradient along the flow direction of the concrete (as a whole), it is analyzed the case of a quarter bond that bonds a horizontal pipe and an angled pipe in vertical direction by ϕ_e angle (Figure 5).

The flow condition with constant flow rate implies the force equilibrium along the flow direction with constant speed (v_m). Thus, it is determined the pressure difference necessary for the concrete flow in a quartered bond of a horizontal pipe bond with a vertical angled pipe under an ϕ_e angle:

$$\Delta p = p_i - p_e = k_2 (\cos \phi_e - \mu_i \sin \phi_e - 1) + 2k_3 \mu_e \phi_e. \quad (7)$$

where $k_2 = \rho_m g R_k$, (ρ_m – concrete density, g – gravity acceleration, R_k – average radius of the quartered bond curvature), and $k_3 = \rho_m v_m^2 / 2$ is the dynamic pressure in the pipe.

If we have the dimensionless pressure difference Δp_a , against the dynamic pressure k_3 , it results:

$$\Delta p_a = \frac{p_i - p_e}{k_3} = \frac{2gR_k}{v_m^2} (\cos \phi_e - \mu_i \sin \phi_e - 1) + 2\mu_e \phi_e. \quad (8)$$

Figure 6 presents the dimensionless pressure difference as a function of the angle made by the quartered bond in vertical plane with the horizontal line.

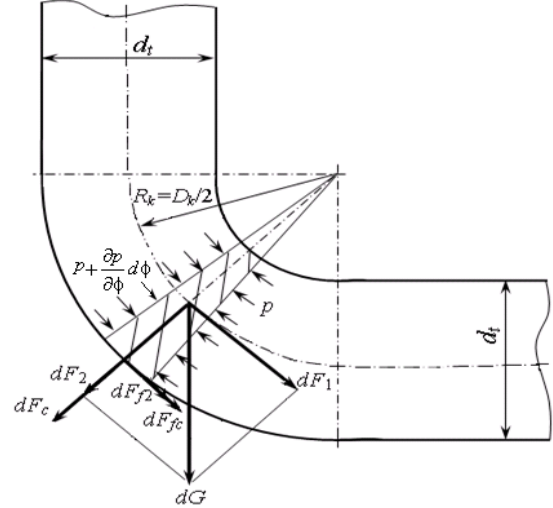


Figure 5. The diagram of the forces for concrete uniform flow in the quarter bond zone

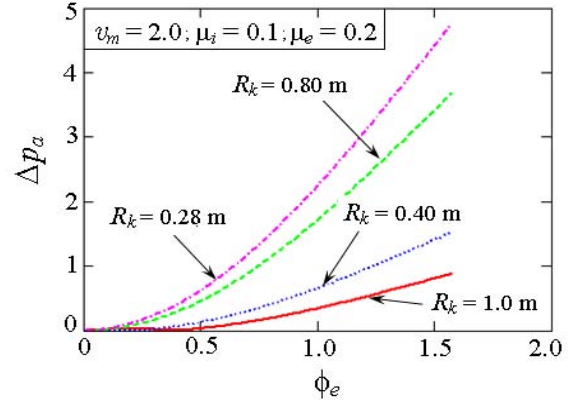


Figure 6. The variation of the dimensionless pressure drop in the pipe’s quarter bond

4. THE WEAR MODEL OF PIPE WITH FRESH CONCRETE IN PUMPING PROCESS

The theory of quasi-static indentation can be used for solid particle impact, which is in fresh concrete. The impact speeds are much smaller than the velocity of elastic and plastic deformation of metallic materials.

On impact the deceleration of solid particle generates the indentation force on the substrate. The impact angle of solid particles in the pipe’s quartered bond is variable. The dimensionless erosion rate (I_{er}) is defined as mass of material removed of pipe per mass of eroding (solid particles in fresh concrete).

We accept the equation of motion of single abrasive particle interacting with the surface (Finnie’s models) [5]. The erosion of ductile or brittle metals comprise two wear mechanisms occurring simultaneously: one caused by cutting action of free moving particles in fluid with impact

angle greater than the critical impact angle; other caused by repeated elastic or plastic deformation during collision with friction (Manson–Miner’s rule) [6].

Figure 7 shows the impact of fresh concrete rigid particle with the pipe wall [7].

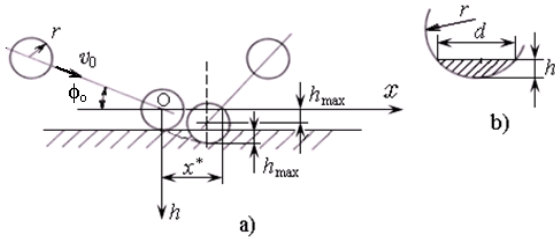


Figure 7. The impact of fresh concrete rigid particle with wall of pipe (a), and the deformed volume (b)

The critical impact angle (ϕ_{cr}) is defined as the angle of particle, which appears a microchip for only one impact. This angle can be calculated by the motion equation of particle and the mechanical properties of target materials [6,7]:

- for the elastic contact between the rigid particle of fresh concrete and the wall of pipe:

$$\phi_{cr}(\mu, v_0) = \arcsin \left[\left(\frac{\sigma_c}{4 \cdot \mu} \right)^{\frac{5}{2}} \cdot \frac{\pi^2 \cdot \theta^2}{v_0 \sqrt{5 \cdot \rho_{ab}}} \right], \quad (9)$$

where μ is the friction coefficient inside the pipe; v_0 – the velocity of the solid particle into the fresh concrete, as a function of the fluid velocity; σ_c – the yield strength of the pipe material; θ – the elasticity parameter of pipe material; ρ_{ab} – the density of solid particle into the fresh concrete.

- for the plastic contact between the rigid particle of the fresh concrete and the wall of pipe:

$$\phi_{crp}(\mu, v_0) = \arcsin \left(\frac{3 e_0^2}{4 \cdot v_0} \cdot \frac{\sigma_c - 2 \mu \cdot HB}{\sigma_c + 2 \mu \cdot HB} \cdot \frac{\sqrt{\sigma_c}}{\sqrt{\rho_{ab}}} \right), \quad (10)$$

where e_0 is the yield specific deformation of the pipe material; HB – the Brinell hardness of the pipe material.

Figures 8 and 9 show the critical angle, as a function of the impact velocity and the friction coefficient.

When the impact angle of particle is smaller than the critical angle, the dimensionless erosion wear rate can be evaluated for three–limit positions of the collision particles:

- 1) $\mu \tan(\phi_0) \geq 1$;
- 2) $0.5 \leq \mu \tan(\phi_0) \leq 1$;
- 3) $\mu \tan(\phi_0) \leq 0.5$.

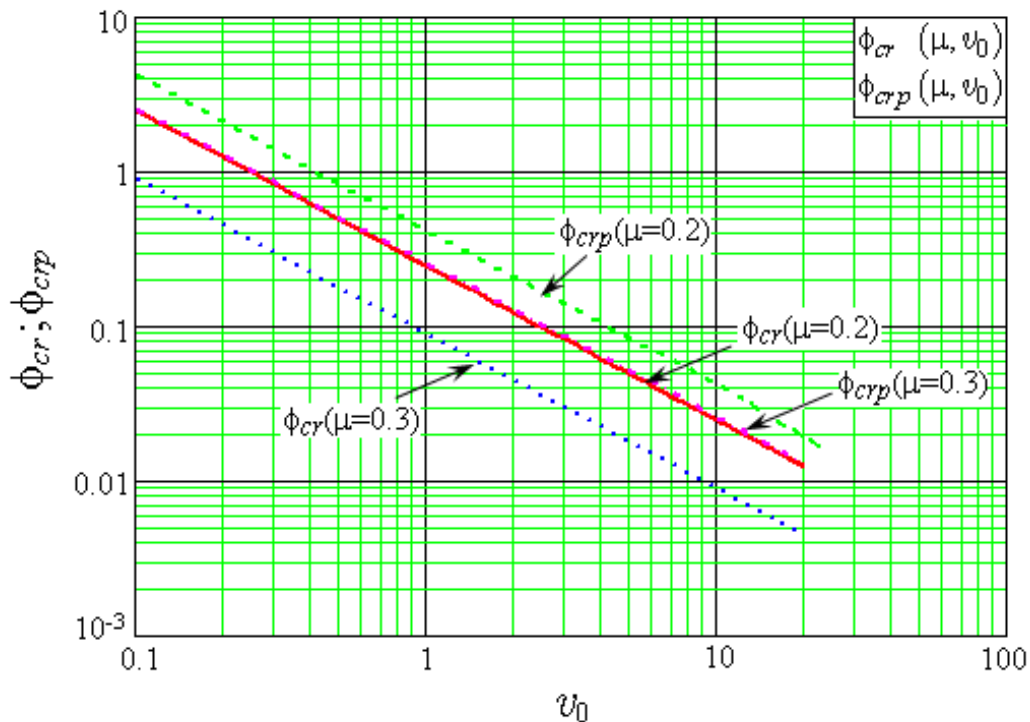


Figure 8. Critical angle vs. impact velocity of fresh concrete

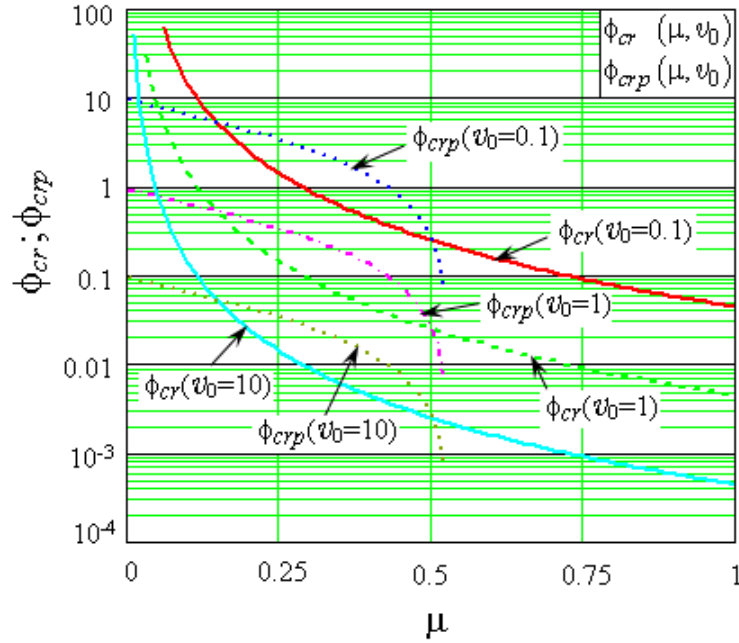


Figure 9. Critical angle vs. friction coefficient of fresh concrete in pipe

The dimensionless erosion rate expression is as follows [8]. For the cases of fresh concrete flow, the erosion rate has the following equations:

- the elastic contact:

$$I_{ere}(\mu, \phi_0, r, v_0, t) = \frac{8}{3} \cdot \frac{\rho_m}{\rho_{ab}} \left(\frac{4 \cdot \mu}{\pi \cdot \sigma_c \cdot \theta} \right)^t \times \left(\frac{5 \cdot \pi}{4} \cdot \rho_{ab} \cdot \theta \cdot v_0^2 \cdot \sin(\phi_0)^2 \right)^{\frac{t+5}{5}} \times H_e(\mu, \phi_0, r, v_0, t), \quad (11)$$

where t is the fatigue parameter of the pipe material, ρ_m – the density of pipe material and H_e – the integral function which has three forms for the limit condition of the collision of the fresh concrete particles;

- the plastic contact

$$I_{erp}(\mu, \phi_0, r, v_0, t) = \frac{8}{3} \cdot \frac{\rho_m}{\rho_{ab}} \left(\frac{\sqrt{\frac{\sigma_c + 2 \cdot \mu \cdot HB}{\sigma_c - 2 \cdot \mu \cdot HB}}}{0.5} \right)^t \times \left(2 \cdot \rho_{ab}^{1/2} \cdot \frac{1}{3 \cdot \sqrt{\sigma_c}} \cdot v_0 \cdot \sin(\phi_0) \right)^{\frac{t+5}{5}} \times H_p(\mu, \phi_0, r, v_0, t). \quad (12)$$

The integral functions H_e or H_p can be evaluated by numerical methods. A comparison between dimensionless erosion rate for all impact angles of the solid spherical fresh concrete particle in transition to horizontal to vertical pipe is given in Figures 10 and 11 in elastic and plastic deformation.

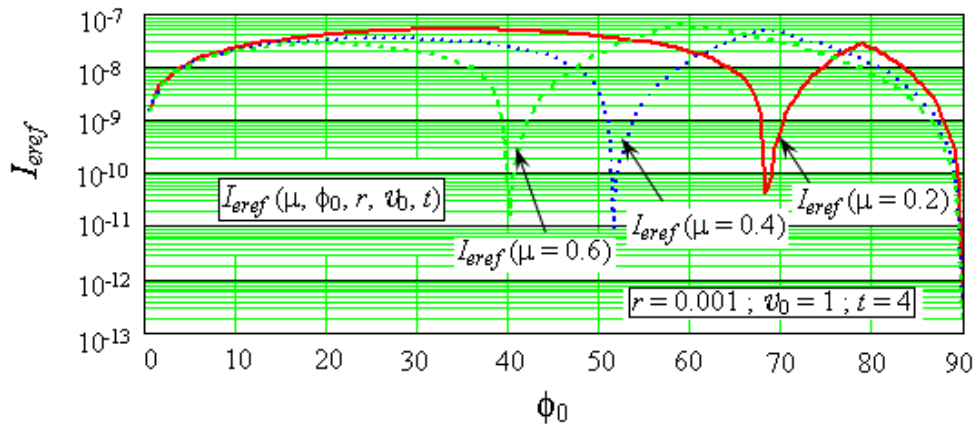


Figure 10. Pipe erosion rate in elastic contact of solid fresh concrete particle vs. impact angle

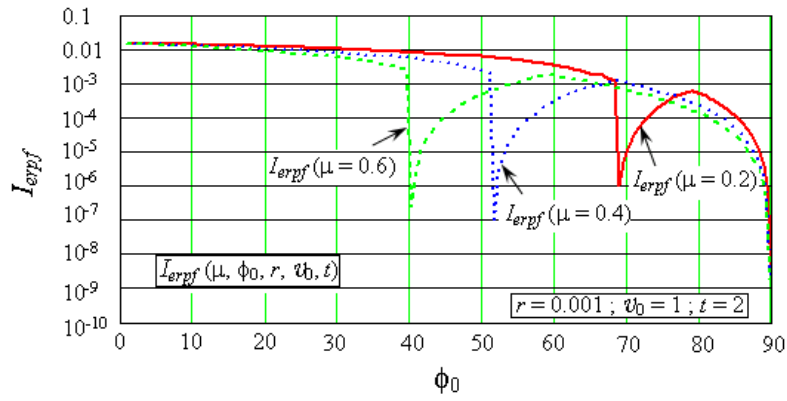


Figure 11. Pipe erosion rate in plastic contact of solid particle fresh concrete vs. impact angle

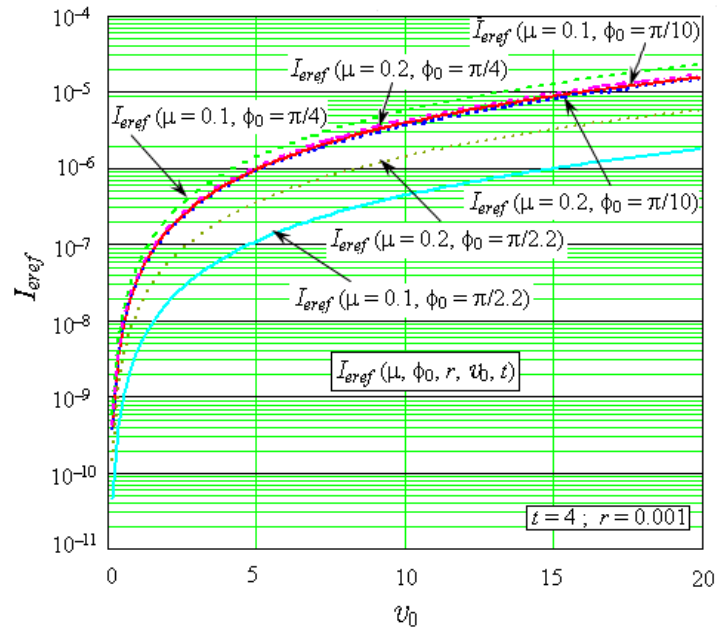


Figure 12. Pipe erosion rate in elastic contact of solid particle fresh concrete vs. velocity

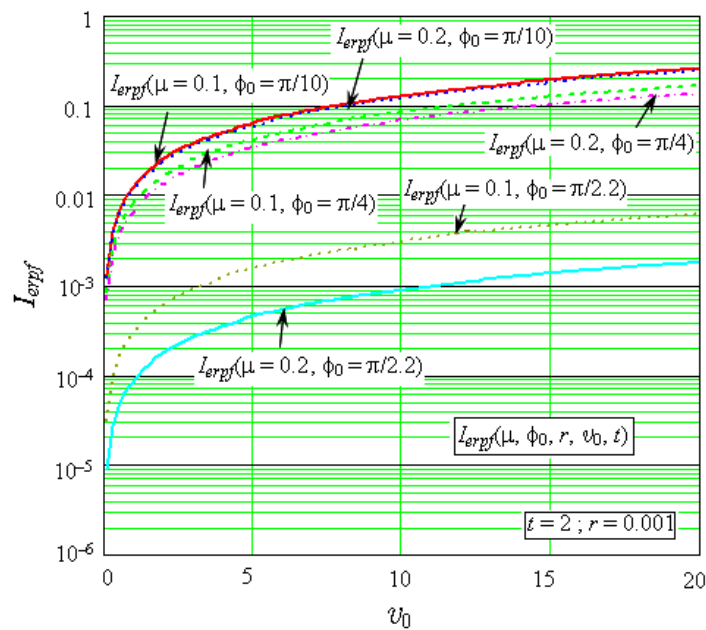


Figure 13. Pipe erosion rate in plastic contact of solid particle fresh concrete vs. velocity

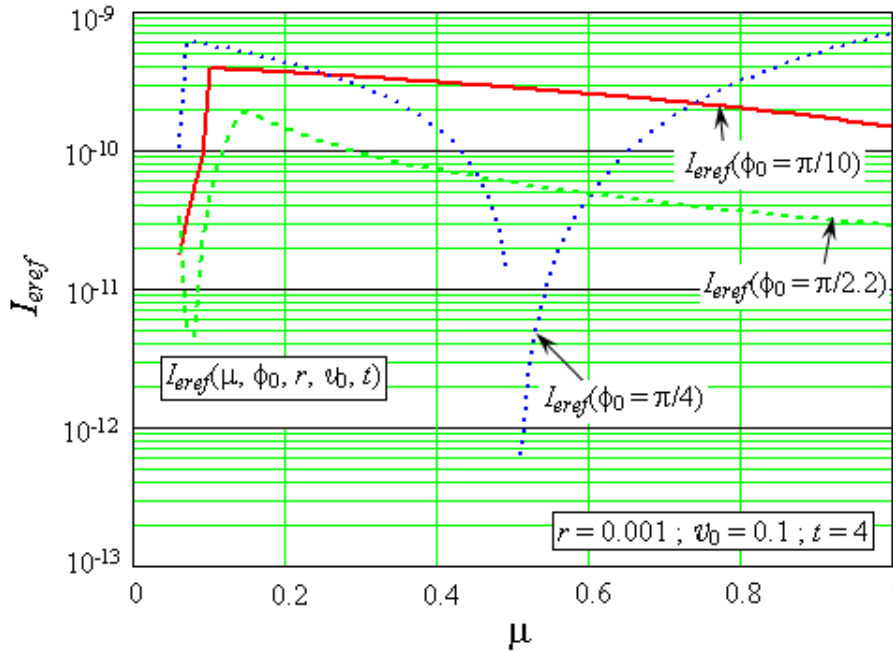


Figure 14. Pipe erosion rate in elastic contact of solid particle fresh concrete vs. friction coefficient

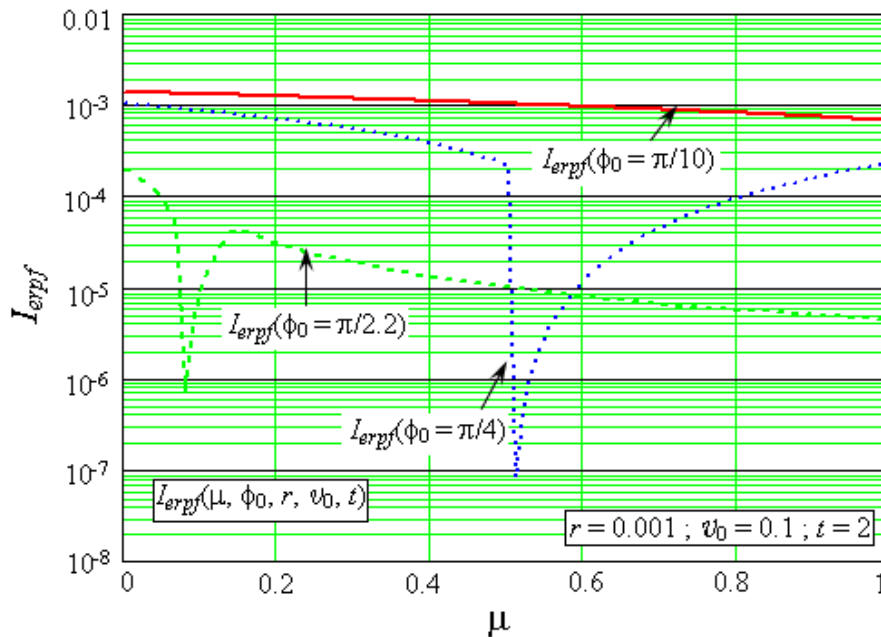


Figure 15. Pipe erosion rate in plastic contact of solid particle fresh concrete vs. friction coefficient

The maximum erosion rate is a function of impact angle of fresh concrete with the vertical direction of pipe, function of friction with the wall and function of velocity of fresh concrete in pipe.

The Figures 12–15 show the effect of velocity and friction coefficient on the erosion rate in elastic and plastic deformation of pipes.

5. CONCLUSIONS

The concrete flow through a circular, curved pipe is different from a circular, straight-lined one.

Thus, the fresh concrete has an axial displacement and angular speed and moves as a „plug”.

The dimensionless contact pressure of fresh concrete increases drastically with the angle of the horizontal pipe in the vertical direction.

The solid particle of fresh concrete acts abrasive and deforms the pipe material. This effect can be used to predict the erosion wear rate in elastic or plastic deformation.

The position of maximum erosive wear rate in the curved pipe is a function of friction and of fresh concrete velocity.

REFERENCES

1. **Balayssac, J.P., Detriche, CH., Grandet, J.**, 1993– “Interet de l’essai d’absorbtion d’eau pour la caracterisation du beton d’enrobage,” *Materials and structures*, 26.
2. **Tattersall, G.H.**, 1983, *The Rheology of Fresh Concrete*, Pitman Publish INC, 1983.
3. **Thomas, N.L. ,Double, D.D.**, 1981, “Calcium and Silicon Concentrations in Solution During the Early Hydration of Portland Cement and Tricalcium Si,” *Cement and Concrete Research*, 11, pp. 675 – 687.
4. **Vlase, M., Tudor, A.**, 2009, *Pumping and Transport of Concrete Through Pipes* (in Romanian), Ed. BREN, Bucure ti.
5. **Finnie, I., McFadden, D.H.**, 1978, On the Velocity Dependence of the Erosion of Ductile Metals by Solid Particles at Low Angles of Incidence, *Wear* 48, pp.181–190.
6. **Kraghelskii, I.V., Dobicin, M.N., Kombalov, V.S.**, 1977, *Osnovi rascetov na trenie i iznos*, Moskva, Ma inostroenie.
7. **Tudor, A.**, 2002, *Frecarea i uzarea materialelor*, Editura Bren, Bucuresti, 2002.
8. **Tudor, A.**, 2003, “An Erosion–Corrosion Wear Model for the Ball Valve Crude Petroleum Extraction Pump,” *Proceeding Nat. Trib. Conf., “ROTRIB 03”*, 24–26 sept, Galati.

(continued from outside back cover)

- 65 S. LE FLOC'H, M.C. CORNECI, A.-M. TRUNFIO-SFARGHIU, M.-H. MEURISSE, J.-P. RIEU, J. DUHAMEL, C. DAYOT, F. DANG, M. BOUVIER, C. GODEAU, A. SAULOT, Y. BERTHIER**
Imagerie Medicale pour Evaluer les Conditions du Fonctionnement Tribologiques des Articulations Synoviales
- 77 M.C. CORNECI, A.-M. TRUNFIO-SFARGHIU, F. DEKKICHE, Y. BERTHIER, M.-H. MEURISSE, J.-P. RIEU, M. LAGARDE, M. GUICHARDANT**
Phospholipides dans le Fluid Synovial - Influence sur le Fonctionnement Tribologique des Articulations Synoviales Pathologiques
- 85 I.C. ROMANU, E. DIACONESCU**
Bioarticular Friction
- 89 A.-M. TRUNFIO-SFARGHIU, M.C. CORNECI, Y. BERTHIER, M.-H. MEURISSE, J.-P. RIEU**
Mechanical and Physicochemical Analysis of the Tribological Operation of Joint Replacements
- 106 D. N. OLARU, C. STAMATE, A. DUMITRASCU, G. PRISACARU**
Rolling Friction Torque in Microsystems
- 113 L. DELEANU, S. CIORTAN**
Evaluating Tribological Damages by 3D Profilometry
- 120 M. RÎPĂ, S. BOICIUC**
Characterisation of Laser Cladding with Ni–Cr–B–Fe–Al Alloy by Profilometric Study of the Scratch Tracks
- 128 M. VLASE, A. TUDOR**
An Analytical Wear Model of the Pipes for Concrete Transportation

CONTENTS

- 1 **A. URZICĂ, S. CRETU**
A Numerical Procedure to Generate Non-Gaussian Rough Surfaces
- 7 **C. CIORNEI, E. DIACONESCU**
Preliminary Theoretical Solution for Electric Contact Resistance between Rough Surfaces
- 12 **C.-I. BARBINTA, S. CRETU**
The Influence of the Rail Inclination and Lateral Shift on Pressure Distribution in Wheel - Rail Contact
- 19 **C. SUCIU, E. DIACONESCU**
Preliminary Theoretical Results upon Contact Pressure Assessment by Aid of Reflectivity
- 27 **S. SPINU**
Numerical Simulation of Elastic-Plastic Contact
- 34 **Y. NAGATA, R. GLOVNEA**
Dielectric Properties of Grease Lubricants
- 42 **J. PADGURSKAS, R. KREIVAITIS, A. KUPČINSKAS, R. RUKUIŽA, V. JANKAUSKAS, I. PROSYČEVAS**
Influence of Nanoparticles on Lubricity of Base Mineral Oil
- 46 **A.V. RADULESCU, I. RADULESCU**
Influence of the Rheometer Geometry on the Rheological Properties of Industrial Lubricants
- 52 **V.-F. ZEGREAN, E. DIACONESCU**
Measurement of Lubricant Oil Microviscosity Based on Resonant Frequency Shift of AFM Cantilever
- 58 **M.C. CORNECI, A.-M. TRUNFIO-SFARGHIU, F. DEKKICHE, Y. BERTHIER, M.-H. MEURISSE, J.-P. RIEU**
Influence of Lubricant Physicochemical Properties on the Tribological Operation of Fluid Phase Phospholipid Biomimetic Surfaces